THE UNIVERSITY of ADELAIDE

A Study of Arching Effect in Soils Incorporating Recycled Tyres

By:

Hamidreza Khatami

A thesis submitted in the fulfilment of the requirements of the degree of

Doctor in Philosophy

School of Civil, Environmental and Mining Engineering,

Faculty of Engineering, Computer and Mathematical Sciences,

The University of Adelaide

September 2018

A Study of Arching Effect in Soils Incorporating Recycled Tyres

By:

Hamidreza Khatami, *M.Sc*.

Supervisors:

Dr An Deng

Prof. Mark Jaksa

A thesis submitted in the fulfilment of the requirements of the degree of

Doctor in Philosophy

School of Civil, Environmental and Mining Engineering,

Faculty of Engineering, Computer and Mathematical Sciences,

The University of Adelaide, SA 5005, Australia

Abstract

The term ‘arching effect’ refers to the phenomenon of stress redistribution in granular materials because of induced differential displacements and/or significant stiffness difference between the substituted and original materials. Arching is frequently observed in different geotechnical practice such as piled and geogrid-reinforced embankments, foundation piles, retaining walls, backfills, tunnelling, buried pipes, and excavation. Knowledge of arching mechanism serves to assist engineers in optimising their soil-structure design.

Investigation of mechanical properties and potential applications of recycled-tyre-based aggregates has been carried out extensively over the last 25 years firstly to exploit the beneficial engineering properties of waste tyres such as their light weight as backfilling material and secondly to mitigate their environmental impact. However, to the author’s knowledge, no previous study of the arching effect in rubber-soil mixtures have been reported in literature at the time of this research. As rubberised soil is gradually establishing its place as a suitable and cost-effective alternative to natural aggregate in geotechnical work, it is worthwhile to have a thorough knowledge of the arching effect in rubber-soil mixtures.

This thesis aims at experimentally investigating the arching effect in a coarse sand and rubber-soil mixtures using the Digital Image Correlation (DIC) technique and stress measurements. Active and passive arching modes in soil and rubberised soil were studied and compared. To do so, a replicate of Terzaghi’s original trapdoor apparatus was manufactured and filled with dyed sand and 10% and 30% (by weight) rubberised sand. Imaging and DIC analysis of the arching effect induced deformation in the trapdoor apparatus for the aforementioned granular material were conducted using VicSnap and VIC-2D computer programs. The distribution regimes of vertical and horizontal displacements

and strains in the specimen cross-sectional area were obtained and interpreted. Additionally, shear strains, major and minor principal strains, and volumetric strains were computed and analysed. The effect of a central 5 kPa surcharge on these variables was also studied. It was observed that the DIC technique provides small-scale information and insights into how and where the arching effect creates zones of different local deformations within soil. The patterns and values of these deformation fields were found to be dependent on the test conditions and material type. As part of the experimental plan, the evolution of stresses over the trapdoor element and its adjacent, static bases, was recorded during the experiments using a number of stress sensors.

Thesis declaration

I, Hamidreza Khatami, certify that this work contains no material which has been accepted for the award of any other degree or diploma in my name, in any university or other tertiary institution and, to the best of my knowledge and belief, contains no material previously published or written by another person, except where due reference has been made in the text. In addition, I certify that no part of this work will, in the future, be used in a submission in my name, for any other degree or diploma in any university or other tertiary institution without the prior approval of the University of Adelaide and where applicable, any partner institution responsible for the joints-award of this degree.

I acknowledge that copyright of published works contained within this thesis resides with the copyright holders of those works.

I give permission for the digital version of my thesis to be made available on the web, via the University's digital research repository, the Library Search and also through web search engines, unless permission has been granted by the University to restrict access for a period of time.

I acknowledge the financial support that I have received from the Adelaide Graduate centre through the Adelaide Scholarship International (ASI) scheme and the Australian Government through an ARC-funded research project. I also acknowledge the editorial services from Professional editor, Ms Leticia Mooney, who provided copyediting and proofreading services for the initial draft of the Chapter 2 of this thesis, according to the guidelines laid out in the university-endorsed national 'Guidelines for editing research theses'.

Signature: Date: 25/09/18

Acknowledgements

I would like to give my sincerest thanks to my wife, Fariba, for her selfless support and patience throughout the course of my PhD studies. She has been my beloved cheerleader from the beginning. I am utterly grateful to my parents and grandparents who have provided me through moral and emotional support in my life. I am also grateful to my other family members and friends who have supported me along the way.

I would like to take this opportunity to thank my principal supervisor, Dr An Deng, for his invaluable support, encouragement, and insightful guidance during the period of my candidature at The University of Adelaide. Without his support and genuine care, I would not be able to complete this thesis. I would like to thank my co-supervisor, Prof. Mark Jaksa, for his constructive suggestions and making time for the timely review of the papers despite an already overloaded schedule. I also would like to thank the technicians of the School of Civil, Environmental and Mining Engineering, especially Gary Bowman, Simon Golding, Ian Cates, Thomas Stanef, and Dale Hudson, for their help and support.

Table of contents

List of figures

List of tables

Notations

δ	Settlement
ε	Strain
ε_1	Major principal strain
ε_2	Minor principal strain
ε_{xx}	Horizontal strain
ε_{yy}	Vertical strain
ε_{xy}	Shear strain
ε_{vol}	Volumetric strain, volume change
ε_n	Normalised displacement
θ	Inclination angle
σ	Stress
σ_{min}	Minimum stress on trapdoor
σ_i	Initial stress on trapdoor
σ_f	Final stress on trapdoor
σ_n	Stress ratio
φ	Angle of internal friction
φ'	Effective angle of internal friction
ψ	Dilation angle
a_t	Arching tangent modulus
CC_{NSSD}	Normalised sum of squared differences criterion
$d\varepsilon$	Strain rate
D_{50}	Diameter that 50% of particles are smaller than
D_{95}	Diameter that 95% of particles are smaller than
$f(x_i, y_j)$	Greyscale intensity function at point (x_i, y_j)
$g(x_i', y_j')$	Greyscale intensity function at point (x_i', y_j')

H	Height
H_n	Normalised height
K	Coefficient of lateral earth pressure
K_a	Rankine's active lateral earth pressure coefficient
K_n	Krynine's active lateral earth pressure coefficient
p_{min}	Minimum stress on trapdoor
t	Shear band thickness
u	Horizontal displacement
v	Vertical displacement
w	Width
∂	partial differential derivative sign

Chapter 1: Introduction

1.1. Background

Approximately 15 million tonnes of tyre are scrapped worldwide every year (Matade, 2016). In Australia, it is estimated that about 500,000 tonnes of scrap tyres are produced annually (http://www.tyrecycle.com.au/). This accounts for over 3% of world waste tyre produced yearly. The main issues associated with waste tyres being stockpiled in large quantities are significant fire hazards and the accompanied air pollution, landscape occupation, and major risk of spreading disease due to vermin sheltered in the abandoned tyres. Rubber tyres are usually manufactured from a blend of natural rubber obtained from the sap of Hevea brasiliensis species or the rubber tree, synthetic rubber derived from petroleum products, and other chemicals such as carbon black and sulphur (Kovac, 1978). Tyres are designed to endure harsh environments and mechanical wear. Therefore, it is only natural to expect a long decomposition process for waste tyres. More specifically, it may take a century for the complete decay of a whole tyre in nature (Bernal, 1996). The large amount of waste tyre produced annually, and the requirements of the environmental protection laws demand effective and sustainable management measures. If the body of a tyre is mechanically sound, re-treading is usually performed to recover the entire tyre (ETRMA, 2013). Otherwise, waste tyres are either recycled and burnt for their calorimetric value as they produce higher energy, which is approximately 35000 kJ/kg, in comparison with coal, which delivers 20000–34000 kJ/kg (Bernal et al., 1996), or shredded for other applications such as geomaterial aggregate in civil engineering projects.

Tyre-Derived Aggregate (TDA) [Fig. 1.1(a)] and rubber-sand mixtures [Fig. 1.1(b)], are the main forms of the use of recycled tyre in geotechnical engineering work. The use of whole tyre tied together in bunches referred to as tyre bales or tyre blocks [Fig. 1.1(c)] in

different projects such as flood embankment (Bo and Yarde, 2006; D'Agostino, 2015), slope stabilisation (Winter et al., 2009), and road construction (Zornberg et al., 2005) is also common.

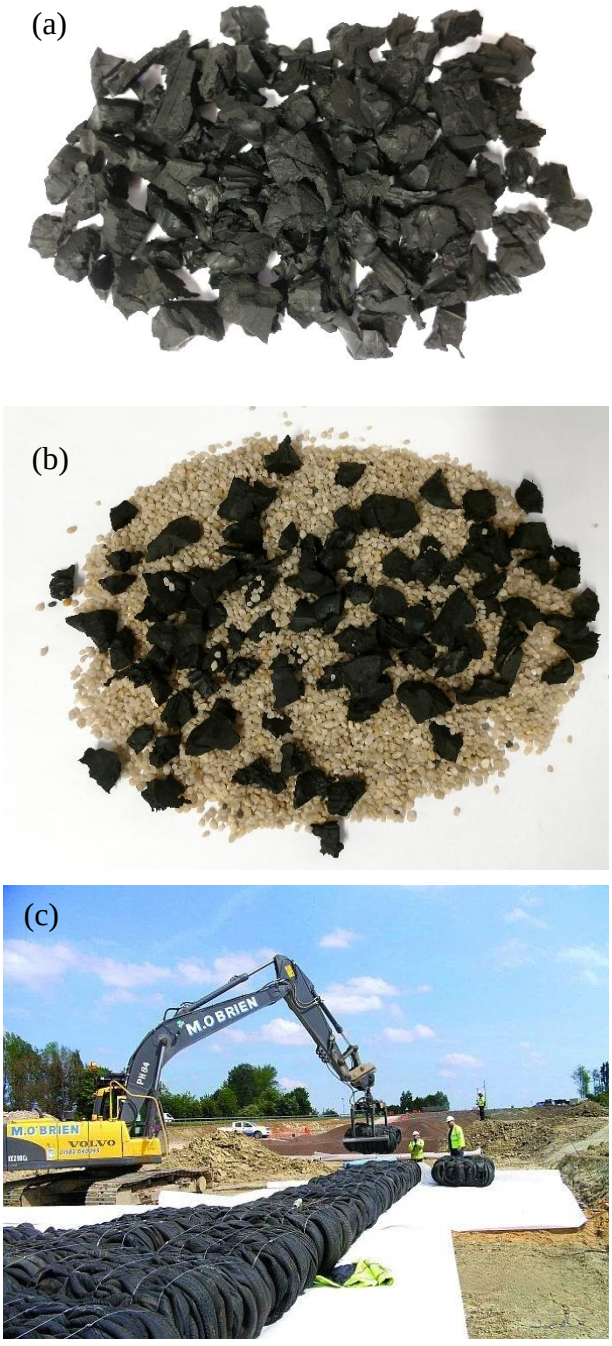

Fig. 1.1. Various types of rubber-based geomaterial: (a) TDA, (b) rubber–sand mixture, and (c) tyre bales, used in the image for road construction in the UK (Source: Goldfingle, 2009, New Civil Engineer website)

Light weight, thermal insulation, high permeability, low horizontal pressures, high damping ratio, and low chemical leachate are considered as the principal and beneficial engineering properties of recycled tyre (Humphrey, 1999; Edil; 2004). According to Ghazavi (2004), waste tyres either as TDA or rubber-soil mixtures are used in civil engineering projects:

- to reinforce soil in road embankment construction;
- to mitigate ground erosion;
- to stabilise slopes;
- as lightweight material for backfilling in retaining structures;
- as aggregate in drainage beds of landfills;
- as additive to asphalt;
- as additive to concrete;
- as sound barrier; or
- as vibration absorbent.

In addition to the above applications, there have been suggestions of other uses for waste tyres. For example, Park et al. (1996, 2003) demonstrated that tyre chips are able to absorb organic chemicals as well as certain heavy metals such as arsenic, mercury, selenium, barium, cobalt and lead. Edil et al. (2004) reported that tyre chips absorb contaminants when installed at locations with high chemicals concentration, probably through the osmosis process. These findings suggest that shredded waste tyres are not only environmentally benign to a great extent but also can be used for water pollution remedies or in septic tanks as chemical absorbent.

Most research so far has focused on the engineering properties and civil applications of TDA. TDA mechanical properties including compressibility, resilient modulus and shear strength parameters for highway and road construction have been studied by Eldin and

Senouchi (1992), Bosscher et al. (1997), Edinçliler et al. (2004), Shalaby and Khan (2005), and Humphrey and Blumenthal (2010). The performance of roads built with TDA depended on tyre chips size, method of placement, and soil-cap thickness and improved when a thick soil-cap was placed on a TDA layer. According to these researchers, TDA showed a high initial plastic compression and a moderate lateral displacement. This would present a challenge for the design engineers. However, it seems that these effects can be mitigated when rubber-soil mixtures are used. Investigations on backfills of retaining walls constructed with TDA have been performed by Humphrey and Sandford (1993), Tweedie et al. (1998), Lee and Roh (2007), and Ahn and Cheng (2014). Lower horizontal pressures and vertical stresses due to TDA lightweight compared to natural soil were reported. Studies on similar applications for rubber-soil mixture have also been conducted; however, these studies are less in number in comparison with the TDA related research. Probably the most important factors driving the research towards rubber-soil applications have been several incidents of self-combustion of thick TDA layers (8 to 15 m) reported by Humphrey (1996), and the substantial compressibility of tyre shreds when used alone. TDAs can also be excessively light for some applications and show low shear strength. Each of these limitations is effectively eliminated by using rubber-soil mixtures instead of TDA. Therefore, this research will focus on rubber-soil geomaterials.

Direct shear tests and triaxial compression tests are the most commonly used methods of evaluating the mechanical properties of TDAs and rubber-soil mixtures. These tests provide shear strength parameters of rubber-soils, i.e. cohesion and angle of internal friction. If tyre shreds have very large particle sizes compared to natural soils, testing of TDAs or rubber-soils becomes challenging. To overcome this problem, large direct shear box apparatuses have been designed and assembled by Moo-Young et al. (2003), Fox (2013) and Xiao et al. (2015). The pre-defined shear plane which may not coincide be the weakest

plane in the matrix is the major drawback of direct shear tests. However, direct shear tests are simple, quick and appropriate for comparison studies. Conversely, modern triaxial machines can accommodate large samples with relatively large particle sizes. Their computerised data acquisition system serves to minimise human error. A considerably wider range of data crucial for geotechnical designing and modelling can be obtained from a triaxial compression apparatus. Datasets for stress-strain curves, volumetric changes, stress paths, cyclic loading responses, and measurement of permeability, all under different confining pressures, are the main advantages of a triaxial apparatus. Stress-strain curves, in particular, are absolutely necessary when a material constitutive model is to be developed or modified. A triaxial compression machine can also be managed in such a way as to incorporate other pieces of equipment for additional data acquisition. For instance, Kikuchi et al. (2010) used a triaxial apparatus equipped with an X-Ray computer tomography (CT) scanner to analyse the deformation of rubberised soils. Using a triaxial compression apparatus, Wu et al. (1997), Lok and Yu (2006), Zornberg et al. (2004), Bałachowski and Gotteland (2007), and Edincliler et al. (2010) carried out experimental investigations into the shear strength of TDAs and rubber-soils. The experimental data from direct shear tests or triaxial compression tests in the literature indicate that TDA shows small cohesion values (3-14 kPa) and internal friction angles in the range of 20° to 37° (Humphrey and Sandford, 1993; Foose et. al, 1996; Bernal et. al, 1997; Strenk et al., 2007; Ahn et al., 2014; Xiao et al., 2015). Since there has been no bonding agent or cementitious materials which would have been able to fuse soil particles together, the cohesion values reported by these researchers have no physical meaning. In other words, these values are mathematical rather than physical and have been obtained by using a mathematical regression for determining the parameters of the Mohr-Coulomb failure criterion. Mathematical regression can sometimes give values that are not necessarily physically meaningful. For this reason, it is

better to use the term cohesion intercept in order to clarify the difference between the actual and apparent cohesions. An increase in shear strength has been observed by a number of researchers when soil was mixed with shredded waste tyre (e.g. Edil and Bosscher, 1994; Tatlisoz et al., 1997; Lee et al., 1999; Zornberg, 2004; Rao and Dutta, 2006; Lok and Yu, 2006; Balachowski and Gotteland, 2007). A dense sand having 30% tyre chips by volume showed high values (as great as 65°) for the friction angle (Foose et al., 1996; Edil, 2004). According to Ahmed and Lovell (1993) and Zornberg et al. (2004) the optimum tyre shred content is approximately 35% by weight.

Over the last three decades, different applications of recycled tyres in civil engineering projects has been subjected to vigorous research. These applications vary from building artificial reefs entirely made of tyres to lightweight backfill incorporating shredded tyres. Because of the extent of earthwork projects, large quantities of recycled tyres in shredded, chipped or ground forms can be used as filler by blending with soils employed in the projects. Processed waste tyres mixed with soils have been introduced as lightweight fills for slopes, retaining walls, and embankments (Tapas and Baleshwar, 2013). For every project, the desired engineering properties of a soil incorporating recycled tyres can be achieved by altering type, gradation and proportion of recycled tyres and/or additives and also geotechnical properties of the soil. For example, the damping capacity of sand mixed with recycled tyre increases. This effect of energy dissipation leads to substantial use of sand-recycled tyre mixtures as substitute soil in seismic areas to reduce the amplitude of ground motions due to earthquake (Abdelhaleem et al., 2013). Designing soil structures require knowledge of mechanical properties of the soil impregnated with recycled tyre and a realistic mathematical model of soil-tyre composite that is called a constitutive model. A constitutive model or equation serves to approximate and predict the response of a material to the applied forces under a given set of physical conditions. Attempts to provide

constitutive models to predict the behaviour of a soil-tyre or soil-tyre-cement mixtures has been done by Lee et al. (1999) and Yeung (2006).

1.2. Research aims

The aims of this research thesis are summarised as follows:

1. To examine the applicability of the Digital Image Correlation (DIC) technique for displacement and strain analyses in granular soil, to identify the most relevant factors for successful implementation of the technique, and to assess the full-field deformation characteristics of sand subjected to arching;
2. To identify the key differences in the arching deformation of sand and rubber–sand backfills, particularly the strain localisation;
3. To analyse and compare the stress redistribution behaviour of sand and rubber–sand backfills at geomaterial–structure interface; and
4. To investigate the effect of a local surcharge on the stress and deformation response of sand and rubberised sand backfill subjected to arching.

1.3. The arching effect

Arching effect in soils refers to the process of stress transfer from a yielding part of soil to the adjacent stationary parts. This active arching phenomenon was first theorised by Terzaghi (1943) using the trapdoor apparatus shown in Fig. 1.2. When the trapdoor with the width of $2B$ moves downward, the shear resistance of the soil tends to oppose the displacement of the soil and maintain the soil in its original position. To do so, the shear strength of the soil is mobilised which results in a stress reduction on the moving soil mass while increasing the stresses on the static bases.

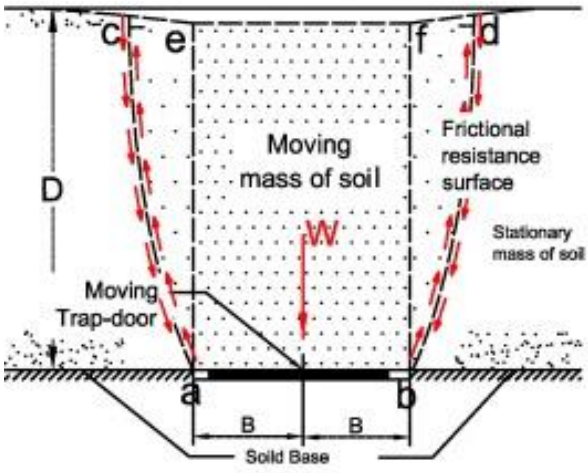

Fig. 1.2. The idealised trapdoor test and shear strength mobilisation of soil (after Pardo and Sáez, with permission from Elsevier)

Assuming ideal vertical slip lines, and performing a limit equilibrium analysis for a soil obeying the Mohr-Coulomb shear resistance relationship, Terzaghi (1943) obtained the following general expression to predict the vertical stress values (σ_v) on the trapdoor centre:

$$\sigma_v = \frac{B\cdot\gamma - c}{K\cdot tan\varphi}\left(1 - e^{-K\cdot\frac{z}{B}tan\varphi}\right) + q\cdot e^{-K\cdot\frac{z}{B}tan\varphi} \quad (1.1)$$

where γ, c, z, K, φ, and q represent the soil unit weight, soil cohesion, backfill depth, the ratio of horizontal to vertical stresses at depth z, the angle of internal friction, and a uniform surface surcharge. Iglesia et al. (2013) summarised the evolution of the arch shape with the trapdoor displacement as depicted in Fig. 1.3. At very small displacements, a curved arch is formed above the trapdoor. With increased displacement, the arch is then refined to a triangular arch and finally a rectangular arch. Eq. (1.1) by Terzaghi (1943) presents the stress value on the trapdoor at the final stage of arching shown in Fig. 1.3(c). More complex arch shapes depending on the height of the soil backfill was identified by Rui et al. (2016) using imaging techniques (Fig. 1.4). There are two schools of thought regarding the angle of slip planes from the vertical direction: the inclination angle of shear or failure planes in the soil are either equated to the angle of internal friction, φ, or the dilation angle, ψ. The former is

shown in Fig. 1.3 while the latter is presented in Fig. 1.5. These are discussed in more details in the following chapters. The height of the arch can therefore be calculated geometrically if the appropriate inclination angle is selected.

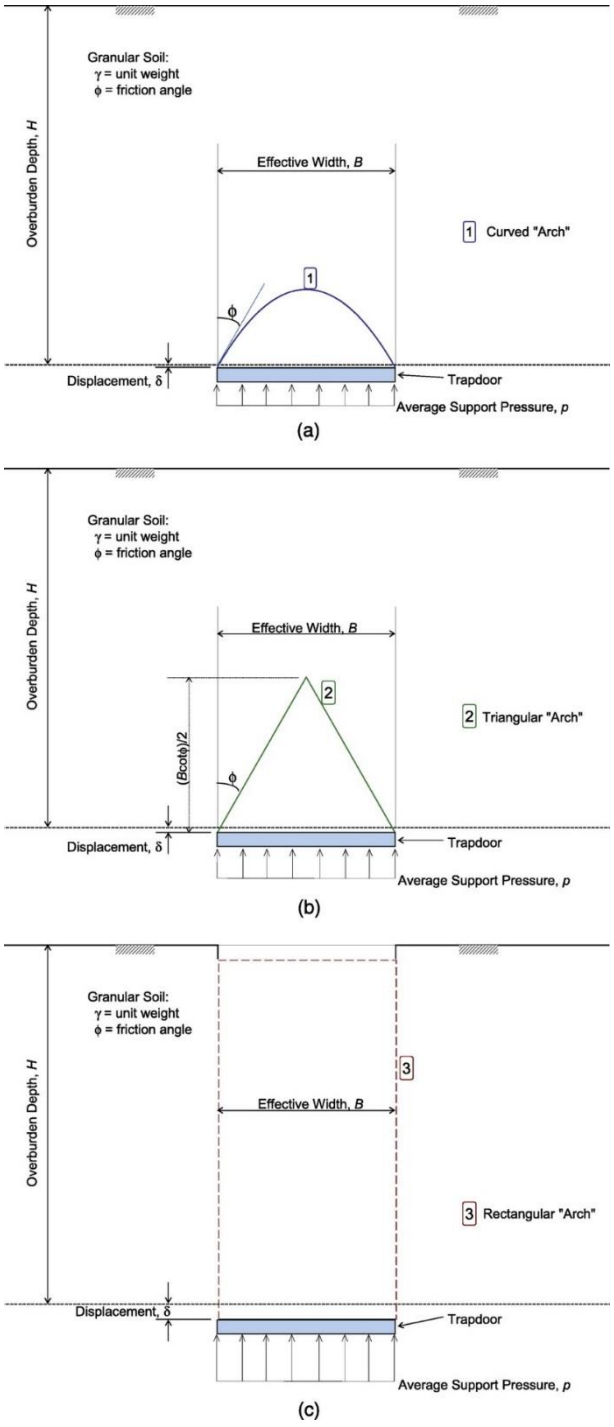

Fig. 1.3. Shape of arch in a granular soil (after Iglesia et al., 2013; with permission from the American Society of Civil Engineers)

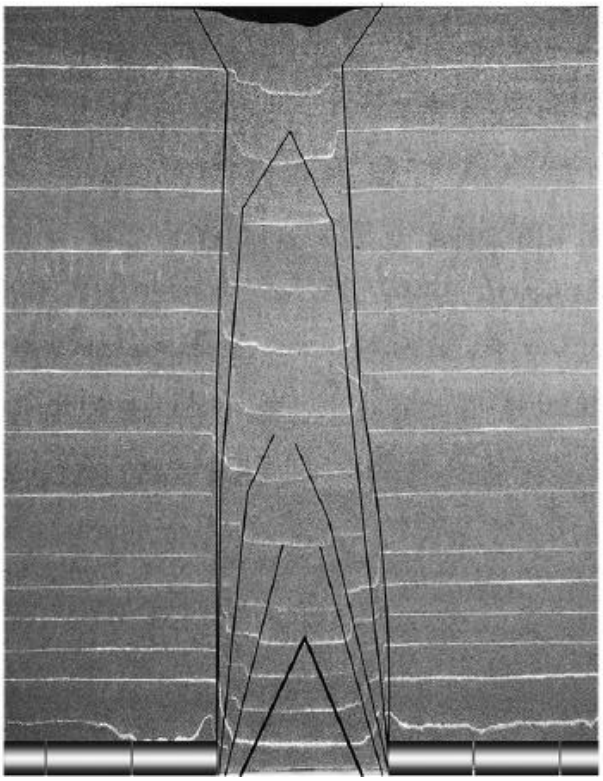

Fig. 1.4. Gradual development of complex arch shapes in a sand backfill with particle range of 0.2–0.425 mm, height of 600 mm, and trapdoor width of 150 mm (after Rui et al., 2016; with permission from ASTM International)

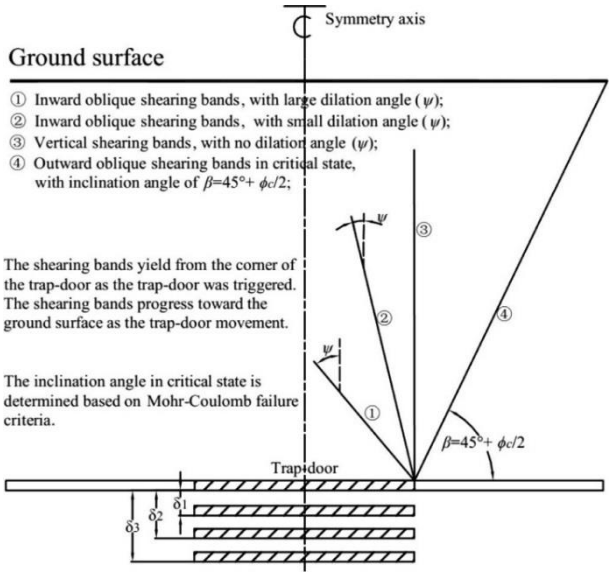

Fig. 1.5. Change of the inclination angle with displacement in a trapdoor (after Zhang et al., 2016; with permission from Elsevier)

Arching is particularly expected when the properties of the filling material are different from those of the ground encompassing the space being filled. The arching effect can work in favour of the geotechnical engineer. Simulation of arching effect in rubber–sand is a new area for research. The 'trapdoor' experiment is the conventional setup to investigate arching effect in soils and used by many researchers, e.g. Terzaghi and Peck (1948), Dewoolkar et al. (2007), Costa et al. (2009) and Pardo and Sáez (2014). Mathematical modelling of the arching effect by using different approaches, e.g. finite element method, discrete element method, and development of differential equations with analytical solutions, has also been performed by Pardo and Sáez (2014), Lai et al. (2014), and Lu and Miao (2015). In all of these studies, simplifying assumptions and ideal conditions such as spherical particles, no volume change due to shearing, and drained state of soil were investigated.

In the current study, the Digital Image Correlation (DIC) technique is used as the main tool for the study of arching effect in sand and rubberised sand backfills. The DIC technique that was developed at the University of South Carolina, US, in the 1980s (Peters and Ranson, 1982; Sutton et al., 1983) is now considered as a successful and widely accepted method in experimental mechanics for deformation measurements. High resolution digital images of a material subject to deformation are continuously being captured as the loading progresses. These images are then compared with each other and a tracking of displacement of marked pixels within the successive material images is recorded in a computer database. Following the imaging process, a numerical analysis using suitable computer codes is carried out to determine the displacements. Once the displacements are obtained, horizontal, vertical, and shear strains are mapped. According to McCormick and Lord (2010), images can be obtained from a wide variety of sources including conventional charge-coupled device (CCD) or consumer digital cameras, high-speed video, macroscopes, and

microscopes, including scanning electron and atomic force microscopes. Once strains have been determined using the DIC technique, if required, stresses within soil or rubberised soil can be back-calculated from the strain values using an appropriate constitutive model (e.g., linear elastic model).

1.4. The outline of the thesis

This research work consists of six chapters and is presented in the format of 'a thesis by publication'. Chapter 1 briefly introduces the rubber–sand geomaterial, its applications and engineering properties, and provides a background to the arching effect in granular material and a concise review of the DIC application in geotechnical engineering in the past. Chapters 2–5 comprise four papers submitted to different peer-reviewed journals.

Chapter 2 includes a paper submitted to *Computers and Geotechnics* and presents the experimental results of the active arching effect in sand using the trapdoor apparatus. A comparison of different mathematical models developed in the past to predict the stress reduction on the trapdoor element is presented. The outputs of these models are then compared with the stresses measured using miniature pressure sensors. The accuracy of the DIC system used throughout of this research and the detailed procedure for image analysis is also examined in this chapter. The horizontal and vertical displacements and vertical strains developed in the sand layer as a result of the trapdoor movement are discussed in detail.

Chapter 3 includes a paper submitted to the *ASCE Journal of Geotechnical and Geoenvironmental Engineering* and presents the results of DIC experiments on a shallow sand layer subjected to active and passive arching in a trapdoor apparatus. Proper alignment of camera and the sand specimens and the appropriate imaging speed for the sand are discussed. Shear strains and shear band characterisation in the sand layer are studied in great

details. Major and minor principal strains and volume change due to the movement of the trapdoor element are obtained and interpreted. Idealised strain localisation and critical volume change regions in the sand layer are presented. The effect of a local surcharge placed above the trapdoor element on the surface on shear, principal, and volumetric strains are also investigated.

Chapter 4 includes a paper submitted to *Geotextiles and Geomembranes* and presents the results of the evaluation of the active arching effect in backfills constructed with sand and two rubber–sand mixtures with different rubber contents. The mathematics of the DIC technique used for the deformation analysis of the backfills is briefly discussed. Displacement and strain regimes developed in the sand and rubber–sand backfills due to lowering the trapdoor are presented. From the DIC results, the arch of equal displacement is introduced. The settlement of sand and rubber–sand backfills are compared. The mechanical behaviour the structure–geomaterial interfaces is investigated using the measurements from several stress sensors lined up on the interfaces. Ground response curves are developed for sand and rubber–sand mixtures. The active arching moduli for these geomaterials at small normalised displacements also obtained.

Chapter 5 includes a paper submitted to the *Canadian Geotechnical Journal* and presents the experimental results of passive arching occurred in a trapdoor apparatus with sand and rubberised sand backfills. Deformability of these backfills subjected to passive arching was investigated using the DIC technique. The distribution of horizontal and vertical displacements and strains in the backfills are compared. Shear strains and the direction of failure planes in the trapdoor apparatus are particularly discussed in more details. It is shown that the angle of inclination of shear bands in the passive arching equates to the dilation angle and not the angle of internal friction. An alternative expression for the dilation angle using the Mohr's circle of strains is presented. From a series of stress measurement experiments,

the passive arching modulus at small normalised displacements is obtained for the sand and rubberised sand backfills. It is shown that the addition of rubber to sand results in lower increase rates in the stresses arose from the passive arching effect.

In the final chapter, the overall conclusions and contributions of the current research thesis are summarised. Potential areas for future work are also discussed in Chapter 6.

References for Chapter 1

Abdelhaleem, A. M., El-Sherbiny, R. M., Lotfy, H., Al-Ashaal, A. A. (2013). Evaluation of rubber/sand mixtures as replacement soils to mitigate earthquake induced ground motions. Proceedings of the 18th International Conference on Soil Mechanics and Geotechnical Engineering, Paris, 2-5 September, pp. 3163–3166.

Ahmed, I., Lowell C.W. (1993). Rubber soils as lightweight geomaterials. Transportation Research Record 1422.TRB, National Research Council of USA, Washington DC.

Ahn, I. S., Cheng, L. (2014). Tyre derived aggregate for retaining wall backfill under earthquake loading. Construction and Building Materials 57: 105–116.

Ahn, I., Cheng, L., Fox, P., Wright, J., Patenaude, S., Fujii, B. (2014). Material properties of large-size tyre derived aggregate for civil engineering applications. Journal Material Civil Engineering: 04014258.

Bałachowski, L, Gotteland, P. (2007). Characteristics of tyre chips-sand mixtures from triaxial tests. Archives of Hydro-Engineering and Environmental Mechanics 54 (1): 25–36.

Bernal, A. (1996). Laboratory study on the use of tire shreds and rubber sand in backfills and reinforced soil applications. PhD Thesis. Purdue University.

Bernal, A. Salgado, R., Swan, R. H., Lovell. C.W. (1997). Interaction between tyre shreds, rubber-sand and geosynthetics. Geosynthetics International 4(6): 623–643.

Bernal, A., Lovell, C. W., Salgado. R., (1996). Laboratory study on the use of tire shreds and rubber-sand in backfilled and reinforced soil applications. Publication FHWA/IN/JHRP-96/12. Joint Highway Research Project, Indiana Department of Transportation and Purdue University, West Lafayette, Indiana.

Bo, M. W., Yarde, A. (2006). Use of waste tyre bales to construct a flood embankment. Proceedings of the Institution of Civil Engineers - Waste and Resource Management 159 (2): 57–64.

Bosscher, P. J., Edil, T. B., Kuraoka, S. (1997). Design of highway embankments using tyre chips. Journal of Geotechnical and Geoenvironmental Engineering 123 (4): 295–304.

Costa, Y. D., Zornberg, J. G., Bueno, B. S., Costa, C. L. (2009). Failure mechanisms in sand over a deep active trapdoor. Journal of Geotechnical and Geoenvironmental Engineering 135 (11): 1741–1753.

D'Agostino, S. J. (2015) The use of tyre bales to raise ground levels behind a fragile floodwall at London Gateway Port. Proceedings of Geotechnical Engineering for Infrastructure and Development: XVI European Conference on Soil Mechanics and Geotechnical Engineering, M. G. Winter, D. M. Smith, P. J. L. Eldred and D. G. Toll (editors) pp. 825–830.

Dewoolkar, M. M., Santichaianant, K., Ko, H.-Y. (2007). Centrifuge modelling of granular soil response over active circular trapdoors. Soils and Foundations 47(5): 931–945.

Edil, T. B. (2004). A review of mechanical and chemical properties of shredded tyres and soil mixtures. In “Recycled Materials in Geotechnics”, Aydilek, A., Wartman, J. (eds.), ASCE Geotechnical Special Publication No. 127.

Edil, T. B., Park, J. K., Kim, J. Y. (2004). Effectiveness of scrap tyre chips as sorptive drainage material. Journal of Environmental Engineering 130 (7): 824–831.

Edil, T.B., Bosscher, P. J. (1994). Engineering properties of tyre chips and soil mixtures. Geotechnical Testing Journal 17(4): 453–464.

Edinçliler, A., Baykal G., Dengili, K. (2004). Determination of static and dynamic behaviour of recycled materials for highways. Resources, Conservation and Recycling 42: 23–237.

Edincliler, A., Cabalar, A. F., Cagatay, A., Cevik, A. (2010). Triaxial compression behaviour of sand and tire wastes using neural networks. Neural Computing and Applications 21(3): 441–452.

Eldin, N. N., Senouti, A. B. (1992). Use of scrap tyre in road construction. Journal of Construction Engineering and Management 118: 561–576.

European Tyre and Rubber Manufacturers Association (ETRMA) annual report, 2013.

Foose, G. J., Benson, C. H., Bosscher, P. J. (1996). Sand reinforced with shredded waste tyres. Journal of Geotechnical Engineering 122 (9): 760–767.

Fox, P. J. (2013). Direct shear test of type B TDA. Interim Report, California Department of Resources Recycling and Recovery (CalRecycle), Sacramento, CA.

Ghazavi, M. (2004). Shear strength characteristics of sand mixed with granular rubber. Geotechnical and Geological Engineering 22: 401–416.

Goldfingle, G. (2009). Recycled tyre bales: Tread carefully https://www.newcivilengineer.com/recycled-tyre-bales-tread-carefully/5208902.article, Accessed September 2018.

Humphrey D. N. (1996). Investigation of exothermic reaction in tyre shred fill located on SR 100 in Ilwaco, Washington. Report to Federal Highway Administration.

Humphrey, D. N. (1999). Civil engineering applications of chipped tyres. Research Report, North Platte, Nebraska.

Humphrey, D. N., Sandford, T. C., (1993). Tyre chips as lightweight subgrade fill and retaining wall backfill. Proceedings of the Symposium on Recovery and Effective reuse of Discarded Materials and By-Products for Construction of Highway Facilities, Federal Highway Administration, Washington, D.C.

Humphrey, D., Blumenthal, M. (2010). The use of tyre-derived aggregate in road construction applications. Green Streets and Highways 2010: An interactive Conference on the State of the Art and How to Achieve Sustainable Outcomes. Weinstein, N., ed., Reston, VA, USA: American Society of Civil Engineers, 2010.

Iglesia, G. R., Einstein, H. H., Whitman, R. V. (2013). Investigation of soil arching with centrifuge tests. Journal of Geotechnical and Geoenvironmental Engineering 140 (2): 04013005.

Kikuchi, Y., Hidaka, T., Sato, T., Hazarika, H. (2010). Deformation characteristics of tyre chips–sand mixture in triaxial compression test by using X-Ray CT scanning. in Advances in Computed Tomography for Geomaterials: GeoX 2010 (eds K. A. Alshibli and A. H. Reed), John Wiley & Sons, Inc., Hoboken, NJ, USA.

Kovac, F. J. (1978). Tyre technology. 5th edition, Goodyear Tyre and Rubber Co., London.

Lai, H. J., Zheng, J. J., Zhang, J., Zhang R. J., Cui, L. (2014). DEM analysis of ‘‘soil’’-arching within geogrid-reinforced and unreinforced pile-supported embankments. Computers and Geotechnics 61: 13–23.

Lee, H. J., Roh, H. S. (2007). The use of recycled tire chips to minimize dynamic earth pressure during compaction of backfill. Construction and Building Materials 21: 1016–1026.

Lee, J. H., Salgado, R., Bernal, A., Lovell, C. W. (1999). Shredded tyres and rubber sand as lightweight backfill. Journal of Geotechnical and Geoenvironmental Engineering 125(2): 132–141.

Lok, T. M. H., Yu, H. J. (2006). Laboratory study on the mechanical behaviour of tyre chip–sand mixture. Pavement Mechanics and Performance, Geotechnical Special Publication No. 154, GeoShanghai, pp.157–164.

Lu, W., Miao, L. (2015). A simplified 2-D evaluation method of the arching effect for geosynthetic-reinforced and pile-supported embankments. Computers and Geotechnics 65: 97–103.

Matade, S. P. (2016). Need to regulate end-of-life tyres market in India. RubberAsia website, https://www.rubberasia.com/2016/06/11/need-to-regulate-end-of-life-tyres-market-in-india/ accessed September 2018.

McCormick, N., Lord, J. (2010). Digital image correlation. Materials Today 13(12): 52–54.

Moo-Young, H., Sellasie, K., Zeroka, D., Sabnis, G. (2003). Physical and chemical properties of recycled tyre shreds for use in construction. Journal of Environmental Engineering 129(10): 921–929.

Pardo, G. S., Sáez, E. (2014). Experimental and numerical study of arching soil effect in coarse sand. Computers and Geotechnics 57: 75–84.

Park, J. K., Kim, J. Y, Edil, T. B. (1996). Mitigation of organic compound movement in landfills by shredded tyres. Waste Environment Research, 68(1): 4–10.

Park, J. K., Kim, J. Y, Edil, T. B., Huh, M., Lee, S. H., Lee, J. J. (2003). Suitability of shredded tyres as a substitute for a landfill leachate collection medium. Waste Management and Research 21(3): 278–289.

Peters, W. H., Ranson, W. F. (1982). Digital imaging techniques in experimental stress analysis. Optical Engineering 21:427–431.

Rao, G. V., Dutta, R. K. (2006). Compressibility and strength behaviour of sand–tyre chip mixtures. Geotechnical and Geological Engineering 24(3): 711–724.

Rui, R., Van Tol, A. F., Xia, Y. Y., Van Eekelen, S. J. M., Hu, G. (2016). Investigation of soil-arching development in dense sand by 2D model tests. Geotechnical Testing Journal 39 (3): 415–430.

Shalaby, A., Khan, R. A. (2005). Design of unsurfaced roads constructed with large-size shredded rubber tyres: a case study. Resources, Conservation and Recycling 44: 318–332.

Strenk, P., Wartman, J., Grubb, D., Humphrey, D., Natale, M. (2007). Variability and scale-dependency of tyre-derived aggregate. Journal Material Civil Engineering 19(3): 233–241.

Sutton, M. A., Wolters, W. J., Peters, W. H., Ranson, W. F., McNeill, S. R. (1983). Determination of displacements using an improved digital correlation method. Image and Vision Computing 1:133–139.

Tapas, D., Baleshwar, S. (2013). Benefits and impacts of scrap tyre use in geotechnical engineering. Journal of Environmental Research and Development 7(3): 1262–1271.

Tatlisoz, N. Benson, C. H., Edil, T. B. (1997). Effect of fines on mechanical properties of soil-tyre chip mixtures. Testing Soil with Waste or Recycled Materials, Wasemiller, M.A. & Hoddinott K. B. (Eds.), ASTM STP 1275, West Conshohocken, 93–108.

Terzaghi K. (1943). Arching in ideal soils. In: Theoretical soil mechanics, chapter V. John Wiley and Sons, New York

Terzaghi, K., Peck, R. B. (1948). Soil mechanics in engineering practice, Wiley, New York.

Tweedie, J. J., Humphrey, D. N. Sandford, T. C. (1998). Full scale field trials of tyre shreds as lightweight retaining wall backfill, at-test condition. Preprint, Transportation Research Board, Washington, D.C.

Winter, M. G., Williammee, R., Prikryl, W. (2009). Application of tyre bales to slope failure repair. Proceedings of the Institution of Civil Engineers - Engineering Sustainability 2009 162 (3): 145–153.

Wu, W., Benda, C., Cauley, R., (1997). Triaxial determination of shear strength of tyre chips. Journal of Geotechnical and Geoenvironmental Engineering 123(5): 479–482.

Xiao, M., Ledezma, M., Hartman, C. (2015). Shear resistance of tyre derived aggregate (TDA) using large-scale direct shear tests. Journal of Materials in Civil Engineering 27(1), DOI: 10.1061/(ASCE)MT.1943-5533.0001007, 04014110.

Yeung, T. (2006). Constitutive model development for lightly cemented scrap rubber tire chips. PhD Thesis, Hong Kong University of Science and Technology.

Zhang, H., Zhang, P., Zhou, W., Dong, S., Ma, B. (2016). A new model to predict soil pressure acting on deep burial jacked pipes. Tunnelling and Underground Space Technology 60: 183–196.

Zornberg, J. G., Cabral, A. C., Viratjandr, C. (2004). Behaviour of tire shred–sand mixtures. Canadian Geotechnical Journal 41(2): 227–241.

Zornberg, J. G., Christopher, B. R., Oosterbaan, M. D. (2005). Tyre bales in highway applications: feasibility and properties evaluation. Colourado Department of Transportation, Report No. CDOT-DTD-R-2005-2, Denver, Colourado.

Statement of Authorship

Title of Paper	An experimental study of the active arching effect in soil using the digital image correlation technique
Publication Status	☐ Published ☐ Accepted for Publication ☑ Submitted for Publication ☐ Unpublished and Unsubmitted w ork w ritten in manuscript style
Publication Details	

Principal Author

Name of Principal Author (Candidate)	Hamidreza Khatami		
Contribution to the Paper	Performed the literature review, conducted the experiments, gathered the data, analysed and interpreted the results, and drafted the manuscript.		
Overall percentage (%)	80%		
Certification:	This paper reports on original research I conducted during the period of my Higher Degree by Research candidature and is not subject to any obligations or contractual agreements with a third party that would constrain its inclusion in this thesis. I am the primary author of this paper.		
Signature		Date	19/09/18

Co-Author Contributions

By signing the Statement of Authorship, each author certifies that:

i. the candidate's stated contribution to the publication is accurate (as detailed above);

ii. permission is granted for the candidate in include the publication in the thesis; and

iii. the sum of all co-author contributions is equal to 100% less the candidate's stated contribution.

Name of Co-Author	An Deng		
Contribution to the Paper	Methodology and reviewing.		
Signature		Date	19/09/18

Name of Co-Author	Mark Jaksa		
Contribution to the Paper	Methodology and reviewing.		
Signature		Date	19/09/18

Please cut and paste additional co-author panels here as required.

Chapter 2: An experimental study of the active arching effect in soil using the digital image correlation technique

Abstract

This paper presents the results of an experimental investigation of the active arching effect in soils using the Digital Image Correlation (DIC) technique. A trapdoor apparatus was filled with a mixture of dyed and natural sand. The redistributions of the loads over the trapdoor and its adjacent, fixed sides, were recorded during the experiments using 15 stress sensors. The distribution regime of displacements in the vertical and horizontal directions, and the vertical strains within the specimen cross-sectional area, were obtained and interpreted. The effect of a surcharge on these variables was also investigated. It was observed that the DIC technique provides rich, small-scale information and insights into how and where the active arching effect creates zones of different local deformations within the soil.

Keywords: Arching effect, digital image correlation, strain analysis, sand.

2.1. Introduction

According to Terzaghi (1943), the arching effect in soil is one of the most frequently encountered phenomena, both in the field and in the laboratory. Civil and mining engineers have long dealt with situations in which arching has played a role in the distribution of loads. In a general sense, *arching* refers to the redistribution of stresses within a medium. The arching effect accompanies the processes of inclusion of a foreign matter into the ground, partial removal of soil or rock, and backfilling of underground voids (Ladanyi and Hoyaux, 1969; Sloan et al., 1990; Singh et al., 2010; Wang et al., 2017). In addition to difference in stiffness, relative displacements in soil, due to partial yielding, induces an arching effect within soil (Terzaghi, 1943; Bosscher and Grey, 1986). Arching has been reported to occur at very small scales, e.g. in the vicinity of, and over, soil stress sensors (Talesnick, 2005), and at large scales, such as in dual underground tunnels (Lee et al., 2006). There have been many research studies in which the practical applications of the arching effect have been examined. For example, geogrid-reinforced and pile-supported embankments, and foundation piles (Zou et al., 2008; Shelke and Patra, 2008; Lai et al., 2014; Lu and Miao, 2015); retaining walls (Nadukuru and Michalowski 2012); mine backfill design (Li, 2014; Ting et al. 2014); excavations in clay (Habash and Writtle, 2002); and soft soil reinforced with stone columns (Indraratna et al. 2013; Basack et al., 2016).

The arching effect has been extensively studied since Terzaghi's first investigation in 1936. The original 'trapdoor' apparatus, and the later, slightly modified variations of both the procedure and apparatus, are commonly used for investigating the arching effect in soils (Rui et al., 2016). The working principle of Terzaghi's trapdoor apparatus is to place a rectangular prism of soil on a bed that has a controllable, moving component in the centre; the so-called 'trapdoor'. The trapdoor can be moved away from the soil or pushed into the

soil. Each scenario disturbs the soil's original geostatic stress regime in a different way. When the trapdoor is lowered, the stresses will immediately be transferred to the stationary parts of the soil, hence creating an active arching effect. When the trapdoor is raised, the stresses on the trapdoor will be increased, while the stresses on the stationary parts of the soil will be decreased (passive arching). In addition to Terzaghi and Peck (1948), who first proposed the design of a trapdoor apparatus, many recent researchers, including Dewoolkar et al. (2007), Costa et al. (2009) and Pardo and Sáez (2014), have also used this apparatus. With an exception of a three-dimensional (3D) cylindrical apparatus with a square trapdoor (Chevalier and Otani 2011), the experimental literature has so far mentioned two-dimensional (2D) trapdoor apparatuses for the study of the arching effect in soil. A limited number of researchers have conducted centrifuge tests on the trapdoor apparatus (Iglesia 1991; Dewoolkar et al. 2007; Costa et al. 2009). It was observed that increased gravitational acceleration (g) remarkably raised the stress level and changed the formation of shear bands. Multiple failure surfaces were detected under high g conditions, while a single failure surface developed under normal gravity conditions.

Past experimental studies have mainly focused on the measurement of the stresses on the surface of the trapdoor apparatus components that are beneath the soil prism when active arching occurs. Various instruments, such as load cells (Sadrekarimi and Abbasnejad, 2010; Chevalier and Otani, 2011; Iglesia et al., 2014; Pardo and Sáez, 2014), pressure sensors (Moradi et al., 2015), and submillimeter, area-pressure profilers, known as tactile pressure sensors (Paikowsky et al., 2003), have been implemented. In each of these studies, a decrease in load or pressure values was observed over the trapdoor area the moment it yielded. An increase in those values for the adjacent, stationary parts was also recorded.

This study extends the body of work outlined above by investigating the active arching effect in soil due to relative displacements in the soil, using the Digital Image

Correlation (DIC) technique and stress measurement on the lower boundary of soil. The DIC technique has not been used extensively in the past to investigate the arching effect phenomenon in soil. However, imaging has been a common element of previous experimental arching effect investigations in order to determine failure surfaces, displacement patterns and surface subsidence (Vardoulakis et al., 1981; Tanaka and Sakai, 1993; Papamichos et al., 2001; Costa et al., 2009). The DIC technique has recently been employed by Pardo and Sáez (2014) and Jenck et al. (2014) for the study of the arching effect, and the particle displacement field above the trapdoor was obtained. The current study aims at assessing stress evolution during arching in a trapdoor apparatus. It also seeks to measure the displacements and strains within a soil cross-section using the DIC technique to evaluate the soil deformation conditions that lead to arching. The effect of applying a local surface surcharge placed above the trapdoor area on the displacement, strain, and stress regimes is investigated.

2.2. Material and methods

This section summarises the soil characteristics, the experimental procedure the instruments used to measure displacement and the stress in the present research.

2.2.1. Soil properties

A coarse-graded sand supplied by Sibelco, South Australia, and commercially branded as sand 8/16 was used in the experiments. The values of 8 and 16 refer to the upper and lower American mesh sizes of the sand particles. Sieve analysis of the soil showed that 98% of the particles were in the range of 1.18 to 2.36 mm. Sand 8/16 is a white-to-yellowish siliceous

sand (99% SiO_2) with angular grains, produced for filtration and drilling applications. The dry minimum and maximum densities of the sand were determined according to the Australian Standard AS 1289.5.5.1 (Standards Australia, 1998a) and found to be 1.49 and 1.71 g/cm^3, respectively. The sand specimens in the trapdoor apparatus had a density of 1.66 g/cm^3. This corresponds to a relative density of 79% and a medium dense consistency. The angle of shear resistance of the sand at this density was 45° as determined by performing direct shear tests following the procedure described by the Australian Standard AS 1289.6.2.2 (Standards Australia, 1998b).

2.2.2. Displacement and stress measurements

The displacement of the trapdoor was monitored by placing a linear variable displacement transducer (LVDT) under the trapdoor. The LVDT was connected to a data acquisition (DAQ) device and the LabView software developed by National Instruments Corporation, USA. The data from the transducer were displayed in real-time on a computer screen to control the displacement of the trapdoor.

Two sets of pressure sensors, calibrated to maximum pressures of 30 and 40 kPa by the manufacturer, a data acquisition system and recording software, were supplied by Jincheng Test Instrument Factory, China. The sensors are cylindrical in shape, with a diameter of 28 mm and a height of 7 mm, and they employ piezoelectric pressure transducer technology. That is, when a mechanical pressure is applied to the surface of the piezoelectric material, an electrical charge proportional to the amount of applied pressure is generated. This charge is then translated into pressure units using a calibration factor, supplied by the manufacturer and confirmed using a Fluke-100*g* electric pressure calibrator device.

2.2.3. The DIC system

The DIC technique developed at the University of South Carolina, USA, in the 1980s (Peters and Ranson, 1982; Sutton et al., 1983), is now a widely accepted method in experimental mechanics for strain measurements. The DIC technique applies mathematical computations to estimate the spatial transformation of a series of images. Translations and distortions in the captured images are determined using various mathematical correlation functions and criteria. According to Hall et al. (2010) and Stanier et al. (2016), a number of developments using the DIC concept have emerged, not only within solid mechanics, but also in fluid mechanics, where the procedure is often referred to as Particle Image Velocimetry (PIV). In addition to the mechanical sciences, the DIC concept has been applied in more diverse fields, such as medical imaging and the motion picture industry (Hall et al., 2010). The technique works by continuously capturing high resolution digital images of a material that is subject to deformation, as loading progresses. These images are then compared with a reference image, and displaced pixels are identified. The displacement of the identified pixels in the successive images is recorded in a computer database. Following this process, numerical analysis using computer software is carried out to determine the displacements and strains with spatial coordinates in a grid format. Many companies and researchers have developed bespoke DIC-PIV algorithms for displacement and strain assessments. For example, VIC-2D and VIC-3D from Correlated Solutions, USA, Q-400 and Q-450 from Dantec Dynamics, Denmark, Ncorr an open-source, MATLAB-based DIC software by Blaber et al. (2015), and GeoPIV a free software developed by Stanier et al. (2016). In this research, two commercially available computer programs, namely VicSnap for image acquisition, and VIC-2D for DIC analysis, and the imaging equipment from Correlated Solutions, USA, were employed for strain analysis.

The experimental apparatus adopted in the present study represents a plane-strain problem and, hence, a 2D DIC system is used, which incorporated a monochrome 2.8-megapixel, conventional charge-coupled device (CCD) camera with a USB3 interface for fast image transfer. It had a sensor size of 7.18 × 5.32 mm and a maximum resolution of 1,928 × 1,448 pixels. The camera lens was a 75-mm Fujinon prime lens with an aperture size range of 1/22-1/2.8. This lens has minimal distortion, therefore, no correction for distortion was necessary.

VicSnap is the standard tethering software for the DIC system, which connects the camera to the computer. It enables the user to observe the captured images on a monitor, and remotely manipulate the imaging conditions, such as resolution, lighting conditions, focus area, exposure times, and allows the images to be saved. The camera enabled the capturing of full-resolution images at a rate of 26 frames per second (fps) in VicSnap. The added advantage of this type of camera is that the user can increase the imaging speed by reducing the resolution.

2.2.4. Experimental procedure

As mentioned in Section 2.1, the Sand 8/16 particles used in the present study were off-white to yellowish in colour. This natural colouration was considered improper for the DIC analysis. Therefore, as the first step in the DIC technique procedure, the surface of the soil specimen was prepared by applying a random speckle pattern. To create this pattern, approximately one third of the mass of the sand specimen was dyed using a water-based matte, black paint. Because specular reflections of natural and artificial light usually interfere with the camera setup and affect the subsequent analysis, a matte paint was used to treat the surface of the specimen to minimise the unfavourable effects of reflection. The black-graded

sand was mixed with the naturally coloured sand and poured into the trapdoor apparatus to a height of 250 mm. The trapdoor apparatus was a rigid cuboid container with an approximate area of 1 × 1 m and a depth of 200 mm, as shown in Fig 1(a). The trapdoor apparatus was large enough to mitigate the effect of the walls on the sensors' readings. The walls were fabricated from transparent acrylic sheets to facilitate imaging. The trapdoor itself was 160 mm wide, and, together with the side stationary bases, was made of rigid timber. The ratio of soil height to trapdoor width was therefore $H/w \approx 1.56 \leq 2$. This corresponds to a shallow trapdoor experiment (Costa et al., 2009). A block of concrete with the same width as the trapdoor was constructed so that a 5 kPa surcharge could be applied to the surface if needed. The surcharge is about 125% of the soil vertical stress. The surcharge was positioned above the trapdoor, on the surface of the soil specimen, in such a way that the centre points of the trapdoor and the surcharge created a vertical line.

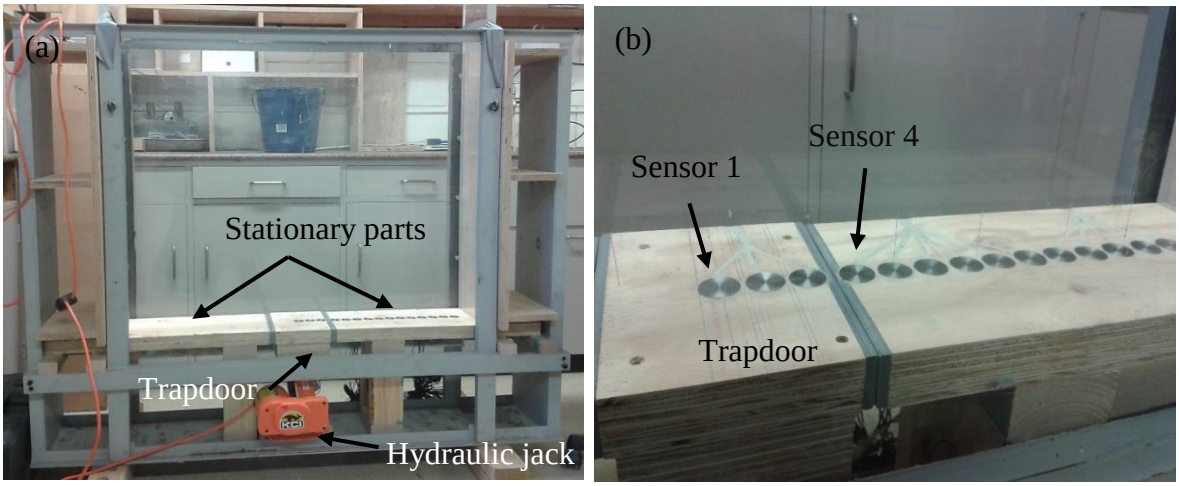

Fig. 2.1. The trapdoor apparatus: (a) overview; and (b) stress sensor arrangement. The sensors are numbered from left to right; such that Sensor 1 is placed in the centre of the trapdoor and Sensor 15 is located at the far right-hand-side of the stationary part of the apparatus.

The arrangement of the sensors in the trapdoor apparatus are shown in Fig. 2.1(b). The stress sensors were fixed into holes drilled to match the diameter and thickness of the sensors, as shown in Fig 1(b). In this way, the upper surface of the sensors was flush with the surface of the timber. This arrangement ensured that the presence of the sensors did not disturb the natural stress regime in the soil. The centre-to-centre spacing of the sensors was 30 mm. Due to the axisymmetric nature of the trapdoor apparatus, all the sensors were placed on one side of the apparatus. The centre of the first sensor (Sensor 1) coincided with the centre of trapdoor. A total of 15 sensors were used, as shown in Fig. 2.1. The stress sensor sampling frequency adopted throughout the testing was 16 Hz.

The container was gradually and carefully filled with layers of the mixture of dyed and naturally-coloured sand using a scoop, while being mildly compacted and leveled with a tamper. This process was conducted to attain the desired relative density. Each layer of soil was 10 mm thick. The soil grains were poured into the apparatus in a random manner by air pluviation, which facilitates the creation of a specimen with minimal internal structure that would otherwise significantly affect test results, such as pressure sensor readings.

The DIC camera was positioned in front of the trapdoor in such a way that the whole region required for strain analysis would be included in the image frame. To obtain accurate 2D image correlation results, the specimen must be planar and parallel to the camera sensor. The camera centre was placed at the same height and lateral position as the centre of the specimen. The trapdoor was then moved 35 mm downwards, at a rate of 3.5 mm/s, using an electrically-controlled hydraulic jack. The displacement values of the trapdoors were observed and recorded using the LVDT installed beneath the trapdoor, also at a rate of 16 Hz. Several test-runs and imaging sessions were carried out initially to determine the appropriate resolution and imaging speed for the DIC analysis. This stage required generating specimens, filming, and analysing the images using VIC-2D. If pattern

degradation appeared in the results, then the imaging speed was increased. The camera resolution adopted, in both the horizontal and vertical directions, was set to 960 × 600 pixels (equivalent to an area of 500 × 312 mm^2) via the VicSnap user interface. This resulted in gaining the camera's highest possible imaging speed of 160 fps for this resolution. Image capture was conducted continuously until the trapdoor had travelled downwards a total of 35 mm. However, the DIC results presented below are pertinent to trapdoor downward displacements of up to 3 mm. Pattern degradation was observed, with respect to correlation, for trapdoor movements of greater than 4.5 mm due to the large soil deformation.

2.2.5. The DIC analysis procedure

DIC analysis generally begins by uploading three types of images; namely, calibration image(s), a reference image and a number of speckle images. In the 2D DIC, one calibration image will usually suffice. It serves to provide geometrical information of the object being imaged. A so-called calibration target, which incorporates large dot grid patterns with known distances used in this study, is shown in Fig. 2.2(a). A reference image was then selected. In the traditional DIC, the term 'reference image' refers to an image taken at the beginning of the experiment, when the specimen is still intact and undeformed [Fig. 2.2(b–c)]. This reference image remained the same for the entire image correlation analysis and it contained the area of interest (AOI). This is the area within which knowledge of deformations is required [Fig. 2.2(d)]. In the DIC technique, a number of small, square image patches that are identical in size are tracked in the AOI, rather than individual particles. These patches are called subsets and comprise the entire AOI. The size of the subsets determines the computational 'costs' and precision of the strain analysis. The remainder of the speckle

images recorded during the experiments went through the correlation analysis, compared with the reference image, and provided deformation datasets.

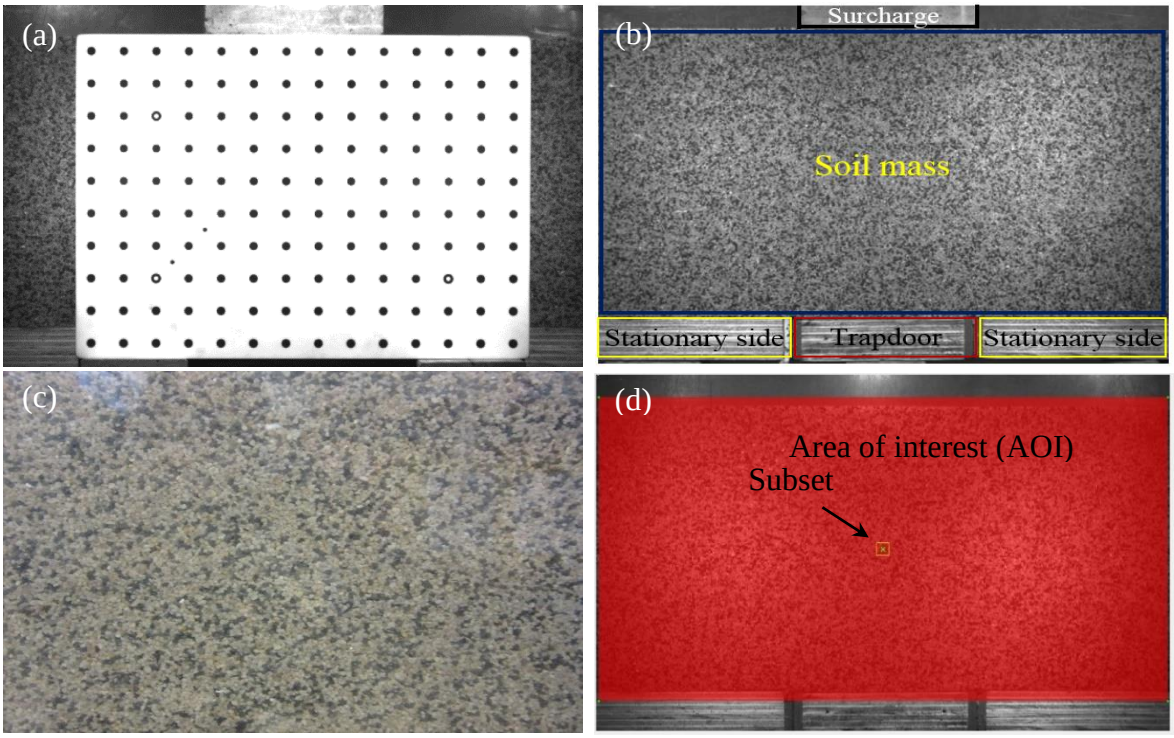

Fig. 2.2. Some image elements of the DIC used; (a) calibration target with 28 mm grid spacing placed over the entire trapdoor apparatus; (b) a typical monochrome reference image of the general specimen case; (c) close-up of the speckle pattern of the soil; and (d) a typical area of interest in the reference image and subset size for the DIC analysis.

In the existing DIC techniques, the subset size is $(2n+1) \times (2n+1)$ pixels, where n is an integer. The correlation technique is centre-weighted and thus only odd numbers can be used for subset size. The minimum subset size is determined by the size of the smallest speckle. Therefore, subsets must contain both the black and white regions, irrespective of their area proportion. The final subset size must be chosen in such way that each subset, although being equal in size, would contain a unique speckle pattern within itself. While large subsets become distinguishable from neighbouring subsets, they yield coarser and less

accurate deformation results (Pan et al., 2008). On the other hand, small subsets tend to generate noisy deformation results (Pan et al., 2008). Consequently, a compromise is required as to the subset size. VIC-2D provided a recommended subset size of 21 × 21 pixels (approximately 11 × 11 mm). This was large enough to ensure that each subset had a unique speckle pattern, without missing information and generating too much noise. In addition to the subset size, two more parameters were needed, the step and filter sizes. The step size dictates the number of points that will be calculated. A step size of 5 was specified, implying that output data points will be obtained every 5 pixels. Large steps can lead to pattern degradation, while small steps can considerably increase the analysis time. The filter size defines the size of the smoothing area for the data calculated. The default filter size in VIC-2D is 21 and this value was adopted as it was deemed suitable. A large filter size results in a very coarse representation of the strain distribution pattern while reducing the output precision significantly. Following the above steps, the strain calculation was completed using a Lagrangian strain tensor.

2.3. Results and discussion

The average initial value for the geostatic stress, from the readings of the 15 sensors where no local surcharge was applied, was approximately 0.3 kPa higher than the theoretically expected value. This is a very good outcome and is consistent with the established fact that the stress sensors used for dry soil usually over-represent the true stresses (Kirby, 1992). When a surcharge was placed on the soil surface, the stress values essentially increased in Sensors 1 to 7. The remaining sensors also showed a marginal increase in stress. While the trapdoor was gradually lowered from its original position to 35 mm downwards, the measurement of stresses and imaging were carried out simultaneously. For each testing

scenario, a fresh soil specimen was generated. The results of stress measurements and image correlation analysis are presented below.

2.3.1. Stress measurement during arching

Figs. 2.3 and 2.4 show the ratio of final measured stress values (σ_f) divided by their initial values (σ_i) as recorded by the 15 stress sensors when the trapdoor was moved downwards to different distances, i.e., 1, 3, 5, 10, 15, 20 and 35 mm. Fig. 2.3 corresponds to the no-surcharge case and Fig. 4 to the 5 kPa central load case. In Fig. 4, the initial stress refers to the value subsequent to the placement of the surcharge load and prior to the trapdoor being activated. The results indicate that when the trapdoor was lowered, the stresses decreased in each of the three trapdoor sensors, regardless of whether a surcharge was applied or not. The amount of decrease depended on the location of the measurement as well as the travel distance of the trapdoor. The stress decrease percentage was not uniform over the width of the trapdoor.

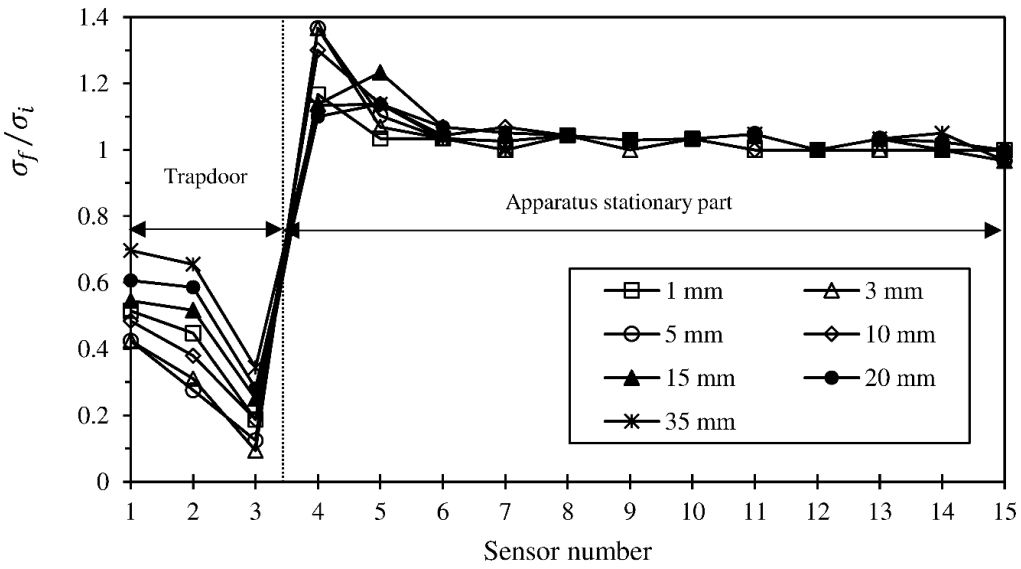

Fig. 2.3. The ratio of final to the initial stress values (σ_f/σ_i) recorded by the stress sensors when the trapdoor travelled downwards under no surcharge condition.

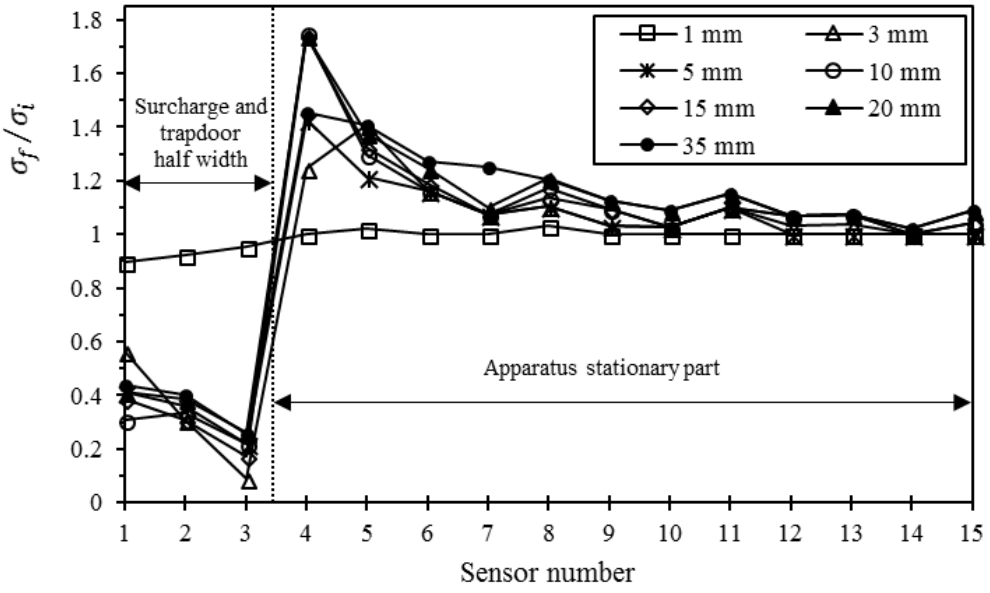

Fig. 2.4. The ratio of final to the initial stress values (σ_f/σ_i) recorded by the stress sensors when the trapdoor travelled downwards under a 5 kPa central surcharge condition.

In the no surcharge load situation (Fig. 2.3), the stress sensor placed in the middle of the trapdoor (Sensor 1) showed a stress reduction of about 30–60% for different trapdoor translations. This was followed by Sensor 2, which registered a reduction of 35–70%. However, the stress value recorded by the sensor closer to the edge of the trapdoor (Sensor 3) resulted in the greatest reduction of 65–90%. The data presented in Fig. 2.3 also show an approximate 5–40% increase in the stresses measured by the two sensors immediately adjacent to the trapdoor on the stationary part. The stress values then gradually level off to their pre-arching values, for the remaining sensors on the stationary part. The stresses on the trapdoor initially deceased with increased trapdoor movement below a maximum travel distance of ≈ 3.5 mm (2.15% of the trapdoor width). Further lowering of the trapdoor to 20 mm and 35 mm resulted in a modest increase in the stresses on the trapdoor. This observation is consistent with other researchers' findings (e.g. Terzaghi 1936, Chevalier and Otani 2011, Han et al, 2017). It should be noted that the stress ratio values are still smaller than the pre-

arching ratio of unity. In Fig. 2.3, the stress ratio in the sensors remote to the trapdoor area showed a slight increase of roughly 3–7%. Moreover, it can be seen from Fig. 2.3 that the disturbance in the soil stress regime due to arching is more pronounced over roughly 38% of the trapdoor width on each side of the trapdoor edges.

As shown in Fig. 2.4, a similar trend can be observed when the surcharge was applied. The three sensors on the trapdoor indicated different reduction percentages depending on their location when the trapdoor was lowered. Sensors 1 to 3 recorded stress reductions of 10–70%, 8–82% and 5–95%, respectively, when the trapdoor was lowered by 35 mm. Here, the minimum stress ratio was reached at a trapdoor displacement of 5.5 mm (3.4% of the trapdoor width), which is almost half of the value when no surcharge was applied. A stress increase of up to 80% was registered by the two sensors placed on the stationary part immediate adjacent to the trapdoor edge (Sensors 4 and 5). It should be noted that the application of a surcharge also resulted in an extension of the arching zone to three sensors on the stationary part (about 56% of trapdoor width), as depicted in Fig. 2.4. The overall decrease in the stresses, in the case of no surcharge, was in the range of 30–90%, while when a surcharge was applied, this range changed to 10–95%. The maximum increase in the stresses, on the other hand, increased from 40% to 80% when a surcharge was applied. Lowering the trapdoor from its zero position to 1 mm resulted in a considerable arching effect when no surcharge was applied (Fig. 2.3). However, for the same trapdoor translation, the arching effect was negligible, when a surcharge was applied. A further comparison of Figs. 2.3 and 2.4, indicates that applying a surcharge extends the zone of increased stresses from 38% to 56% of the trapdoor width, on the stationary side. The maximum stress reduction was 5% higher when the surcharge was applied. The trapdoor travel at which the minimum stress ratio was achieved also increased from 3.5 mm to 5.5 mm due to the 5 kPa

surcharge. Application of the surcharge further increased the stresses on the stationary side from 5–40%, where no surcharge was applied, to 40–80%.

Several theoretical approaches have been developed to predict the minimum value of stress ratio at the centre of a trapdoor for the case of active arching with no surcharge. Some of these that have been reviewed by Iglesia et al. (2014) are summarised in Table 2.1. A comparison of the measured and calculated values of the minimum stress ratio (p_{min}), according to different theoretical approaches, are also presented in Table 2.1. As can be seen from Table 2.1, for coarse-grained soil, p_{min} in most cases is related to Rankine's active lateral earth pressure coefficient (K_a), soil height (H), trapdoor width (w), and the internal friction angle (φ) of the soil. Rankine's active lateral earth pressure coefficient was calculated from Eq. (2.1):

$$K_a = tan^2(45° - \frac{\varphi}{2}) \tag{2.1}$$

However, Ladanyi and Hoyaux (1969) adopted Krynine's lateral earth pressure coefficient (Krynine, 1945), denoted by (K_n), and included, in their mathematical formulation, the rise of a structural arch (f) in Engesser's (1882) approach (cited by Iglesia et al., 2014). These two parameters are calculated as follows:

$$K_n = \frac{1}{1+2\,tan^2\varphi} \tag{2.2a}$$

$$f = \frac{w \cdot \tan\varphi}{4} \tag{2.2b}$$

Terzaghi (1943) assumed equal horizontal and vertical stresses at the trapdoor depth (also shown in Table 2.1) to obtain a match between the experimental and theoretical minimum stress ratios (Han et al., 2017). On the other hand, Iglesia (1991) proposed the following equation for the lateral earth pressure coefficient:

$$K' = \frac{cos^2\varphi}{1+ sin^2\varphi} \tag{2.3}$$

Table 2.1 compares the theoretical approaches mentioned above with the measured minimum stress values in this research. The mathematical models of Evans (1983) and Terzaghi (1943) with respectively 17% and 27% differences for the trapdoor centre, and Iglesia's (1991) and Terzaghi's (1943) models with respectively 18% and 22% differences for average of three sensor readings on the trapdoor were closest to the experimental data in this study. In all cases, the predicted p_{min} was lower than the measured value. The issue of overestimation or underestimation of minimum stress ratio by mathematical models has been reported by others as well (e.g., Iglesia, 1991; Han et al., 2017). This is mainly because different arch shapes, lateral earth pressure coefficients, and soil deformation conditions were assumed in order to derive the mathematical expressions.

Table 2.1. Calculation of minimum stress ratio on an active trapdoor

Researcher	Mathematical expression	Calculated value
Engesser (1882) (cited by Iglesia et al., 2014)	$\frac{w\,K_a}{w\,K_a + 2\,\mathrm{H}\tan\varphi} + \frac{\mathrm{w}\tan\varphi}{6\,H}$	0.15
Bierbaumer (1913) (cited by Iglesia et al., 2014)	$\frac{w}{4\,H\tan\varphi}$	0.16
Marston and Anderson (1913)	$\frac{w}{2\,H\,K_a\tan\varphi}(1 - e^{-2\frac{H}{w}K_a\tan\varphi})$	0.77
Terzaghi (1943)	$\frac{w}{2\,H\tan\varphi}\left(1 - e^{-2\frac{H}{w}K_a\tan\varphi}\right)$ for $\frac{w}{H} \le 2$	0.31
Ladanyi and Hoyaux (1969)	$\frac{w}{2\,H\,K_n\tan f}\left(1 - e^{-2\frac{H}{w}K_n\tan f}\right)$	0.68
Evans (1983)	$\frac{w}{2.4\,H\sin\varphi}\left(1 - e^{-2.4\frac{H}{w}\sin\varphi}\right)$ For $\frac{w}{H} \le 2$	0.35
Iglesia (1991)	$\frac{w}{H}\left(\frac{K'}{2\cot\varphi + \frac{w}{H}\,K'} + \frac{\cot\varphi}{6}\right)$	0.20
Present study	Experimentally measured (trapdoor centre)	0.42
Present study	Experimentally measured (average)	0.26

2.3.2. DIC analysis results

In order to assess the accuracy of the DIC results, which is greatly influenced by camera noise, micro-vibrations in the testing equipment and pattern noise (Rubino et al., 2015), 40 soil specimen images were analysed for vertical displacements prior to the initiation of the test. Ideally, the vertical displacements should be equal to zero in every image and any deviation from zero corresponds to an error. The mean vertical displacement in every image was obtained and analysed statistically using the SPSS 2015 software (IBM, 2015). The results are shown in Fig. 2.5. The average spatial value of vertical displacements was 2×10^{-4} mm for the 40 images. This is a very low error and corresponds to highly accurate results from the DIC system used in this study.

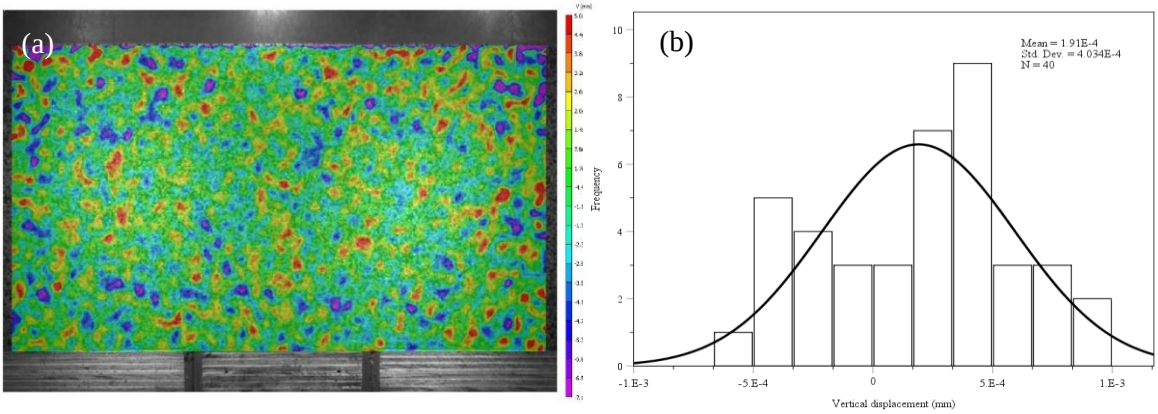

Fig. 2.5. Assessment of the accuracy of the DIC system; (a) sample spatial vertical displacement variable in an image of undeformed soil specimen, and (b) its distribution of errors in 40 undeformed images.

The important variables in analysing the active arching effect in the trapdoor are horizontal displacements (u), vertical displacements (v), and vertical strains (ε_{yy}). The Green-Lagrange vertical strains are calculated from partial derivatives of horizontal and vertical displacements as follows:

$$\varepsilon_{yy} = \frac{\partial v}{\partial y} + \frac{1}{2}\left[\left(\frac{\partial u}{\partial y}\right)^2 + \left(\frac{\partial v}{\partial y}\right)^2\right] \quad (2.4)$$

The area distributions of these variables were obtained from the DIC analyses for downward movements of the trapdoor of 1 and 3 mm. These results are presented in Figs. 2.6–2.11.

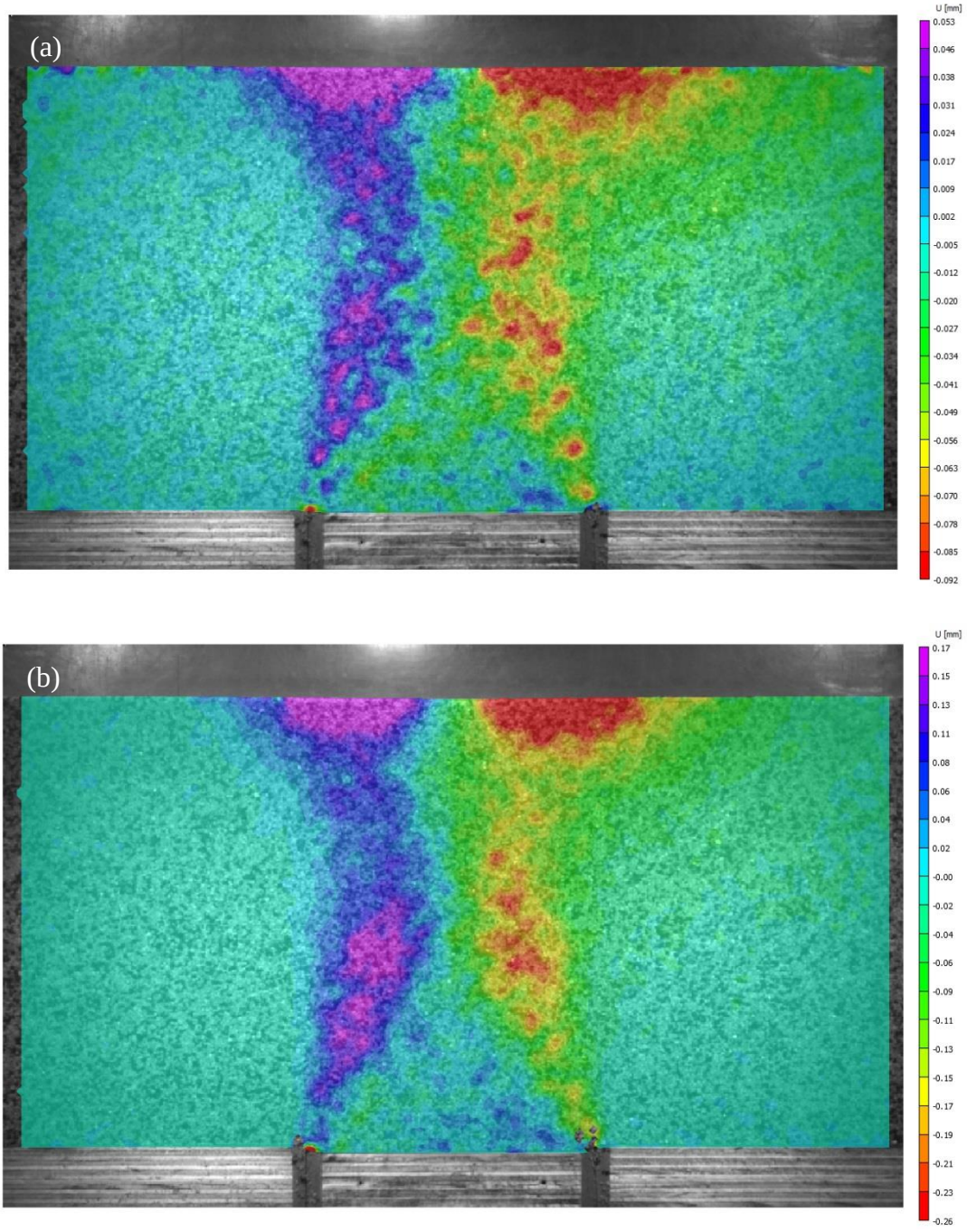

Fig. 2.6. Horizontal displacements in a trapdoor apparatus with no surcharge for (a) 1 mm (b) and 3 mm yield of the trapdoor.

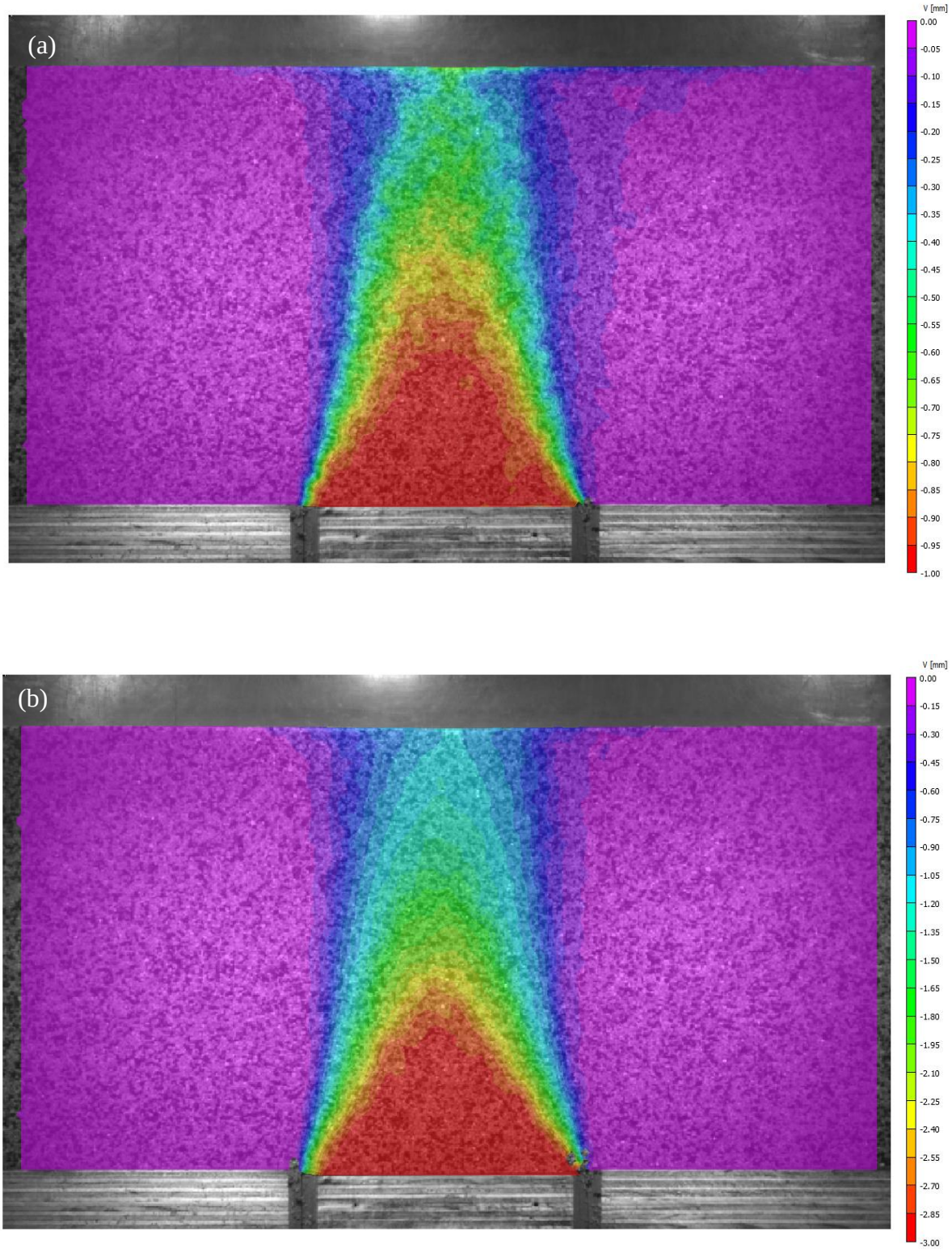

Fig. 2.7. Vertical displacements in a trapdoor apparatus with no surcharge for (a) 1 mm (b) and 3 mm yield of the trapdoor.

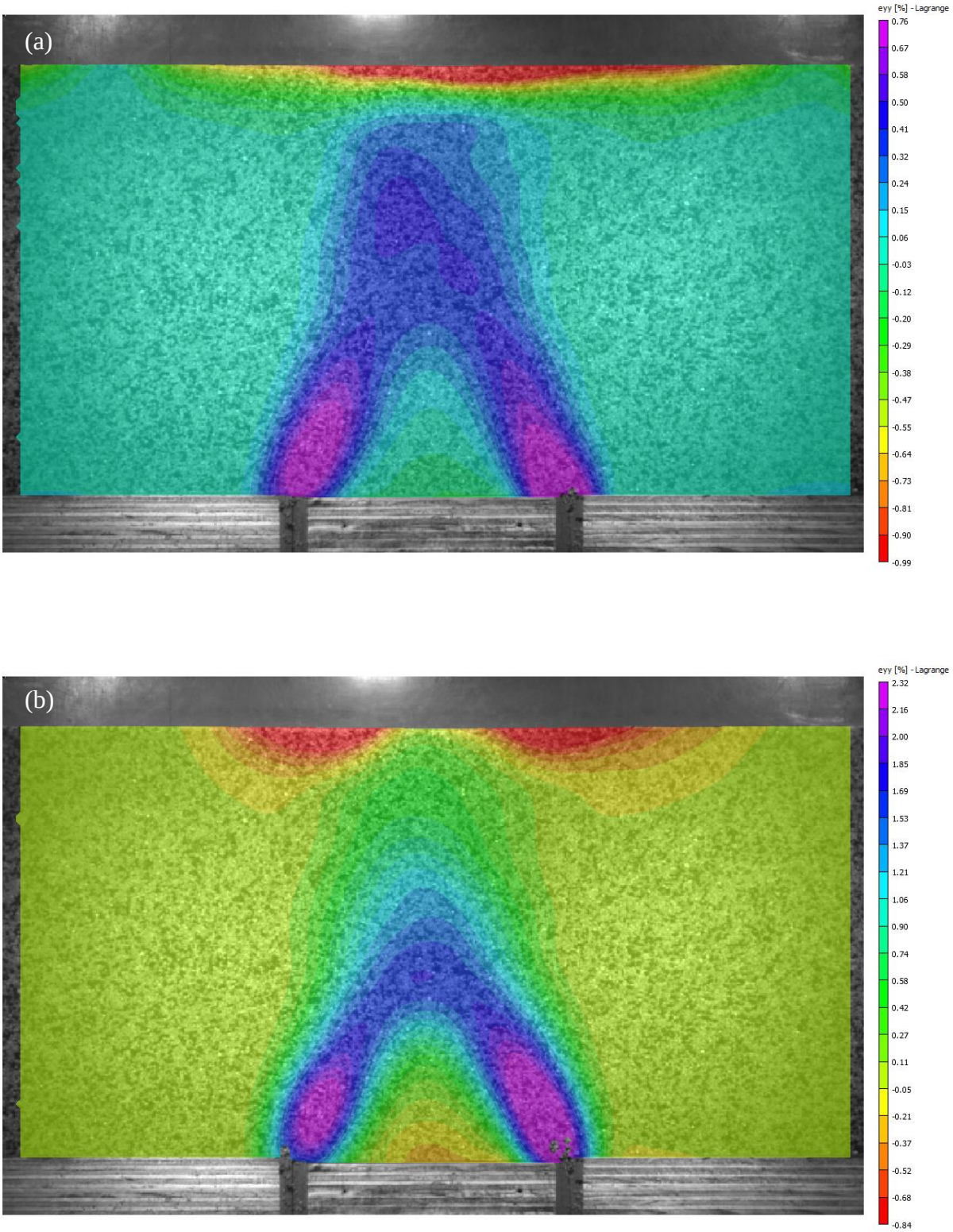

Fig. 2.8. Vertical strains in a trapdoor apparatus with no surcharge for (a) 1 mm and (b) 3 mm yield of the trapdoor.

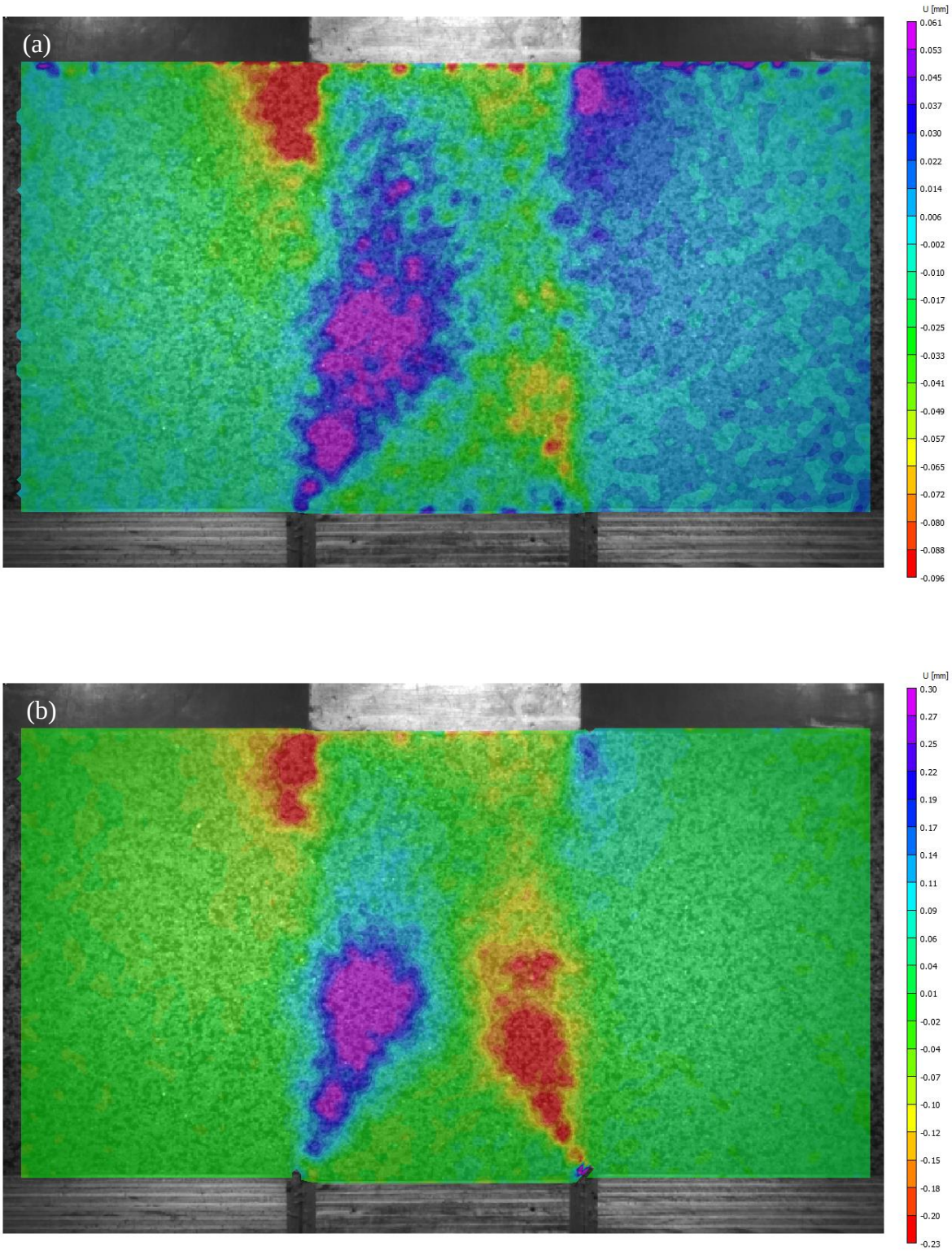

Fig. 2.9. Horizontal displacements in a trapdoor apparatus with a surcharge for (a) 1 mm and (b) 3 mm yield of the trapdoor

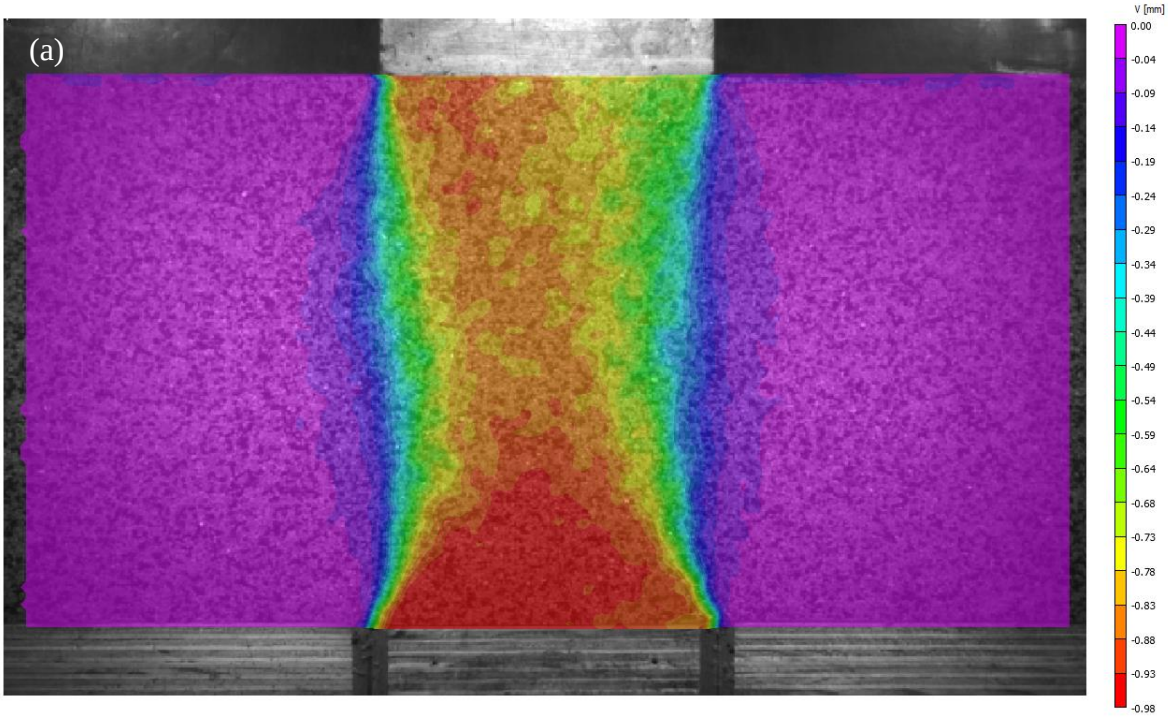

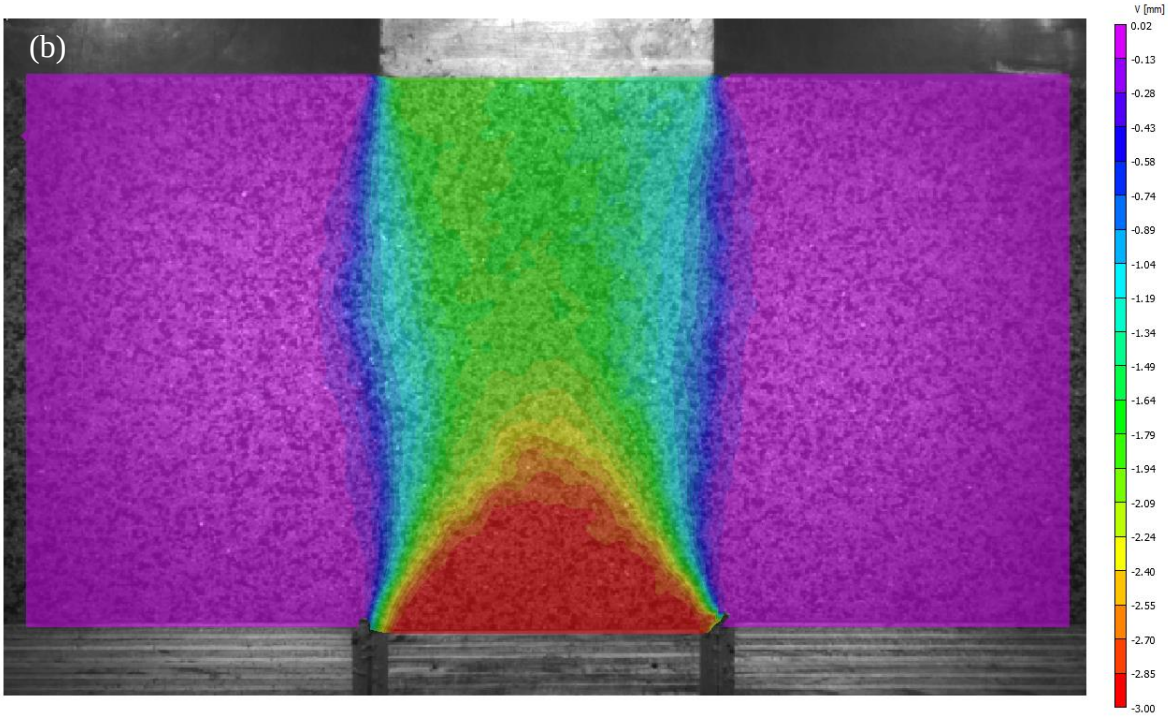

Fig. 2.10. Vertical displacements in a trapdoor apparatus with a surcharge for (a) 1 mm and (b) 3 mm yield of the trapdoor.

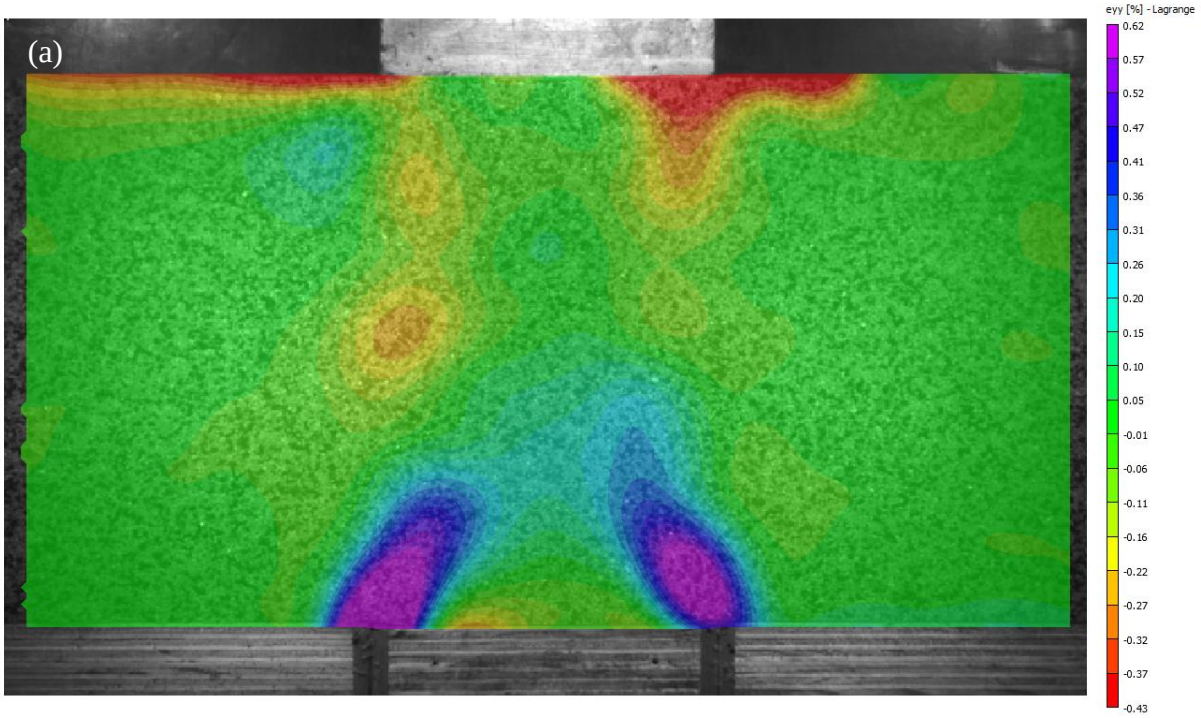

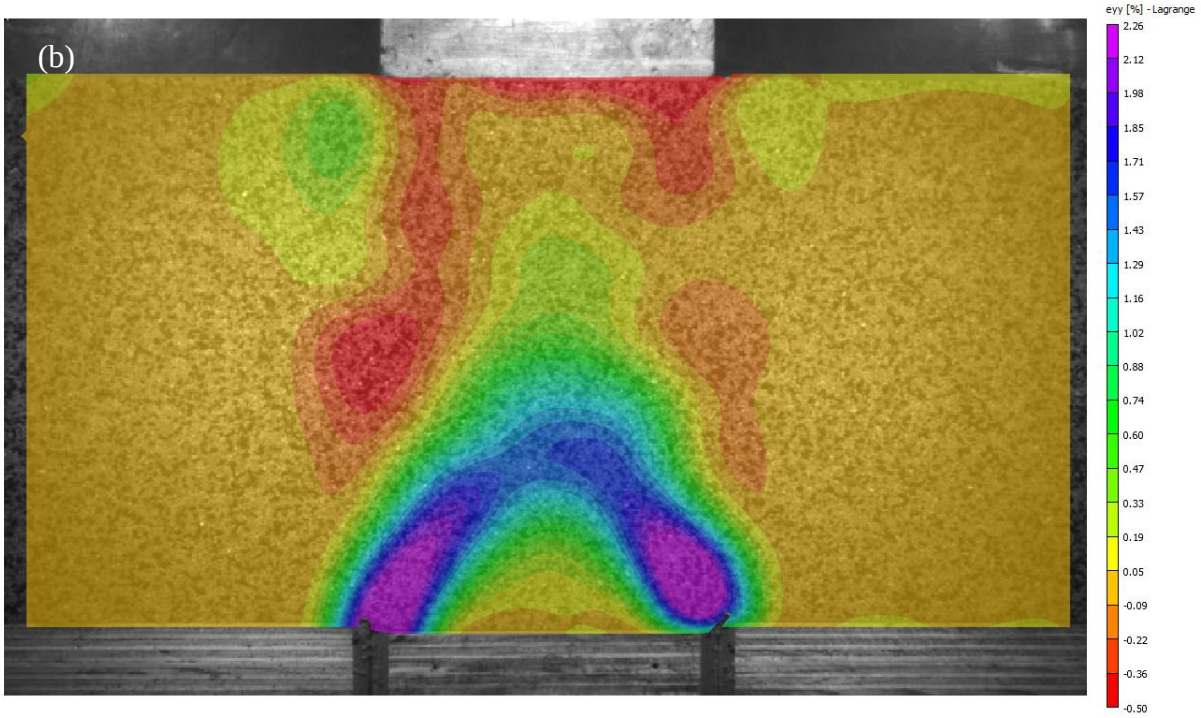

Fig. 2.11. Vertical strains in a trapdoor apparatus with a surcharge for (a) 1 mm and (b) 3 mm yield of the trapdoor.

It can be seen in both Figs. 2.6 and 2.9 that the displacements in the horizontal direction are very modest for both test cases: 0.05–0.25 mm for the no surcharge case; and 0.06–0.3 mm when the 5 kPa surcharge was applied, with the surcharge marginally increasing the horizontal displacements. These figures also show that a triangular area in the soil above the trapdoor has virtually no horizontal displacement. This area is slightly larger when there is no surcharge.

The distribution of vertical displacements when the trapdoor was lowered is shown in Figs. 2.7 and 2.10, respectively with no surcharge and with the application of the 5 kPa surcharge. A triangular area can be observed in both cases. The gradients of vertical displacements in the horizontal direction, in the soil above the stationary parts, where there is zero displacement to the soil above the trapdoor, are extremely steep. However, the vertical displacement values decrease uniformly and gradually in a vertical direction from the centre of the trapdoor surface to the soil surface. Figs. 2.7 and 2.10 also indicate that a roughly triangular area in the soil above the trapdoor exhibited the same amount of displacement as the trapdoor. The displacements of the soil encompassing this triangular area were always lower. When the surcharge was applied (Fig. 2.10), the area immediately above the trapdoor was confined to a more triangular shape, with the affected region being limited to the soil beneath the surcharge.

The shape of arch has been an interesting subject for research in the past. This is mainly because mathematical modellings rely heavily on the assumed shape of the arch. It has been established in the literature that a curved arch forms initially when the trapdoor translation is minimal. The arch then evolves into a triangular-curved arch, triangle, and finally a rectangle as the trapdoor translation increases (Ladanyi and Hoyaux 1969; Vardoulakis et al. 1981; Dewoolkar et al. 2007, Iglesia et al., 2014).

The results of the DIC analysis in this study confirms the formation of the triangular arch within which vertical displacement is a maximum and equal to that of the trapdoor itself (Fig. 2.7). The DIC results in Fig. 2.7 also present a clear picture of the shape of the arch by showing that this triangle, in the no surcharge case, is encompassed by a trapezoidal area where a significant vertical displacement gradient exists. However, the local surcharge reformed the arch configuration into two trapezoids attached from one base similar to the shape of an hourglass (Fig. 2.10).

Figs. 2.8 and 2.11 present the vertical strains, without and with the surcharge, respectively, and it can be observed that a region enclosed by two triangles above the trapdoor was subject to the highest vertical strains. These strains were tensile in nature. Where no surcharge was applied (Fig. 2.8), three main regions, one on the top and two on the flanks, experienced even greater vertical strain. Identifying these high strain areas can be very useful for design purposes. Adding a surcharge (Fig. 2.11) resulted in these areas contracting, and practically eliminating the upper region. This is more visible for low trapdoor translation in Fig. 2.11(a), where the strain levels were also reduced. However, they increased when the trapdoor was lowered further to 3 mm. This is possibly due to the surcharge initially contributing to soil compaction beneath, thus reducing the vertical strain values in the case of the 1 mm trapdoor movement. Surface subsidence can be detected for both scenarios. However, their patterns are different.

An idealised representation of the vertical strains for the two cases of active arching are illustrated in Fig. 2.12. This figure shows that partial yielding of the soil, which induces relative displacements of the soil particles, results in the development of a rather complex internal structure within the soil. With no surcharge, the compression zones are restricted to a shallow depth; however, when a local surcharge is applied they extend to a great depth along the edges of the surcharge, forming a ‘stool’ shaped area. Trapezoidally-shaped

tension zones are formed above the trapdoor, inside of which is a triangle of high tension. This high-tension zone is formed due to the gradual separation of displaced, immediate overburden soil on the trapdoor and the self-supporting soil above the immediate overburden. These zones are quite similar for both cases, except that the height of the tension zone is smaller when a surcharge is applied.

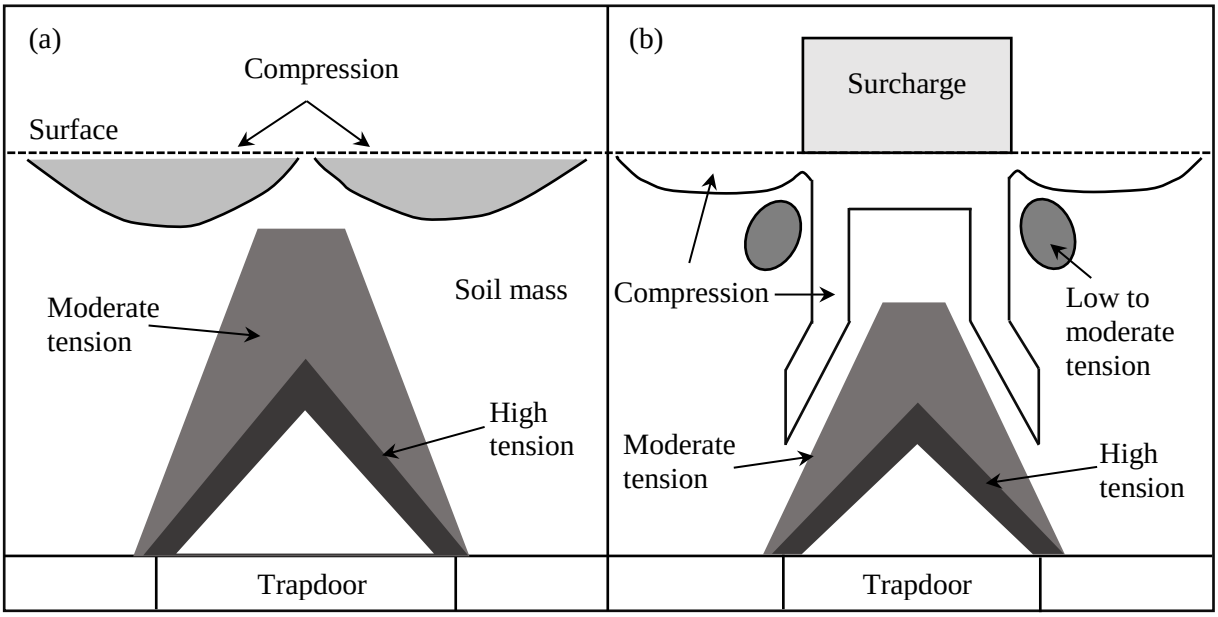

Fig. 2.12. Schematic representation of vertical strains in shallow ideal soil subject to active arching in a trapdoor apparatus; (a) no surcharge, (b) with a local surficial surcharge

The positions along the Y-axis (vertical axis), variable (*Y*), of the deformed soil for a 3 mm translation of the trapdoor are presented in Fig. 2.13. As can be seen, the soil is divided into 20 layers in order to obtain the subsidence and failure surfaces. These layers are horizontal in the beginning of the tests. With the translation of the trapdoor, the portions of layers located above the trapdoor sag to varying degrees amount of which increasing with depth. The broken lines of the soil layers from the horizontal due to subsidence construct the failure surfaces as depicted in Fig. 2.13. Although determining the exact location of the

failure surfaces would be rather subjective, Fig. 2.13 shows that the slope and the extent of failure surfaces are greater when the surcharge was applied. The direction of the displacements is also illustrated in this figure. The arrow sizes are proportional to the total displacement values. The total displacements vectors were considerably larger within a triangular area above the trapdoor when there was no surcharge on the soil surface. The layers near the specimen surface showed minimal displacement. However, applying a surcharge changed this behaviour. The displacements became more uniform in each soil layer, and the triangular pattern faded to some extent, and the surficial layers displacements became noticeable.

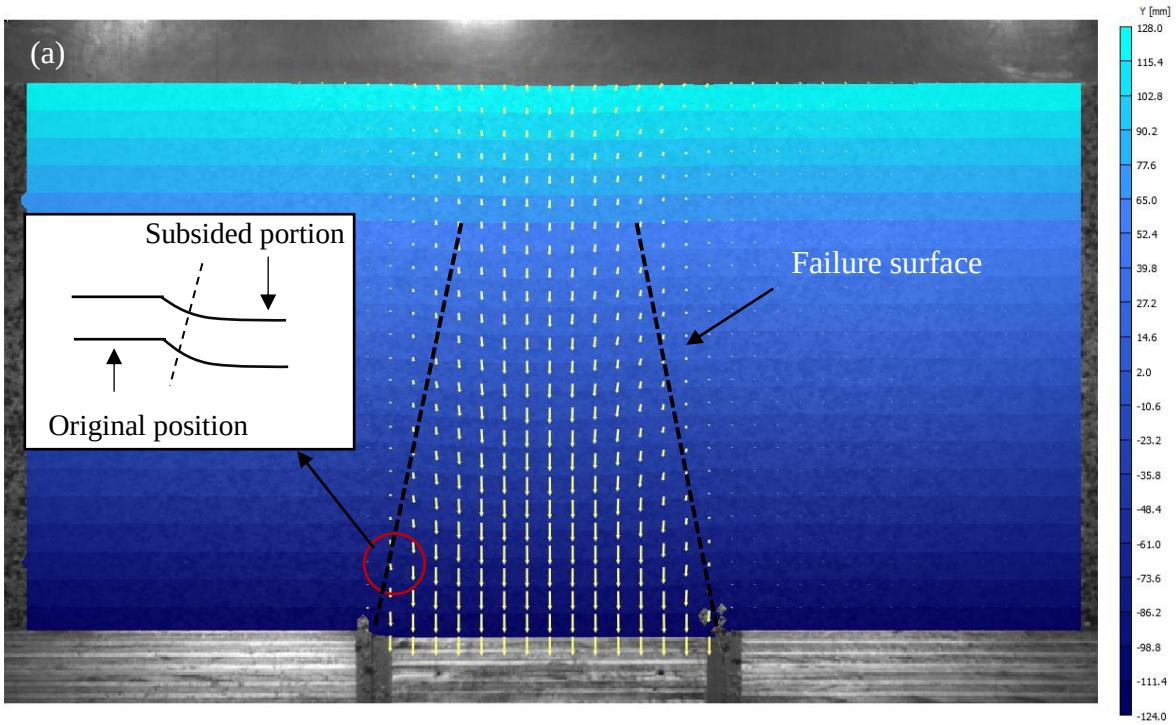

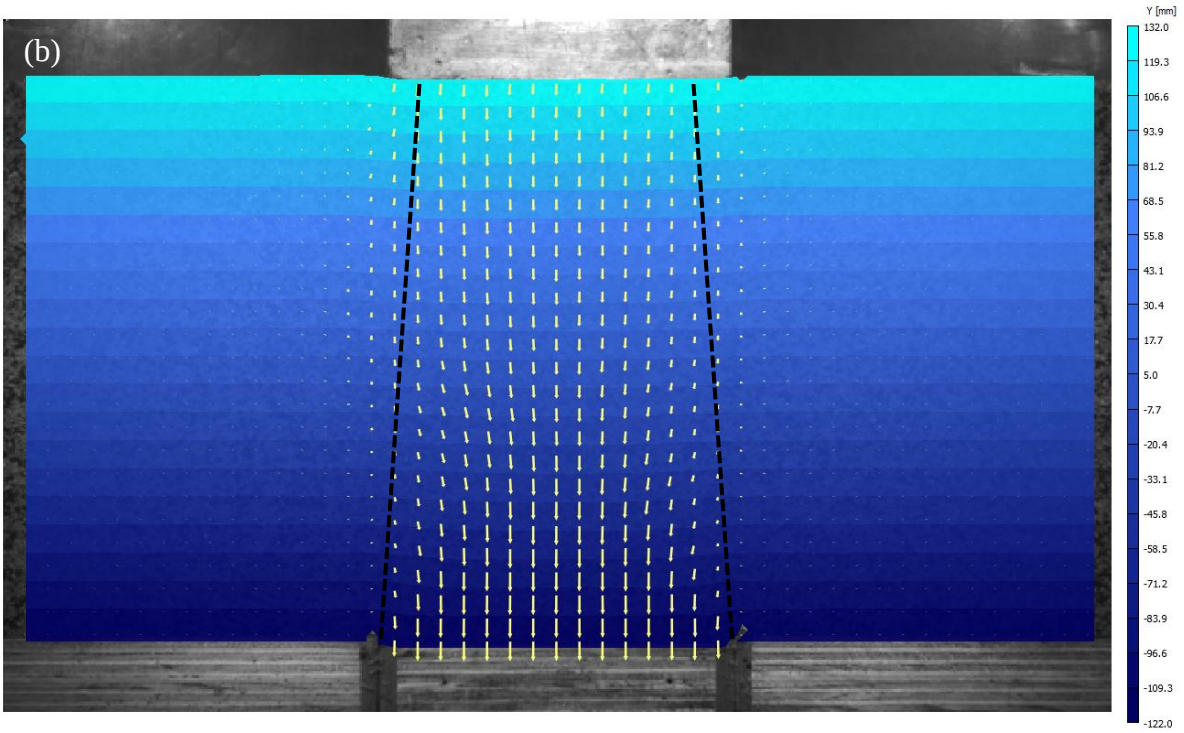

Fig. 2.13. The vertical position variable graphs showing gradual layer-by-layer subsidence and total displacements in a trapdoor apparatus (a) with no surcharge and (b) with a surcharge for a 3 mm yield of the trapdoor. The dash lines represent the failure surfaces.

To achieve a clearer understanding of the arching effect, the shear strains along four profiles were computed using the VIC-2D program, as depicted in Fig. 2.14. Here, the profiles are located in two regions: a short distance above the trapdoor (A–A' and C–C') and near the soil surface (B–B' and D–D') where in the former the vertical displacements are large, while in the latter they are small. The results of the shear strain computations are presented in Figs. 2.14(c) and (d). The centre of the AOI is the coordinate origin; therefore, shear strains on the left side have a negative sign.

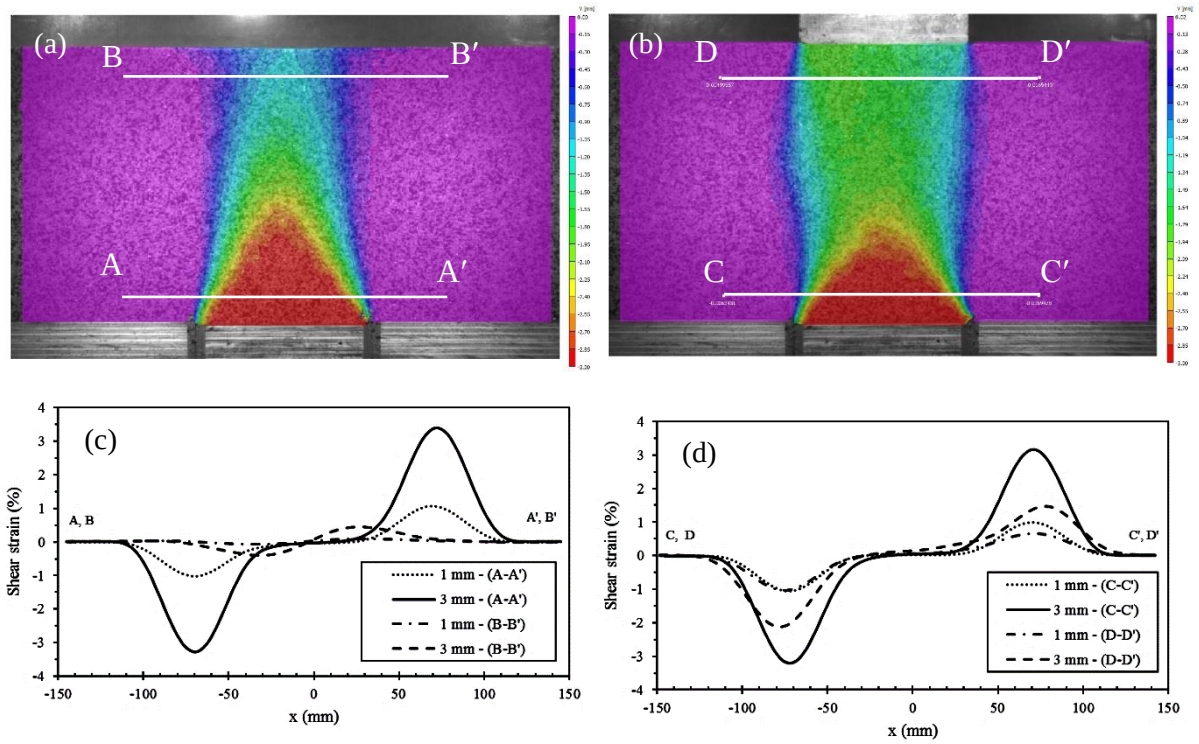

Fig. 2.14. Shear strains calculations; (a–b) profile locations for analysis; (c–d) shear strains on the profiles in soil for 1 and 3 mm downward movements of the trapdoor, (c) without a surcharge and (d) with a surcharge.

As Fig. 2.14 shows, an increase in shear strain occurs over regions in the soil directly above the trapdoor edges. However, the shear strains inside the area above the trapdoor remained close to zero. Shear strains became noticeably larger when the trapdoor was lowered from 1 to 3 mm. Where no local surcharge was applied, shear strains in the area closer to surface became significantly smaller when compared to those in the profile closer to the base of the specimen. In addition, the maximum shear strain values occurred above the centre of the trapdoor. However, due to the presence of the local surcharge, the near-surface shear strains presented high values. Their pattern was also similar to the shear strains at the base of the specimen.

2.4. Conclusions

The Digital Image Correlation (DIC) technique was able to capture effectively the displacement and strain development during active soil arching in a shallow trapdoor apparatus. Applying this technique to study the arching effect yielded valuable information about soil deformation, especially the shape of the arch. The regions that experienced shear and vertical strains were also determined. This information will aid researchers to understand better the arching phenomenon due to relative displacements in soils in more detail, provide an enhanced basis for mathematical modelling, and enable designers to provide more appropriate geotechnical designs.

The displacement and strain analysis showed that, as the arching progresses, a few distinctive zones develop within the soil. A triangular area with the greatest vertical displacement developed above the trapdoor as it yielded. This area was enclosed by a trapezoidal region of gradually-varying vertical displacements. Within the triangular area, the soil experienced small vertical strains, but no shear strains. A high tensile vertical strain region, roughly bounded between two triangles in the immediate overburden of the trapdoor was appeared. Three relatively large regions with significantly higher vertical strains developed in this area, due to the arching effect. The two lower regions were located in the adjacent soil, above the trapdoor edges, and the upper zone was well above the centre of the trapdoor. Application of a surcharge on the soil surface above the trapdoor caused a noticeable change in the displacement and strain distributions in the soil. The zone of soil deformation contracted to an approximately rectangular region beneath the surcharge, while the strain values generally increased. Surficial subsidence with different patterns was observed for the active arching cases in this study.

Appropriate sample preparation is critical for obtaining accurate results from the DIC technique, because heterogeneity and anisotropy of soil specimens may introduce inaccuracies in the results. This is the case with most experimentation in geotechnical engineering. Optical distortion can be another major source of inaccuracy. Employing a high-quality lens will contribute to the reliability and accuracy of the DIC results. Unless the soil used in the experiments has naturally varying colours, soil colouration will be required in order to create a suitable speckle pattern in advance of the DIC imaging. Finally, special attention must be paid to the limitations of the DIC technique for soils. Pattern degradation will eventually occur in the DIC results if the soil is allowed to deform continuously. The upper limit for the use of the 'conventional' DIC analysis, before pattern degradation begins to emerge, in case of the trapdoor apparatus and the soil adopted in this study, was a 4.5 mm translation of the trapdoor. This limit will vary from case to case and will depend on soil compaction, particle size, and analysis parameters, such as subset and step size. The most important factor limiting the application of DIC, however, is postulated to be the imaging frame rate. The cost of a camera capable of imaging at rates in excess of 10,000 fps for example, with high resolutions, would be prohibitively expensive for most geotechnical investigations. An alternative solution for extending the applicability of the DIC technique to larger deformations is to perform a so-called 'incremental' DIC analysis. This, however, is beyond the scope of the present study.

Acknowledgements

The first author acknowledges the financial support provided by the University of Adelaide under the Adelaide International Scholarship (ASI) scheme 2015 and the Australian Research Council. The authors also wish to thank Mr Gary Bowman for his valuable

assistance in manufacturing the apparatus and with the laboratory tests. Special thanks also go to Mr Ian Cates, Mr Thomas Stanef and Mr Simon Golding from the Instrumentation Section of the School of Civil, Environmental and Mining Engineering, Prof. Andrei Kotousov and Dr Zhuang He from the School of Mechanical Engineering, and Mr Micah Simonsen from Correlated Solutions, USA, for their technical advice and assistance, and Ms Leticia Mooney for her editorial support.

References for Chapter 2

Basack, S. Indraratna, B., Rujikiatkamjorn, C. (2016). Analysis of the behaviour of stone column stabilised soft ground supporting transport infrastructure, Procedia Engineering 143: 347–354.

Blaber, J., Adair, B., Antoniou, A. (2015). Ncorr: Open-source 2D digital image correlation MATLAB software. Experimental Mechanics 55(6): 1105–1122

Bosscher, P. J., Grey, D. H. (1986). Soil arching in sandy slopes. Journal of Geotechnical Engineering 112(6): 626–645.

Chevalier, B. Otani, J. (2011). Arching observation in three-dimensional trapdoor problem with X-ray CT and discrete element method. Soils and Foundations 51(3): 459–469.

Correlated Solutions Inc., USA. 2013. The Vic-2D user manual.

Costa, Y. D., Zornberg, J. G., Bueno, B. S., Costa, C. L. (2009). Failure mechanisms in sand over a deep active trapdoor. Journal of Geotechnical and Geoenvironmental Engineering 135(11): 1741–1753.

Dewoolkar, M. M., Santichaianant, K., Ko, H. Y. (2007). Centrifuge modelling of granular soil response over active circular trapdoors. Soils and Foundations 47(5): 931–945.

Evans, C. H. (1983). An examination of arching in granular soils. M.Sc. thesis, Department of Civil Engineering, MIT, Cambridge, MA.

Habash, Y., Whitttle, A. (2002). Mechanisms of load transfer and arching for braced excavations in clay. Journal of Geotechnical and Geoenvironmental Engineering 128(3): 187–197.

Hall, S.A., Muir Wood, D., Ibraim, E., Viggiani G. (2010). Localised deformation patterning in 2D granular materials revealed by digital image correlation. Granular Matter 12(1): 1–14.

Han, J., Wang, F. Al-Naddaf, M., Xu, C. (2017). Progressive development of two-dimensional soil arching with displacement. International Journal of Geomechanics 17(12): 04017112.

Iglesia, G. R. (1991). Trapdoor experiments on the centrifuge: A study of arching in geomaterials and similitude in geotechnical models. Ph.D. thesis, Department of Civil Engineering, MIT, Cambridge, MA.

Iglesia, G. R., Einstein, H. H., Whitman, R. V. (2014). Investigation of soil arching with centrifuge tests. Journal of Geotechnical and Geoenvironmental Engineering 140(2): 1–13.

Indraratna, B., Basack, S., Rujikiatkamjorn, C. (2013). Numerical solution of stone column improved soft soil considering arching, clogging and smear effects. Journal of Geotechnical and Geoenvironmental Engineering 139(3): 377–394.

Jenck, O., Combe, G., Emeriault, F., De Pasquale, A. (2014). Arching effect in a granular soil submitted to monotonic or cyclic loading: A kinematic analysis. Proceedings of the 8th International Conference on Physical Modelling in Geotechnics 2014, ICPMG 2014, eds, Gaudin and White, pp. 1243-1249.

Kirby, J. M. (1992). Soil stress measurement: Part I. Transducer in a uniform stress field. Journal of Agricultural Engineering Research 72(2): 151–160.

Krynine, D. P. (1945). Discussion of 'Stability and stiffness of cellular cofferdams,' by Karl Terzaghi. Transactions of American Society of Civil Engineers 110: 1175–1178.

Ladanyi, B., Hoyaux, B. (1969). A study of the trap-door problem in a granular mass. Canadian Geotechnical Journal 6(1): 1–15.

Lai H. J., Zheng, J. J., Zhang, J., Zhang, R. J., Cui, L. (2014). DEM analysis of soil-arching within geogrid-reinforced and unreinforced pile-supported embankments. Computers and Geotechnics 61: 13–23.

Lee, C. J., Wu, B. R., Chen, H. T., Chiang, K. H. (2006). Tunnel stability and arching effects during tunnelling in soft clayey soil. Tunnelling and Underground Space Technology (21):119–32.

Li. L. (2014). Generalized solution for mining backfill design. International Journal of Geomechanics. 14(3): 1–11.

Lu, W., Miao, L. (2015). A simplified 2-D evaluation method of the arching effect for geosynthetic-reinforced and pile-supported embankments. Computers and Geotechnics 65: 97–103.

Marston, A., Anderson, A. O. (1913). The theory of loads on pipes in ditches and tests of cement and clay drain tile and sewer pipe. Bulletin 31, Iowa Engineering Experiment Station, Iowa State College, Ames, IA.

Moradi, G., Hajialilue Bonab, M., Abbasnejad, A. (2015). Experimental modelling and measuring stresses and strains during arching phenomenon. Geosciences 5(2): 53–61.

Nadukuru, S. S., Michalowski, R. L. (2012). Arching in distribution of active load on retaining walls. Journal of Geotechnical and Geoenvironmental Engineering. 138(5): 575–584.

Paikowsky, S. G., Rolwes, L. E., Tien, S. H. (2003). Visualization and measurements of stresses around a trap door. Proceedings of Soil and Rock America (SARA) 2003, 12th Pan-American Conference on Soil Mechanics and Geotechnical Engineering and the 39th U.S. Rock Mechanics Symposium. MIT, Cambridge, MA, VGE Pub. Culligan, Einstein and Whittle editors, Vol. 1, pp. 1171–1177.

Pan, B., Xie, H., Wang, Z., Qian, K., Wang, Z. (2008). Study on subset size selection in digital image correlation for speckle patterns. Optic Express 16(10): 7037–7048.

Papamichos, E., Vardoulakis, I., Heil, L. K. (2001). Overburden modelling above a compacting reservoir using a trap door apparatus. Physics and Chemistry of the Earth, Part A: Solid Earth and Geodesy 26(1–2): 69–74.

Pardo, G. S., Sáez, E. (2014). Experimental and numerical study of arching soil effect in coarse sand. Computers and Geotechnics 57: 75–84.

Peters, W. H., Ranson, W. F. (1982). Digital imaging techniques in experimental stress analysis. Optical Engineering 21: 427–431.

Rubino, V., Lapusta, N., Rosakis, A. J., Avouac, J. P. (2015). Static laboratory earthquake measurements with the digital image correlation method. Experimental Mechanics 55(1): 77–94.

Rui, R., van Tol, F., Xia, X., van Eekelen, S., Hu, G., Xia, Y. (2016). Evolution of soil arching; 2D DEM simulations. Computers and Geotechnics 73:199–209.

Sadrekarimi, J., Abbasnejad, A. (2010). Arching effect in fine sand due to base yielding. Canadian Geotechnical Journal 47(3): 366–374.

Shelke, A. Patra, N. R. (2008). Effect of arching on uplift capacity of pile groups in sand. International Journal of Geomechanics 8(6): 347–354.

Singh, S., Sivakugan, N., Shukla, S. (2010). Can soil arching be insensitive to φ? International Journal of Geomechanics 10(3): 124–128.

Sloan, S. W., Assadi, A., Purushothaman, N. (1990). Undrained stability of a trapdoor. Geotechnique 40(1): 45–62.

Standards Australia (1998a). Australian Standard AS 1289.5.5.1, Soil compaction and density tests– Determination of the minimum and maximum dry density of a cohesionless material-Standard method.

Standards Australia (1998b). Australian Standard AS 1289.6.2.2, Methods of testing soils for engineering purposes - Soil strength and consolidation tests–Determination of shear strength of a soil - Direct shear test using a shear box.

Stanier, S. A., Blaber, J., Take, W. A., White, D. J. (2016). Improved image-based deformation measurement for geotechnical applications. Canadian Geotechnical Journal 53(5): 727–739.

Statistical Package for the Social Sciences (SPSS) version 2015, IBM Corporation, 2015.

Sutton, M. A., Wolters, W. J., Peters, W. H., Ranson, W. F., McNeill, S. R. (1983). Determination of displacements using an improved digital correlation method. Image and Vision Computing 1:133–139.

Talesnick, M. (2005). Measuring soil contact pressure on a solid boundary and quantifying soil arching. Geotechnical Testing Journal 28(2): 171–179.

Tanaka, T., Sakai, T. (2008). Progressive failure and scale effect of trap-door problems with granular materials. Soils and Foundations 33(1): 11-22.

Terzaghi K. (1943). Arching in ideal soils. In: Theoretical soil mechanics, chapter V. John Wiley and Sons, New York

Terzaghi, K. (1936). Stress distribution in dry and in saturated sand above a yielding trap-door. Proceedings. First International Conference on Soil Mechanics and Foundation Engineering, Cambridge, Massachusetts, pp. 307–311.

Terzaghi, K., and Peck, R. B. (1948). Soil mechanics in engineering practice, Wiley, New York.

Ting, C. H., Sivakugan, N., Read, W., Shukla, S. K. (2014). Analytical expression for vertical stress within an inclined mine stope with non-parallel walls. Geotechnical and Geological Engineering 32(2): 577–586.

Vardoulakis, I., Graf, B., and Gudehus, G. (1981). Trap-door problem with dry sand: A statical approach based upon model test kinematics. International Journal of Numerical and Analytical Methods in Geomechanics 5(1): 57–78.

Wang, L., Leshchinsky, B. T., Evans, M., Xie, Y. (2017). Active and passive arching stresses in c′-ϕ′ soils: A sensitivity study using computational limit analysis. Computers and Geotechnics 84: 47–57.

Zou, X., Mei Y., Zhao, M., Yang, X. (2008). Pile-soil stress ratio in bidirectionally reinforced composite ground by considering soil arching effect. Journal of Central South University of Technology (English Edition) 15(2): 1–7.

Statement of Authorship

Title of Paper	Mapping soil arching-induced shear, principal and volumetric strains
Publication Status	☐ Published ☐ Accepted for Publication ☑ Submitted for Publication ☐ Unpublished and Unsubmitted work written in manuscript style
Publication Details	

Principal Author

Name of Principal Author (Candidate)	Hamidreza Khatami		
Contribution to the Paper	Performed the literature review, conducted the experiments, gathered the data, analysed and interpreted the results, and drafted the manuscript.		
Overall percentage (%)	80%		
Certification:	This paper reports on original research I conducted during the period of my Higher Degree by Research candidature and is not subject to any obligations or contractual agreements with a third party that would constrain its inclusion in this thesis. I am the primary author of this paper.		
Signature		Date	19/09/18

Co-Author Contributions

By signing the Statement of Authorship, each author certifies that:

i. the candidate's stated contribution to the publication is accurate (as detailed above);
ii. permission is granted for the candidate in include the publication in the thesis; and
iii. the sum of all co-author contributions is equal to 100% less the candidate's stated contribution.

Name of Co-Author	An Deng		
Contribution to the Paper	Methodology and reviewing.		
Signature		Date	19/09/18

Name of Co-Author	Mark Jaksa		
Contribution to the Paper	Methodology and reviewing.		
Signature		Date	19/09/18

Please cut and paste additional co-author panels here as required.

Chapter 3: Mapping soil arching-induced shear, principal and volumetric strains

Abstract

Arching alters the soil stress regime in many geotechnical situations. The new stress field may result in deformation and stability problems associated with infrastructure systems. This study applies the Digital Image Correlation (DIC) technique to map the soil deformation field where soil arching occurs in a trapdoor apparatus. Model tests were conducted under different conditions, including active arching, passive arching and surcharge loading. In each of the tests, shear strains, principal strains, displacement fields and volumetric strains were obtained and analysed. The patterns and values of these deformation fields, as well as the arches formed, were found to be dependent on the test conditions. The arch developed in the passive arching condition is greater in size than that developed in the active arching situation.

Keywords: Arching, digital image correlation, shear band, volume change, trapdoor test

3.1. Introduction

Soil arching is one of the ubiquitous processes in geotechnical engineering. Where arching occurs in the ground, the stresses redistribute and often influence the performance of the associated infrastructure. Arching can be induced by a variety of factors such as soil yielding, soil-structure interactions, and differences in material stiffness. To examine the causes, Terzaghi (1936) developed the so-called trapdoor apparatus to conduct model testing. The trapdoor apparatus is considered as an effective tool and, since then, has been either replicated to study the arching effect (Harris, 1974; Tanaka and Sakai, 2008; Chevalier et al. 2012; Pardo and Sáez, 2014) or modified in many studies for different purposes or test conditions, such as a depleting petroleum reservoir (Papamichos et al. 2001), buried pipelines (Costa et al. 2009), surface subsidence due to underground tunnelling (Thongprapha et al., 2015) and sinkhole development (Jacobsz, 2016). Most of these studies were focused on stress redistribution at the boundaries (i.e. on the trapdoor or soil-structure interface) and preliminary soil imaging in the absence of strain analysis. In addition to the experimental studies, finite element modelling of the arching effect has been carried out by Lee et al. (2006), Chen et al. (2011), Pardo and Sáez (2014), Lin et al. (2018), and Li et al. (2018). Numerical simulations are as accurate as their backbone theories and are sometimes prone to inaccuracies due to idealisation or over-simplification. First-hand observations from experiments, on the other hand, offer results accounting for the actual conditions and provide invaluable information about soil behaviour. There is a notable lack of full-field measurements in the area of soil arching. The main reason for this information void is the challenge associated with in situ sensors measuring stresses or strains in the ground (Talesnick 2005). The sensors are significantly larger in size than the soil particles and, when present, disturb soil arching development (Hanna 1985; Talesnick 2013). In addition, it is not always possible to bond strain or stress sensors on the surface of a granular soil specimen.

The expansive surface deformation due to arching is also another case where physical surface sensors will be of limited value.

The Digital Image Correlation (DIC) technique provides a solution to measure full-field deformation present in particulate bodies. DIC enables non-contact measurement and therefore has no influence on the soil behaviour. DIC is relatively affordable and simple to implement. When the specimen of interest is subjected to a load and begins to deform, a digital camera is used to take a reference image, and a subsequent series of images are captured during the deformation process. Pixel information, in terms of greyscale intensity contained in each of the images, is examined in the form of correlation analysis. Each of the images is divided into a grid of subsets. Pixel greyscale intensity information in a subset is correlated with the subsets in the reference image. The greatest correlation governs the displacement of the subset of interest (VIC-2D user manual, Correlated Solutions, 2009). DIC techniques are also used quantitatively to examine shear bands, which cannot be captured by other optical techniques, such as X-ray imaging.

The objective of this study is, firstly to capture full-field shear strains, principal strains and volume changes in sand due to arching and, secondly, to analyse the associated strain localisations using the DIC technique. Active and passive states of arching are tested using the trapdoor apparatus. The strain and volume change measurements provide useful evaluation of shear band formation and soil dilatancy and compression. The effects of a local surface surcharge and trapdoor travel distance are also investigated. The interpretation of the results obtained from the DIC analysis will contribute to an improved understanding of the arching effect in granular soil.

3.2. Materials and methods

This section presents the soil properties, speckle pattern used in the adopted soil specimen, DIC imaging equipment, trapdoor apparatus and the procedures implemented in the testing and imaging.

3.2.1. Tested soil

The soil adopted for testing was a silica sand with approximately 98% and 2% particles by dry mass, passing the No. 8 (2.38 mm) and No. 16 (1.19 mm) sieves, respectively. This synthetically-graded soil is known as Sand 8/16 and has angular particles with a specific gravity of 2.65. The minimum and maximum densities are 1,490 kg/m^3 and 1,710 kg/m^3, respectively based on tests conducted in accordance with Australian Standard AS 1289 (Standards Australia, 1998). Most of the sand particles have a bright grey colour; however, a very small fraction of the sand particles are light brown in colour. For the purposes of DIC imaging, the natural soil colouration was inadequate, as the success or otherwise of DIC image correlation is greatly influenced by particle colouration and, in order to optimise the accuracy, an artificial particle speckle pattern is adopted. Therefore, in this study, 30% of the sand used in the trapdoor testing was dyed using a water-based, matte black paint. The selected matte colour helps eliminate spectral light reflections which would otherwise introduce noise into the images.

3.2.2. Trapdoor apparatus

The adopted trapdoor apparatus is a cuboid container manufactured using a 1.4 m × 1.4 m rigid, steel frame with Perspex sheets at the front and back, with each being 1 m high × 1 m wide and 20 mm thick. Perspex was adopted as it is smooth, relatively frictionless, abrasion

resistant and clear for the purposes of imaging. The container has an internal depth of 200 mm, which enables a plane-strain environment and is open at the top to facilitate the placement and discharge of the sand layer. The trapdoor is 160 mm wide and located in the centre of the base of the apparatus. The trapdoor is able to displace vertically with the assistance of a hydraulic jack installed underneath. The movement of the trapdoor induces two arching states in the sand: active arching due to downward movement; and passive arching as a result of upward movement. The trapdoor vertical translation was monitored using a linear variable displacement transducer (LVDT) that was fixed beneath the trapdoor.

3.2.3. DIC system

The DIC system was developed by Correlated Solutions Inc., USA, and includes a camera, light source, image capturing software and image processing software. The camera used for imaging is a FLIR (formerly known as Point Grey) Grasshopper3 model, equipped with a 7.18 mm × 5.32 mm Sony ICX687 conventional charge-coupled device (CCD) sensor. The camera can capture images with a resolution of up to 1928 × 1448 pixels at a speed of 26 frames per second (fps). A low-distortion, Fujifilm lens, with a focal length of 75 mm and an aperture size range of 1/22–1/2.8, was attached to the camera body. A pair of cool, light emitting diode (LED) lights was placed in appropriate positions, close to the front face of the container. These LEDs can operate over a long time period without causing heat problems and therefore induce negligible thermal stresses on the sample surface.

VicSnap is the image capturing software that comes with the DIC system and was developed to adjust the size and location of the area of interest (AOI), and to manage the resolution and thereby the imaging rate. The AOI is the section of the specimen surface where soil associated with arching and the soil in close proximity is examined. It is important to note that the camera imaging rate is one of the main factors governing the performance of

the DIC system in applications of granular material imaging. The imaging rate in machine-vision cameras is inversely proportional to the resolution of the imaging system. This implies that higher imaging rates can be achieved, provided that the image resolution is reduced. From trial-and-error photography and post-processing, a baseline imaging rate of 80 fps for soil deformation is suggested. This minimum value was determined by starting imaging at a low speed of 10 fps and subsequently analysing the deformations in the soil. Pattern degradation was observed and thus the rate increased gradually. For the current study, the imaging speed and photographical resolution were established at 160 fps and 960 × 600 pixels, respectively. This coincides with the camera's maximum imaging rate at the specified resolution. The images obtained using VicSnap during the deformation of the soil specimens were then input into the VIC-2D software developed by Correlated Solutions for correlation analysis.

The traditional procedure of the DIC technique is based on mapping the images of a deformed body against a predetermined reference image of the body in its undeformed state (Pan et al. 2010). Deformation data can then be obtained while the mapping equations are solved. The detailed procedure and mathematics of the DIC analysis is well documented in the literature (e.g., Schreier et al., 2009; Sciammarella and Sciammarella, 2012). Only the practical steps undertaken to obtain the final output results from VIC-2D software are summarised here.

Calibration of the scale in DIC analysis, in a length unit suitable for the application, is the first step in obtaining displacement results. Otherwise, the results indicated by the software will be solely in pixels, which is clearly sub-optimal. Correlation analysis is then conducted on the AOI of each of the images. In this study, the AOI dimension is set to 500 mm × 250 mm (the soil specimen size is 950 mm × 250 mm) and covers the soil areas directly influenced by arching and a reasonable zone adjacent to these areas. The AOI is sub-

divided into a grid and cells, which are referred to as subsets. To perform accurate correlation calculations, each subset should exhibit a distinctive speckle pattern and to achieve this, a suitable size of the subset in the form of pixels is required. Based on recommendations by Pan et al. (2008), a subset size of 21 × 21 pixels (11 mm × 11 mm) is deemed appropriate for the current study.

Correlation analysis is also dependent on the step and filter sizes. The step size determines the number of points in the specimen image that data will be analysed for. A step size of 5, for example, means that data will be obtained for every 5 pixels in both the horizontal and vertical directions. The filter size, together with the step size, represents the extent of the smoothing area for the calculated data. The step and filter sizes were set to 5 and 21 pixels, respectively. Therefore, the smoothing area was 21 × 5 = 105 pixels, or, in other words, the size of the virtual strain gauge used in the calculations was 105 pixels. The size of the subsets, and the step, filter and image resolutions dictate the time required to undertake the DIC analysis. For this study, the DIC analysis of every 1,000 images, with a resolution of 960 × 600 pixels, and subset, step and filter sizes of 21, 5 and 21, respectively, was completed in 25 minutes using a desktop computer comprised of a 3.40 GHz CPU, 16 GB RAM, 16 GB graphic memory and Windows 7 64-bit operating system.

3.2.4. Testing procedure

Layers of dyed-natural sand mixture were placed using the air pluviation method. This method avoids possible development of small-scale internal structures in the soil, such as prestressing or arching. Each of the layers was compacted to a thickness of 10 mm using a wooden tamper. The compaction energy applied to each layer was determined to attain a density of 1,657 kg/m^3, which is equivalent to a relative density of 79%. The sand layer measured 250 (H) × 200 (D) × 950 (W) mm. Therefore, the soil cover ratio; that is, the soil

height divided by the trapdoor width (TW), was 1.56. The soil cover ratio is less than 2 and, based on the criteria for arching conditions (Costa 2009), defines a shallow condition for the trapdoor system adopted in this study. A block of concrete was used to apply a surcharge of 5 kPa when required. The block was 160 mm wide and 200 mm deep and was placed on the surface of the sand layer, with its centre in alignment with the trapdoor centre. The camera should be placed appropriately in relation to the specimen surface, so as to produce an accurate correlation analysis. This was achieved by using the geometrical configuration depicted in Fig. 3.1. As can be seen from this figure, a hypothetical right pyramid is constructed between the DIC camera and the specimen surface. The camera lies at the apex and the imaging area, which is slightly larger than the AOI, forms the base. The pyramid measured a height, h = 3.25 m and base $a \times b$ = 0.5 m × 0.312 m. At the beginning of each of the trapdoor tests, a calibration image was captured by placing the dot grid pattern on the front surface of the specimen, as shown in Fig. 3.2. The images were scaled using this dot grid calibration target.

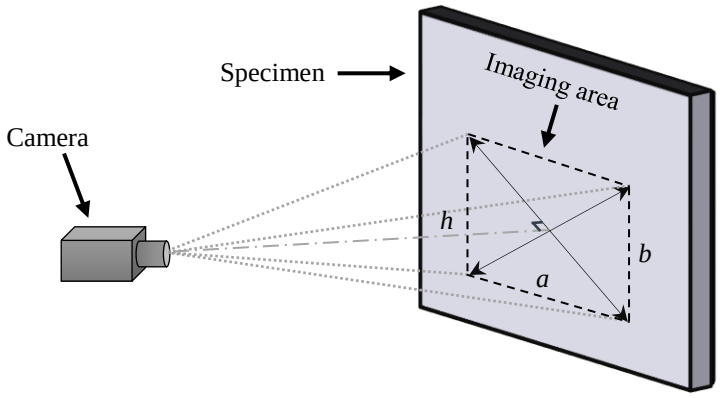

Fig. 3.1. A camera aligned with a 2D area of interest

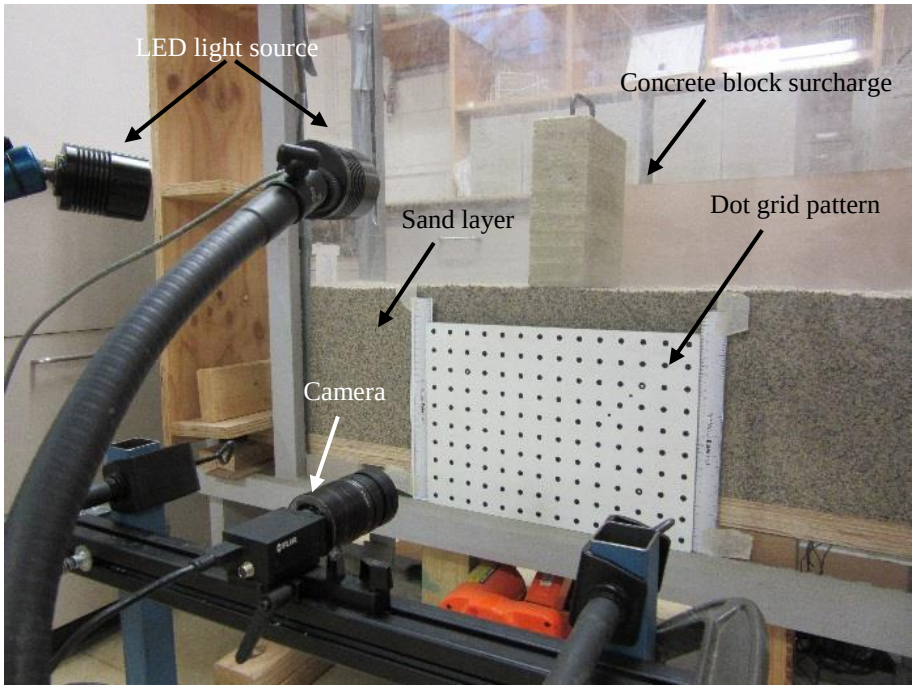

Fig. 3.2. The photographic setup, sand layer with a speckle pattern, and the surcharge. A calibration target covering the area of interest is placed on the front wall of the trapdoor apparatus. The camera and LED lights are intentionally placed in the positions shown, solely for illustrative purposes. More appropriate positions were adopted during the testing phase

3.3. Test results

This section presents the DIC results obtained from the trapdoor tests. The results include the shear strains, particle displacements, principal strains and volume changes in the sand layer which is subjected to active or passive arching with and without surcharge loading.

3.3.1. Shear strains

Investigation of shear strains and their possible localisation during arching is particularly important. This is because localisation of shear deformation is indicative of imminent shear failure along a narrow region (Batra and Kim, 1992; Lade, 2003). Strain localisation develops readily in plane-strain specimens and their failure always occurs along a single,

well-defined shear plane (Lee, 1970; Peters et al., 1988; Alshibli et al., 2003). The movement of the trapdoor element further facilitates strain localisation when pushed into or pulled away from the sand layer. The areal distributions of the shear strains were obtained using the DIC system. The development of the shear strains that occurred in the sand layer when the trapdoor moved to 1 or 3 mm, in the downward or upward directions is presented in Figs. 3.3 and 3.4, respectively. With the translation of the trapdoor, clear shear bands or strain localisations originate from the trapdoor edges, where the soil layer is in different arching modes. Each of the arching modes leads to a unique deformation pattern of the sand layer.

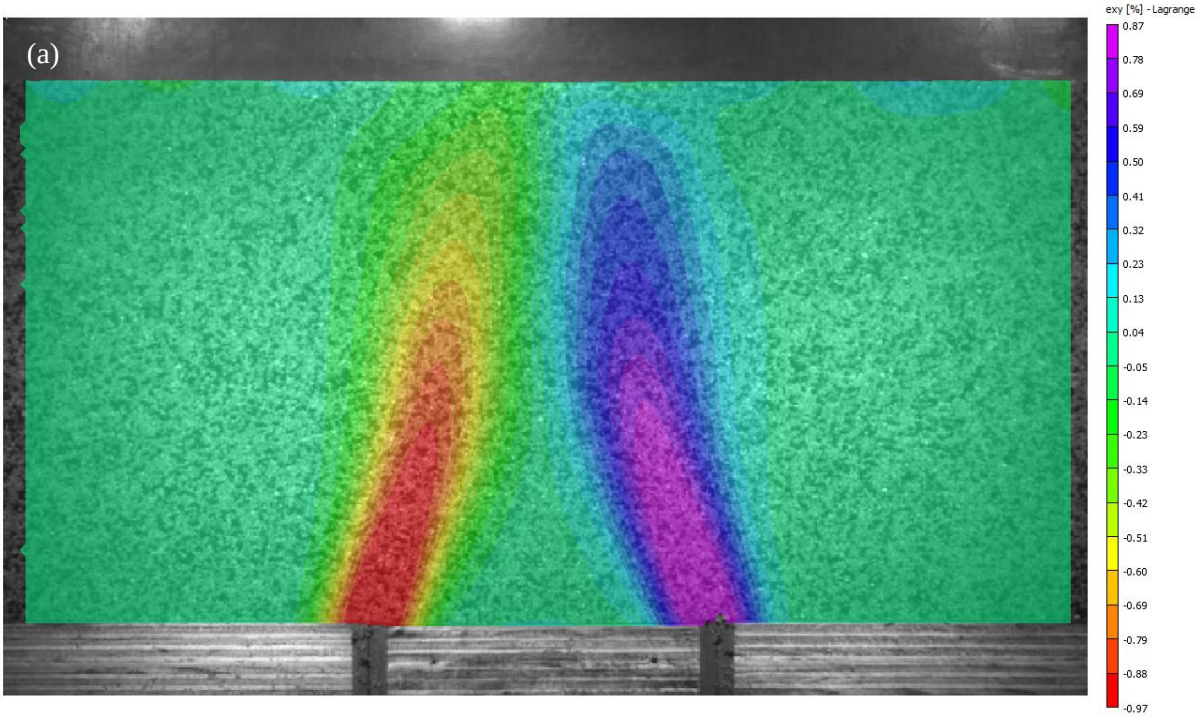

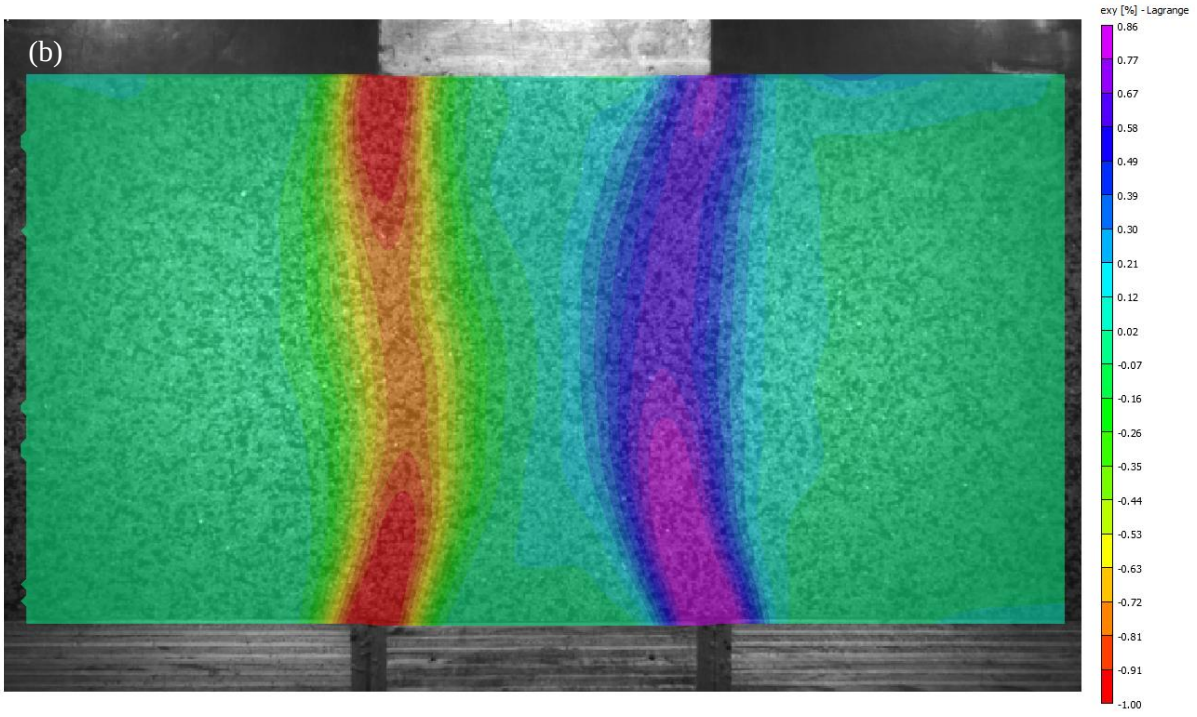
(b)
exy [%] - Lagrange
0.86
0.77
0.67
0.58
0.49
0.39
0.30
0.21
0.12
0.02
-0.07
-0.16
-0.26
-0.35
-0.44
-0.53
-0.63
-0.72
-0.81
-0.91
-1.00

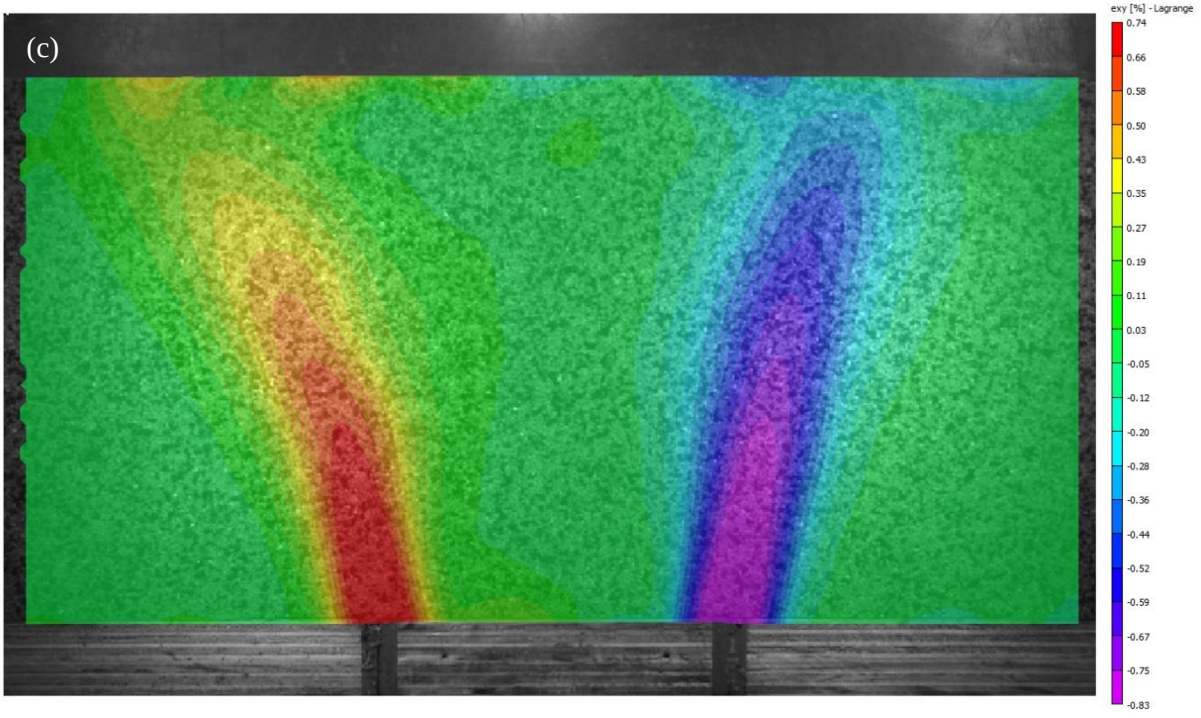
(c)
exy [%] - Lagrange
0.74
0.66
0.58
0.50
0.43
0.35
0.27
0.19
0.11
0.03
-0.05
-0.12
-0.20
-0.28
-0.36
-0.44
-0.52
-0.59
-0.67
-0.75
-0.83

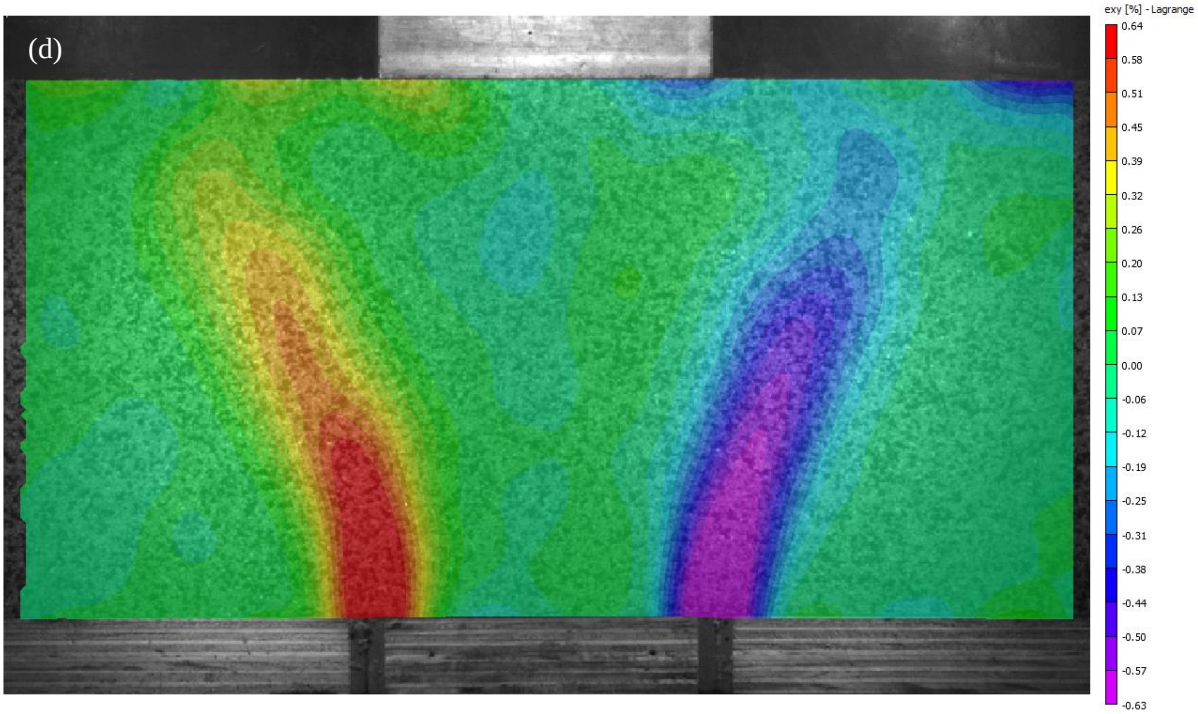

Fig. 3.3. Shear strain distribution in the sand layer caused by a 1 mm trapdoor translation under: (a) active arching with no surcharge, (b) active arching with a 5 kPa central surcharge, (c) passive arching with no surcharge, and (d) passive arching with a 5 kPa central surcharge

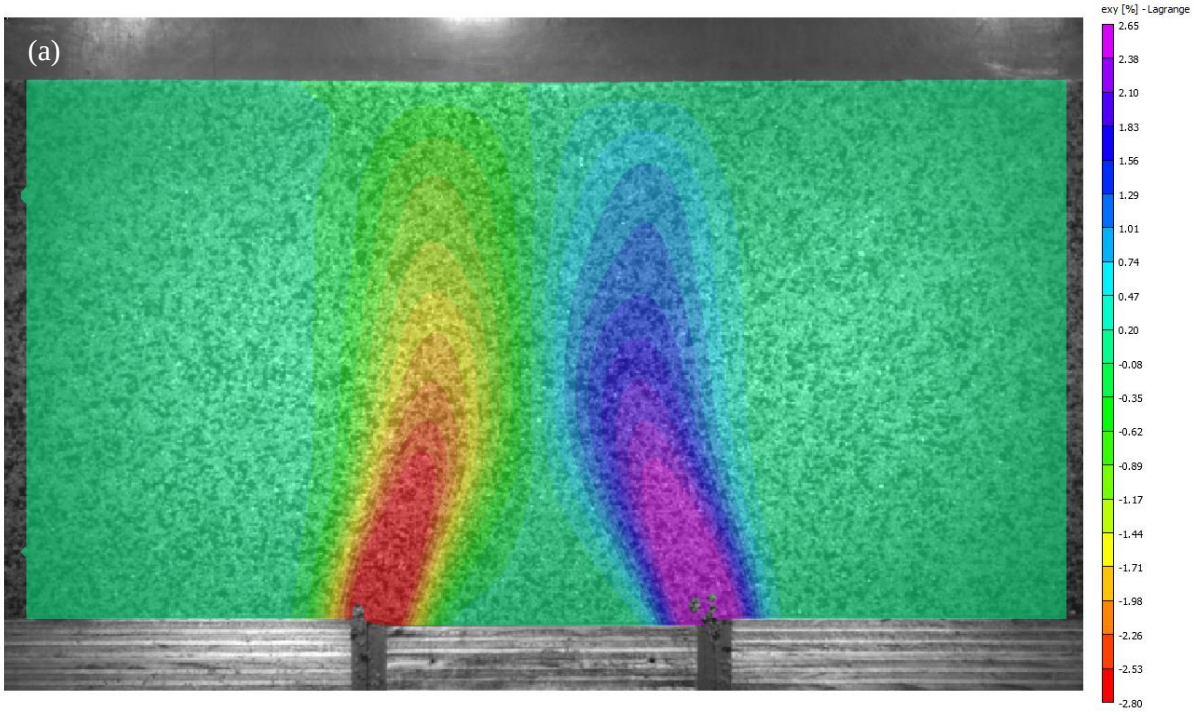

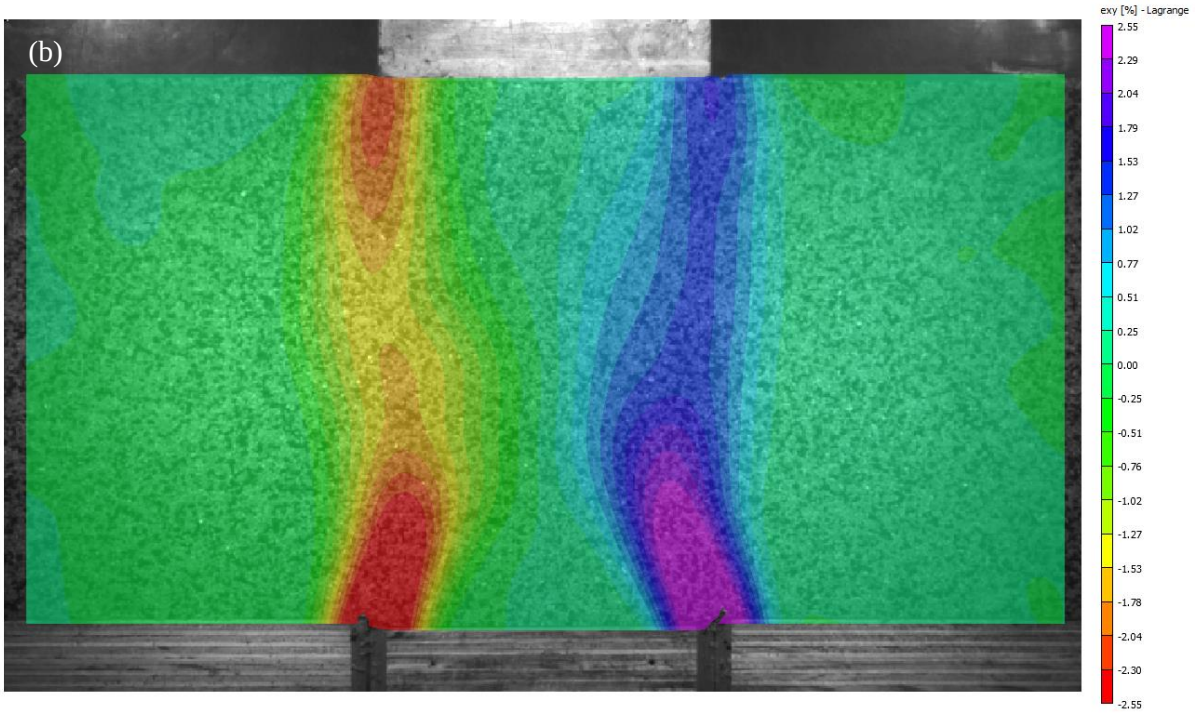
(b)
exy [%] - Lagrange
2.55
2.29
2.04
1.79
1.53
1.27
1.02
0.77
0.51
0.25
0.00
-0.25
-0.51
-0.76
-1.02
-1.27
-1.53
-1.78
-2.04
-2.30
-2.55

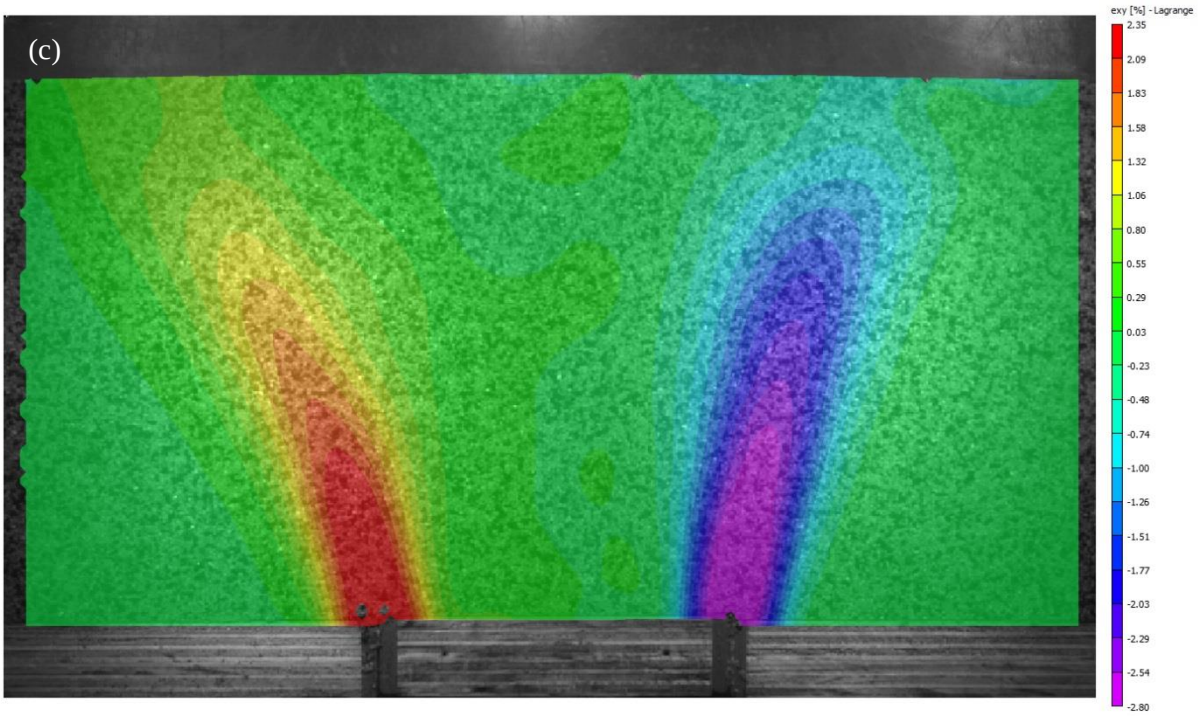
(c)
exy [%] - Lagrange
2.35
2.09
1.83
1.58
1.32
1.06
0.80
0.55
0.29
0.03
-0.23
-0.48
-0.74
-1.00
-1.26
-1.51
-1.77
-2.03
-2.29
-2.54
-2.80

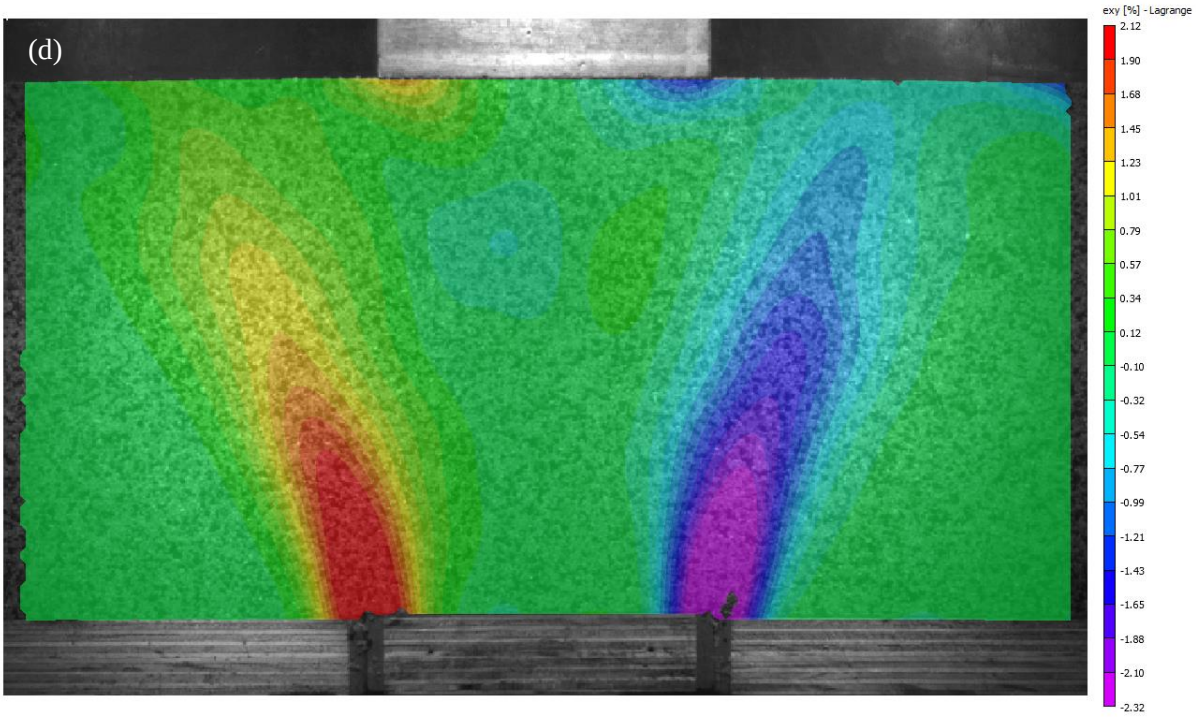

Fig. 3.4. Shear strain distribution in the sand layer caused by a 3 mm trapdoor translation under: (a) active arching with no surcharge, (b) active arching with a 5 kPa central surcharge, (c) passive arching with no surcharge, and (d) passive arching with a 5 kPa central surcharge

When no surcharge is placed on the surface and the trapdoor is lowered, two shear bands originate from both trapdoor edges [Fig. 3.3(a)]. The two shear bands rise symmetrically and incline inward to a depth up to roughly 110% of TW. The shear band tips then continue, at reduced intensity, vertically towards the surface. The contours of the shear bands suggest that the greatest shear strains are located directly above the trapdoor edges. For these sand particles, the shear strain values are as high as ≈1%, whereas the sand between the bands remains mainly undeformed. Where the trapdoor is further lowered to 3 mm [Fig. 3.4(a)], the triangular form of the shear band remains, but the form slightly increases in size and magnitude (≈3%) when compared with the results obtained in the 1 mm translation case.

The surface surcharge influences the shear strain development, while the sand layer is subjected to the same active arching condition. As shown in Fig. 3.3(b), where a 1 mm

trapdoor translation occurs, the shear bands originate similarly from the trapdoor edges, but upon rising upward, the bands incline inward to a vertical distance (approximately 75% of TW), then turn slightly outward, and stretch straight up, touching the edges of the surcharge block. The shear bands adjacent to the trapdoor edges become shorter and less inclined in comparison with the case without the surcharge. In Fig. 3.3(b), the shear bands seem slightly irregular and asymmetric, which may be caused by a small degree of heterogeneity in the soil sample. In Fig. 3.4(b), where the trapdoor moves down by 3 mm, the sand particles seem to have equilibrated and the shear bands develop into a more established pattern. Similar to the no surcharge case, lowering the trapdoor increases the shear strain values, while the other conditions remain the same.

Where passive arching occurs [Figs. 3.3(c–d) and 3.4(c–d)], the shear bands develop in a pattern different from those developed in the active arching case. The most noticeable change is that the shear bands orient outward rather than inward, for both the no surcharge and surcharge loading conditions. Passive arching also increases the extent of the shear bands. For the no-surcharge and 5 kPa central surcharge situations, the shear bands progress up to the surface of the sand layer. The shear bands nearly touch the sand layer surface when the trapdoor translation is 1 mm [Fig. 3.3(c–d)]. When the translation increases to 3 mm [Fig. 3.4(c–d)], the shear bands reduce in length, but increase in their level of strain. The strain values, at the same locations, increase by a factor of 2.5, when compared with those observed after 1 mm translation. The trapdoor displacement, however, does not influence the angle of inclination of the shear bands. In the passive arching situation, the surface surcharge also influences the shear band development. As shown in Figs. 3.3(d) and 3.4(d), the shear bands originate vertically at the trapdoor edges and orient more outwardly than in the no-surcharge case [see Figs. 3.3(c) and 3.4(c)]. The clear outward orientation of the shear bands with the surcharge loading is associated with the additional stress applied to the sand

by the surcharge block. The additional stress increases the density of the sand and, hence, its resistance to shear. The stresses decrease with distance from the edges of the surcharge block. Therefore, the shear bands are pushed slightly more outward. With the application of the surcharge, the extent of trapdoor translation (from 1 to 3 mm) does not significantly influence the development of the shear bands. Unlike, in the case of active arching, the shear bands do not develop toward the surcharge block corners, rather they meet the soil surface some distance from the corners.

From the shear band development shown in Figs. 3.3 and 3.4, a general representation of the strain localisation is illustrated in Fig. 3.5. As can be seen, the shear bands in all four cases exhibit a piecewise linear development, which is composed of two segments at different angles of inclination. From the patterns and magnitudes of shear strains observed in Figs 3.3, it can be observed that the upper segments, which are closer to the surface, show lower shear intensity but are more diffused. Fig. 3.5 indicates the complexity of strain localisation caused by arching in the soil, which will be further investigated in the following paragraphs.

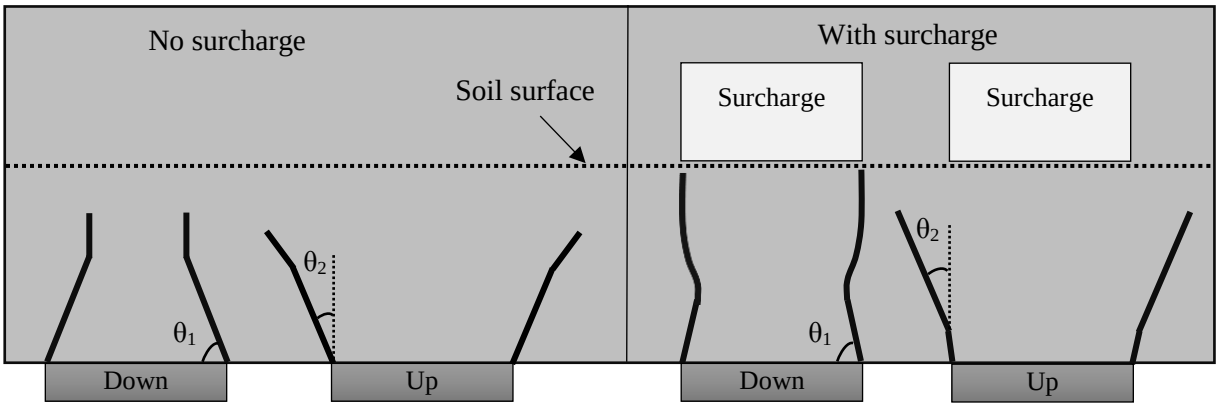

Fig. 3.5. Schematic representation of general shearing band patterns in different aching modes in the trapdoor apparatus

To gain additional insight into the sand particle arrangement in response to arching, the particle displacement vectors and their variation across the shear bands, are shown in Fig. 3.6(a–d). In addition, several sections are identified across the shear bands at selected locations and the vertical displacement of the sand along the sections is captured using the VIC-2D software. The locations of the sections and the corresponding vertical displacement profiles are presented in Figs. 3.6(a–d) and 3.6(e–h), respectively. Each of the previous arching conditions, corresponding to the state of the 3 mm trapdoor translation, are considered. The sections are oriented perpendicular to the shear band from point *A*, which is close to the trapdoor centre, to point *A*', which is outside the arching affected zone. The sections are chosen at similar locations in each of the four arching conditions, for comparison purposes. It is noteworthy that the VIC-2D program selects the origin of the Cartesian coordinates to be the geometrical centre of the AOI. Therefore, downward displacements have a negative sign, as are shear strains to the left. On each of the DIC graphical outputs in Fig. 3.6(a–d), the total displacements of the sand caused by arching are represented by arrows that are drawn to scale.

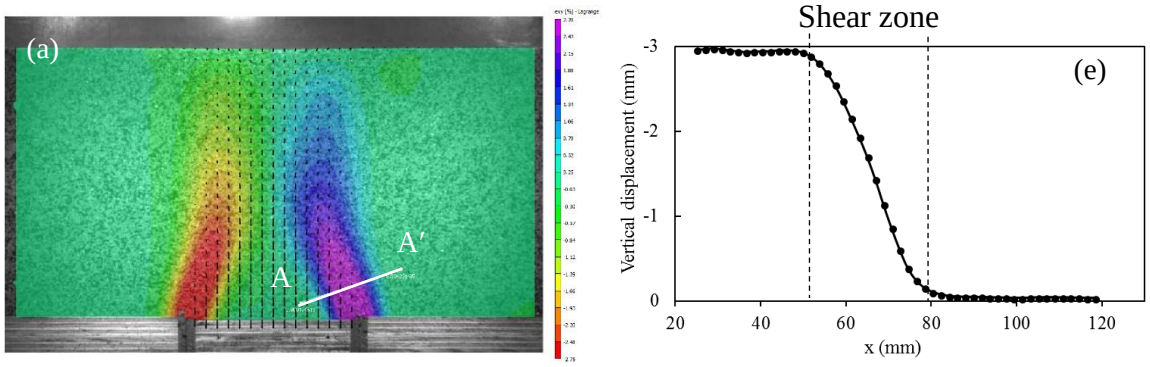

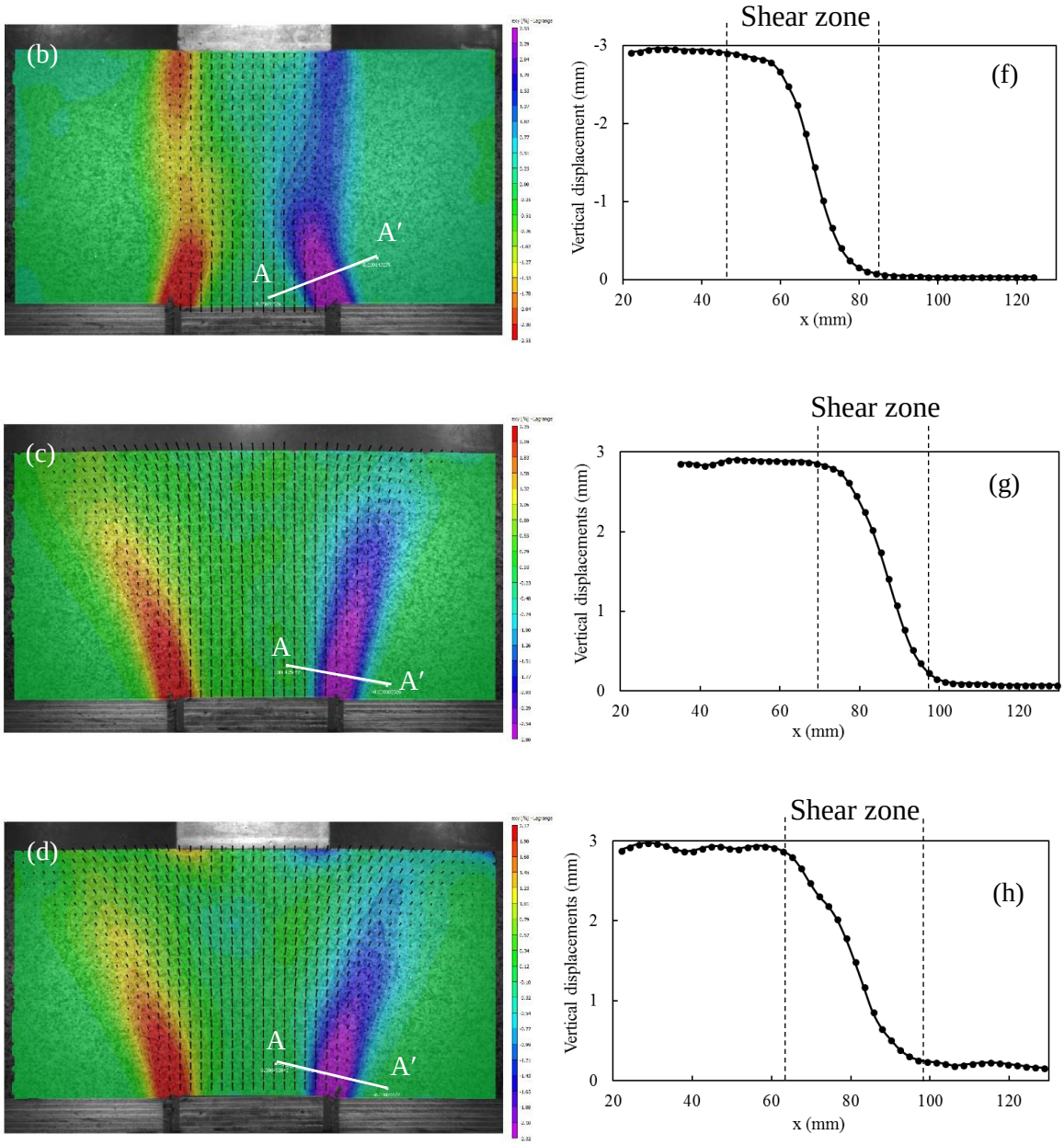

Fig. 3.6. Analysis of sand displacements after a 3 mm trapdoor translation under: (a) active arching with no surcharge, (b) active arching with a 5 kPa central surcharge, (c) passive arching with no surcharge, (d) passive arching with a 5 kPa central surcharge; and (e–h) their corresponding vertical displacements along the *A*–*A′* sections

As shown in Figs. 3.6(a–d), the zone within which the sand particles displace falls into the area encompassed by the shear bands or 'arch'. For example, in the case of the active arching without surcharge [Fig. 3.6(a)], the sand displacement zone lies in a triangular

pattern formed by the pair of shear bands, with the sand noticeably displacing inside the arch and less markedly at the arch crown. This suggests that the arch supports the sand above. A similarly progressive displacement profile occurs in the case of active arching with the surcharge [Fig. 3.6(b)], however, due to the surcharge, the arch crown becomes more open and a greater volume of sand displaces than in the case with no surcharge. Where passive arching occurs [Figs. 3.6(c–d)], the volume of sand encompassed by the shear bands, or the 'inversed arch', moves up in a similar scale. It is plausible to suggest that the arch behaves as a 'pocket', displacing the volume of sand inside the arch to the distance approximately equal to the trapdoor translation. The displacements of sand particles outside the arches are negligible. Therefore, the sand surface deforms to a smaller degree in the case of active arching and heaves noticeably when the sand layer is subjected to passive arching. Clear differences in the vertical displacement of the sand, within the shear bands, are shown in Figs. 3.6(g–h). For all of the four arching conditions, the vertical displacement decreases from about 3 mm, for the particles to the left of the shear band, to zero for the particles to the right. This displacement difference of 3 mm is in fact equal to the trapdoor translation. The horizontal projected lengths of the formed shear zone measure 30–40 mm, depending on the arching scenario.

To examine further the phenomenon of strain localisation due to arching, the thickness and inclination angles of the shear bands developed are characterised. Generally, the shear band thickness for granular materials is a function of stress level, relative density, particle size and shape, dilation and internal friction angles, loading and testing type, confining pressures, geometric configuration, and boundary conditions (Vermeer, 1990; Lade, 2003; Alshibli et al., 2006; Alshibli and Hasan, 2008; Guo, 2012; Borja et al., 2013). Some of these variables are interconnected; for example, dilatancy depends on relative density and stress level. The shear band thickness (t) is usually normalised with respect to

the median particle size (D_{50}). The normalised shear values for different test cases are presented in Table 3.1. The values are averaged over four sections, similar to those depicted in Fig. 3.6, in the trapdoor overburden soil on both the left and right hand shear bands, which are clear and well-formed. The distance over which the shear strains are greater than 50% of the maximum shear strain in each band define the limits of both sides of the shear band. This distance also corresponds to the greatest gradient of vertical displacements, as shown in Figs. 3.6(e–h). From sieve analysis data, Sand 8/16 has a D_{50} of 1.75 mm. As can be seen from Table 3.1, the shear band thickness is greater under passive arching when compared with active arching. In addition, it marginally increases with trapdoor translation. The effect of surcharge is also minimal, though it reduced the shear band thickness in active arching and increased the thickness in passive arching. Different ranges of values of normalised shear band thickness have been reported in the literature. For example, Muir Wood (2002) obtained a 7.3–18.5 range from experimental data in the literature; Batiste et al. (2009) determined an average range of 8.3–16.7, with a maximum of 37, by measuring the distance within which porosity increases across visible shear bands; and Vardoulakis (1981) and Santichaianaint (2002) suggested a 10–21 range from their trapdoor experiments. However, a significantly wider range of 16–67 has been reported by Costa et al. (2009) from normal gravity trapdoor tests. Therefore, the normalised shear band thickness values in this study fall within the general range reported in the literature.

Table 3.1. Measured inclination angle and normalised shear band thickness (t/D_{50})

Arching mode	Surcharge (kPa)	Inclination angle	Normalised shear band thickness with respect to trapdoor translation	
			1 mm	3 mm
Active	0	71°	23.7	24.1
Active	5	73°	22.9	23.4
Passive	0	13.5°	24.6	24.9
Passive	5	15°	24.9	26.7

In relation to the inclination angle, a number of different approaches are examined and compared. The inclination angles of the shear bands in Fig. 3.5 can be estimated by adopting a Coulomb's ideal, frictional soil, with an effective internal friction angle (φ') from Eqs. (3.1) and (3.2). The Mohr-Coulomb friction angle of dry Sand 8/16 was determined as 45° from direct shear tests conducted at the same density as that adopted in the trapdoor tests. Therefore, the theoretical (minimum) inclination angles of the shear band are calculated as follows:

$$\theta_1 = 45° + \frac{\varphi'}{2} = 67.5° \tag{3.1}$$

$$\theta_2 = 45° - \frac{\varphi'}{2} = 22.5° \tag{3.2}$$

where θ_1 and θ_2 correspond to the active and passive arching inclination angles, respectively (Fig. 3.5). The measured inclination angles from Figs. 3.3 and 3.4 are also listed in Table 3.1. As can be seen, there is relatively good agreement between the calculated and measured values of θ_1 and θ_2. The deviation from the theoretical values in Eqs. (3.1) and (3.2) are greater with respect to passive arching, when compared with active arching.

For a translating trapdoor, the angle of inclination with respect to vertical, θ_1^s (supplementary angle to θ_1), was proposed by Evans (1983) to be equal to the dilation angle of a dense soil. A non-associated flow rule, with peak values of dilation angle occurring at the onset of plastic behaviour, and gradually declining as strain softening progresses, was considered. To examine this assumption, the dilation angle of Sand 8/16 was obtained from a single direct shear test that was carried out with an applied normal stress equal to the geostatic stress at the base of the sand layer. The soil deformation in a direct shear box test can be approximated with reference to the schematic illustration provided in Fig. 3.7. The angle of dilation (ψ) is then calculated from:

$$\psi = \arctan\left(\frac{\Delta y}{\Delta x}\right) \tag{3.3}$$

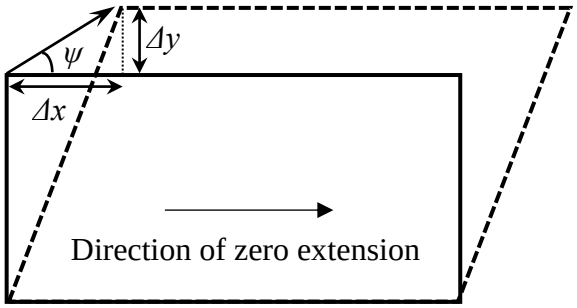

Fig. 3.7. Angle of dilation in a direct shear box test (modified after Bolton, 1986)

The vertical and horizontal displacements of the soil sample were recorded during shearing using two LVDTs and the results are shown in Fig. 3.8. Negative vertical displacements indicate expansion. The dilation angle was determined from the linear part of the graph in Fig. 3.7 for a displacement of up to 3 mm (maximum travel of the trapdoor) and was found to be 19.2°. The θ_1^s values from Table 3.1 are respectively computed as 19° and 17° for the no surcharge and 5 kPa surcharge active arching cases. As can be inferred, the inclination angles suggested by Evans (1983) are in very good agreement with the measured

values in Table 3.1 for active arching. The reduction in θ_1^s, when the surcharge block was applied, is attributed to the increased stress level in the soil, which in turn results in a decrease in dilation and hence θ_1^s value. Similar agreements have been observed by other researchers in the case of active arching (e.g. Dewoolkar et al., 2007; Costa et al., 2009). Taking the associated flow rule into account, Iglesia et. al (2014) concluded that the dilation angle approaches the friction angle, and therefore equated the slip line inclination, θ_1^s, to the friction angle for the active arching case. Comparing the friction angle value of Sand 8/16 and the measured inclination angles, one would see that this is an invalid assumption for trapdoor experiments. More importantly, it is established in the literature that granular soils do not usually follow the associated flow rule (Lade et. al, 1987; Manzari and Dafalias, 1997; Collins and Houlsby, 2001; Liu, 2013).

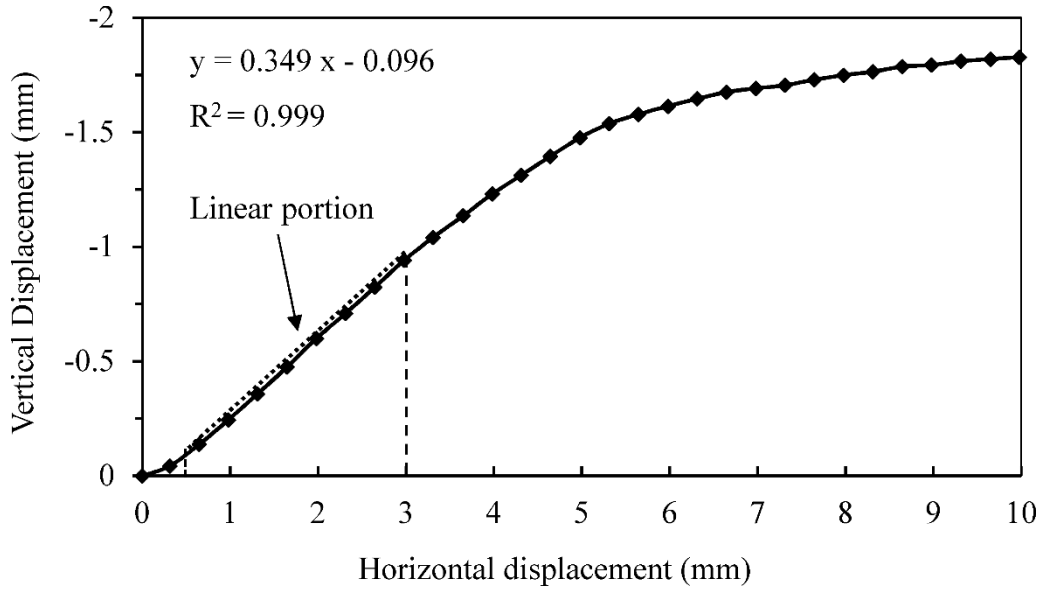

Fig. 3.8. Dilatancy of Sand 8/16 in a direct shear box test with low normal stress

3.3.2. Principal strains

If an element of interest is subjected to plane-strain deformation in the *x*–*y* plane, as shown in Fig. 3.9(a), the *x*–*y* plane can be converted to the principal strain plane P_1–P_2, in Fig. 3.9(b), where the element is transformed into a principal state: the shear strains are nullified, and the principal strains are presented as the major principal strain, $\varepsilon_1=\overline{MM'}/\overline{OM}$, and minor principal strain, $\varepsilon_2=\overline{NN'}/\overline{ON}$. Using the knowledge of geometry, one could derive the following expression for major and minor principal strains under plane-strain conditions:

$$\varepsilon_{1,2} = \frac{\varepsilon_{xx}+\varepsilon_{yy}}{2} \pm \sqrt{\left(\frac{\varepsilon_{xx}-\varepsilon_{yy}}{2}\right)^2 + \left(\frac{\gamma_{xy}}{2}\right)^2} \tag{3.4}$$

where ε_{xx}, ε_{yy}, and γ_{xy} are horizontal strains, vertical strains and shear strains, respectively. As with the convention for stress, the strains ε_1 and ε_2 can be mapped using contours. A map of the scaled principal strains over the area of concern assists in gaining an insight into the occurrences of principal stress rotation, which is important for examining the development of arching.

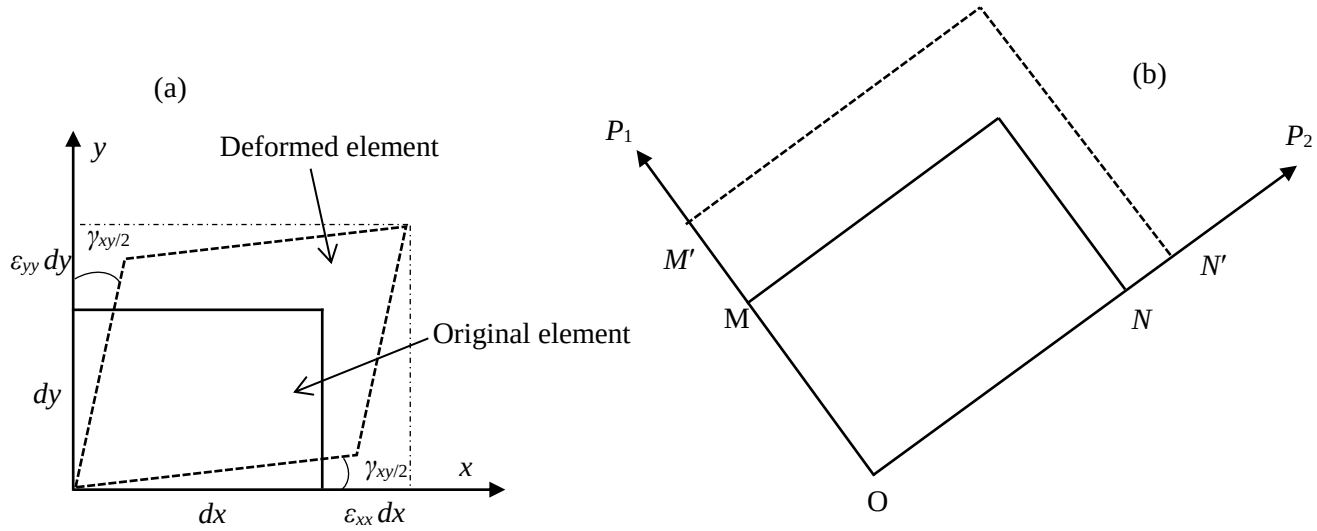

Fig. 3.9. Schematic representation of deformation of the same element in two planes: (a) Cartesian *x*–*y* plane, and (b) principal strain P_1–P_2 plane

The DIC software VIC-2D is programmed to calculate the strains and principal strains and the results for all of the test cases are presented in Figs. 3.10–3.13. The strain at the point of interest acts in the direction of the corresponding short line. As shown in Figs. 3.10–3.13, the distributions of the major and minor principal strains reproduce the corresponding distribution patterns of the shear strains (Figs. 3.3 and 3.4). Moreover, where the surface surcharge is applied, an additional deformation mechanism appears below the surcharge block. This mechanism can also be observed in the shear strain plots. However, the extent and intensity of the deformation pattern, pertinent to the presence of the surcharge, are more pronounced in the major and minor principal strain plots. For a continuous solid and if the material is isotropic, the directions of major and minor principal strains are aligned with the directions of major and minor principal stresses.

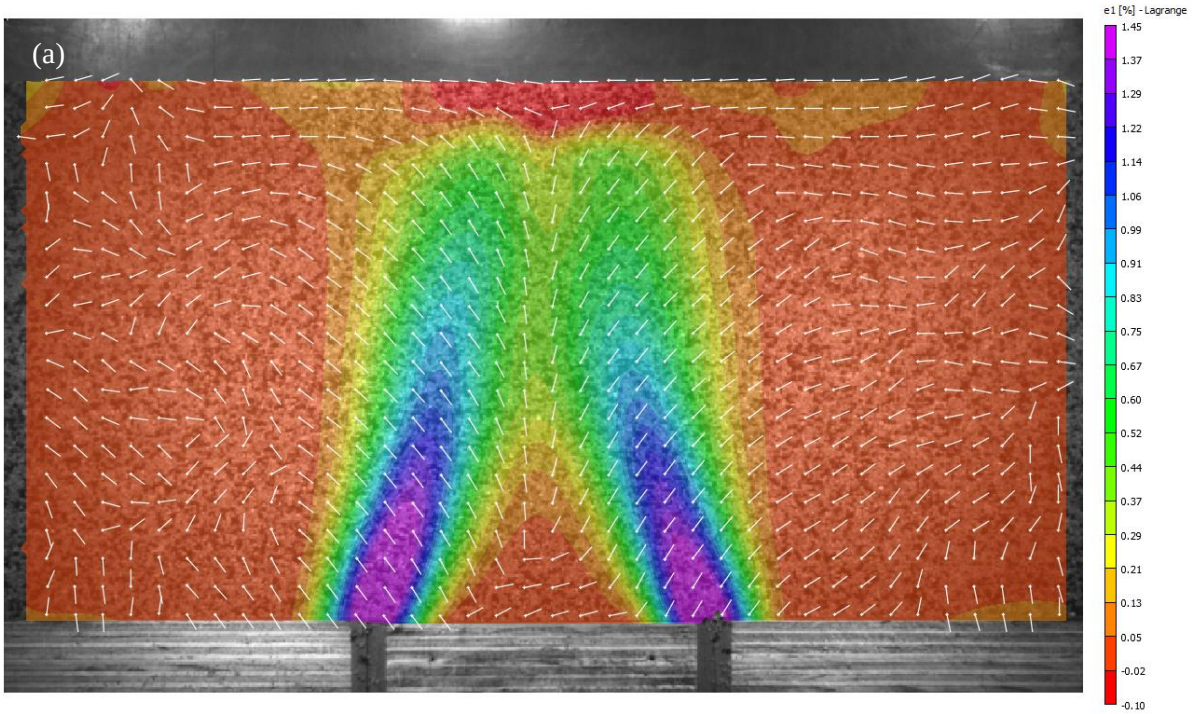

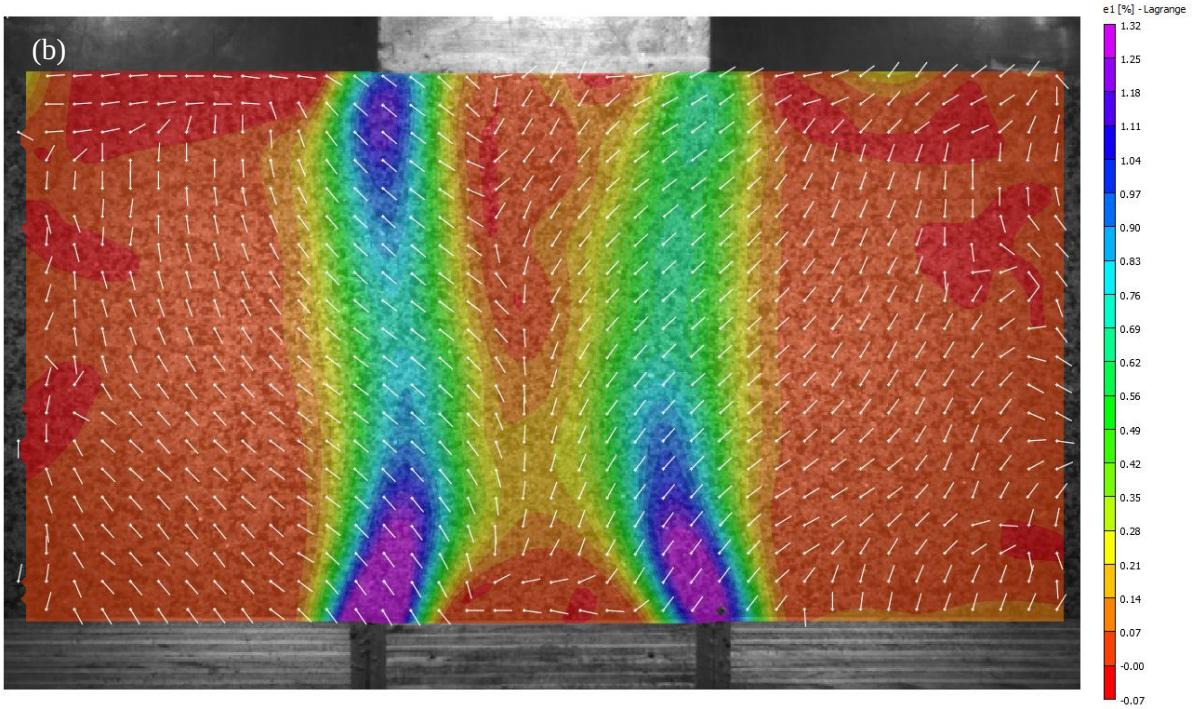
(b)
e1 [%] - Lagrange
1.32
1.25
1.18
1.11
1.04
0.97
0.90
0.83
0.76
0.69
0.62
0.56
0.49
0.42
0.35
0.28
0.21
0.14
0.07
-0.00
-0.07

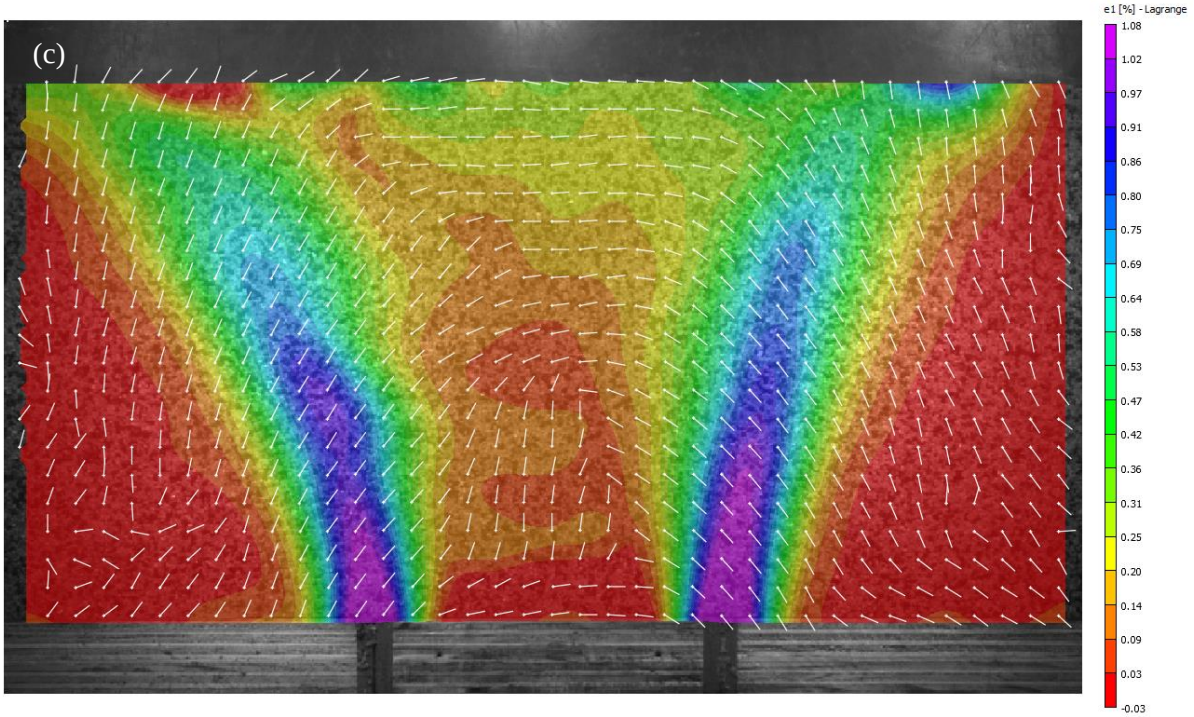
(c)
e1 [%] - Lagrange
1.08
1.02
0.97
0.91
0.86
0.80
0.75
0.69
0.64
0.58
0.53
0.47
0.42
0.36
0.31
0.25
0.20
0.14
0.09
0.03
-0.03

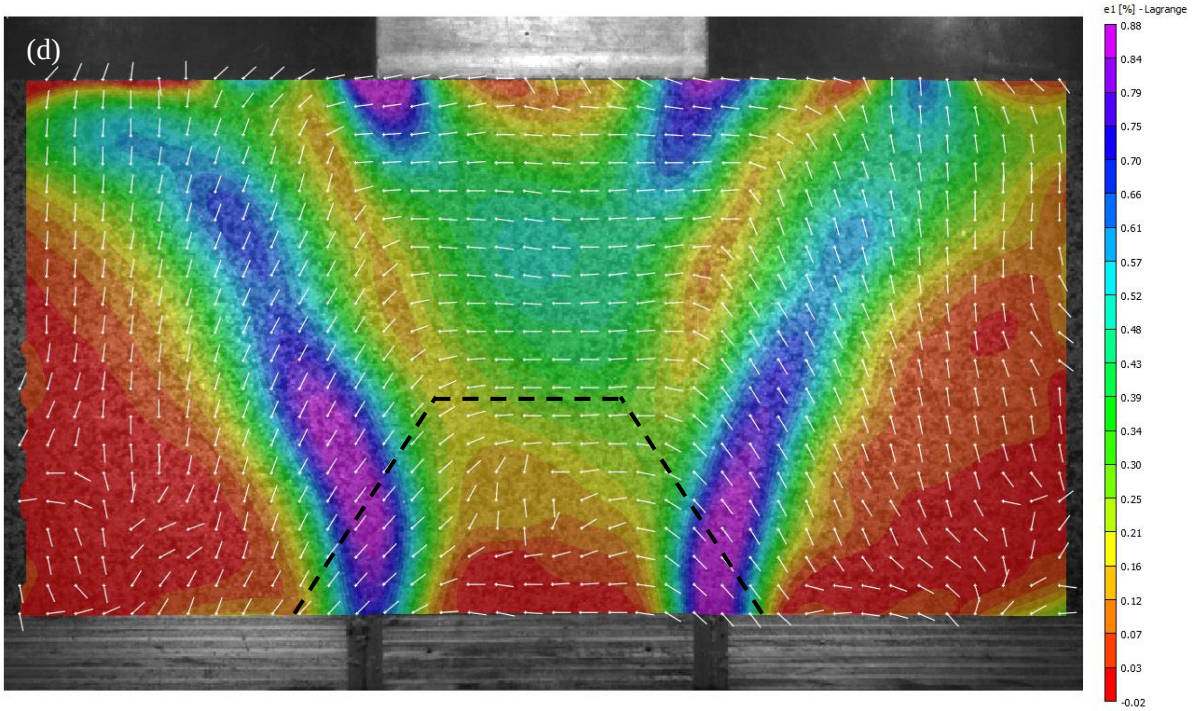

Fig. 3.10. Major principal strain distribution in the sand layer caused by a 1 mm trapdoor translation under: (a) active arching with no surcharge, (b) active arching with a 5 kPa central surcharge, (c) passive arching with no surcharge, and (d) passive arching with a 5 kPa central surcharge

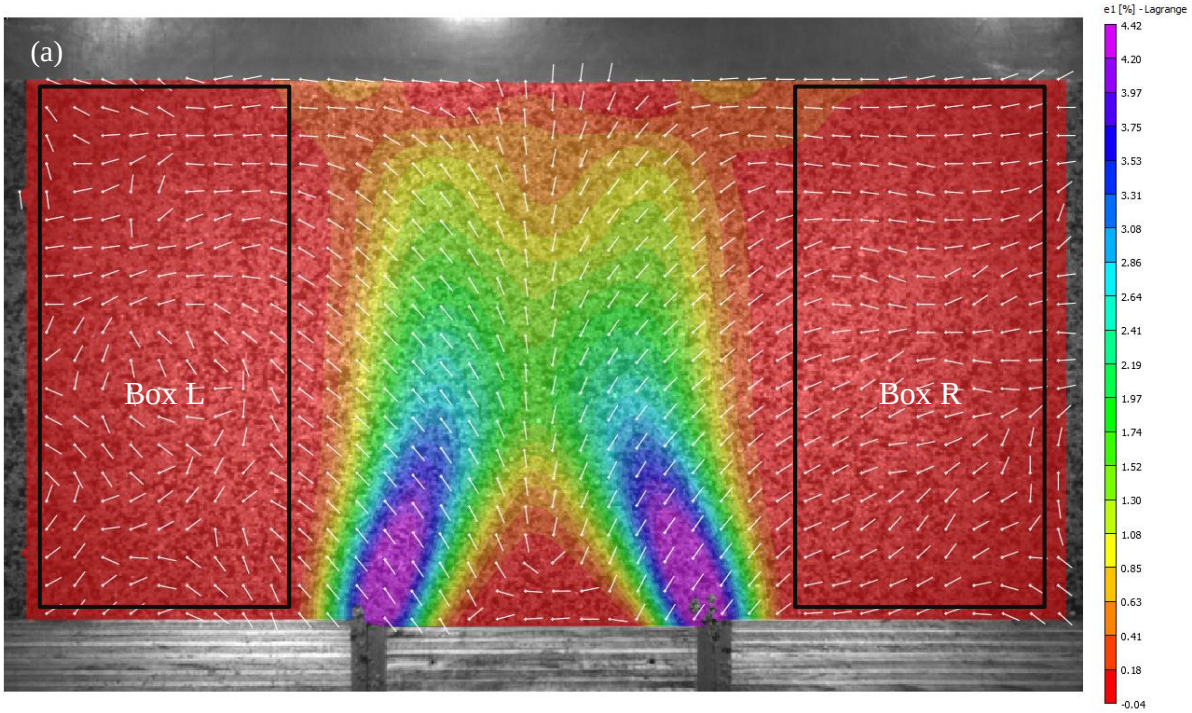

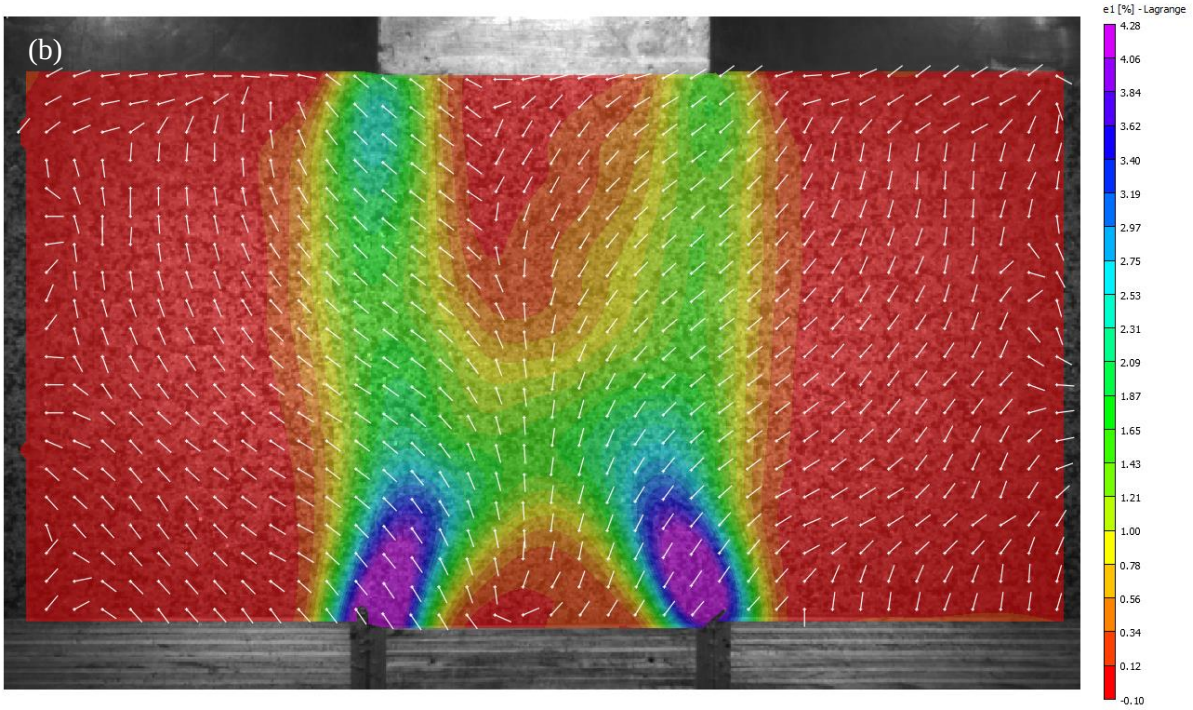
(b)
e1 [%] - Lagrange
4.28
4.06
3.84
3.62
3.40
3.19
2.97
2.75
2.53
2.31
2.09
1.87
1.65
1.43
1.21
1.00
0.78
0.56
0.34
0.12
-0.10

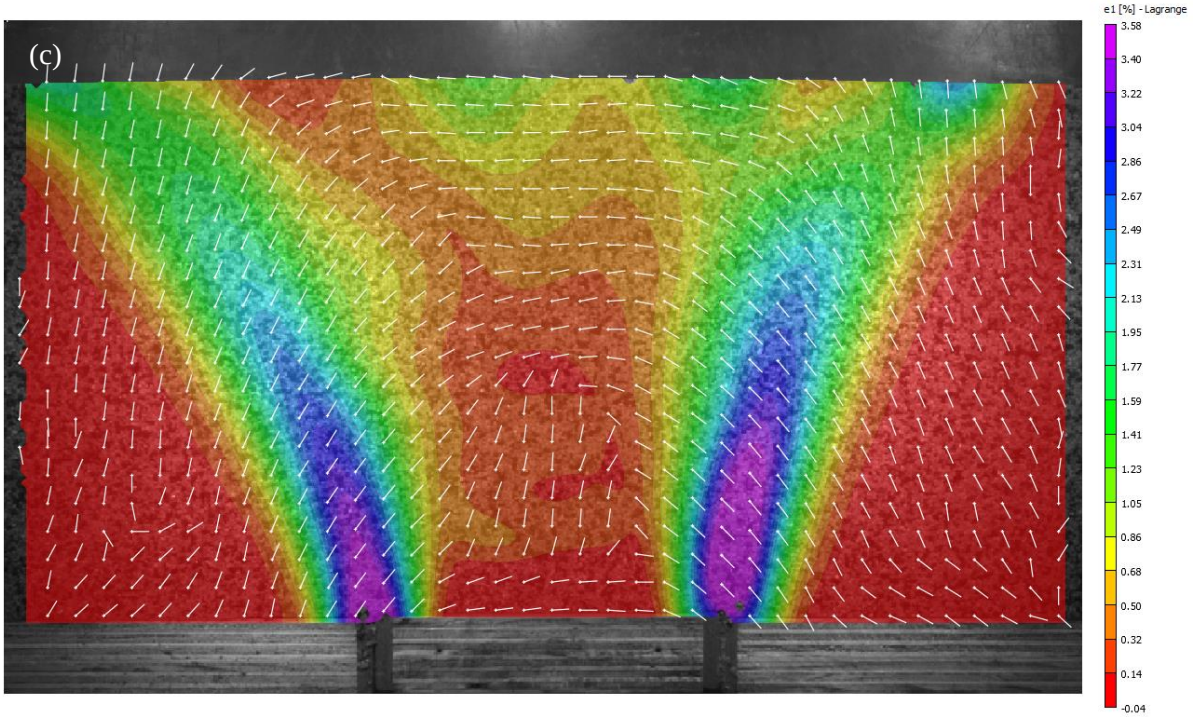
(c)
e1 [%] - Lagrange
3.58
3.40
3.22
3.04
2.86
2.67
2.49
2.31
2.13
1.95
1.77
1.59
1.41
1.23
1.05
0.86
0.68
0.50
0.32
0.14
-0.04

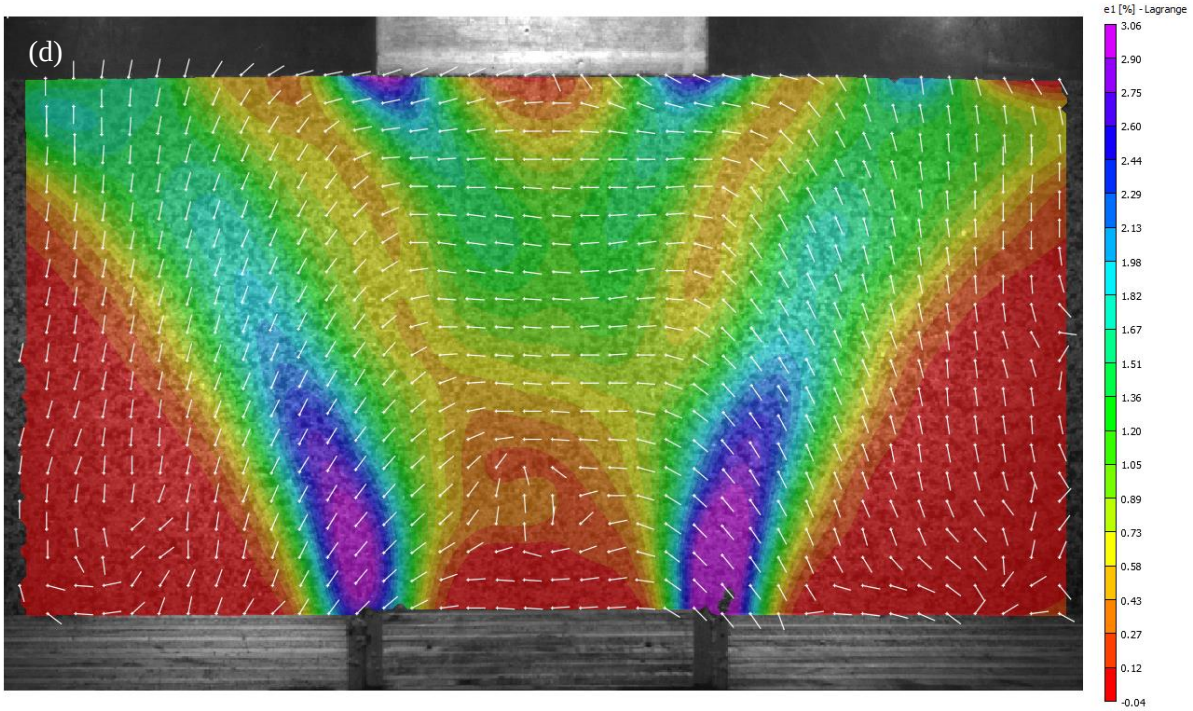

Fig. 3.11. Major principal strain distribution in the sand layer caused by a 3 mm trapdoor translation under: (a) active arching with no surcharge, (b) active arching with a 5 kPa central surcharge, (c) passive arching with no surcharge, and (d) passive arching with a 5 kPa central surcharge

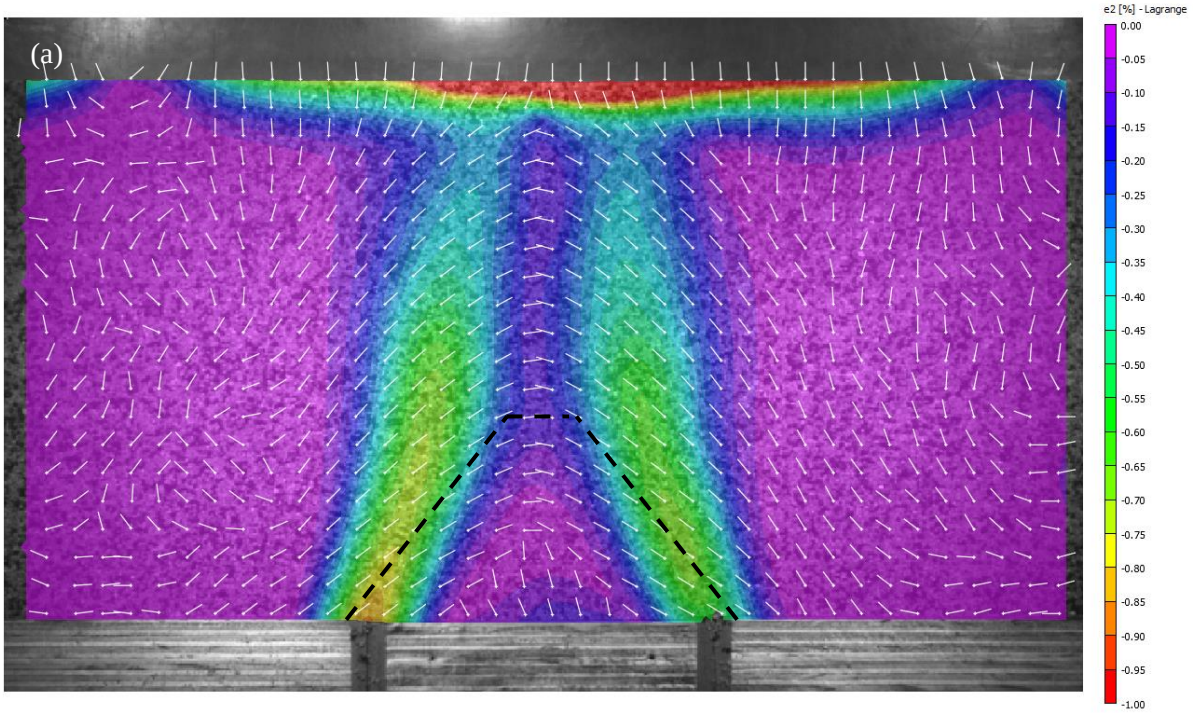

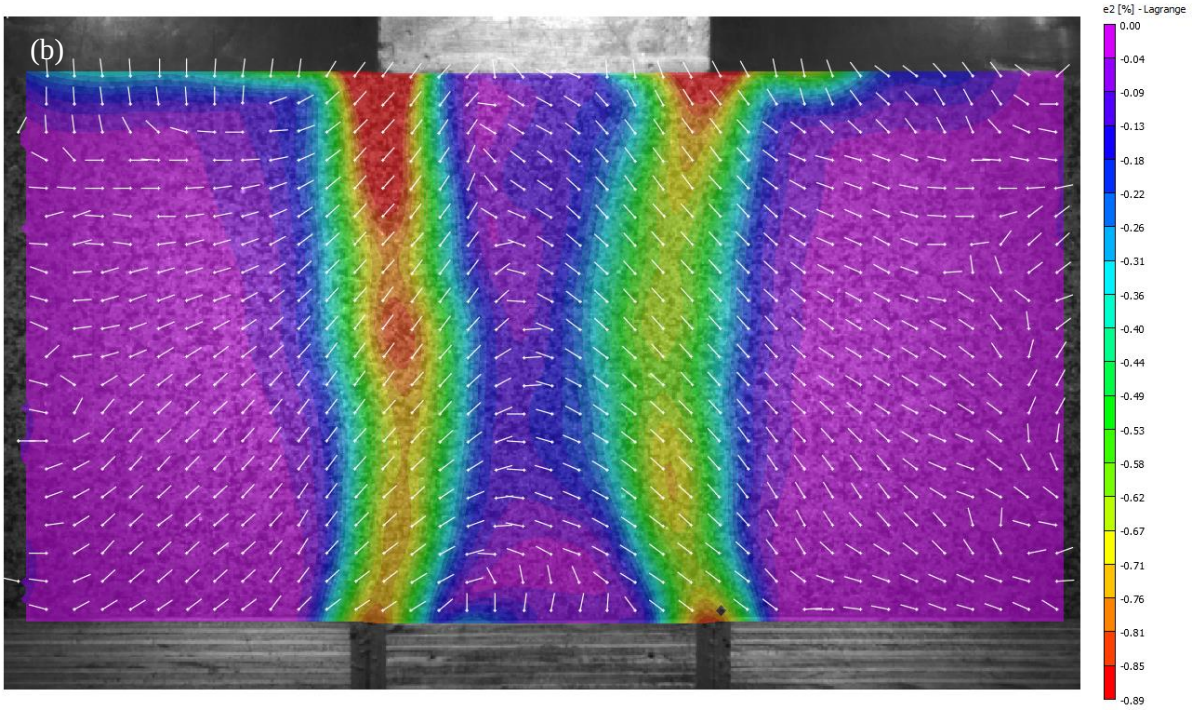
(b)
e2 [%] - Lagrange
0.00
-0.04
-0.09
-0.13
-0.18
-0.22
-0.26
-0.31
-0.36
-0.40
-0.44
-0.49
-0.53
-0.58
-0.62
-0.67
-0.71
-0.76
-0.81
-0.85
-0.89

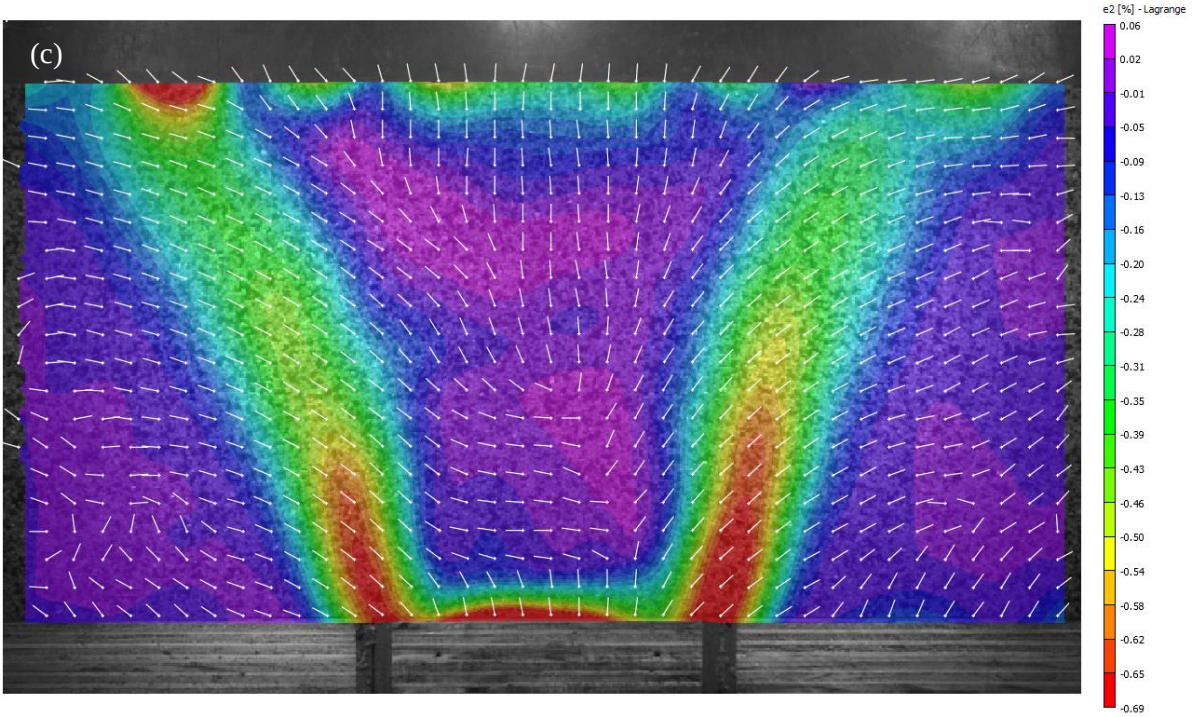
(c)
e2 [%] - Lagrange
0.06
0.02
-0.01
-0.05
-0.09
-0.13
-0.16
-0.20
-0.24
-0.28
-0.31
-0.35
-0.39
-0.43
-0.46
-0.50
-0.54
-0.58
-0.62
-0.65
-0.69

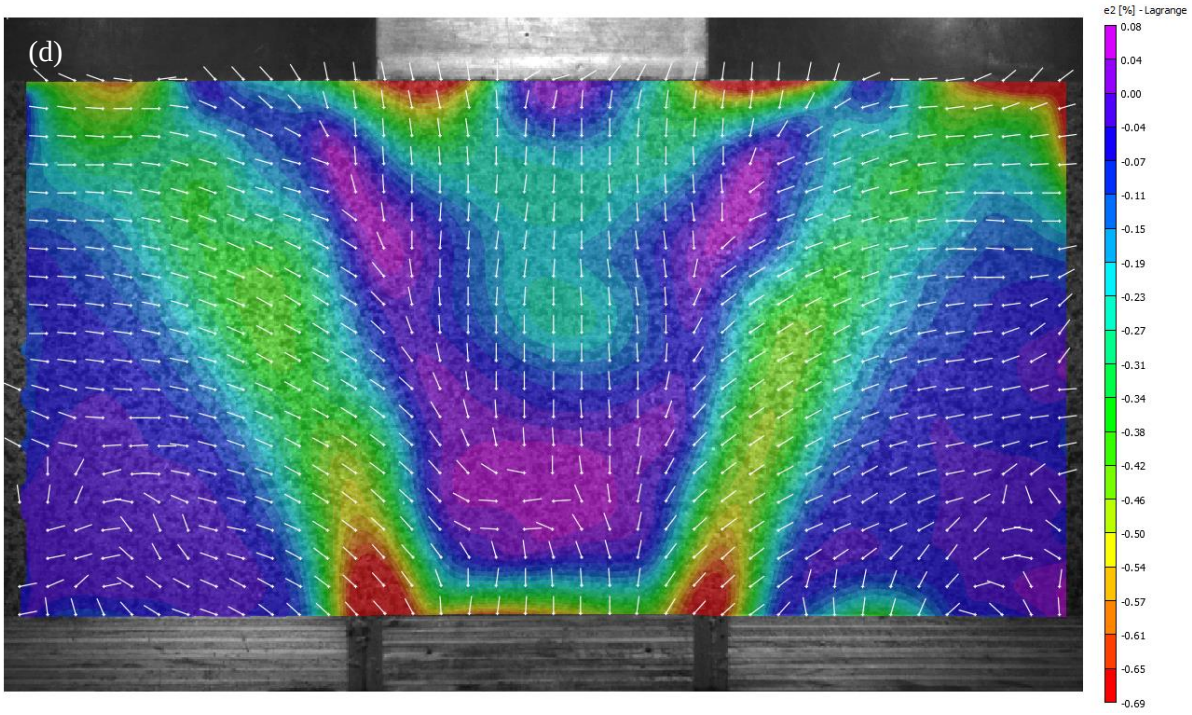

Fig. 3.12. Minor principal strain distribution in the sand layer caused by a 1 mm trapdoor translation under: (a) active arching with no surcharge, (b) active arching with a 5 kPa central surcharge, (c) passive arching with no surcharge, and (d) passive arching with a 5 kPa central surcharge

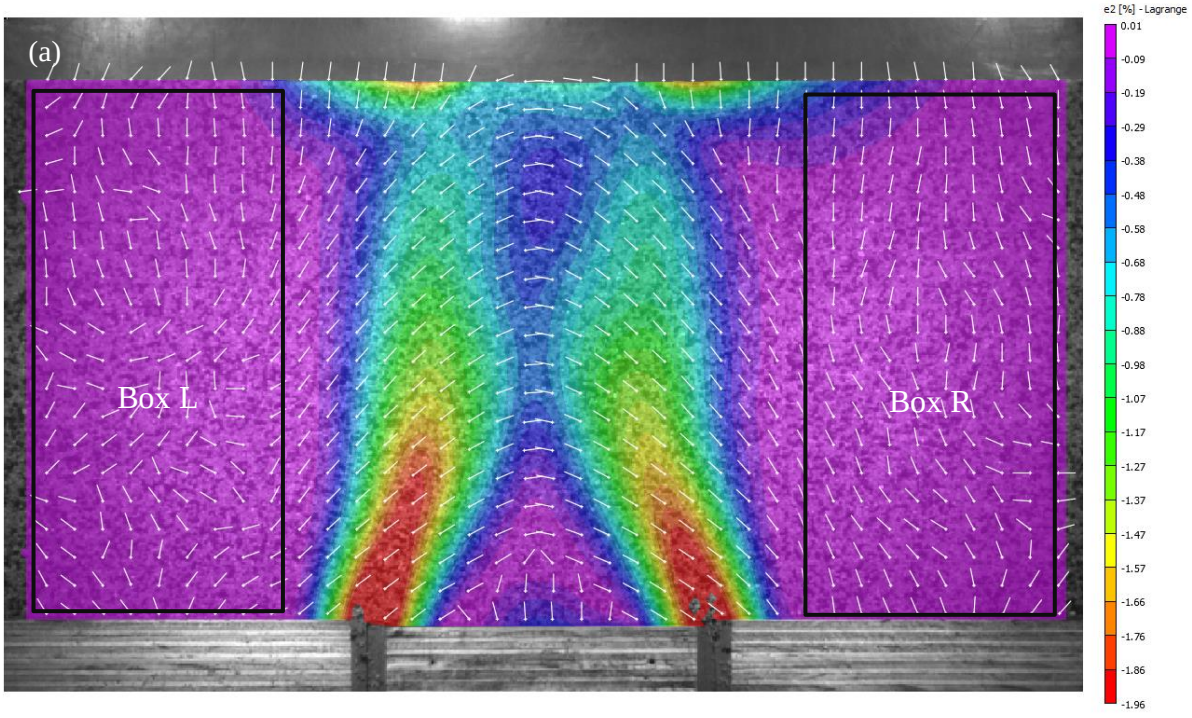

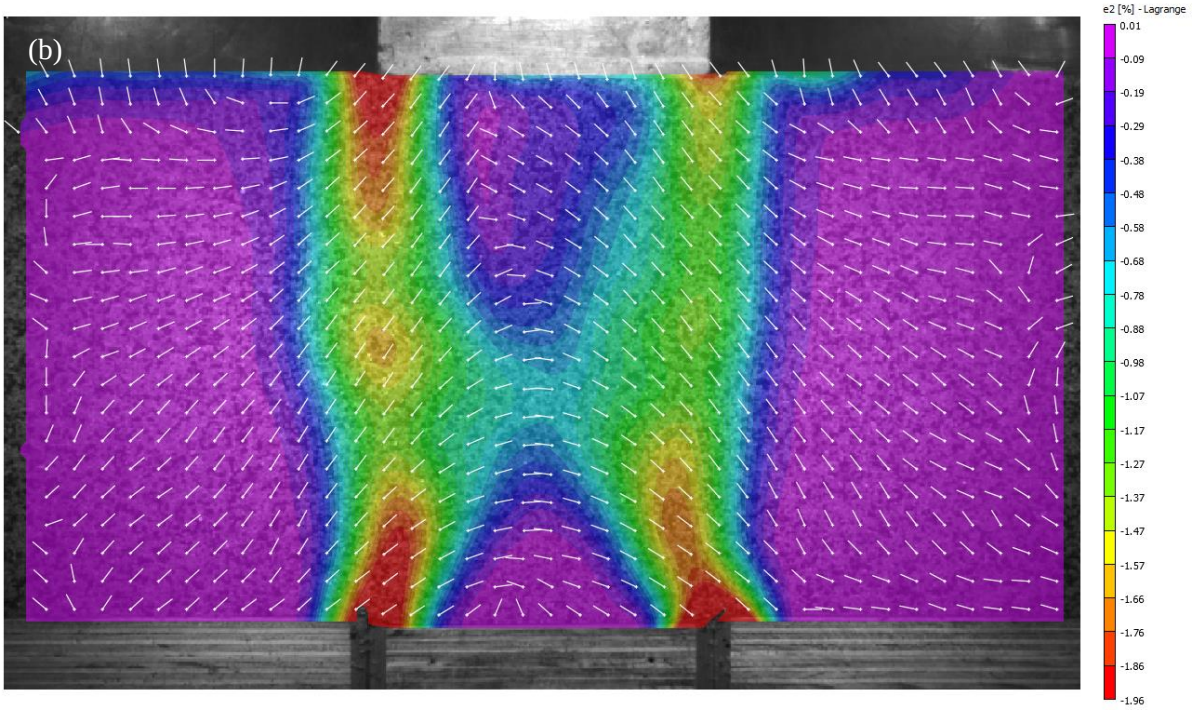
(b)
e2 [%] - Lagrange
0.01
-0.09
-0.19
-0.29
-0.38
-0.48
-0.58
-0.68
-0.78
-0.88
-0.98
-1.07
-1.17
-1.27
-1.37
-1.47
-1.57
-1.66
-1.76
-1.86
-1.96

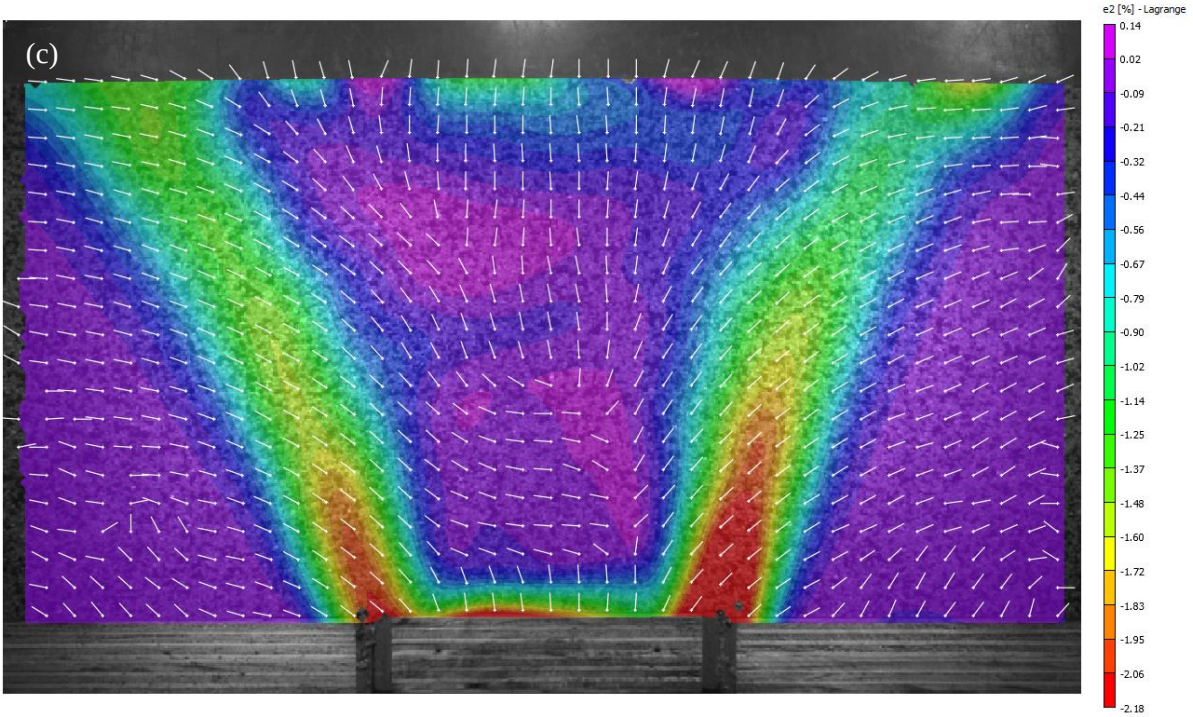
(c)
e2 [%] - Lagrange
0.14
0.02
-0.09
-0.21
-0.32
-0.44
-0.56
-0.67
-0.79
-0.90
-1.02
-1.14
-1.25
-1.37
-1.48
-1.60
-1.72
-1.83
-1.95
-2.06
-2.18

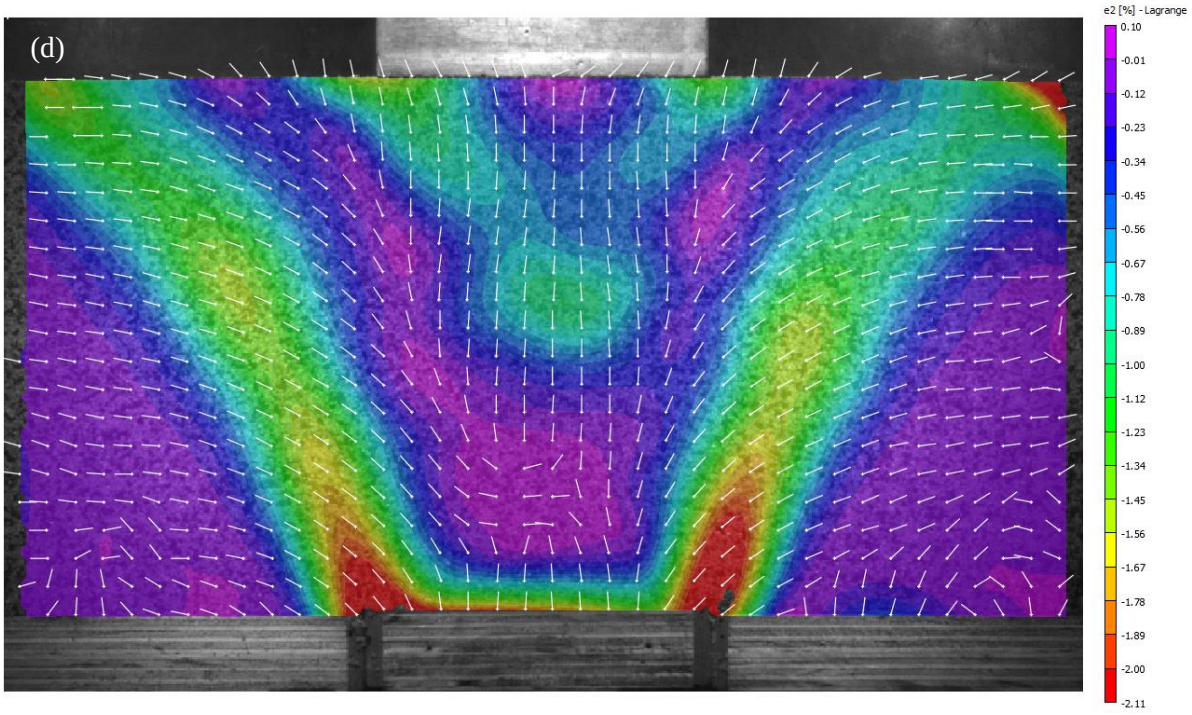

Fig. 3.13. Minor principal strain distribution in the sand layer caused by a 3 mm trapdoor translation under: (a) active arching with no surcharge, (b) active arching with a 5 kPa central surcharge, (c) passive arching with no surcharge, and (d) passive arching with a 5 kPa central surcharge

As can be inferred from Figs. 3.11–3.13, principal strains ε_1 and ε_2 should be approximately zero in the areas outside the arching zone. A closer examination of the output data was carried out by averaging the principal strains within two rectangular regions: L on the left-hand side, and R on the right-hand side of the arch, as shown in Figs. 3.11(a) and 3.13(a). The ε_1 and ε_2 values were essentially zero (around 10^{-3} %), as expected. This indicates that the VIC-2D generated values of ε_1 and ε_2 data in these regions are negligible and thus irrelevant for further analysis. Focus is, therefore, placed on the strains that were measured in the deformed region. The distinctive feature that can be highlighted from Figs. 3.11–3.13, is that the Lagrangian minor principal strain directions obtained in the active arching tests form an arch above the trapdoor. In the passive arching tests, however, the

major principal strain directions create a wide trapezoidal shaped arch. The placement of the surcharge did not influence this pattern.

3.3.3. Volumetric strains

Volumetric strains provide very useful information about the dilatancy and contraction characteristics of a deforming soil. Other techniques, such as X-ray detections used by some researchers (Roscoe et al. 1963; Stone 1988; Muir Wood 2002), only indicate shear bands or displacement discontinuities but cannot quantitatively assess the accompanying volumetric strains (Muir Wood, 2002). The DIC system not only captures the shear bands developed in the soil layer but also provides the volumetric strains that occur across the sand layer. The volumetric strains, $(\frac{\nabla V}{V})$, for the element shown in Fig. 3.9(b), is calculated as:

$$\frac{\nabla V}{V} = \frac{\left(\overline{OM} + \overline{MM'}\right) \cdot \left(\overline{ON} + \overline{NN'}\right) - (\overline{OM}) \cdot (\overline{ON})}{(\overline{OM}) \cdot (\overline{ON})} = (\varepsilon_1 + 1) \cdot (\varepsilon_2 + 1) - 1$$

$$= \varepsilon_1 + \varepsilon_2 + \varepsilon_1 \cdot \varepsilon_2 \qquad (3.5)$$

The results of the volumetric strain of the sand layer due to the 1 and 3 mm trapdoor displacements, under the active and passive arching conditions, are presented in Figs. 3.14 and 3.15, respectively. It should be noted that positive values correspond to dilation whereas negative values represent compression. It can be seen from these figures that the major changes in the volume of the sand possessed a dilative nature, as expected from the strain localisation phenomenon illustrated in Figs. 3.3 and 3.4. Although, to a smaller extent, compressive volume change can also be observed near the soil surface and above the trapdoor element.

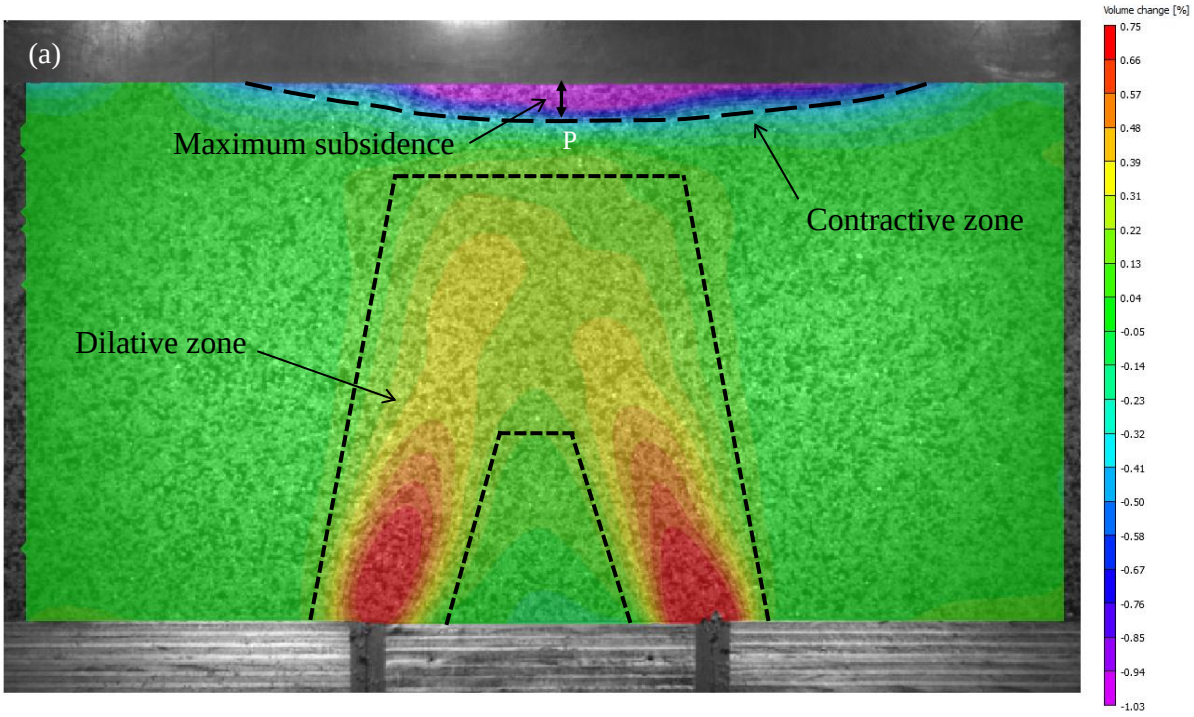
(a)
Maximum subsidence
P
Contractive zone
Dilative zone
Volume change [%]
0.75
0.66
0.57
0.48
0.39
0.31
0.22
0.13
0.04
-0.05
-0.14
-0.23
-0.32
-0.41
-0.50
-0.58
-0.67
-0.76
-0.85
-0.94
-1.03

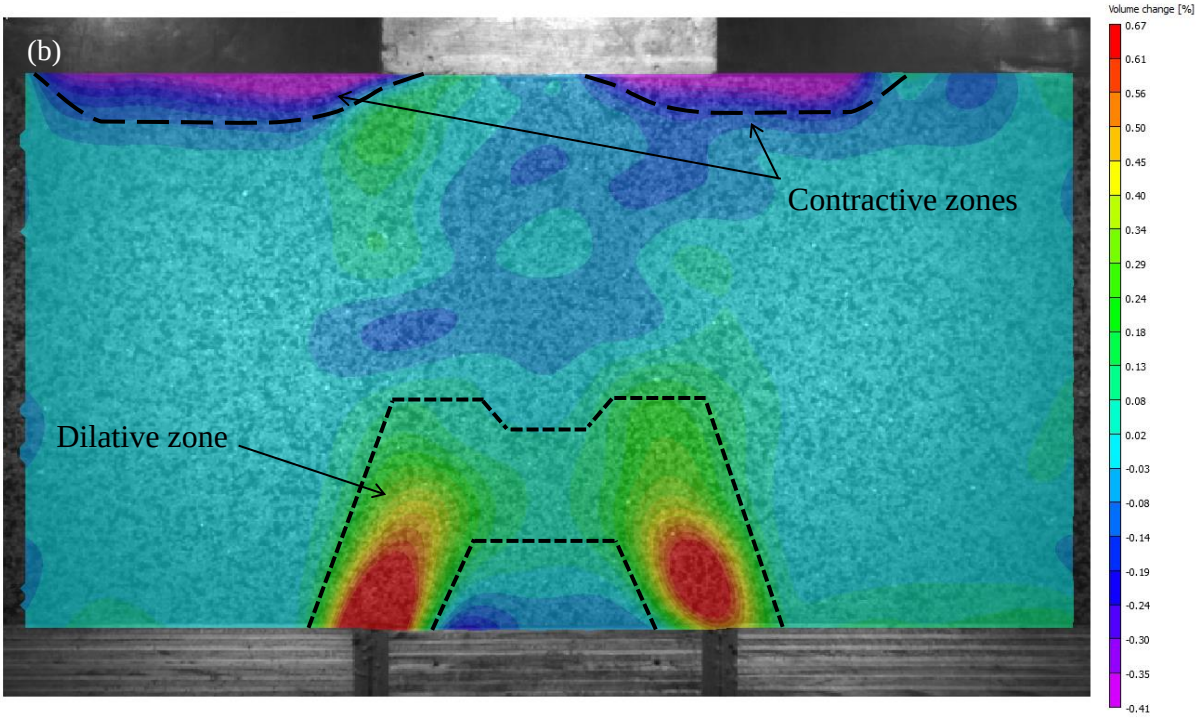
(b)
Contractive zones
Dilative zone
Volume change [%]
0.67
0.61
0.56
0.50
0.45
0.40
0.34
0.29
0.24
0.18
0.13
0.08
0.02
-0.03
-0.08
-0.14
-0.19
-0.24
-0.30
-0.35
-0.41

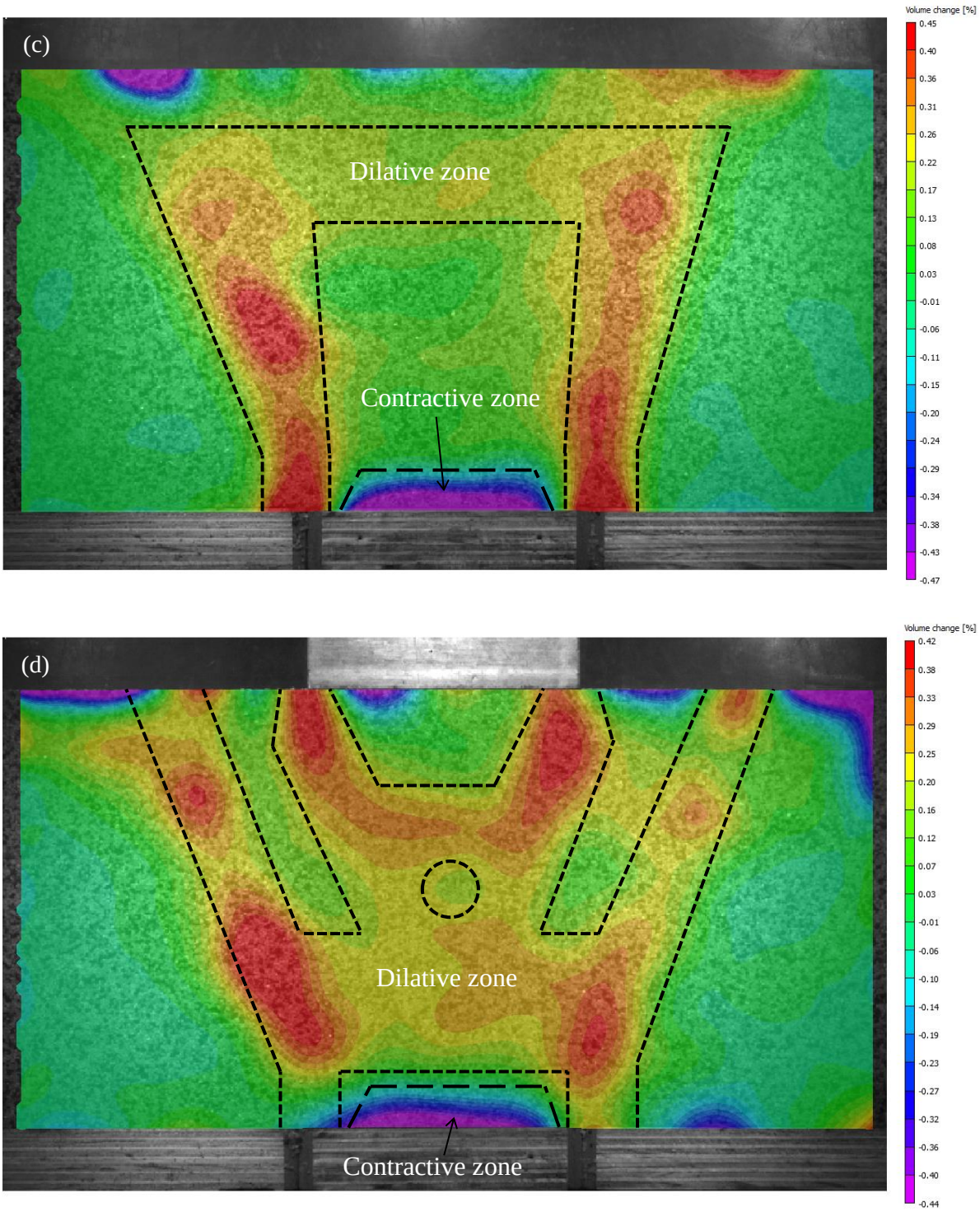

Fig. 3.14. Volumetric strain distribution in the sand layer caused by a 1 mm trapdoor translation under: (a) active arching with no surcharge, (b) active arching with a 5 kPa central surcharge, (c) passive arching with no surcharge, and (d) passive arching with a 5 kPa central surcharge

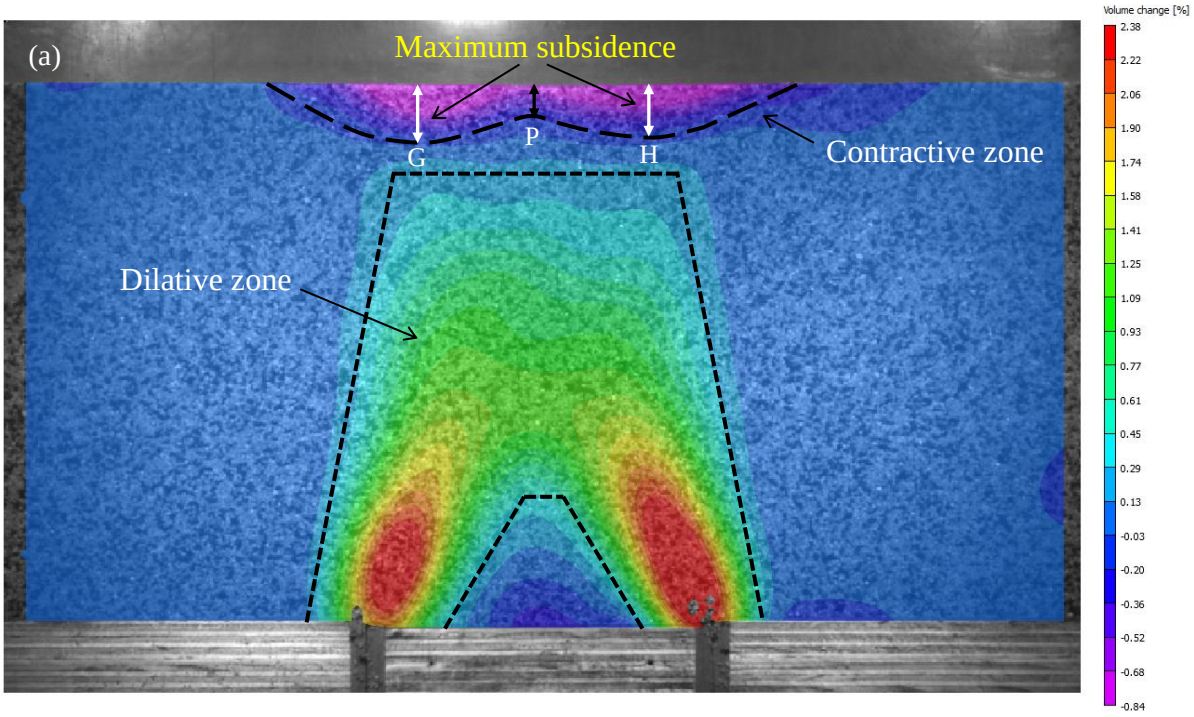
(a)
Maximum subsidence
G
P
H
Contractive zone
Dilative zone
Volume change [%]
2.38
2.22
2.06
1.90
1.74
1.58
1.41
1.25
1.09
0.93
0.77
0.61
0.45
0.29
0.13
-0.03
-0.20
-0.36
-0.52
-0.68
-0.84

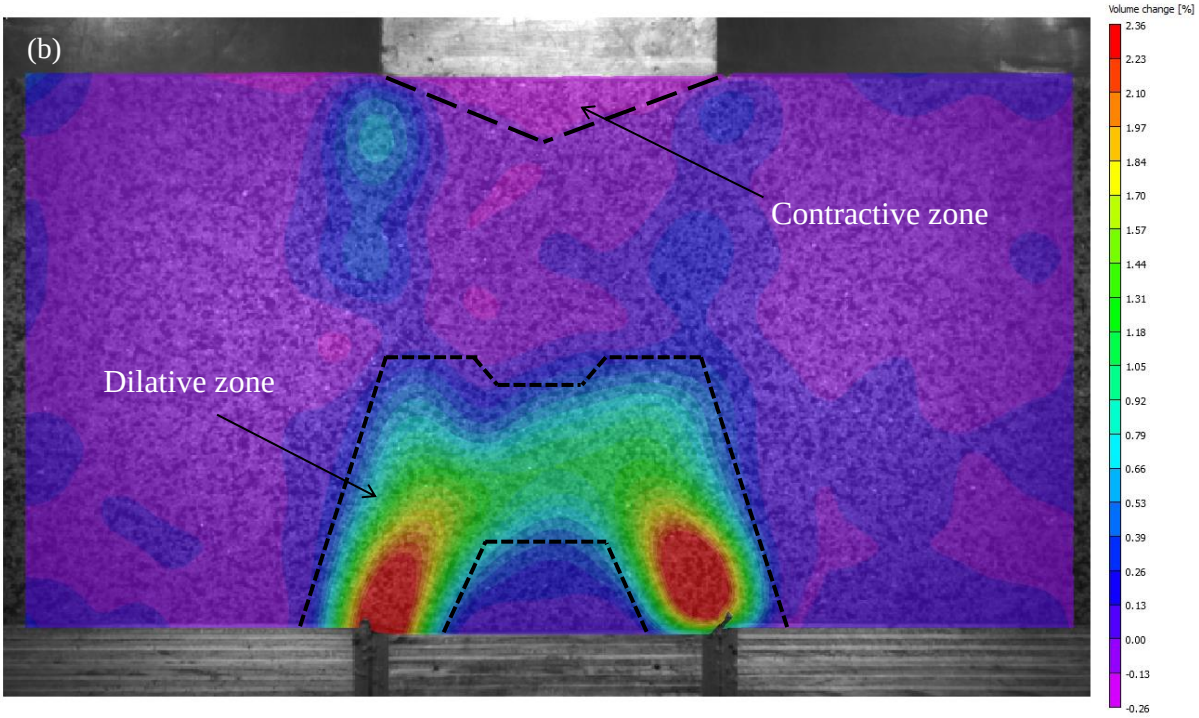
(b)
Contractive zone
Dilative zone
Volume change [%]
2.36
2.23
2.10
1.97
1.84
1.70
1.57
1.44
1.31
1.18
1.05
0.92
0.79
0.66
0.53
0.39
0.26
0.13
0.00
-0.13
-0.26

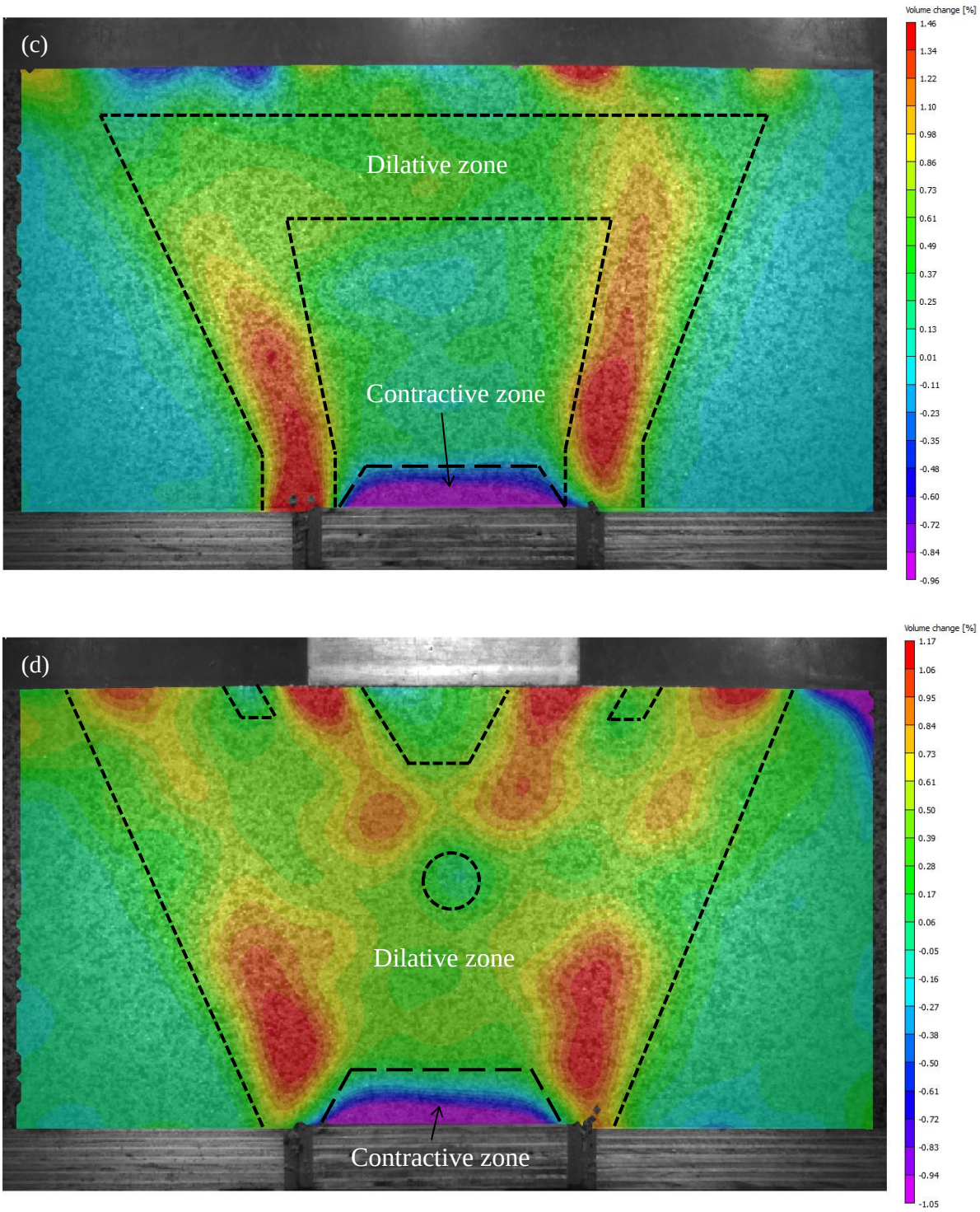

Fig. 3.15. Volumetric strain distribution in the sand layer caused by a 3 mm trapdoor translation under: (a) active arching with no surcharge, (b) active arching with a 5 kPa central surcharge, (c) passive arching with no surcharge, and (d) passive arching with a 5 kPa central surcharge

The significant volumetric strain regions are delineated in Figs. 3.14–3.15. However, the regions of minor volume changes are neglected. It can be observed from Figs. 3.14–3.15 that the arrangement patterns of the dilative regions resemble those of the shear strains and principal strains shown in Figs. 3.3–3.4 and Figs. 3.12–3.13. For the active arching scenarios shown in Figs. 3.14(a) and 3.15(a), the dilative body within the sand layer is manifested as 'stool' shaped regions, where the oblique legs of the stool originate from the trapdoor edges and possess the peak values of the volumetric strains. The maximum height of this region is 133% of TW for both the 1 and 3 mm trapdoor displacements, although the peak volumetric strain values more than tripled due to the increased trapdoor displacement. The application of the 5 kPa surcharge block, firstly reduced the size of the stool crown, as illustrated in Figs. 3.14(b) and 3.15(b), and secondly decreased the height of the expanded soil. In this case, the maximum heights of the expansion regions are, respectively, 72% and 95% of TW for the 1 and 3 mm trapdoor displacements. As can be seen, the increase in trapdoor displacement raised the height of the expansion region by 23% when the surcharge was applied. However, the increased trapdoor displacement had no effect on the height of the expansion region when no local surcharge was applied. A small degree of compression, of up to ≈ 0.25%, can be observed in the areas inside of the expansion stool in Figs. 3.14(a–b) and 3.15(a–b) for the active arching tests.

In case of passive arching, displayed in Figs. 3.14 (c–d) and 3.15(c–d), the most expansive regions originate from the trapdoor edges and propagate in an outwardly oriented manner to a shallow depth beneath the soil surface. In the case of no surcharge, the tips of these regions are connected together through a roof, whose shape is rather difficult to idealise. Yet, analogous to the corresponding cases of active arching, it seems that the dilative regions in passive arching also create a stool of expansion, where the legs are oriented outwardly, rather than inwardly. The local surcharge applied at the soil surface

added two additional smaller dilative regions initiating from the surcharge block corners parallel to the main dilative regions to a depth of 60% of TW, irrespective of the extent of the trapdoor displacement [Figs. 3.14(d) and 3.15(d)]. Moreover, the surcharge generalised soil dilation to greater areas, while slightly reducing the intensity of the volumetric change from up to 1.5% to 1.2%. This is because the surcharge increases the normal stresses and thereby reduces the dilative volumetric strains. Overall, the dilative regions in passive arching extend to considerably larger regions when compared with active arching. It should be noted that in a few instances the dilative regions do not originate precisely from the trapdoor edges. This is due to smoothing of the data contained in the DIC subsets and data noise.

As Figs. 3.14 and 3.15 show, soil compression is more significant in passive arching than in active arching. Compressions as great as 1% can be observed in a roughly trapezoidal area above the trapdoor, with a height of up to 15% of the TW in Figs 3.14(c–d) and 3.15(c–d). This is due to the upward trapdoor displacement against the overburden soil, which sandwiches this trapezoidal area between the trapdoor element and the rest of the sand layer, resulting in compaction of the intermediate sand mass (the trapezoidal area) sitting on the trapdoor. Surface subsidence is also denoted by negative volumetric strains or shrinkage in Figs. 3.14(a) and 3.15(a). In the active case with no surcharge, where the trapdoor was lowered by 1 mm, the area of sand exhibiting surface subsidence creates a parabola with maximum subsidence depth (about 10% of TW) occurring at point *P* in Fig. 3.14(a) above the trapdoor centre. As the trapdoor is displaced by 3 mm, the shape of the subsidence area is refined to two parabolic regions, where two maximum subsidence depths appear [Fig. 3.15(a)]. The maximum settlement depths increased to over 17% of TW and shifted to points *G* and *H* on the left and right sides of point *P* in Fig. 3.15(a).

When the 5 kPa surcharge was applied, the subsidence area again adopted a new pattern. The area spreads from the surcharge edges towards the corners of the AOI in Fig. 3.14(b). In these surficial regions, subsidence reached a maximum depth of 14% of TW after the trapdoor was lowered by 1 mm. In addition, as shown in Fig. 3.14(b), a large area beneath the surcharge block, extending to the half of the sand layer depth, underwent moderate compaction due to the presence of the surcharge with a trapdoor displacement of 1 mm. Further trapdoor displacement to 3 mm, as shown in Fig. 3.15(b), led to three effects: firstly, a widespread small compaction (up to 0.26%) within the sand layer, excluding the area formed by the shear band; secondly, emerging of a new pattern of compression within a triangular area beneath the surcharge block with a maximum depth reaching 18% of TW; and thirdly, in Fig. 3.14(b), a reduction in the surface volumetric strains from up to 0.41% to 0.26% and the subsidence zone essentially vanishing beneath the surcharge block. This is caused by a marginal heave of the soil mass above the static base in reaction to further settlement of the surcharge block and shear band formation.

3.4. Conclusions

The digital image correlation (DIC) technique was used to monitor and capture deformations of a sand due to the active and passive arching in a trapdoor apparatus. Shear strains, shear band development, particle displacement, and principal and volumetric strains of the sand were mapped and analysed. The effect of a local surface surcharge on these strains during the arching process was also investigated. The following conclusions are drawn:

- The DIC technique is a non-intrusive tool capable of measuring the full-field strains within a sand layer. The application of DIC for granular soil layers requires the creation of a high-quality speckle pattern. This can be achieved by generating a blend of natural and dyed sands. DIC processes, including imaging rate and subset, step

and filter sizes, can be optimised through trial-and-error tests. The DIC applicability is, however, restricted to the strain levels where the image correlation pattern does not degrade.

- Strain localisations develop in the soil layer in different patterns depending on the arching conditions the layer is subjected to. The shear bands originate from the trapdoor edges and rise upward into the sand layer at different angles of inclination. The shear bands incline inward under active arching and outward under passive arching. It was also observed that the soil does not shear along vertical planes from the trapdoor edges to the surface, as assumed by some previous mathematical modelling studies (e.g. Terzaghi and Peck 1948). The arch in the passive state is greater in size than that in the active state. The surface surcharge modifies the pattern of shear band development and its magnitude.
- Volume change computations from the DIC outputs showed that soil deformation was principally accompanied by dilatancy as a consequence of shearing. Compression also occurred to a lesser extent and magnitude in some parts of the soil due to arching. This indicates that volume change should not be neglected in mathematical modelling as has been routine practice in the past. (McKelvey, 1994).
- Where the soil layer is subjected to arching in a trapdoor apparatus, the trapdoor element bears only the weight of a triangular area. The remainder of the soil, outside the arching region, remains stable or experiences minimal deformation.
- Given the complexity of strain patterns observed in the trapdoor apparatus using the DIC technique, the results of this study provide an enhanced understanding of soil-structure interaction, in terms of the arching effect, and identifying the critical regions of strain localisation and substantial volume change.

- The paper presents trapdoor testing under shallow layer conditions. Strain analysis of deep layer conditions will be explored in the future. The region affected by arching or strain localisations, for example, can be assessed under deep layer conditions as, has been demonstrated, the DIC technique is particularly valuable for examining such circumstances.

Acknowledgements

The first author acknowledges the University of Adelaide for financial support under the Adelaide International Scholarship (ASI) scheme and the Australian Research Council. The authors also would like to thank Mr Gary Bowman for his help with the manufacture of the apparatus and assistance during the laboratory tests. Special thanks are also due to Mr Micah Simonsen from Correlated Solutions, USA, for his technical advice and help.

References for Chapter 3

Alshibli, K. A., Alsaleh, M. I., Voyiadjis, G. Z. (2006). Modelling strain localisation in granular materials using micropolar theory: numerical implementation and verification. International Journal of Numerical and Analytical Methods in Geomechanics 30(15): 1525–1544.

Alshibli, K. A., Batiste, S. N., Sture, S. (2003). Strain localisation in sand: Plane strain versus triaxial compression. Journal of Geotechnical and Geoenvironmental Engineering 129(6): 483–494.

Alshibli, K. A., Hasan, A. (2008). Spatial variation of void ratio and shear band thickness in sand using X-ray computed tomography. Geotechnique 58(4): 249–257.

Batiste, S. N., Alshibli, K. A., Sture, S., Lankton, M. (2004). Shear band characterisation of triaxial sand specimens using computed tomography. Geotechnical Testing Journal 27(6): 568–579.

Batra, R. C., Kim, C. H. (1992). Analysis of shear banding in twelve materials. International Journal of Plasticity 8(4): 425–452.

Bolton, M. D. (1986). The strength and dilatancy of sands. Geotechnique, 36(1): 65–78.

Borja, R. I., Song, X., Rechenmacher, A. L., Abedi, S., Wu, W. (2013). Shear band in sand with spatially varying density. Journal of the Mechanics and Physics of Solids 61(1): 219–234.

Chen, C. N., Huang, W., Tseng, C. (2011). Stress redistribution and ground arch development during tunnelling. Tunnelling and Underground Space Technology 26(1): 228–235.

Chevalier, B., Combe, G., Villard, P. (2012). Experimental and discrete element modelling studies of the trapdoor problem: influence of the macro-mechanical frictional parameters. Acta Geotechnica 7(1): 15–39.

Collins, I. F., Houlsby, G. T. (1997). Application of thermomechanical principles to the modelling of geotechnical materials. Proceedings of the Royal Society A: Mathematical, Physical and Engineering Science 453(1964): 1975–2001.

Correlated Solutions Inc., USA, (2009). VIC-2D v. 6 user manual.

Costa, Y. D., Zornberg, J. G., Bueno, B. S., Costa, C. L. (2009). Failure mechanisms in sand over a deep active trapdoor. Journal of Geotechnical and Geoenvironmental Engineering 135(11): 1741–1753.

Dewoolkar, M. M., Kitidech, S., Ko, H. Y. (2007). Centrifuge modelling of granular soil response over active circular trapdoors. Soils and Foundations 47(5): 931–945.

Guo, P. (2012). Critical length of force chains and shear band thickness in dense granular materials. Acta Geotechnica 7(1): 41–55.

Hanna, T. H. (1985). Field instrumentation in geotechnical engineering, First edition, Clausthal-Zellerfeld, Trans Tech Publications, Germany.

Harris, G. W. (1974). A sandbox model used to examine the stress distribution around a simulated longwall coal-face. International Journal of Rock Mechanics and Mining Science and Geomechnical Abstracts 11(8): 325–335.

Jacobsz, S. W. (2016). Trapdoor experiments studying cavity propagation. Proc. 1st Southern African Geotechnical Conference, Jacobsz, S. W., (ed.), Chapman and Hall/CRC, Boca Raton, 159–165.

Lade, P. (2003). Analysis and prediction of shear banding under 3D conditions in granular materials. Soils and Foundations 43(4): 161–172.

Lade, P. V., Nelson, R. B., Ito, M. Y. (1987). Nonassociated flow and stability of granular material. ASCE Journal of Engineering Mechanics 113(9): 1302–1318.

Lee, C. J., Wu, B. R., Chen, H. T., Chiang, K. H. (2006). Tunnel stability and arching effects during tunnelling in soft clayey soil. Tunnelling and Underground Space Technology 21(2): 119–132.

Lee, K. (1970). Comparison of plane strain and triaxial tests on sand. Journal of the Soil Mechanics and Foundations Division 96(SM3): 901–923.

Li, X., Miao, Y., Cheng, K. (2018). Soil arching effect analysis via a modified finite element model based on a field test. Journal of Testing and Evaluation 46(5): 20160324.

Lin, X., Liu, Y., Kang, X., Chen, J., Chen, R. (2018). Numerical simulation on the development of soil arching induced by EPBS tunnelling. Proceedings of 2nd International Symposium of Asia Urban GeoEngineering, Chen, R., Zheng, G., Ou, C. (eds.), Springer, Singapore, 75–582.

Liu, H. (2013). Unified sand modelling using associated or non-associated flow rule. Mechanics Research Communications 50: 63–70.

Manzari, M. T., Dafalias, Y. F. (1997). A critical state two-surface plasticity model for sands. Geotechnique, 47(2): 255–272.

McKelvey, J. A. (1994). The anatomy of soil arching. Geotextiles and Geomembranes 13(5): 317–329.

Muir Wood, D. (2002). Some observations of volumetric instabilities in soils. The International Journal of Solids and Structures 39(13): 3429–3449.

Pan, B., Wang, Z., Lu, Z. (2010). Genuine full-field deformation measurement of an object with complex shape using reliability-guided digital image correlation. Optics Express 18(2): 1011–1023.

Pan, B., Xie, H., Wang, Z., Qian, K., Wang, Z. (2008). Study on subset size selection in digital image correlation for speckle patterns. Optics Express 16(10): 7037–7048.

Papamichos, E., Vardoulakis, I., Heil, L. K. (2001). Overburden modelling above a compacting reservoir using a trap door apparatus. Physics and Chemistry of the Earth, Part A: Solid Earth and Geodesy 26(1–2): 69–74.

Pardo, G. S., Sáez, E. (2014). Experimental and numerical study of arching soil effect in coarse sand. Computers and Geotechnics 57: 75–84.

Peters, J., Lade, P., Bro, A. (1988). Shear band formation in triaxial and plane strain tests. Advanced triaxial testing of soil and rock, ASTM, STP 977, Donaghe, R., Chaney, R., Silver, M., (eds.), ASTM, 604–627.

Roscoe, K. H., Arthur, J. R. F., James, R. G. (1963). The determination of strains in soils by an X-ray method. Civil Engineering and Public Works Review, 58(684), 873–876, and 58(685), 1009–1012.

Schreier, H., Orteu, J., Sutton, M. (2009). Image correlation for shape, motion and deformation measurements. Springer US, Boston, MA.

Sciammarella, C. A., Sciammarella, F. M. (2012). Digital Image Correlation (DIC). Book chapter, in Experimental Mechanics of Solids (607–629). Chichester, John Wiley & Sons, UK.

Standards Australia (1998). Australian Standard AS 1289.5.5.1, Soil compaction and density tests– Determination of the minimum and maximum dry density of a cohesionless material–Standard method.

Stone, K. J. L. (1988). Modelling of rupture development in soils. PhD thesis, University of Cambridge.

Talesnick, M. (2005). Measuring soil contact pressure on a solid boundary and quantifying soil arching. Geotechnical Testing Journal 28(2): 171–179.

Talesnick, M. (2013). Measuring soil pressure within a soil mass. Canadian Geotechnical Journal 50(7): 716–722.

Tanaka, T., Sakai, T. (2008). Progressive failure and scale effect of trap-door problems with granular materials. Soils and Foundations 33(1): 11–22.

Terzaghi, K. (1936). Stress distribution in dry and in saturated sand above a yielding trap-door. Proceedings of 1st International Conference of Soil Mechanics and Foundation Engineering, Cambridge, Massachusetts, 307–311.

Terzaghi, K., Peck, R. B. (1948). Soil mechanics in engineering practice, Wiley, New York.

Thongprapha, T., Fuenkajorn, K., Daemen, J. J. K. (2015). Study of surface subsidence above an underground opening using a trap door apparatus. Tunnelling and Underground Space Technology 46: 94–103.

Vermeer, P. A. (1990). The orientation of shear bands in biaxial tests. Geotechnique 40(2): 223–236.

Statement of Authorship

Title of Paper	The arching effect in rubber–sand mixtures
Publication Status	☐ Published ☐ Accepted for Publication ☑ Submitted for Publication ☐ Unpublished and Unsubmitted work written in manuscript style
Publication Details	

Principal Author

Name of Principal Author (Candidate)	Hamidreza Khatami		
Contribution to the Paper	Performed the literature review, conducted the experiments, gathered the data, analysed and interpreted the results, and drafted the manuscript.		
Overall percentage (%)	80%		
Certification:	This paper reports on original research I conducted during the period of my Higher Degree by Research candidature and is not subject to any obligations or contractual agreements with a third party that would constrain its inclusion in this thesis. I am the primary author of this paper.		
Signature		Date	19/09/18

Co-Author Contributions

By signing the Statement of Authorship, each author certifies that:

i. the candidate's stated contribution to the publication is accurate (as detailed above);

ii. permission is granted for the candidate in include the publication in the thesis; and

iii. the sum of all co-author contributions is equal to 100% less the candidate's stated contribution.

Name of Co-Author	An Deng		
Contribution to the Paper	Methodology and reviewing.		
Signature		Date	19/09/18

Name of Co-Author	Mark Jaksa		
Contribution to the Paper	Methodology and reviewing.		
Signature		Date	19/09/18

Please cut and paste additional co-author panels here as required.

Chapter 4: The arching effect in rubber–sand mixtures

Abstract

The arching effects that occur to rubber–sand layers are examined in this paper. The digital image correlation technique and a series of pressure sensors are employed to capture the deformation characteristics and stress evolution developed in the sand and rubber–sand layers, which are subjected to active arching with and without a central surcharge in a trapdoor apparatus. A range of deformation measures, including horizontal and vertical displacements and strains, shear strains, and volume change variables are obtained and compared for different backfill materials. Ground response curves for sand and rubber–sand mixtures were developed using the stress measurement data. From the deformation data, an arch of equal displacement is introduced. It was observed that the use of rubber particles reduces the surface settlement of the sand layer and the arch heights and higher stress reduction was obtained in the rubberised backfills.

Keywords: Rubber–sand, arching effect, digital image correlation, strain analysis, trapdoor apparatus.

4.1. Introduction

Over the last few decades, waste rubber has been examined as a new geosynthetic material to reinforce and improve soil. Laboratory studies on rubber–sand mixtures using direct shear box or triaxial compression tests have shown a significant improvement in the shear strength of sand mixed with rubber up to 35% by weight (Edil and Bosscher, 1996; Tatlisoz et al., 1997; Lee et al., 1999; Zornberg et al., 2004; Rao and Dutta, 2006; Lok and Yu, 2006; Edincliler and Ayhan, 2010, Soganci, 2015, Anvari et al., 2017). This has led to the development of standards by the American Society for Testing and Materials used to evaluate material and permeability properties of tyre-derived aggregates (ASTM 2017, 2018). In addition to soil reinforcement, other benefits of using recycled rubber include decreased weight of the geomaterial, a cost-effective replacement for natural aggregate, and reduced environmental impacts of waste rubber (Edil, 2004; Ghazavi, 2004). Primary geotechnical field applications of rubber–sand mixtures include backfilling in embankments, road construction, and retaining walls structures (Bosscher et al., 1997; Yoon et al., 2006; Lee et al., 2011; Vinot and Singh, 2013; Reddy and Krishna, 2015; Zhang et al., 2018). Feasibility studies on the capability of rubberised soil for vibration isolation against earthquake have also been carried out by Tsang et al. (2009a, 2009b), Boominathan et al. (2015), Panah and Khoshay (2015), and Argyroudis et al. (2016). In these studies, it was observed that the vibration is isolated mainly by the high damping ratio and energy absorbing attributes of the rubber inclusions. Additionally, waste tyre shreds have been combined with commercially available geocells to improve ground performance (Moghaddas Tafreshi et al., 2013, 2014; Tavakoli Mehrjardi et al., 2012, 2015).

Although rubberised soils are gradually being accepted as reinforced backfills in different projects, the backfills exhibit behaviours different from the traditional materials. One of these important behaviours is the geomaterial arching, which is crucial to the load

distribution of the backfill and thus its stability. The term ‘arching’ was originally coined by Terzaghi in 1936 to describe an intriguing load transfer mechanism by which the stresses in a soil, supported by a two-part structure, ‘arch over’ the yielding part to the stationary part of the structure. This structure was simulated using a so-called trapdoor apparatus. The shear strength (friction) of the soil was gradually mobilised as the relative displacement of the structural parts continued to increase. Shear stresses, therefore, were developed in the opposite direction to the yielding, reducing the normal stresses acting on the yielding part. Subsequent studies by Ladanyi and Hoyaux (1969), Evans (1983), Iglesia, (1991), and Ono and Yamada (1993) reported similar results. Among the most recent contributions, using the single or multi-door trapdoor apparatuses, research work by van Eekelen et al. (2012a, 2012b), Rui et al. (2016), Chen et al. (2016), Fagundes et al. (2017), Pham et al. (2018), Marx and Jacobsz (2018) studied the design of geosynthetic reinforced piled embankments. Although numerous analytical (e.g. Terzaghi, 1943; Evans, 1983) and experimental studies have been conducted in the past, a full capture of the arching phenomenon in a range of situations, for example, the stress drop under the centre of stockpiled sand (Michalowski and Park, 2004; Nadukuru and Michalowski, 2012), remains somewhat elusive to this date. In addition, less attention has been paid in the literature to the deformation attributes of the arching effect.

The objective of the present work is to investigate the arching effect that occurs in rubber–sand mixtures. To do so, a trapdoor apparatus was manufactured and full-field measurements and analyses of deformation for the active mode of arching were performed using the digital image correlation (DIC) technique. Stress measurements were also conducted on the boundaries of the geomaterial backfills in the trapdoor apparatus. The response of rubberised sand backfills to the induced differential strains was compared with that of a layer consisting solely of sand. Previous research in this field has focused

predominantly on the active arching mode, as it is commonly observed in geotechnical practice. For this reason, only the active arching was considered for the experimentation presented in this paper.

4.1. Experimental setup

In this section, the geotechnical characteristics of the sand, rubber, and rubberised sand specimens, the testing apparatus, sensors, and the DIC system are presented. Details of each experimental component are also provided.

4.2.1. Geomaterial characterisation

The soil adopted in the testing was a cohesionless sand that was sourced from Sibelco South Australia, is branded as 'Sand 8/16' and is a coarse silica sand with angular particles. The rubber granules were provided by Tyrecycle, Victoria, Australia, and described as washed, dust-free, and steel belt removed. The rubber granules were mixed with the sand at two ratios of 10% and 30% by weight. These two proportions are hitherto referred to as low and high rubber contents, respectively. The particle size distributions of the sand, rubber particles, and rubber–sand mixtures are presented in Fig. 4.1 and the other material properties are provided in Table 4.1. The particle densities of the sand and rubber were found to be 2,650 kg/m^3 and 1,140 kg/m^3, respectively. The minimum and maximum dry densities of the geomaterial were determined in accordance with the Australian Standard AS 1289 (Standards Australia, 1998). To obtain the internal friction angle, direct shear box tests were performed on dry samples of sand and rubber–soil mixtures. The size of shear box samples was 60 mm × 60

mm × 38 mm. To eliminate the size effect, 'sample scalping' (Zeller and Wullimann, 1957) was carried out. The material scalping approach has been confirmed as being appropriate for obtaining a reliable measure of the shear strength (Hamidi et al., 2012; Azéma et al., 2017). Table 4.1 summarises the effective internal friction angle of the sand and rubberised sand samples obtained. The internal friction angle remained relatively unchanged when the rubber content is of a low percentage (i.e. 10%). However, the density of the sample reduced. A high rubber content (i.e. 30%) resulted in a significant density reduction and increase in the friction angle. Therefore, rubber inclusions help reduce material weight and improve the shear strength of the mixtures.

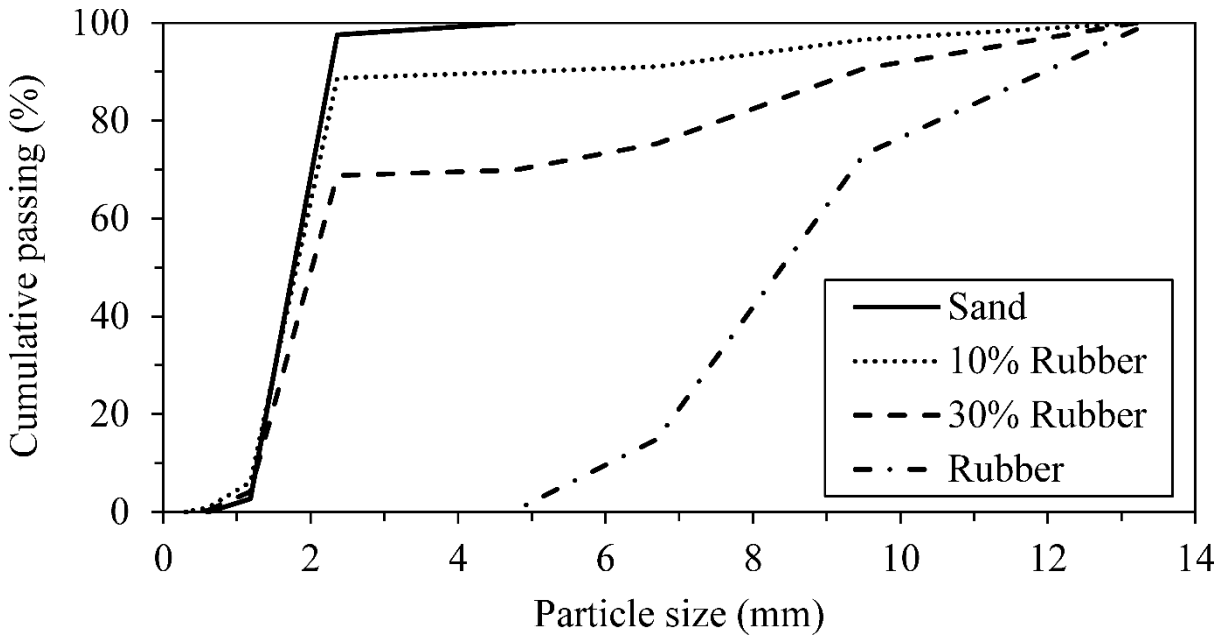

Fig. 4.1. Size distribution of geomaterial particles

Table 4.1. Geotechnical characteristics of the geomaterial used

Material	Minimum density (kg/m^3)	Maximum density (kg/m^3)	Sample density (kg/m^3)	Friction angle
Sand	1,486	1,709	1,657	45°
10% Rubber–sand	1,367	1,574	1,515	44.5°
30% Rubber–sand	1,270	1,433	1,387	51°

In order to perform the DIC procedure a speckled pattern is required to be imprinted on the sample surface. The sand's natural colouration is not contrasting enough to provide a satisfactory speckled pattern. Hence, to facilitate this, approximately one third by weight of the sand particles were dipped in a slightly diluted matte black paint, and then allowed to set, adsorb the colour, and air-dry. These black particles were mixed thoroughly with the original sand batch. Finally, the rubber particles were then added to and mixed with the soil to generate the speckled rubber–soil mixtures, as shown in Fig. 4.2.

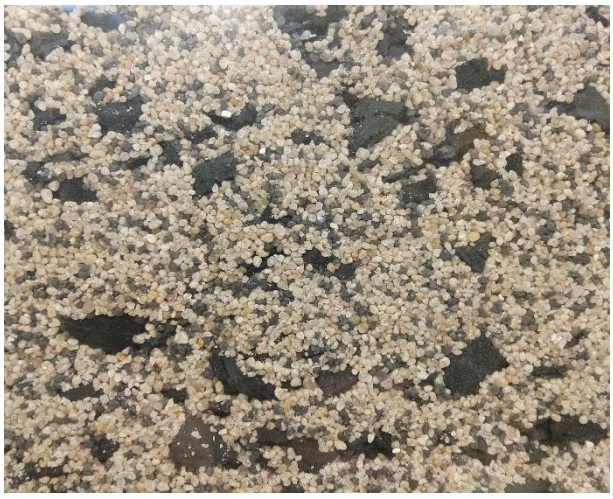

Fig. 4.2. Speckled mixture of 30% rubber–sand used in the trapdoor apparatus

4.2.2. Trapdoor apparatus and instrumentation

The trapdoor apparatus manufactured for this study is a replicate of that used by Terzaghi. The front side of the trapdoor was made of a transparent, flat and smooth, 20 mm thick acrylic sheet. The internal depth of the apparatus was 200 mm. The space is large enough to eliminate possible boundary effects. To simulate shallow conditions, where the ratio of the soil height to the trapdoor width is less than 2 (Costa et al., 2009), a 160 mm wide trapdoor and rubber–sand height of 250 mm was selected. The moving trapdoor and the adjacent stationary parts of the trapdoor were made of 35 mm thick, rigid timber. The trapdoor was mounted on an electrically-operated hydraulic jack with a 2,000 kg capacity. The granular material was poured into the apparatus from its open top in equal batches and modestly compacted in layers. The relative density of the sand and rubber samples tested in the trapdoor apparatus were 79% and 74%, respectively, classifying the samples into a medium-dense consistency. Due to differences in the densities and sizes of the sand and rubber particles, rubber–sand mixtures tend to segregate. Efforts, such as thorough mixing and careful pouring, were taken to ensure the formation of a uniform layer, with minimal segregation. A concrete block of 160 mm × 200 mm × 230 mm was cast and used as a surcharge placed on the surface of the sample layer.

The trapdoor was instrumented with a series of stress sensors and a linear variable displacement transducer (LVDT). The stress sensors were calibrated using a Fluke-100g electrical pressure calibrating instrument and connected to a data acquisition device, and subsequently post-processed using ancillary computer software. To record the stress values at the base of the sample layer, the stress sensors were secured into a series of cylindrical recesses, located at 30 mm centre-to-centre spacings onto the surfaces of the trapdoor and adjacent stationary base. The recesses matched the outer diameter of the sensors, thereby eliminating disturbance to the stress regime. Since the sample layer is in an axisymmetric

plane-strain condition, all the sensors were placed on the right-hand-side of the apparatus, with respect to its centreline. The sensors were numbered from 1 to 15, with Sensors 1–3 being placed from the trapdoor centre to edge and Sensors 4–15 on the right-hand-side of the stationary base. The stress sensor arrangement and numbering are shown in Fig. 4.3. To measure the vertical translations of the trapdoor, an LVDT was installed under the trapdoor and connected to a data acquisition system and the LabView software from National Instruments, USA.

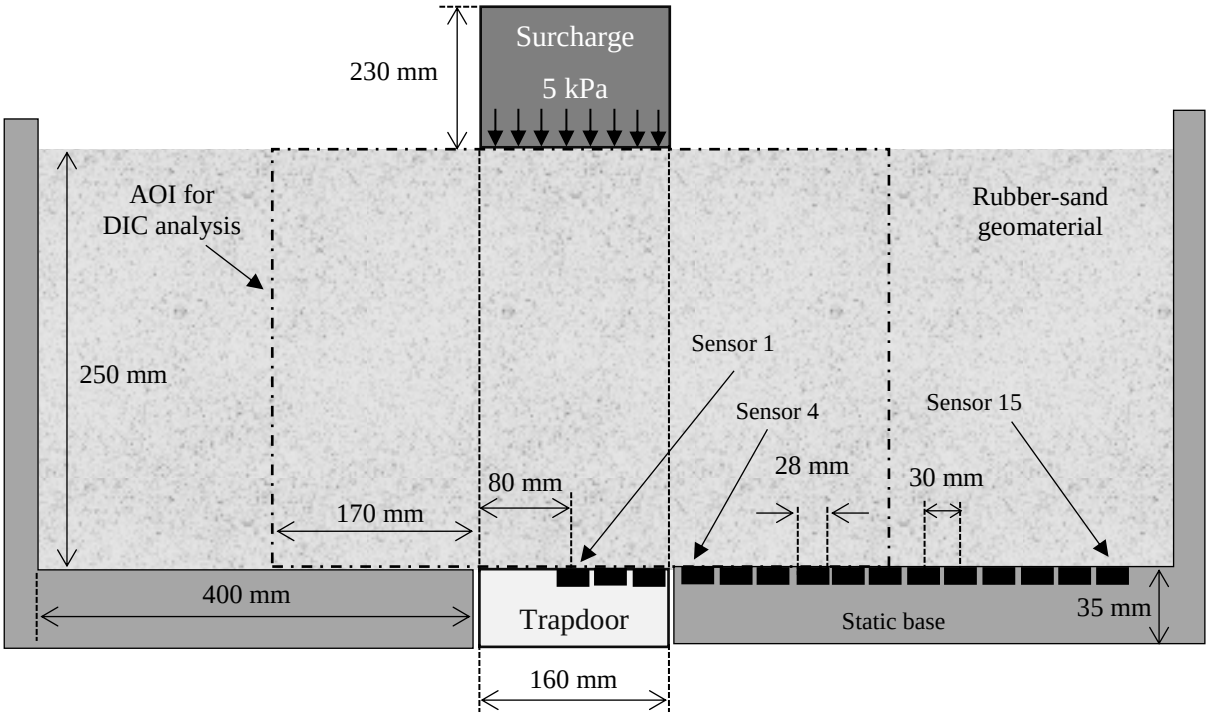

Fig. 4.3. Cross-section presentation of the trapdoor apparatus instrumented with stress sensors (AOI: area of interest)

4.2.3. DIC equipment

Subsequent to the geomaterial sample layer being placed in the trapdoor apparatus, the digital camera was setup to capture images from the front as the trapdoor translation

progressed. The imaging equipment, VicSnap image capturing software, and the VIC-2D program for the DIC analysis were supplied by Correlated Solutions Inc., USA. With reference to the imaging equipment, a conventional charge-coupled device camera, with a low distortion 75 mm prime lens aperture size range of 1/22–1/2.8, was used. The images were captured using a frame rate of 160 frames per seconds and a resolution of 960 × 600 pixels, within the VicSnap environment, and these were subsequently post-processed using the VIC-2D program. This software computes the displacements and strains using an image correlation algorithm which is discussed in the following section.

4.3. Image correlation analysis

Photogrammetric techniques, such as the DIC technique, can provide valuable and quantitative information about the deformation of a material in a non-intrusive fashion. DIC images are analysed on the basis of their pixel information. Computerised pixel depth allows for 256 different intensities or shades of grey. These values are stored as 8-bit integers in the computer, where 0 and 255 represent black and white, respectively. The intermediate values comprise shades of grey or greyscale intensity values. The greyscale intensity functions in the reference and deformation images are used in the correlation analysis to obtain displacement and strain data.

In the DIC analysis, an area of interest (AOI) on the front surface is defined. This is the location where deformation measurements are required. The AOI of the trapdoor apparatus is shown in Fig. 4.3 and is then discretised into non-overlapping squares known as ‘subsets’. Each subset can cover an area with different pixel length sizes, in the form of $(2m+1) \times (2m+1)$ pixels, where m is an integer. The pixel length of the subsets must be odd numbers because the correlation algorithm tracks the displacement of the central pixel of

each subset to map deformations, as shown in Fig. 4.4(a). The value of *m* is selected in such a way that the random dot pattern, framed in each subset, is unique. If the subset centre is point, *A*, (x_0, y_0), in the reference image, the corresponding position in the deformation image, (x_0^*, y_0^*), can be found by determining the displacement vector in Fig. 4.4(a). The displacement vector is dependent on the identification of the corresponding subset in the deformation image. The subset identification is attained by assessing the normalised sum of the squared differences correlation criterion, CC_{NSSD}, which is defined by Pan et al. (2009) as:

$$CC_{NSSD} = \sum_{i=-m}^{m}\sum_{j=-m}^{m}\left(\frac{f(x_i, y_j)}{\sqrt{\sum_{i=-m}^{m}\sum_{j=-m}^{m}\left[f(x_i, y_j)\right]^2}} - \frac{g(x_i^*, y_j^*)}{\sqrt{\sum_{i=-m}^{m}\sum_{j=-m}^{m}\left[g(x_i^*, y_j^*)\right]^2}}\right)^2 \quad (4.1)$$

where $f(x_i,\ y_j)$ and $g(x_i^*,\ y_j^*)$ are the greyscale intensity functions at points $(x_i,\ y_j)$ in the reference image and $(x_i^*,\ y_j^*)$ in the subsequent deformed image, respectively. The corresponding position of the subset considered in the reference image in the deformation images is determined by finding the subset with the least CC_{NSSD} value. Since any arbitrary point in the reference subset, $B(x_i, y_i)$, can geometrically be related to the subset central point, the resultant coordinates of this point in the deformed image, $B(x_i^*, y_j^*)$, can also be calculated as follows:

$$x_i^* = x_i + \left[u + \frac{\partial u}{\partial x}(x_i - x_0) + \frac{\partial u}{\partial y}(y_j - y_0)\right] \quad i, j = -m{:}\,m \quad (4.2a)$$

$$y_j^* = y_j + \left[v + \frac{\partial v}{\partial x}(x_i - x_0) + \frac{\partial v}{\partial y}(y_j - y_0)\right] \quad (4.2b)$$

where *u* and *v* are the horizontal and vertical displacement components of the centre of reference subset $A\ (x_0, y_0)$, respectively, and $\partial u/\partial x$, $\partial u/\partial y$, $\partial v/\partial x$, and $\partial v/\partial y$ denote the first-order displacement gradients of the reference subset (Bruck et al., 1989). The terms on

the right side in Eq. (4.2) are known as the first-order shape function (Schreier and Sutton, 2002). Image correlation is performed by determining the shape function variables in Eq. (4.2) that minimise the correlation criterion in Eq. (4.1). Displacements and strains in the AOI are obtained by tracking the discrete subset points in both the reference and deformed images and applying an interpolation technique. In this study, an *m* value of 10 and the Newton-Raphson numerical method were used to complete the image correlation and to calculate the deformation datasets for every 5 pixels horizontally and vertically in the selected AOI, which measured 500 (L) × 250 (H) mm. The DIC results were interpolated using a cubic B-spline function in the VIC-2D software and are presented in the next section. The deformation of four adjacent subsets in pixel level obtained for the sand is provided in Fig. 4.4(b).

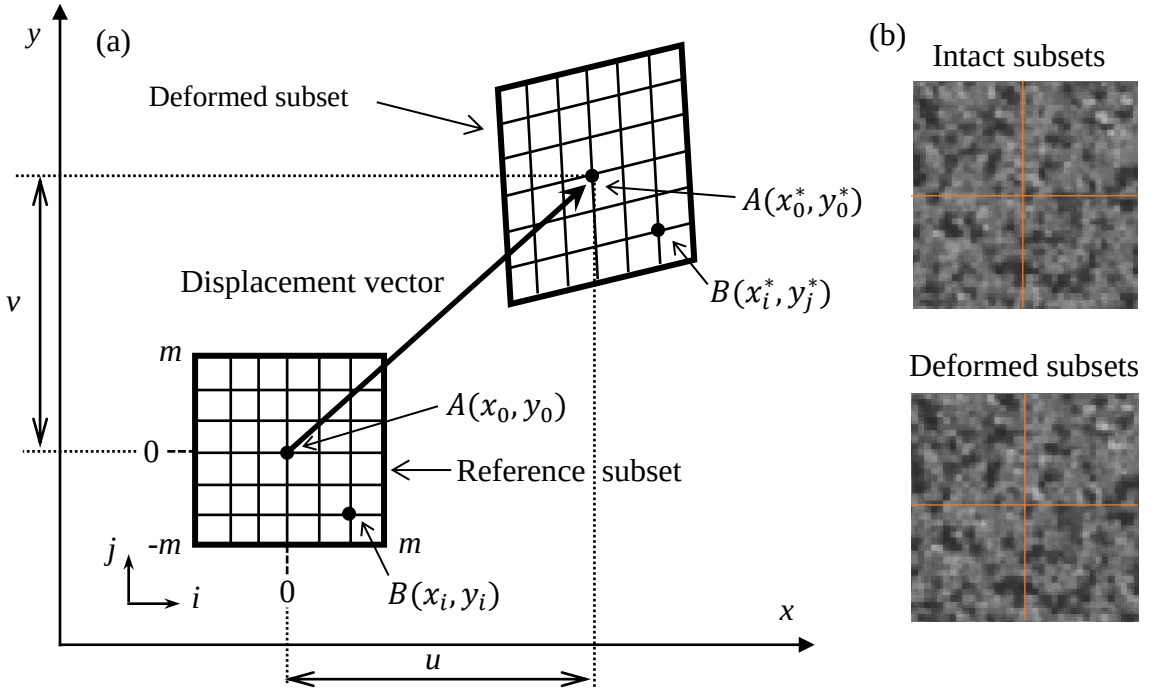

Fig. 4.4. DIC analysis of subset deformation; (a) schematic presentation (modified after Pan et al., 2008), (b) four neighbouring subsets of 21 × 21 pixels size in a reference image (top) and deformation image (bottom).

4.4. Experimental scope

To study the arching effect in sand and rubberised sand, full-field displacement and strain measurements, and geomaterial-structure interface stress measurements were carried out under two testing conditions. They include active arching with no surcharge (AANS) and active arching with an applied surcharge (AAWS). The trapdoor was able to travel 35 mm downwards creating an active mode of arching. The trapdoor element could displace at a speed of 3.2 mm per second. The interface stress values were measured continuously at a frequency of 16 Hz. In order to compare the response of the geomaterials used, the DIC results captured at 2 mm trapdoor translation are presented in this paper.

4.5. Results and discussion

The results of the DIC deformation analysis, in terms of displacements and strains, are presented in this section. Following the interpretation of the DIC results, the stress measurement data are also presented and analysed.

4.5.1. DIC results

The trapdoor apparatus operates by inducing a differential strain field in the geomaterial mass. The field is represented by horizontal displacements (u), vertical displacements (v), and a set of strain variables, including horizontal strains (ε_{xx}), vertical strains (ε_{yy}), shear strains (ε_{xy}), and volume change ($\varepsilon_{vol.}$). These strain variables were calculated using the so-called large deformation strain tensor or Lagrangian strain tensor, in the VIC-2D program, and are expressed as:

$$\varepsilon_{xx} = \frac{\partial u}{\partial x} + \frac{1}{2}\left[\left(\frac{\partial u}{\partial x}\right)^2 + \left(\frac{\partial v}{\partial x}\right)^2\right] \tag{4.3}$$

$$\varepsilon_{yy} = \frac{\partial v}{\partial y} + \frac{1}{2}\left[\left(\frac{\partial u}{\partial y}\right)^2 + \left(\frac{\partial v}{\partial y}\right)^2\right] \tag{4.4}$$

$$\varepsilon_{xy} = \frac{1}{2}\left[\frac{\partial u}{\partial y} + \frac{\partial v}{\partial x} + \frac{\partial u}{\partial x}\frac{\partial u}{\partial y} + \frac{\partial v}{\partial x}\frac{\partial v}{\partial y}\right] \tag{4.5}$$

$$\varepsilon_{vol.} = \varepsilon_{xx} + \varepsilon_{yy} + \varepsilon_{xx}\varepsilon_{yy} - \varepsilon_{xy}^2 \tag{4.6}$$

Figs. 4.5 and 4.6 show the horizontal displacements of sand, 10% Rubber–sand, and 30% Rubber–sand backfills under AANS and AAWS conditions, respectively. Fig. 4.5 indicates that the overall pattern of horizontal displacements was similar for the three geomaterials used. However, where the rubber particles were added to the sand, the lateral boundaries of the horizontal displacements extended slightly. The maximum *u* values occurred at four places: two half-elliptical regions near the surface and two triangular zones above the trapdoor. In Fig. 4.5, the horizontal displacement values fall into a small range of less than 0.2 mm. In Fig. 4.6, when the surcharge block was used, the top regions of concentrated horizontal displacement diminished with increased rubber content. These changes are not noticeable in the high rubber content specimen [Fig 6(c)]. Moreover, the *u* values remained below 0.2 mm for all specimens.

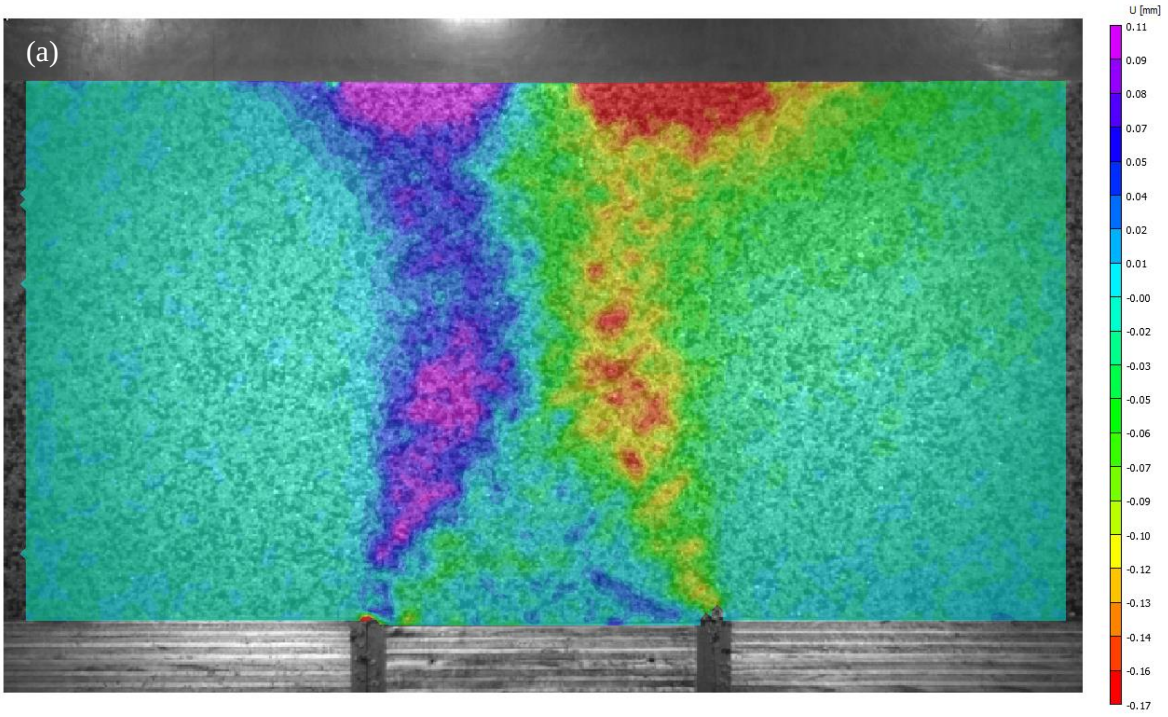
(a)
U [mm]
0.11
0.09
0.08
0.07
0.05
0.04
0.02
0.01
-0.00
-0.02
-0.03
-0.05
-0.06
-0.07
-0.09
-0.10
-0.12
-0.13
-0.14
-0.16
-0.17

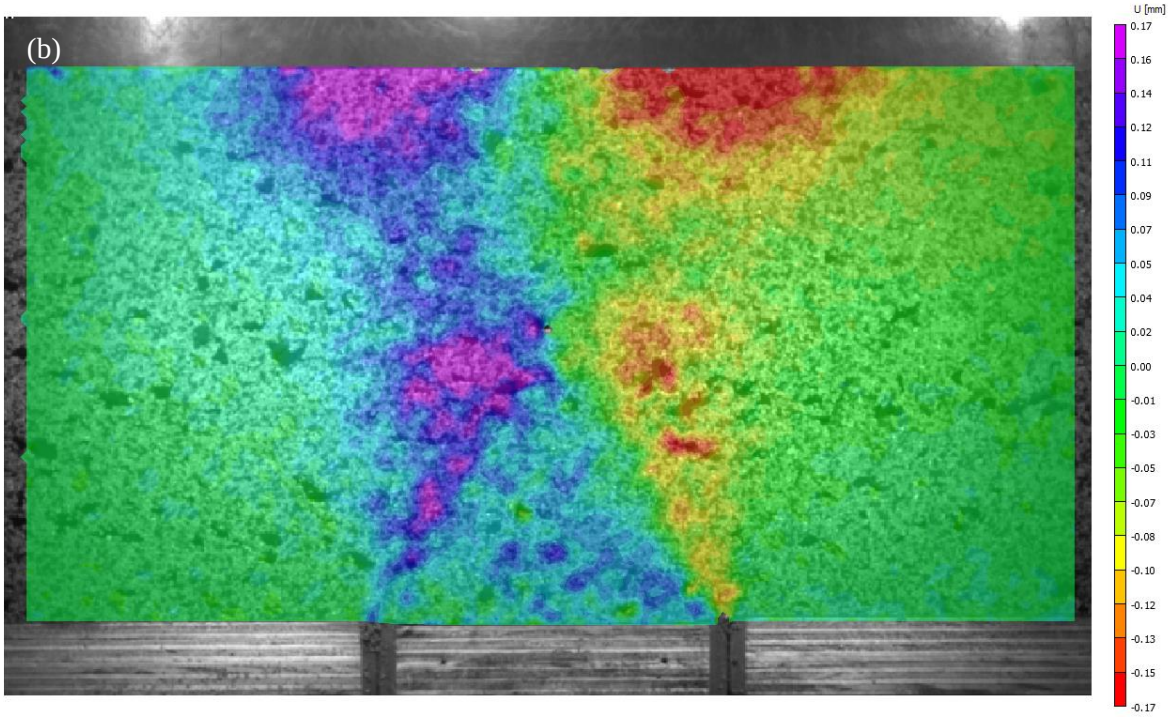
(b)
U [mm]
0.17
0.16
0.14
0.12
0.11
0.09
0.07
0.05
0.04
0.02
0.00
-0.01
-0.03
-0.05
-0.07
-0.08
-0.10
-0.12
-0.13
-0.15
-0.17

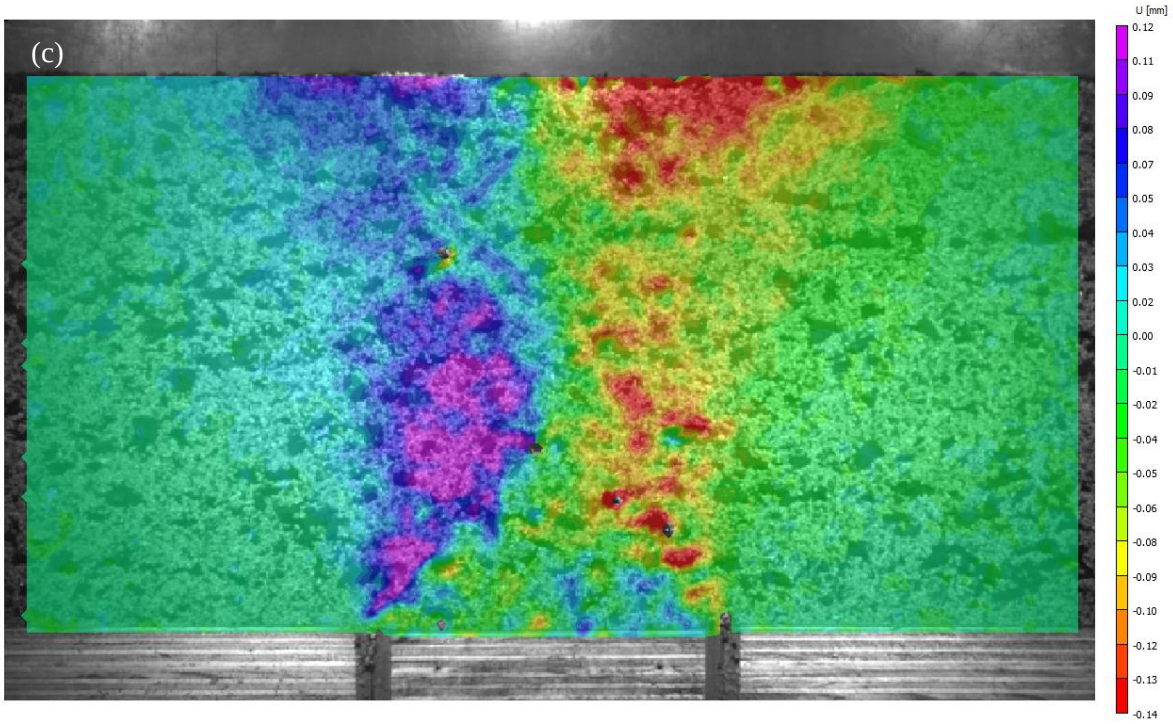

Fig. 4.5. Distribution of horizontal displacements under AANS conditions for the three materials: (a) Sand, (b) 10% Rubber–sand mixture, and (c) 30% Rubber–sand mixture.

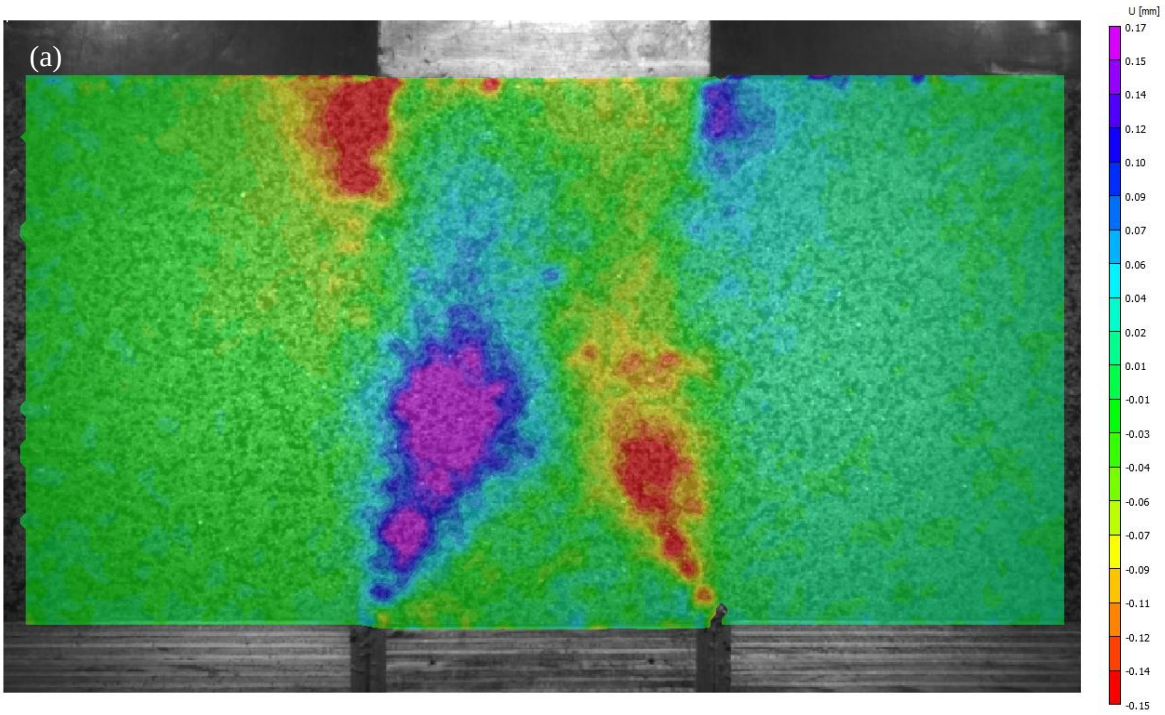

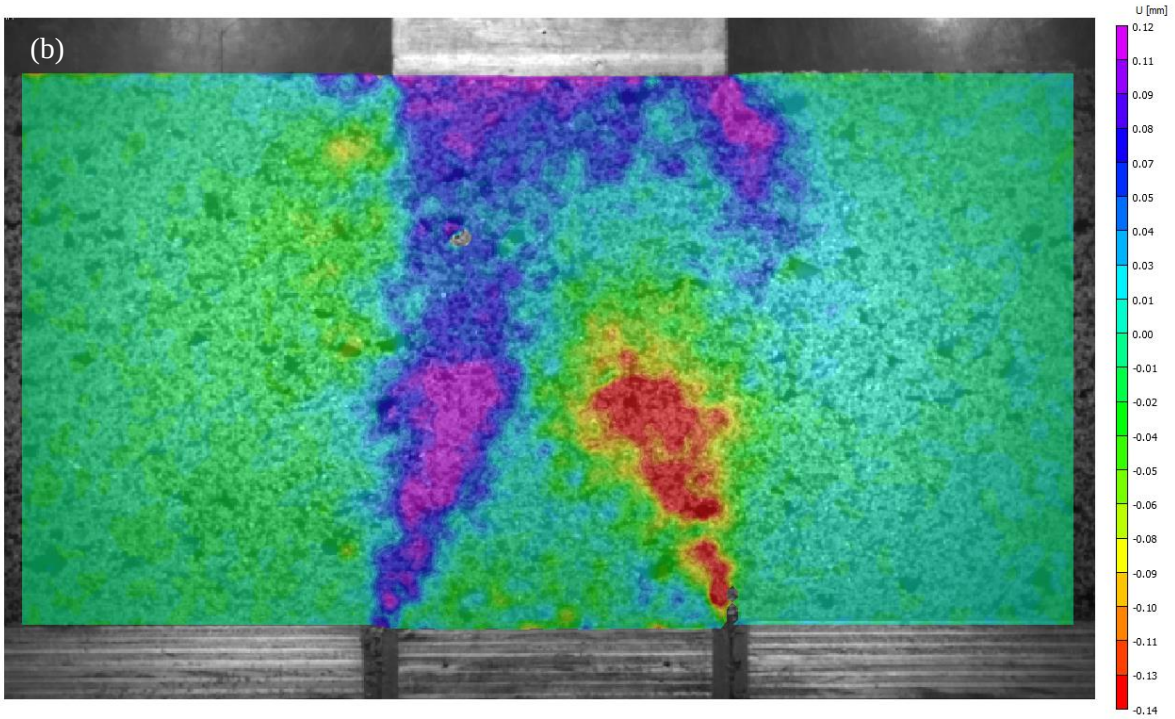

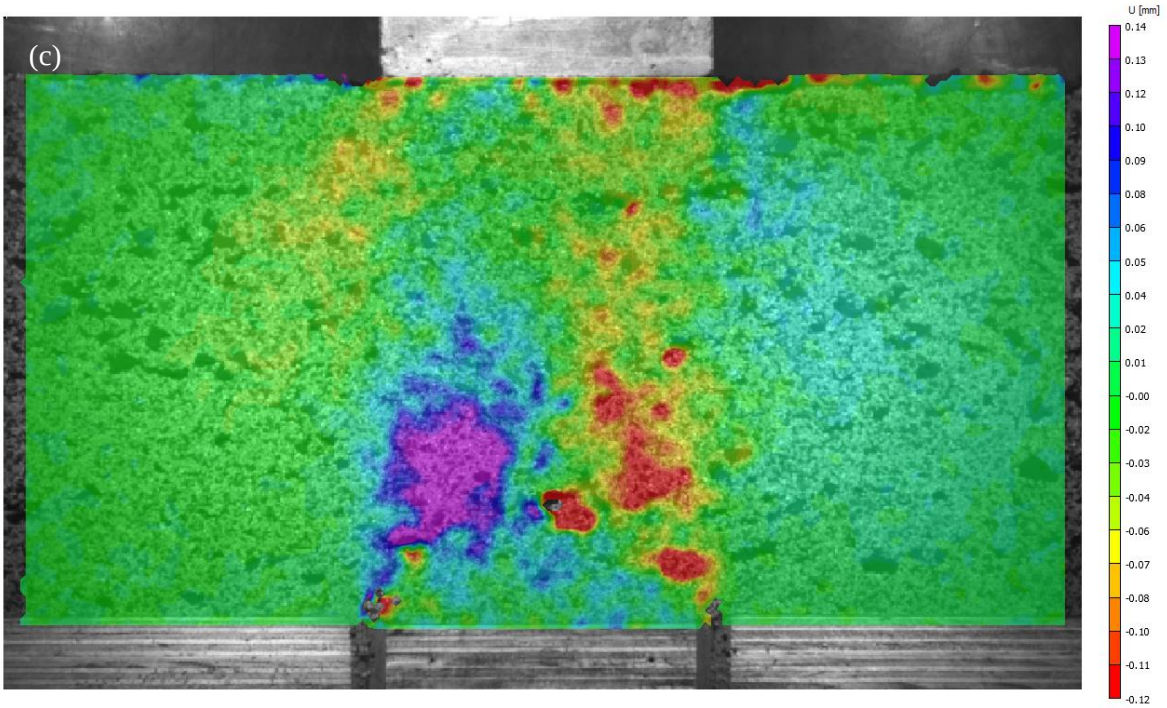

Fig. 4.6. Distribution of horizontal displacements under AAWS conditions for the three materials: (a) Sand, (b) 10% Rubber–sand mixture, and (c) 30% Rubber–sand mixture

Figs. 4.7 and 4.8 present the areal distributions of horizontal strains for sand and rubberised sand subjected to active arching conditions. As observed previously, the deformation maps extended laterally where the rubber content increased, as shown in Fig. 4.7. In addition, a two-fold compression and tension strain regime occurred simultaneously within the geomaterials as a result of the trapdoor displacement. The compressive region is located above the trapdoor and is encompassed by two tensile regions originating from the trapdoor edges. These two regions are indicated in Fig. 7 by the dashed lines. The dashed-dotted lines in this graph identify a narrow gap of null horizontal strains that separates the compressive and tensile areas. When the rubber content increased from 0% in the sand layer to 30%, the area of compression decreased while the boundaries of the tensile regions extended laterally. A concentration of peak values can be regarded as another feature of the horizontal strains in Fig. 4.7. A surface and an internal concentration zone of horizontal strains exist within every compressive or tensile region, although the surface zones appear to diminish for the 30% Rubber–sand geomaterial. For the AANS case, the horizontal strains exhibit a minute maximum value of 0.38% in compression and 0.23% in tension.

Fig. 4.8 indicates that the application of a surcharge suppressed the formation of the surface peak region for the compressive ε_{xx} values for all the geomaterials tested and the corresponding tensile region in the 30% rubber–sand specimen. However, two additional, mildly strained regions appeared on the surface, in response to the downward movement of the surcharge. Fig. 4.8 also shows that the lateral boundaries of the horizontal strains became confined between approximately two vertical lines connecting the surcharge block corners to the trapdoor edges. In the case of the surcharge loading, the maximum compressive values were reduced to 0.36%, while the maximum tensile values increased to 0.38% in comparison to the corresponding results obtained under AANS conditions.

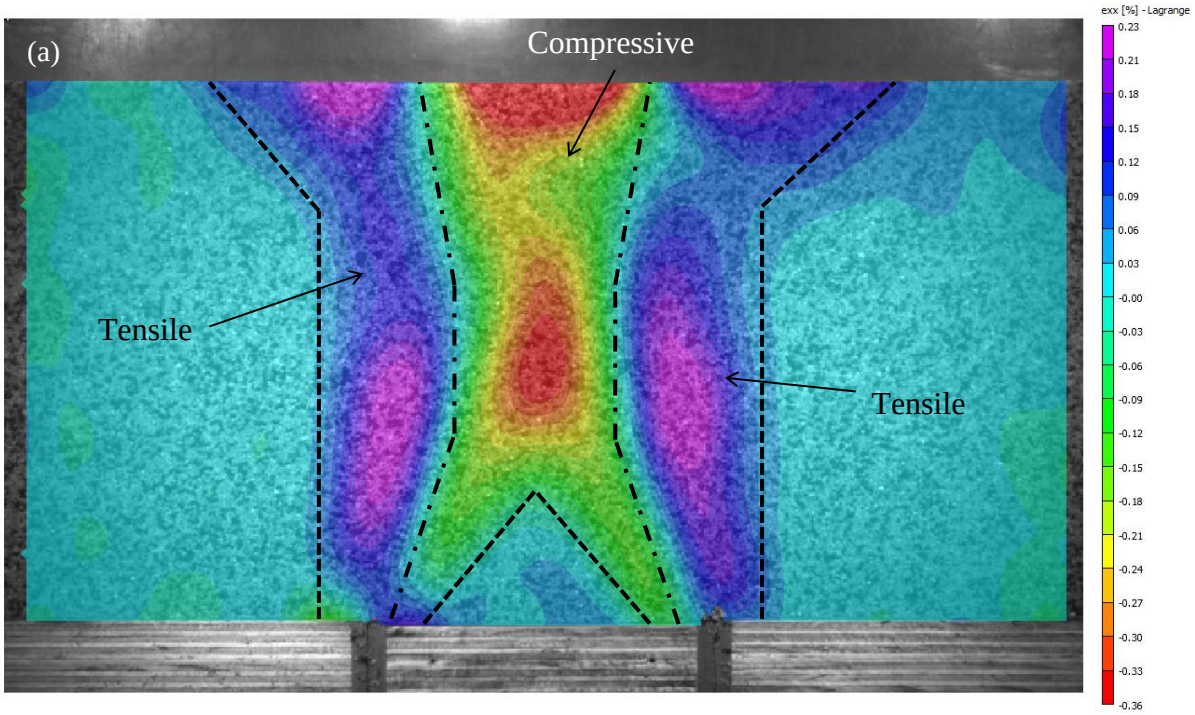
(a)
Compressive
Tensile
Tensile
exx [%] - Lagrange
0.23
0.21
0.18
0.15
0.12
0.09
0.06
0.03
-0.00
-0.03
-0.06
-0.09
-0.12
-0.15
-0.18
-0.21
-0.24
-0.27
-0.30
-0.33
-0.36

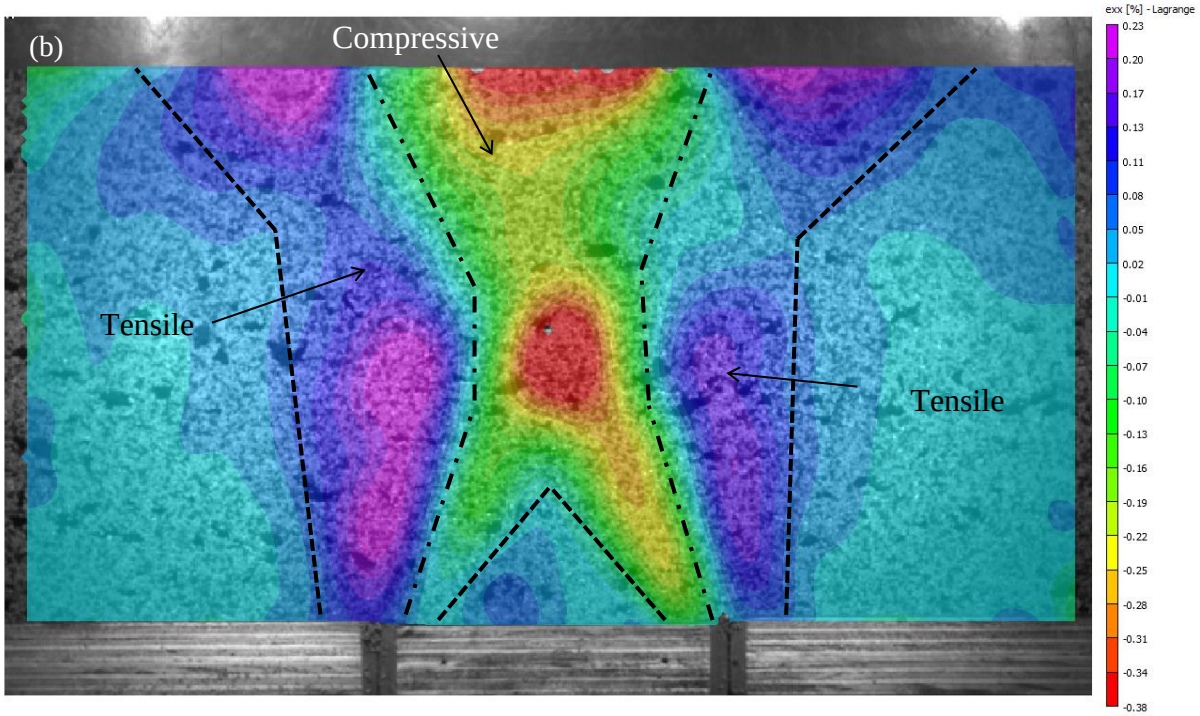
(b)
Compressive
Tensile
Tensile
exx [%] - Lagrange
0.23
0.20
0.17
0.13
0.11
0.08
0.05
0.02
-0.01
-0.04
-0.07
-0.10
-0.13
-0.16
-0.19
-0.22
-0.25
-0.28
-0.31
-0.34
-0.38

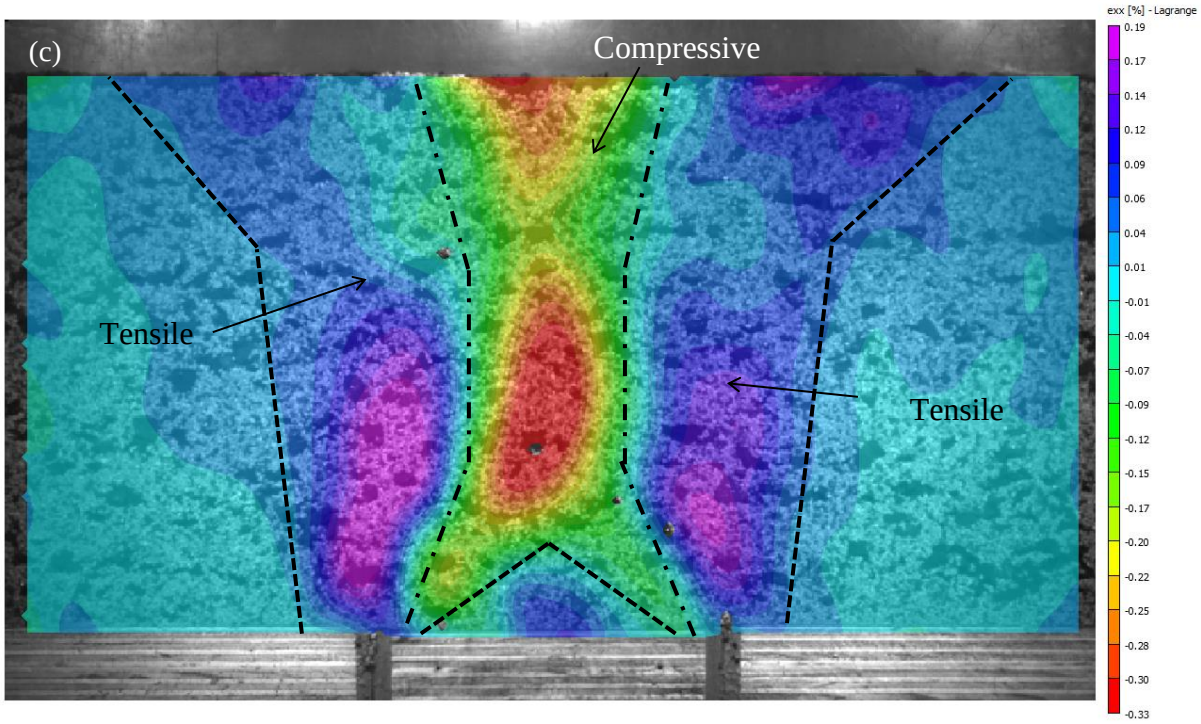

Fig. 4.7. Horizontal strain distribution under AANS conditions for the three materials: (a) Sand, (b) 10% Rubber–sand mixture, and (c) 30% Rubber–sand mixture

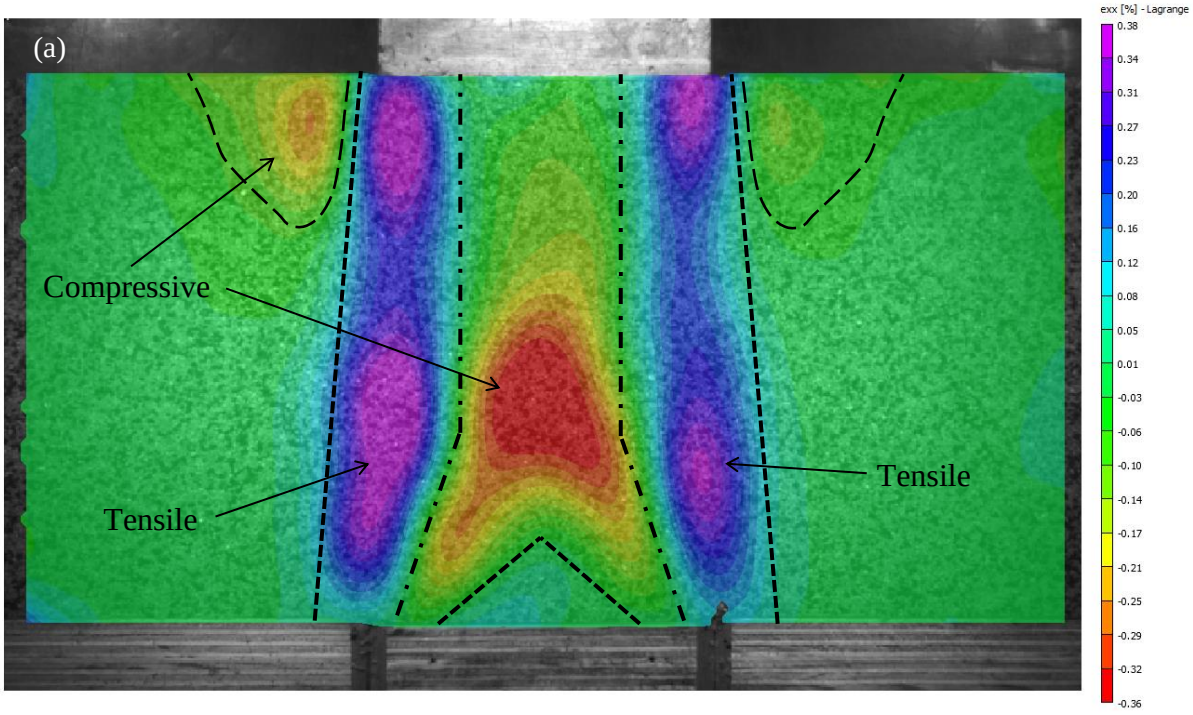

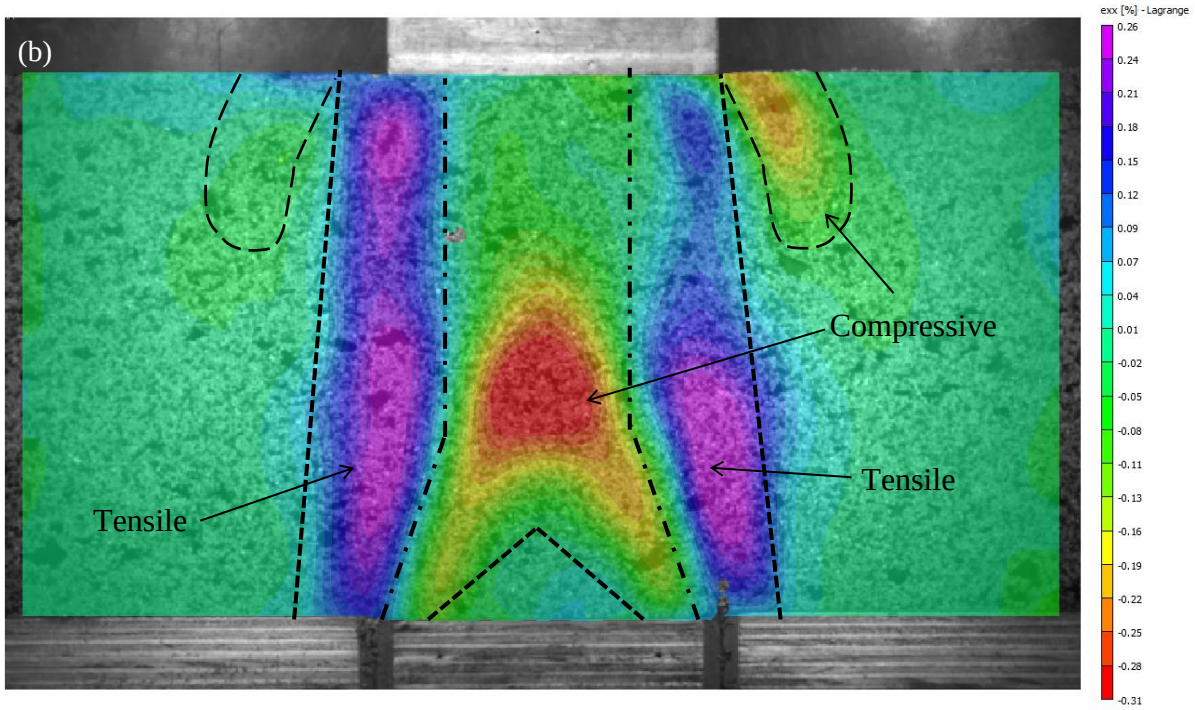

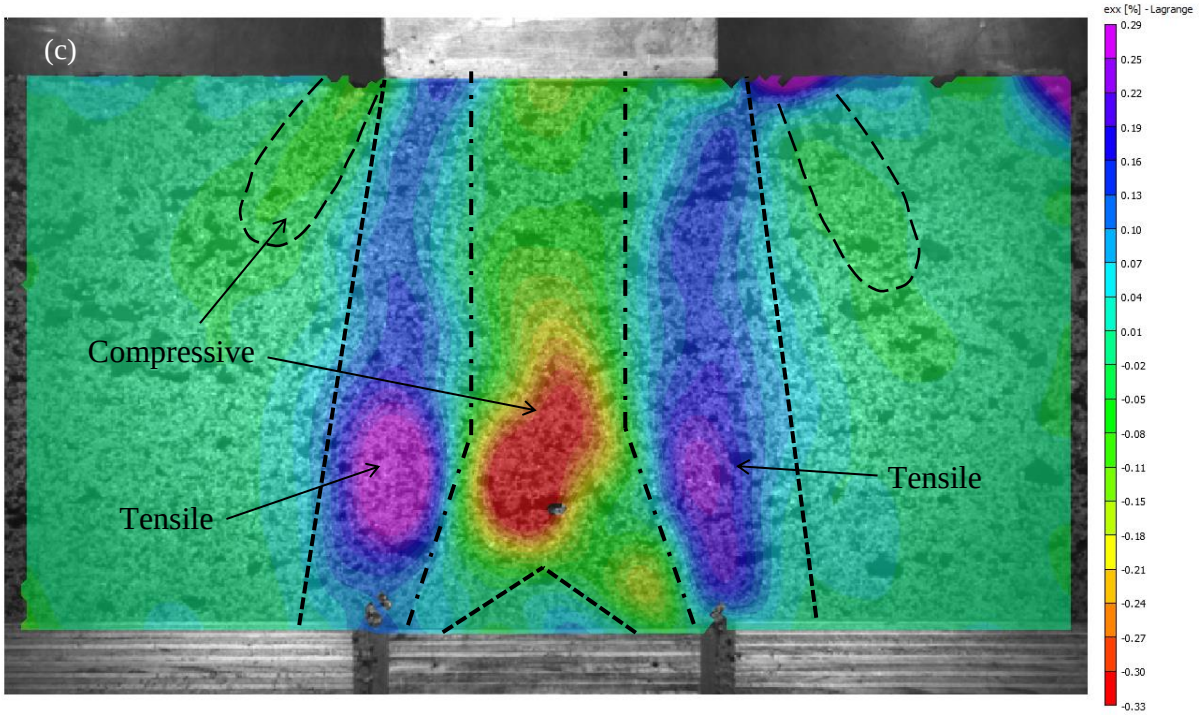

Fig. 4.8. Horizontal strain distribution under AAWS conditions for the three materials: (a) Sand, (b) 10% Rubber–sand mixture, and (c) 30% Rubber–sand mixture

The vertical displacement distributions obtained for the three geomaterials tested, with no surcharge and with the surcharge, are shown in Figs. 4.9 and 4.10, respectively. It can be observed that a curved triangular area formed above the trapdoor. The particles in this section displaced together with the trapdoor. This area is referred to here as 'the arch of equal displacement', or 'the arch' for short. The granular material outside the arch was subjected to a gradient of vertical displacements, as illustrated by the zone of transitional gradient vertical displacements in Fig. 4.9(a). The slope of this gradient is significantly higher in the horizontal direction when compared with the vertical direction. The 'total arch height' can then be defined as the sum of the arch height (H^*) and the height of the zone of transitional gradient vertical displacements (H), as shown in Fig. 4.9(a).

To provide a quantitative comparison, the Normalised arch height (H_n) is calculated as follows:

$$H_n = \frac{H^*}{trapdoor\ width} \tag{4.7}$$

Table 4.2 lists the values of arch height obtained for the different geomaterial and testing conditions. As can be seen from this table, in both the AANS and AAWS cases, the arch height increased initially with the addition of 10% rubber material to the sand. A further increase in rubber content to 30% reduced the arch height to a level equal to or smaller than the original sand. Interestingly, the total arch height, H_n, decreased constantly with the rubber inclusion. In the AANS condition, the total arch height gradually reduced from 154% of the trapdoor width (TW), in the case of Sand, to 148% of TW in the case of 10% Rubber–sand, and further to 140% of TW in the case of 30% Rubber–sand. Although, it seems that the total arch height may have been greater than the depth of the Sand backfill in Fig. 4.9(a). This requires a modicum of objective judgement. Applying the surcharge block resulted in a significant decrease in the arch height. Under the AAWS condition, the arch height reduction rate was greatest for the 10% Rubber–sand backfill, followed by Sand and 30%

Rubber–sand. The surcharge also altered the pattern of vertical displacements. The outer boundaries of the *v* variable became approximately vertical and were confined between the surcharge block corners and the trapdoor edges. Further investigation of arch formation will be presented later when shear strains are examined.

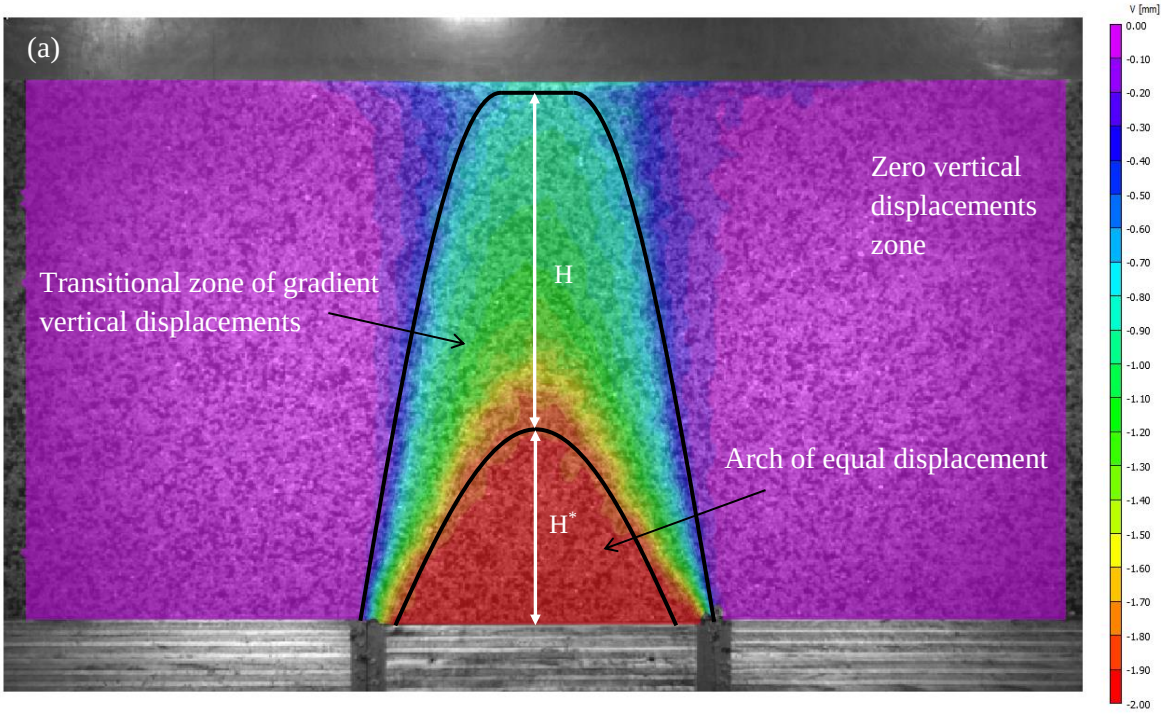

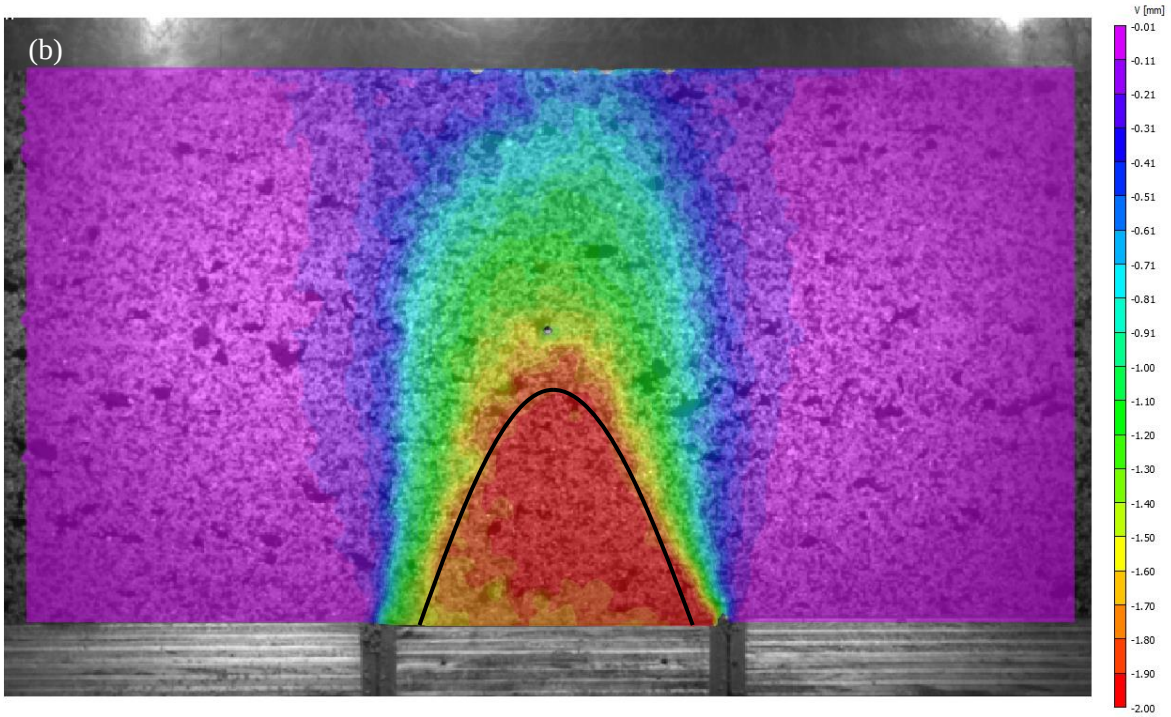

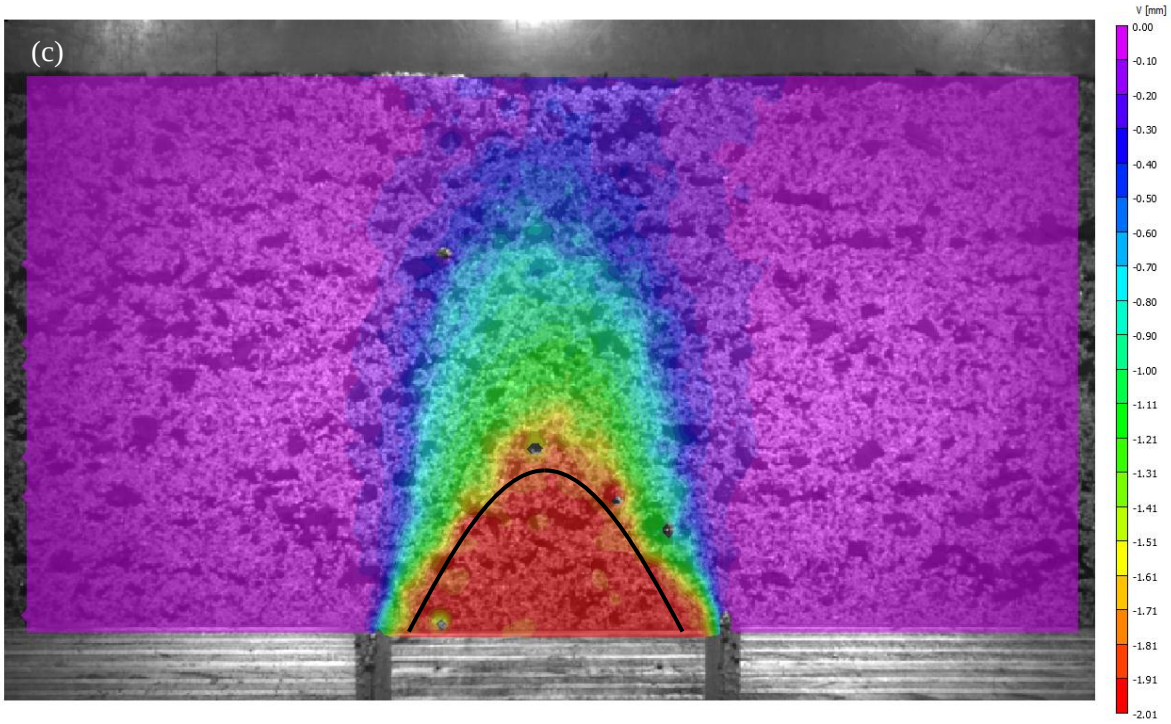

Fig. 4.9. Distribution of vertical displacements under AANS conditions for the three materials: (a) Sand, (b) 10% Rubber–sand mixture, and (c) 30% Rubber–sand mixture

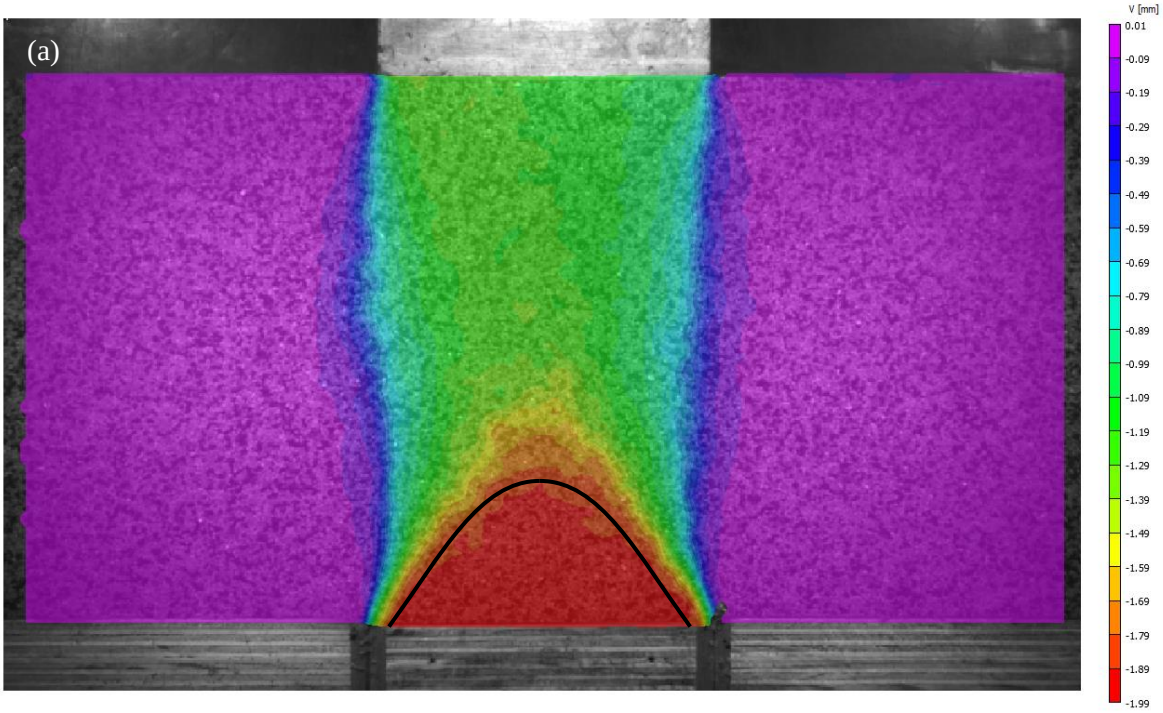

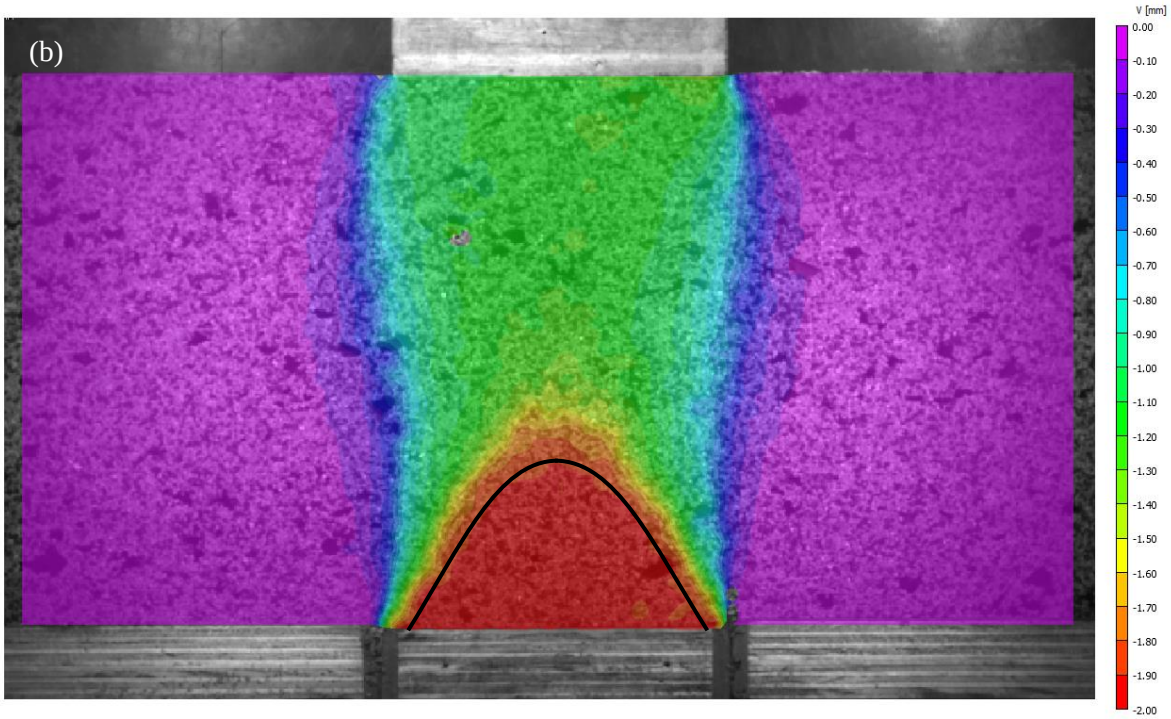

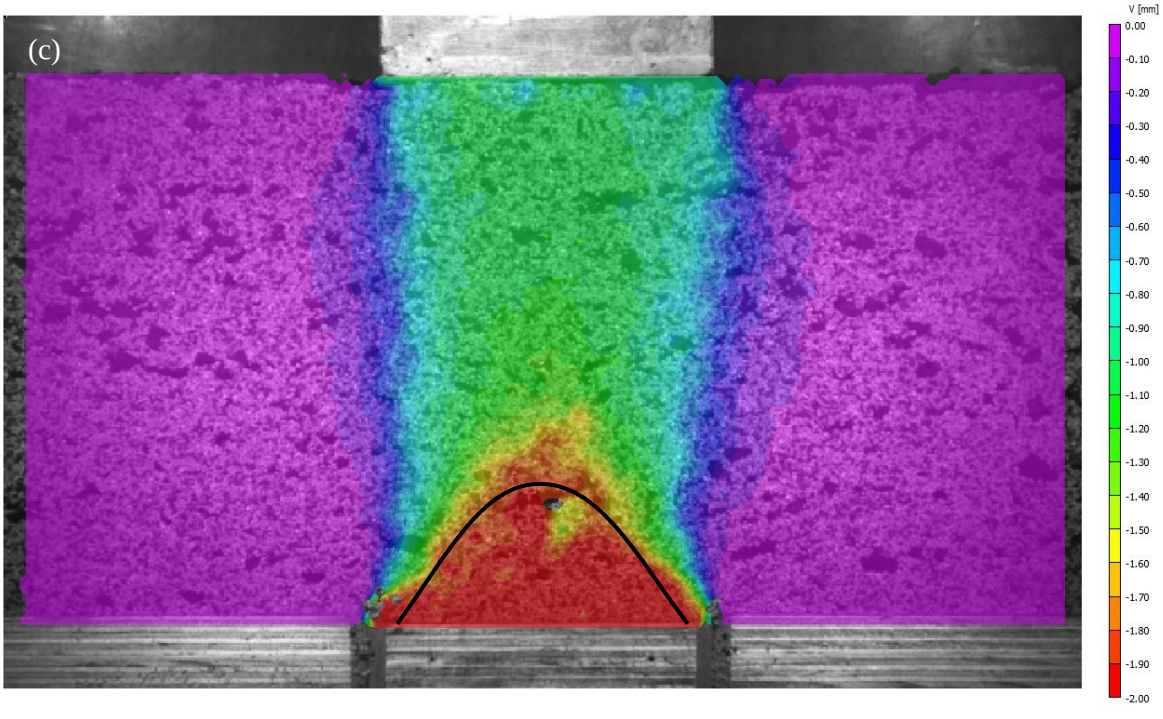

Fig. 4.10. Distribution of vertical displacements under AAWS conditions for the three materials: (a) Sand, (b) 10% Rubber–sand mixture, and (c) 30% Rubber–sand mixture

The DIC results of the vertical strain distributions obtained for the three materials tested with no surcharge and with the surcharge are shown in Figs. 4.11 and 4.12, respectively. For the AANS case, where the Sand was used as backfill material, tensile vertical strains were contained within a stool-shaped region over the trapdoor, with maximum values forming a bisected annulus. Mixing rubber with sand notably refined the shape of the tensile region, as depicted in Fig. 4.11(b–c). The contours of the maximum tensile vertical strains propagated to a larger area in the annulus crown for both the low- and high-rubber-content backfills. These contours slightly diminished in the high-rubber-content backfill in Fig. 4.11(c). The maximum tensile vertical strains decreased with the 10% Rubber–sand by 10% and increased to a value slightly above the sand-level strains when 30% Rubber–sand was tested. This suggests that the inclusion of 10% rubber is less prone to vertical straining in the AANS arching condition. On the other hand, the sand layer and the high rubber content mixture are vertically strained to similar intensities. Therefore, it is plausible to recommend the use of a 30% Rubber–sand mixture, which results in less noticeable disturbance. Meanwhile, the high rubber content lowers the density of the mixture and prompts the use of low-cost materials. The surface subsidence caused by the active arching is also depicted in Fig. 4.11. For the backfills tested under the AANS conditions, the values of surface subsidence decreased with the addition of rubber content. This is because the total arch height in Fig. 4.9 was reduced with the increase of rubber content and, therefore, the backfill surfaces became less affected. This is reflected by the reduced compressive vertical strains as shown in Fig. 4.11(b–c).

As Fig. 4.12 shows, the vertical strain pattern changed considerably in response to the application of the central surcharge. Although to a smaller extent within the backfill, the tensile vertical strains still formed a stool-shaped region. In terms of magnitude, the tensile vertical strains increased very modestly by up to 0.36% in the rubberised backfills, and

decreased negligibly by 0.04% in the Sand backfill. Fig. 4.12 also shows that additional tensile zones with small values emerged at shallow depths within the Sand layer and on the surface in the Rubber–sand backfills. In the Sand, in addition to the widespread surface subsidence, the compressive vertical strains evolved to a greater depth, forming the pattern depicted in Fig. 4.12(a). However, the surface subsidence disappeared in the cases of the 10% and 30% Rubber–sand backfills. Due to the rubber inclusion, the compressive strain ε_{yy} profiles were also modified, as shown in Fig. 4.12(b–c). A comparison between Figs. 4.7–4.8 and Figs. 4.11–4.12 shows that the maximum vertical strains were almost 5 times higher than those of the horizontal strains. This implies that the direction of major straining was vertical.

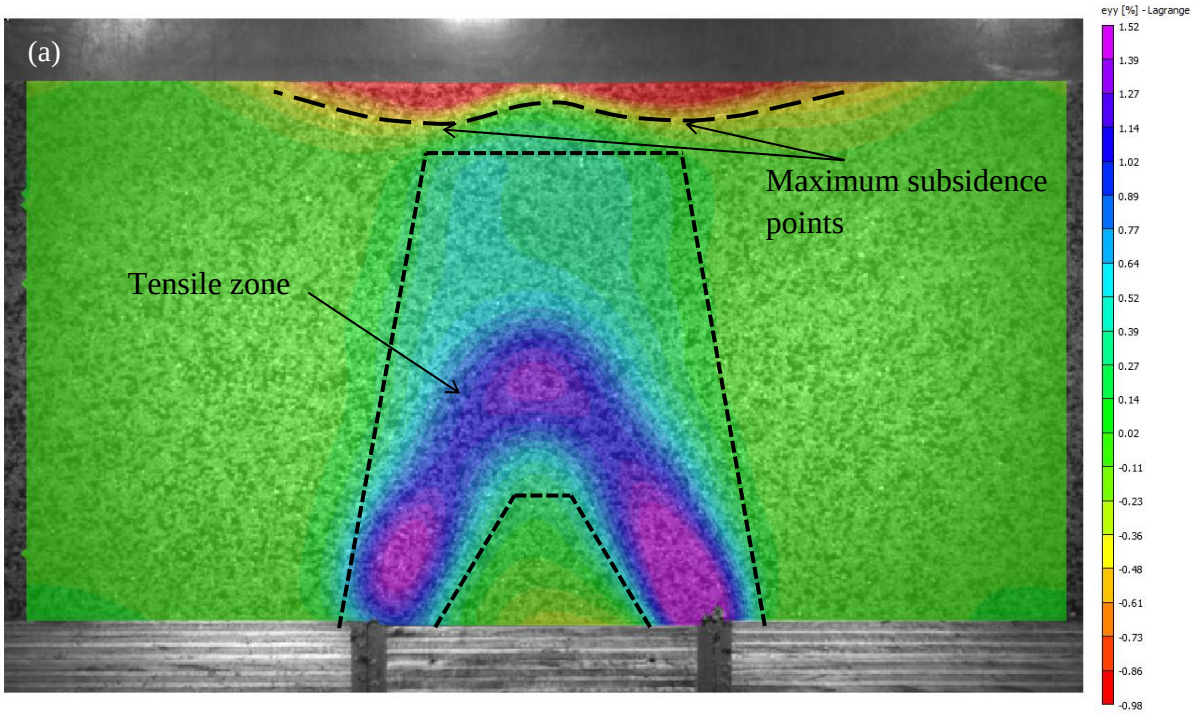

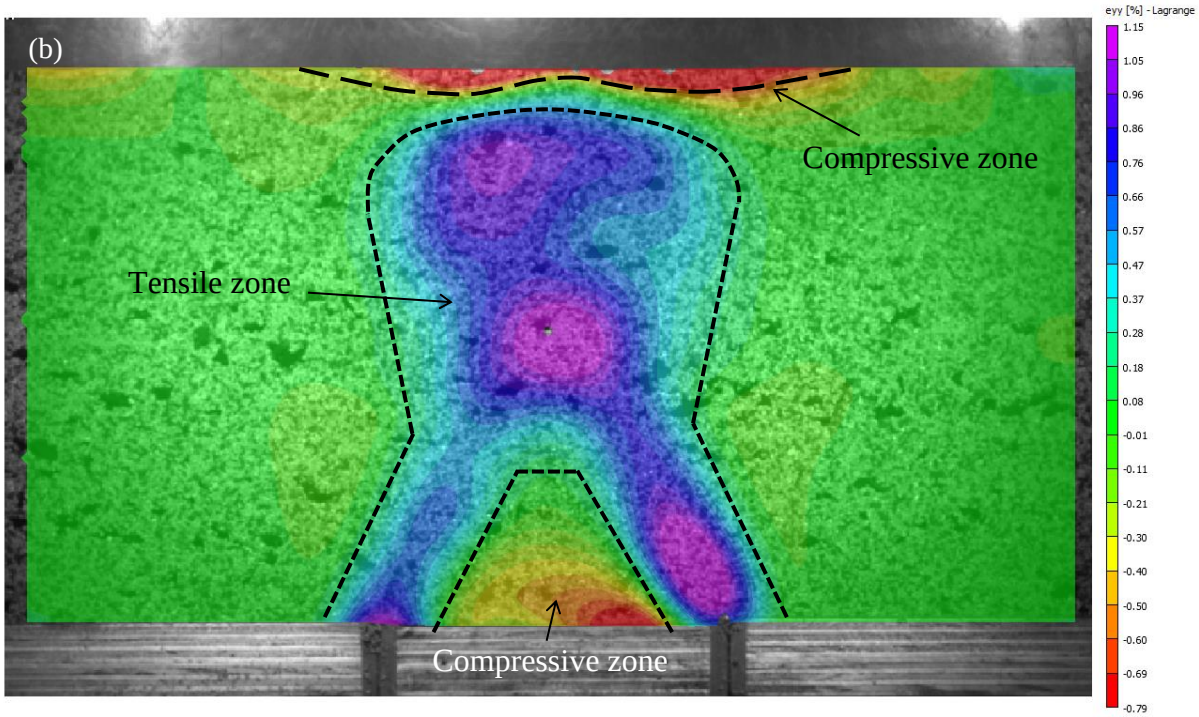

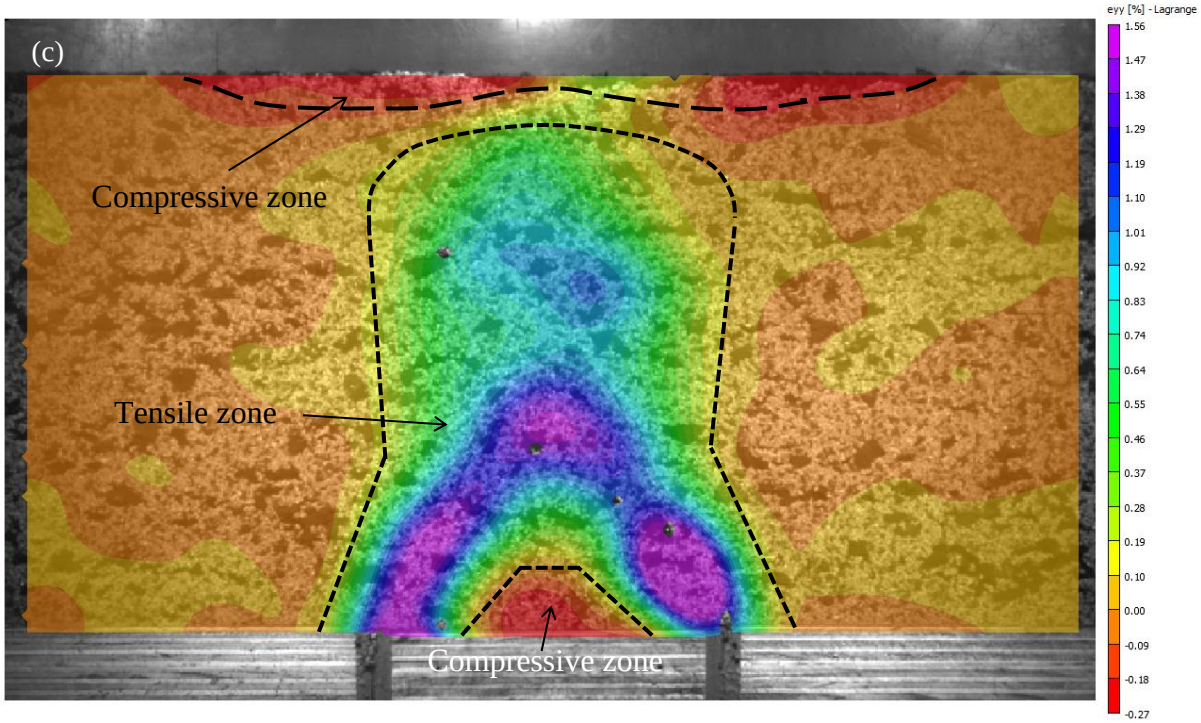

Fig. 4.11. Vertical strain distributions under AANS conditions for the three materials: (a) Sand, (b) 10% Rubber–sand mixture, and (c) 30% Rubber–sand mixture

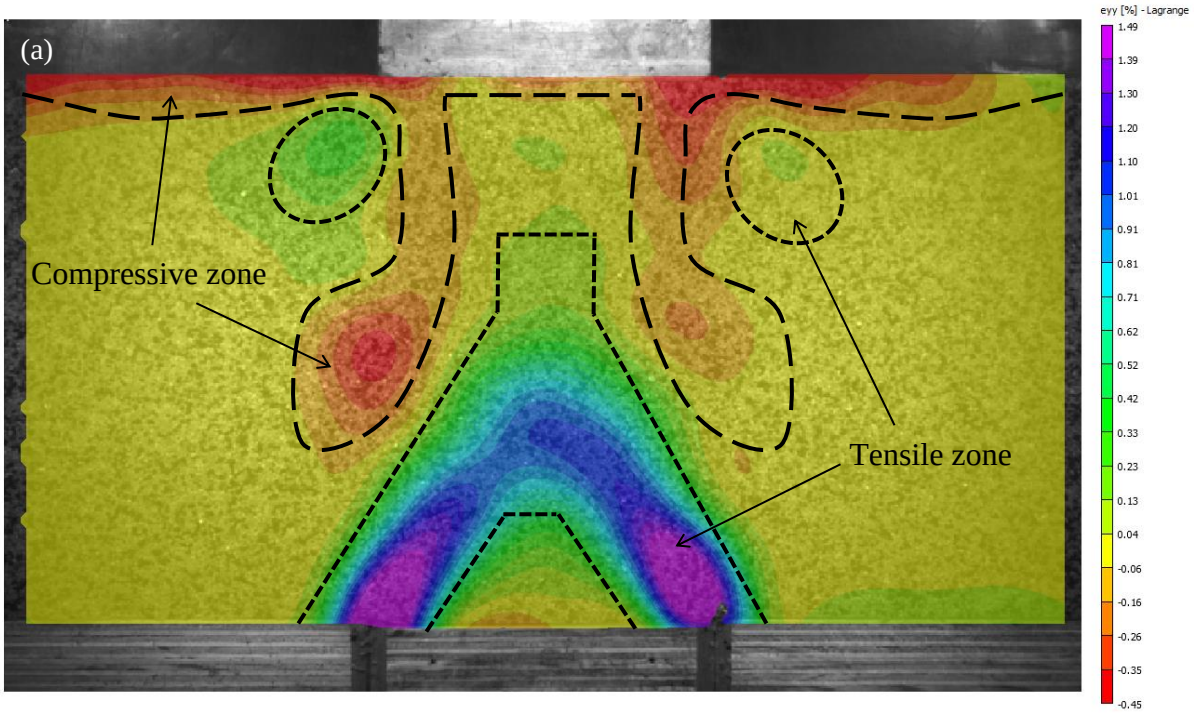
(a)
Compressive zone
Tensile zone
eyy [%] - Lagrange
1.49
1.39
1.30
1.20
1.10
1.01
0.91
0.81
0.71
0.62
0.52
0.42
0.33
0.23
0.13
0.04
-0.06
-0.16
-0.26
-0.35
-0.45

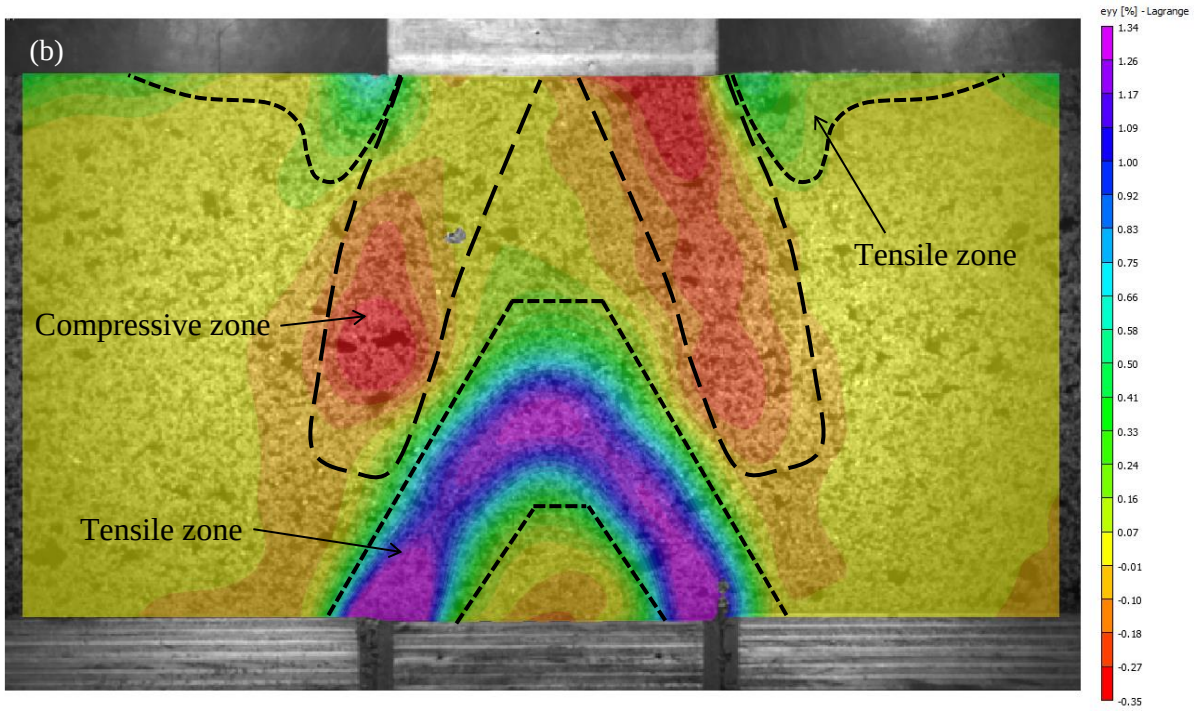
(b)
Tensile zone
Compressive zone
Tensile zone
eyy [%] - Lagrange
1.34
1.26
1.17
1.09
1.00
0.92
0.83
0.75
0.66
0.58
0.50
0.41
0.33
0.24
0.16
0.07
-0.01
-0.10
-0.18
-0.27
-0.35

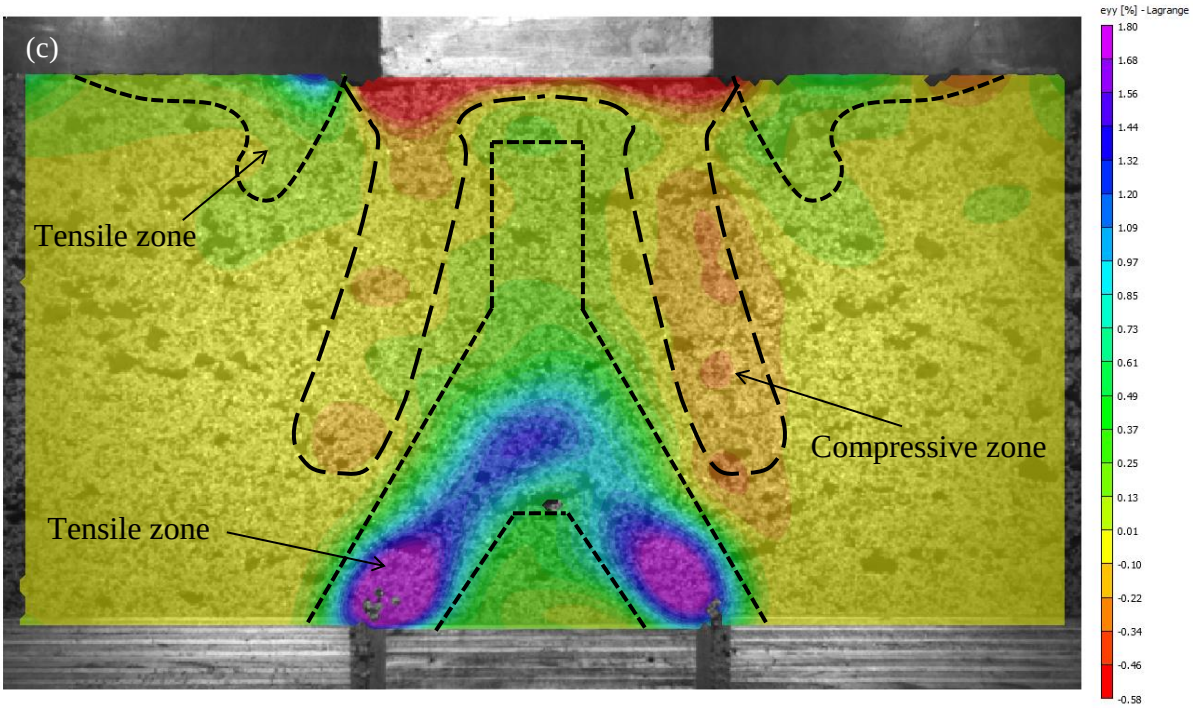

Fig. 4.12. Vertical strain distributions under AAWS conditions for the three materials: (a) Sand, (b) 10% Rubber–sand mixture, and (c) 30% Rubber–sand mixture

The shear strain distributions obtained for the three materials tested with no surcharge and with the surcharge are presented in Figs. 4.13 and 4.14 respectively. As can be seen from these figures, the shear strains were localised when the trapdoor moved downward. It is reported in literature that the localisation of shear strains is readily initiated in plane-strain specimens (Peters et al., 1988; Han and Drescher, 1993; Alshibli et al., 2003; Alshibli and Hasan, 2008). Materials with non-associated behaviour or strain softening, such as soil, are extremely prone to strain localisation or shear band formation (Lewis and Khoei, 2001). With continued loading, further deformation within these materials will be directed only into these narrow regions of intensified shear strains, while the rest of the material usually remains undeformed.

To examine shear band formation, the arch of equal displacement from Figs. 4.9 and 4.10 are superimposed on the graphs of shear strains in Figs. 4.13 and 4.14, respectively. As mentioned earlier in the analysis of vertical displacements, the term 'arch' refers to the 'pocket' of geomaterial particles that mounted on the trapdoor when it moved downwards and displaced as much. In the AANS case, the shear bands originated from the trapdoor edges and propagated inwardly into the backfills to a distance approximately equal to the height of the arch of equal displacement. The shear strains then propagated vertically with reduced intensity, but to a greater extent, from the tips of these oblique bands towards the surface. In the AAWS case, two sets of major and minor shear bands can be observed in Fig. 4.14. The major set of shear bands also initiated from the trapdoor edge and continued inwardly up to the arch height. The shear strains then oriented outwardly and propagated towards the surface and reached the surcharge block corners. These formed the minor set of shear strains in Fig. 4.14. In terms of magnitude, the shear strains were slightly lower in the rubberised backfills than in the Sand layer.

Localised shear strains or shear bands are characterised by determining their angle of inclination, θ, as specified in Fig. 4.13(a), and normalised thickness, which is defined as the ratio of the shear band width, t, to the representative particle size of a given soil or the median particle size, D_{50}. For a granular soil, the normalised shear band thickness is usually in the range of (10–20) × (D_{50}) (Muir Wood, 2002), although higher values were obtained in different experiments (e.g. Costa et al., 2009). As to the angle of inclination, it has been postulated in previous studies that θ equals the dilatation angle of granular soil (Evans, 1983, Dewoolkar et al., 2007, Costa et al. 2009). The shear band widths were measured across four profiles in the lower and upper parts of the major shear bands, as shown in Fig. 4.13(a). The measurements were averaged and used to compare the bands between the Sand and Rubber–sand layers. The length over which the shear strain values were greater than 50% of the peak

shear strain was considered for evaluation. The results of the normalised shear band thickness and angle of inclination for the geomaterials tested in this study are listed in Table 4.2.

Table 4.2. Arch and shear band characterisation for different geomaterial

Testing conditions	Material	Normalised AED[1] height (%)	Inclination angle (degrees)	Normalised shear band thickness
AANS	Sand	54	19	24.3
AANS	10% Rubber–sand	66	17	25
AANS	30% Rubber–sand	40	23	21
AAWS	Sand	41	17	23.6
AAWS	10% Rubber–sand	48	16	24.4
AAWS	30% Rubber–sand	41	23	21.6

[1] Arch of equal displacement

The data in Table 4.2 show that the shear band thickness initially increased when 10% rubber was added to Sand for both the AANS and AAWS conditions. However, when the rubber content increased to 30%, the shear band thickness decreased. The use of the surcharge reduced the shear band thickness for the cases of Sand and 10% Rubber–sand backfills. The decrease in the shear band thickness was caused by the increase in the stress level in the backfills. The surcharge marginally increased, by less than 3%, the shear band thickness in the 30% Rubber–sand backfill. This can be attributed to the presence of a high-quantity of significantly larger rubber particles in this backfill. Table 4.2 also indicates that the angle of inclination decreased when a low-rubber content was used and increased when

the rubber content increased to 30%. The inclination angle in the 30% Rubber–sand backfill remained unchanged when the local surcharge was used. The backfill with 30% rubber showed the greatest value of inclination angle, under both AANS and AAWS test conditions. Another interesting pattern in Fig. 4.13 is that the lower boundary of the shear bands in the AANS test condition was tangential to the linear section of the maximum displacement arch. This suggests that the angle of inclination of the shear bands was approximately parallel to the boundary of the arch of equal displacement. This pattern was modified to some extent when the local surcharge was applied. A comparison of Figs. 4.9 and 4.10 with Figs. 4.13 and 4.14 indicates that the shear bands formed within the area where the peak gradient of vertical displacements occurred.

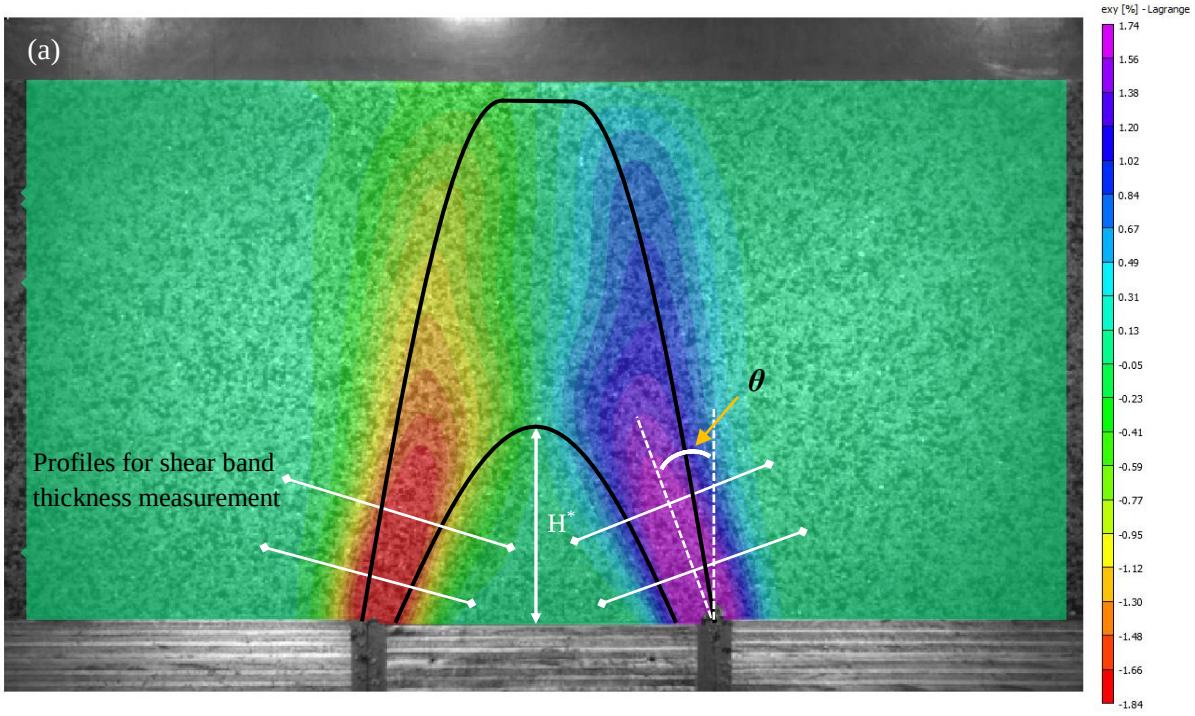

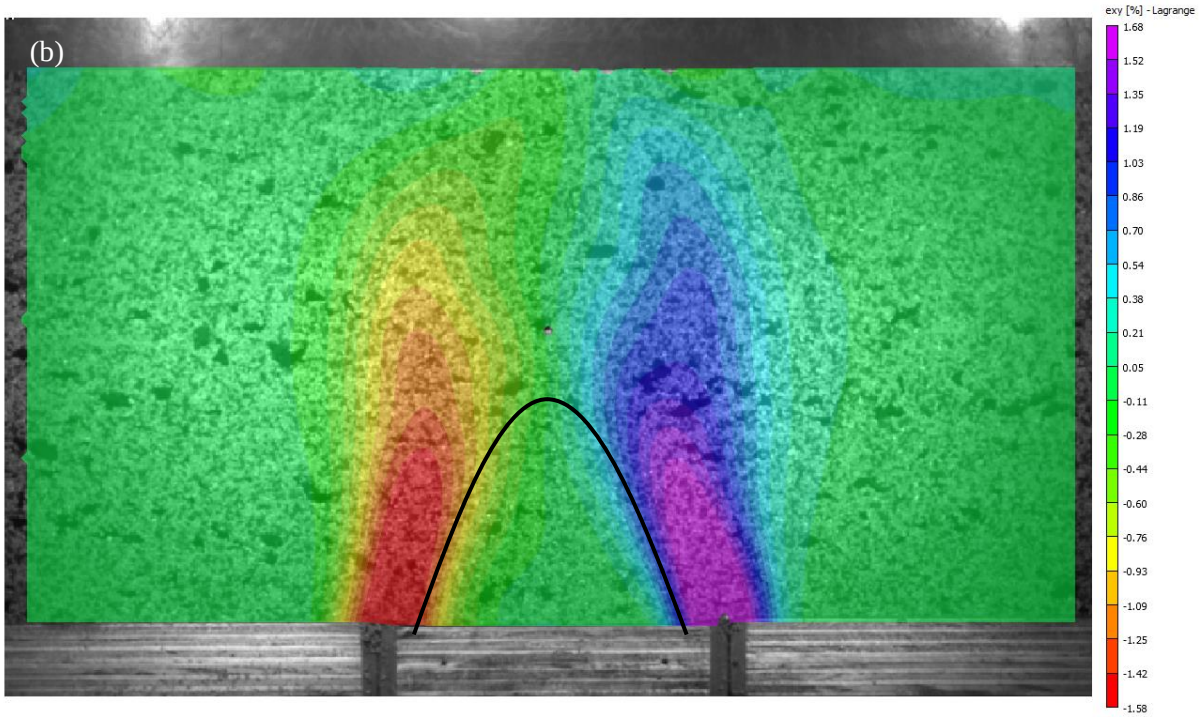

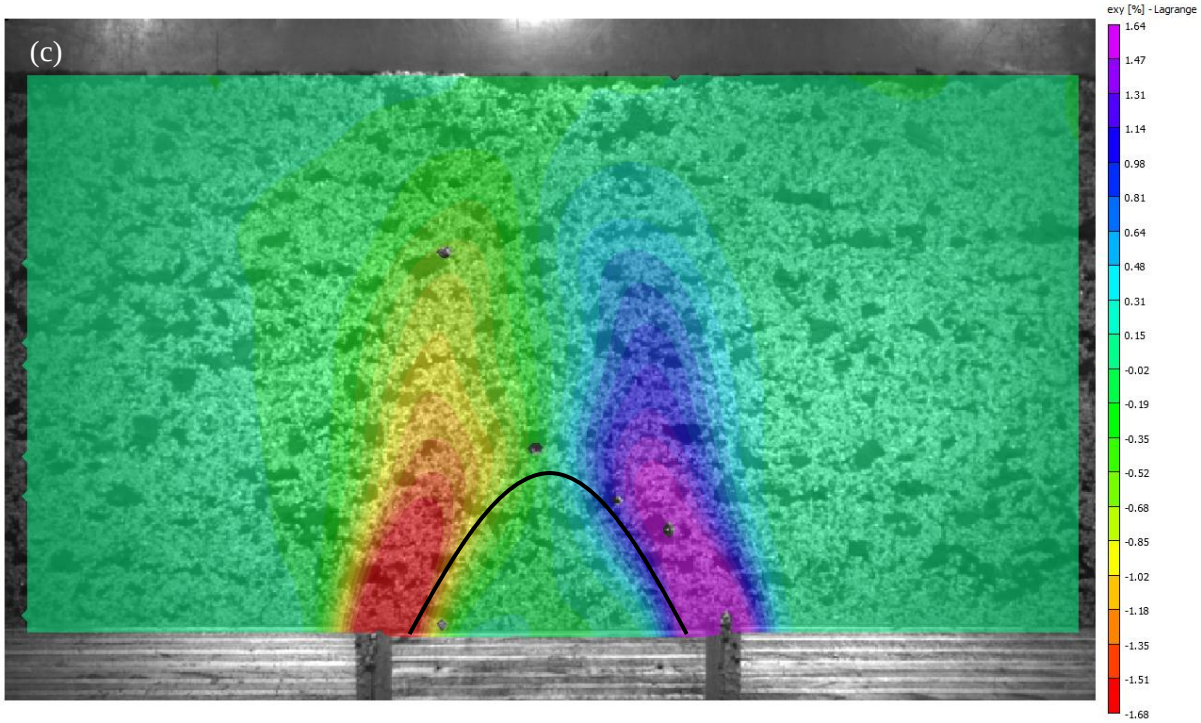

Fig. 4.13. Shear strain distributions under AANS conditions for the three materials: (a) Sand, (b) 10% Rubber–sand mixture, and (c) 30% Rubber–sand mixture

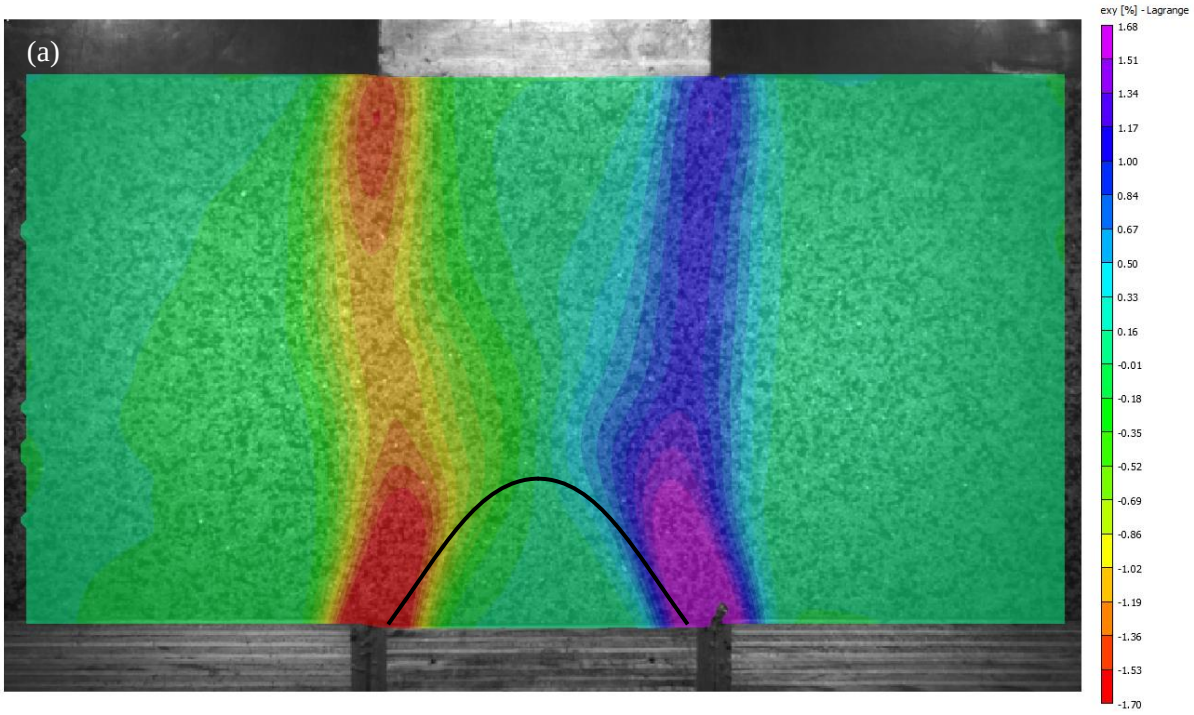
(a)
exy [%] - Lagrange
1.68
1.51
1.34
1.17
1.00
0.84
0.67
0.50
0.33
0.16
-0.01
-0.18
-0.35
-0.52
-0.69
-0.86
-1.02
-1.19
-1.36
-1.53
-1.70

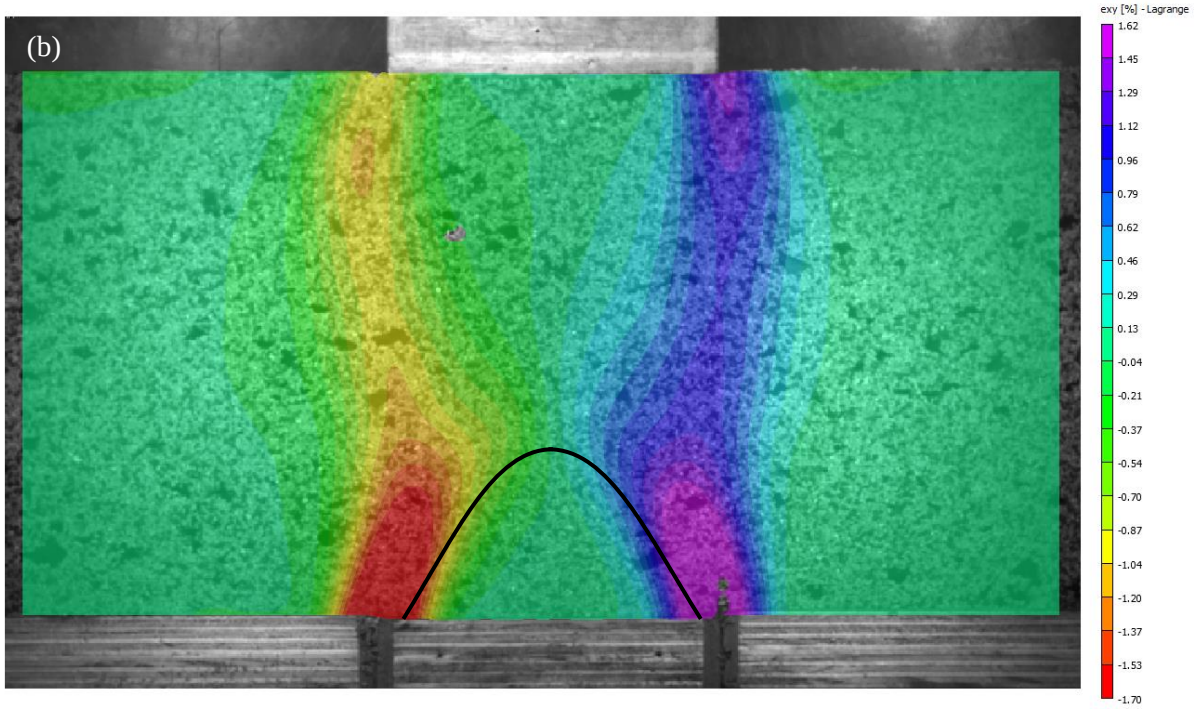
(b)
exy [%] - Lagrange
1.62
1.45
1.29
1.12
0.96
0.79
0.62
0.46
0.29
0.13
-0.04
-0.21
-0.37
-0.54
-0.70
-0.87
-1.04
-1.20
-1.37
-1.53
-1.70

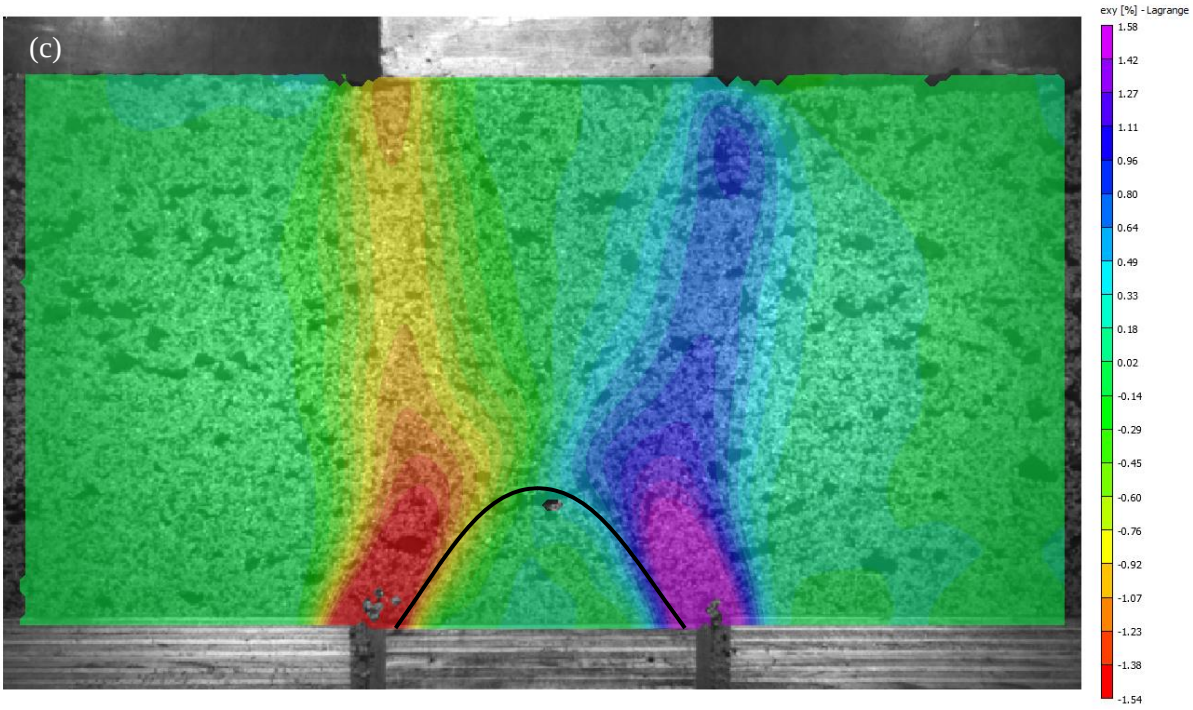

Fig. 4.14. Shear strain distributions under AAWS conditions for the three materials: (a) Sand, (b) 10% Rubber–sand mixture, and (c) 30% Rubber–sand mixture

A high inclination angle is normally favourable in certain applications, such as piled embankments, where a minimal spread of settlements caused by arching is desired for structural safety. Since the high-rubber content backfill exhibited a relatively high inclination angle, this material is a preferred choice for adoption in practice. The settlement properties of the backfills are discussed here. To do so, each of the three backfill samples was divided into 20 layers and the change of subsidence values (δ) along vertical profiles (A—A′ in Fig. 4.15) from the trapdoor centre to the surface were calculated for every layer. As an example, the settlement of each layer for the Sand backfill with no surcharge is shown in Fig. 4.15. The results of the settlement computations in the different backfills and testing conditions are presented in Figs. 4.16 and 4.17.

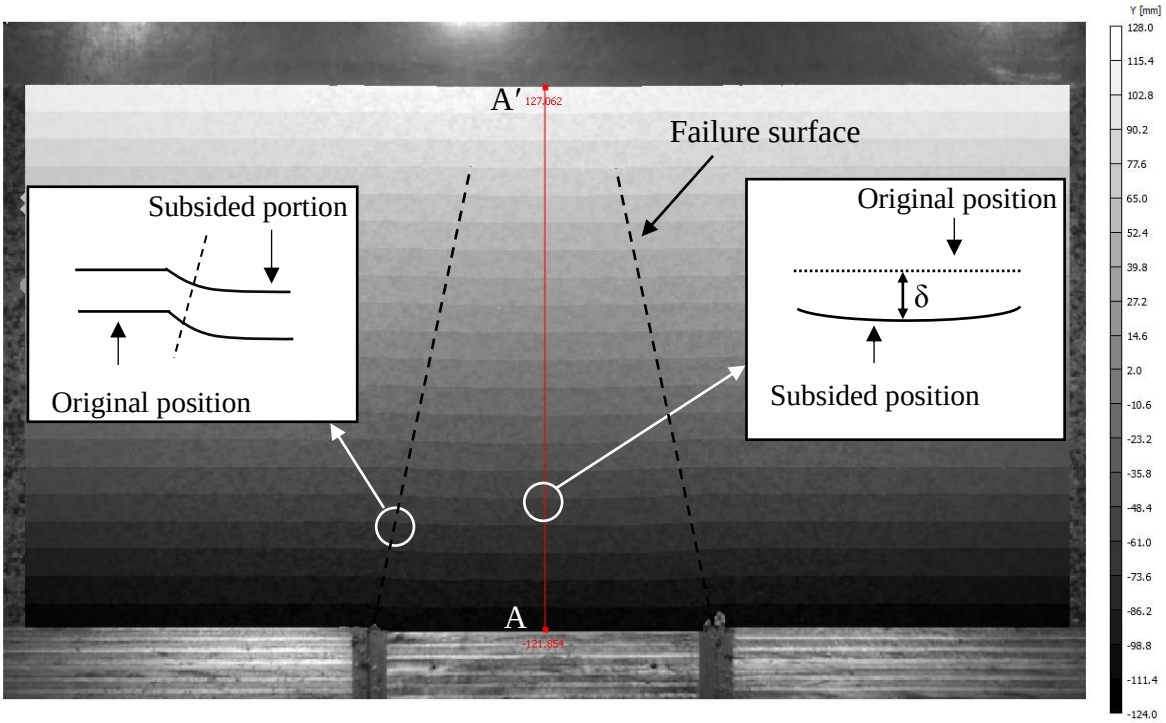

Fig. 4.15. Layer-by-layer settlement in the Sand backfill

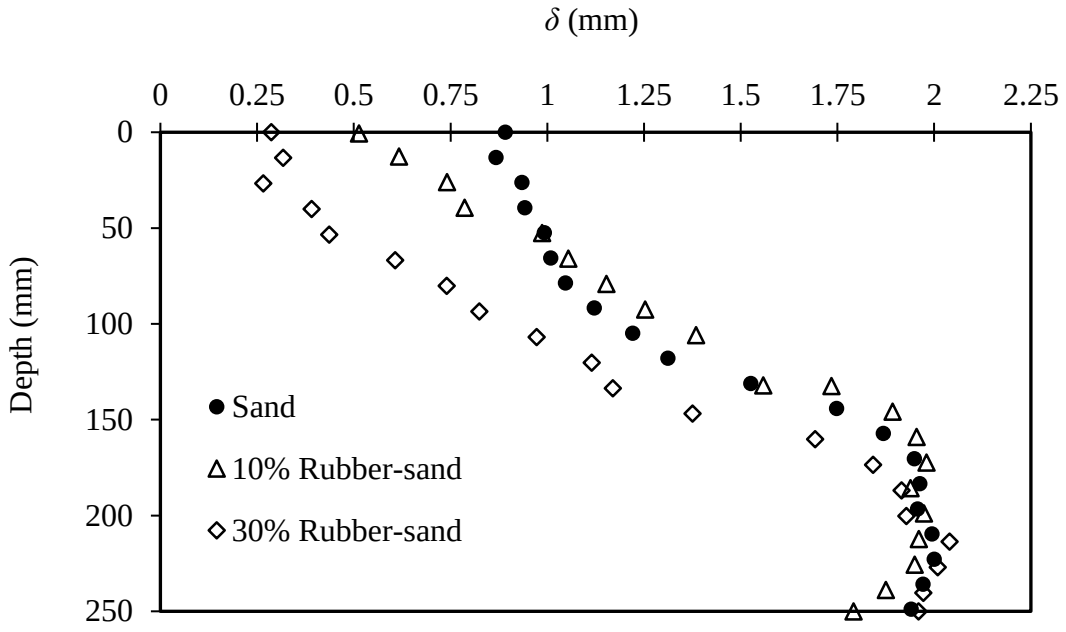

Fig. 4.16. Settlement profile in different backfills tested with no surcharge

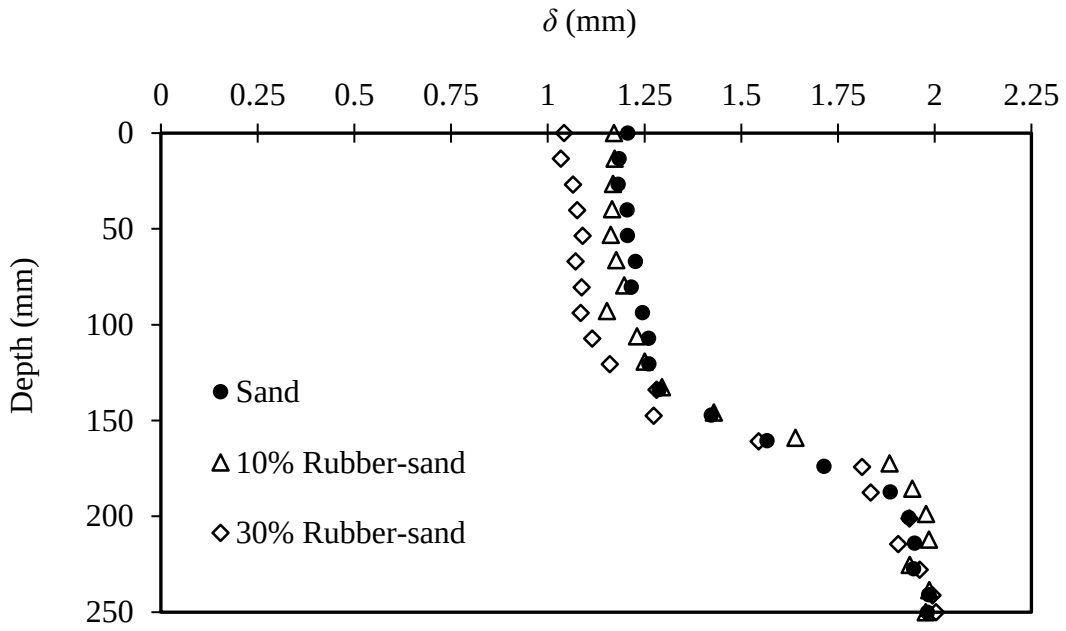

Fig. 4.17. Settlement profiles in different backfills tested with the surcharge

In Figs. 4.16 and 4.17, the settlement remains at 2 mm from depths 250 to 160 mm and the depth range is approximately 56% of TW. This observation confirms the existence of the arch of equal displacement. For the layers above the 160 mm depth, the settlement abruptly decreased over a very short distance (≈20% of TW), along the A—A′ profile within the backfills. Beyond that, where there was no surcharge, the layer-by-layer settlement values reduced gradually to the minimum on the surface, whereas under the AAWS condition, the settlement change to the surface was negligible following the abrupt reduction. The maximum surface settlement was observed in the Sand backfill in both testing conditions. Figs. 4.16 and 4.17 show that the surface settlement and the rubber content are inversely proportional. That is, the 30% Rubber–sand backfill exhibited significantly lower surface subsidence when compared with the other backfills. For example, where no surcharge was applied, the surface subsidence was less than one-third of the value for the Sand layer.

The volume change distributions obtained for the Sand and Rubber–sand backfills, tested with no surcharge and with the surcharge are presented in Figs. 4.18 and 4.19, respectively. Expansions and contractions were developed in different areas across the profile of the backfills. The zones of major expansions or contractions are plotted in these figures. As can be seen, the expansion zones are significantly greater in size and magnitude when compared with the contraction zones. A comparison of Figs. 4.11–4.12 and Figs. 4.18–4.19 indicates that the volume change distributions mirrored the pattern of vertical strains to a considerable degree. For example, the expansion zones in Figs. 4.18 and 4.19 mimicked the bisected annulus shape of tensile vertical strain regions, observed previously in Figs. 4.11 and 4.12. In the case of no surcharge, surface settlement patterns were also very similar in both the vertical strain and volume change figures. However, this similarity notably declined when the surcharge block was placed on the surface.

Comparing Figs. 4.13–4.14 with Figs. 4.18–4.19 shows that shear was accompanied by expansion, in particular, in the zone above the trapdoor. The backfill materials expanded within a stool-shaped area, whose supports oriented inwardly and initiated from above the trapdoor edges. In the AANS case, the expansion area propagated within a significantly large zone that connected the supports and formed the stool ‘crown’ above the trapdoor. The support and crown areas are illustrated in Fig. 4.18(a). The greatest expansive volume changes occurred within the supports of the expansion stool in the Sand layer (= 1.52%) and 30% Rubber–sand layer (= 1.53%). However, the most expansive area shifted to the crown region in the 10% Rubber–sand backfill and decreased to 0.63%. For Sand and Rubberised–sand backfills, the expansive areas progressed to a shallow depth near the surface, under AANS conditions. However, when the surcharge was applied, the crown height decreased to 80% or less of TW, depending on the materials tested. The variation in crown heights, in the different backfill materials, was only 3% of TW. The overall volume change in the 10%

Rubber–sand differed noticeably from that of the Sand and 30% Rubber–sand mixture, under the AAWS conditions. The magnitudes of peak expansion under the AANS and AAWS conditions exhibited the same trend across the three materials. That is, the peak expansion magnitude decreased with the increase of rubber content to 10% and then grew when the rubber content increased to 30%. The surcharge did not influence the maximum expansion magnitude in the Sand. However, the surcharge increased the peak values of expansive volume change from 0.63% to 1.31%, for 10% Rubber–sand mixture, and from 1.53% to 1.81% for 30% Rubber–sand. Therefore, the maximum contractive volume change in the backfills tested under the surcharge loading showed an initial reduction at low-rubber content and an increase at high-rubber content. Under the AANS conditions, the peak values of contractive volume change halved with each step of the increase in rubber content. These values reduced from 1.06% in the Sand to 0.46% in the 10% Rubber–sand and further reduced to a minimal amount of 0.23% in the 30% Rubber–sand. The maximum values of the contractive volume change obtained under AAWS conditions were less than those obtained under AANS conditions. The low-rubber backfill showed a small peak of contractive volume change (= 0.24%), followed by the Sand (= 0.47%) and the high-rubber backfill (= 0.60%).

Subsidence was associated with contractive volume change at the surface. The surface trough length, however, was obtained from analysing the subsidence data in Figs 16–17. In the case of no surcharge, the maximum depth of surface settlement was 12% of TW for the Sand, 5% of TW for the 10% Rubber–sand, and 10.5% of TW for the 30% Rubber–sand. Similar trends can be obtained from analysing the vertical strain data in Figs. 4.11–4.12. Where the surcharge is applied, the surface contractive regions varied with material type. For the Sand, the contractive area originated from the surcharge corners, reached a maximum depth of 13.5% of TW and progressed outward to an average length as

great as TW [Fig. 4.19(a)]. In the 10% Rubber–sand mixture, the surface contractive region was confined to beneath the surcharge block and advanced downward. The surface contractive region was again reshaped in the high-rubber content backfill. Specifically, both the maximum depth and horizontal extension length were the same and equal to 12.5% of TW.

From the above analysis, it is suggested that the surcharge increased the stress values in the backfills, and the increase in stress reduced the zone of expansion but increased the magnitude of the corresponding volume change. Except for the 10% Rubber–sand, the contractive areas diminished, both in size and magnitude, when the surcharge was applied.

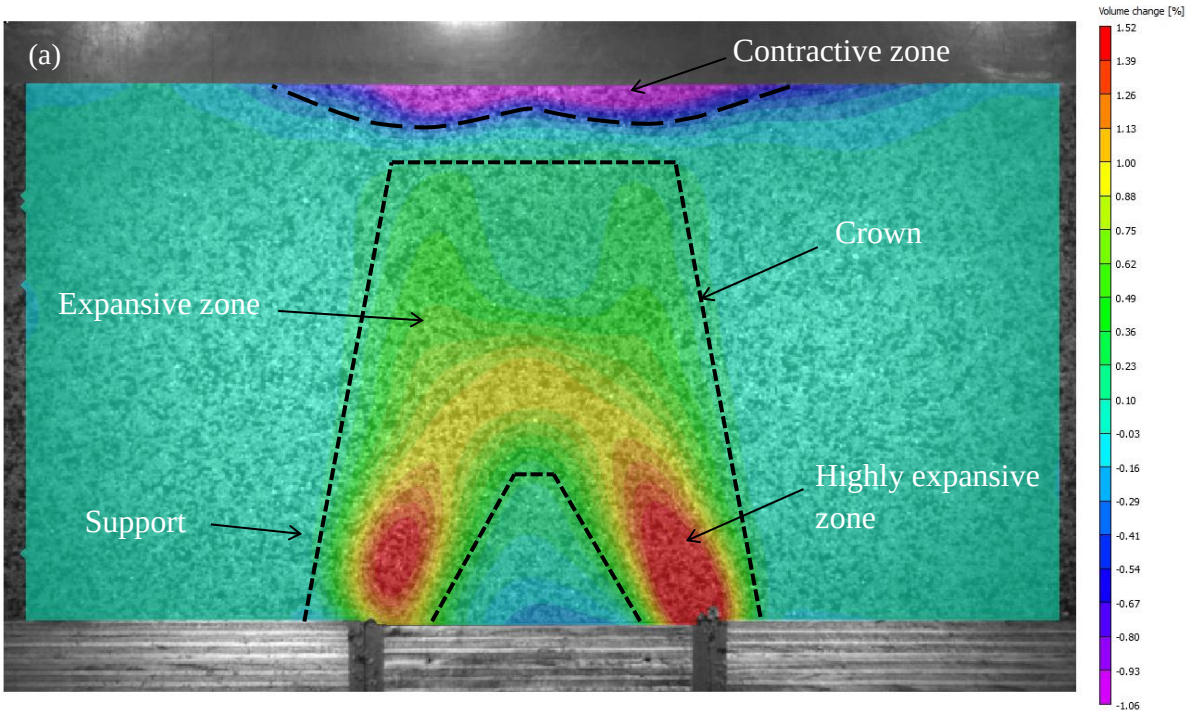

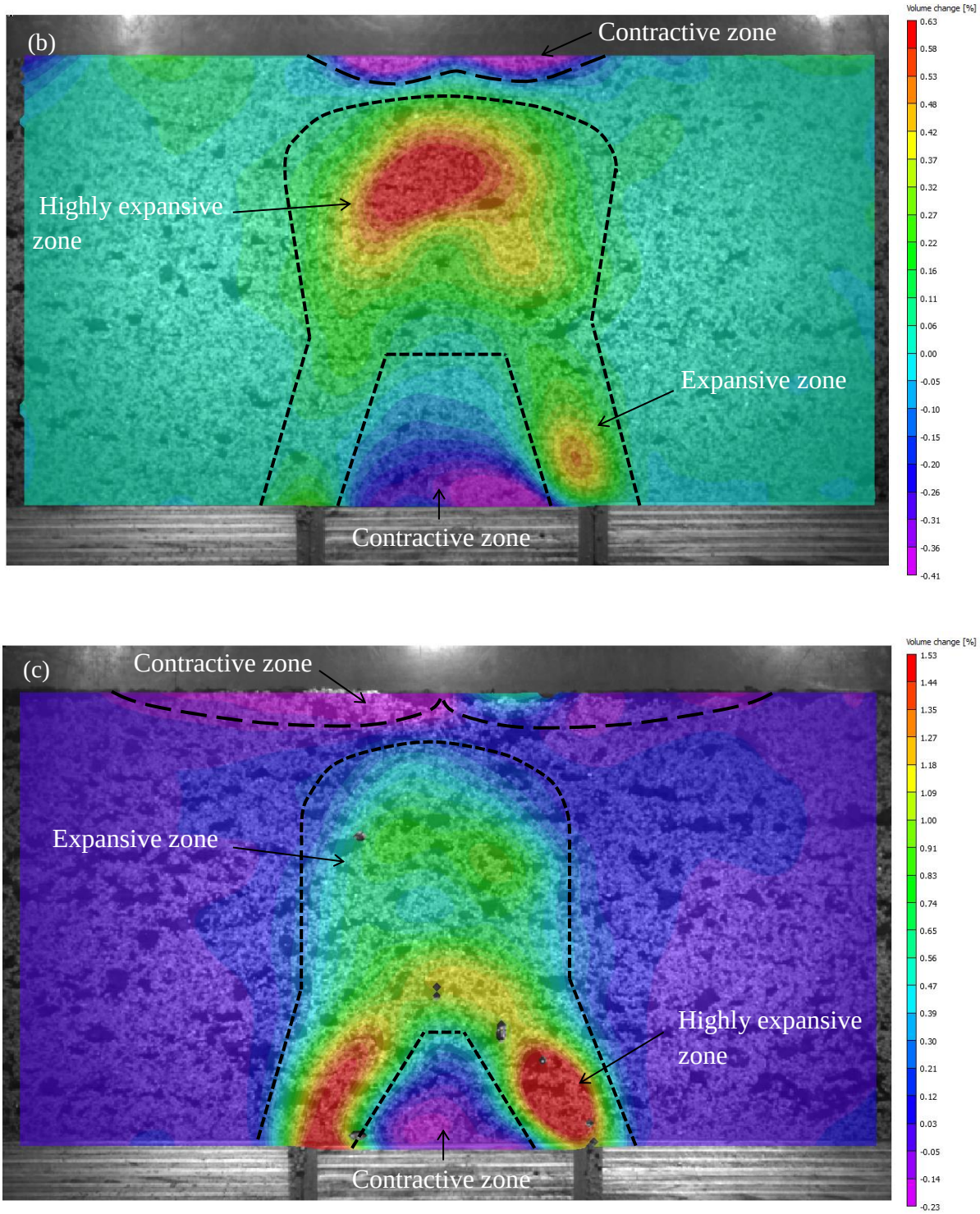

Fig. 4.18. Volume change occurred in AANS conditions for three materials: (a) Sand, (b) 10% Rubber–sand mixture, and (c) 30% Rubber–sand mixture

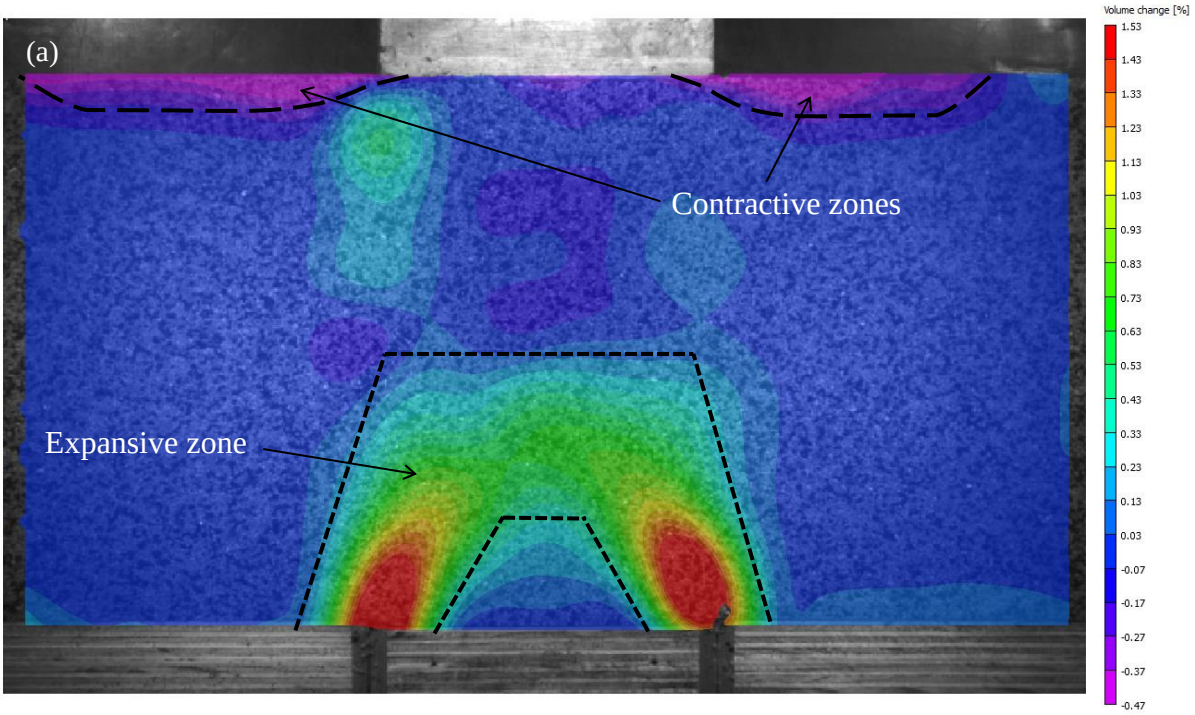
(a)
Contractive zones
Expansive zone
Volume change [%]
1.53
1.43
1.33
1.23
1.13
1.03
0.93
0.83
0.73
0.63
0.53
0.43
0.33
0.23
0.13
0.03
-0.07
-0.17
-0.27
-0.37
-0.47

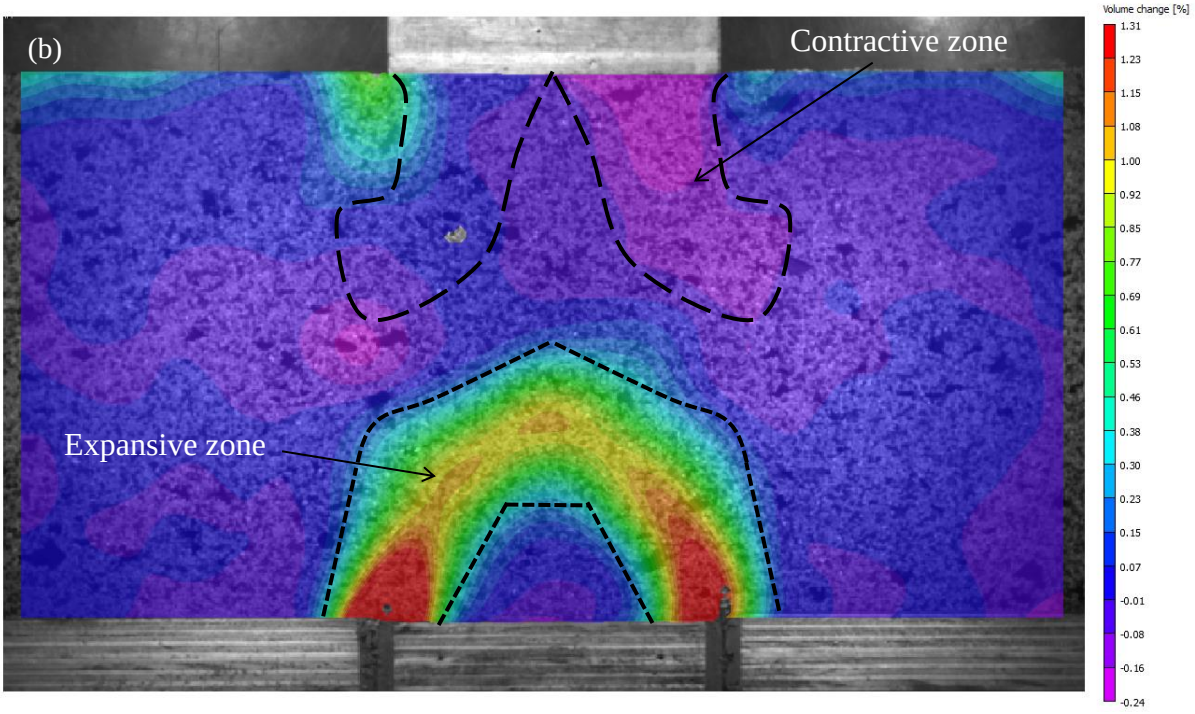
(b)
Contractive zone
Expansive zone
Volume change [%]
1.31
1.23
1.15
1.08
1.00
0.92
0.85
0.77
0.69
0.61
0.53
0.46
0.38
0.30
0.23
0.15
0.07
-0.01
-0.08
-0.16
-0.24

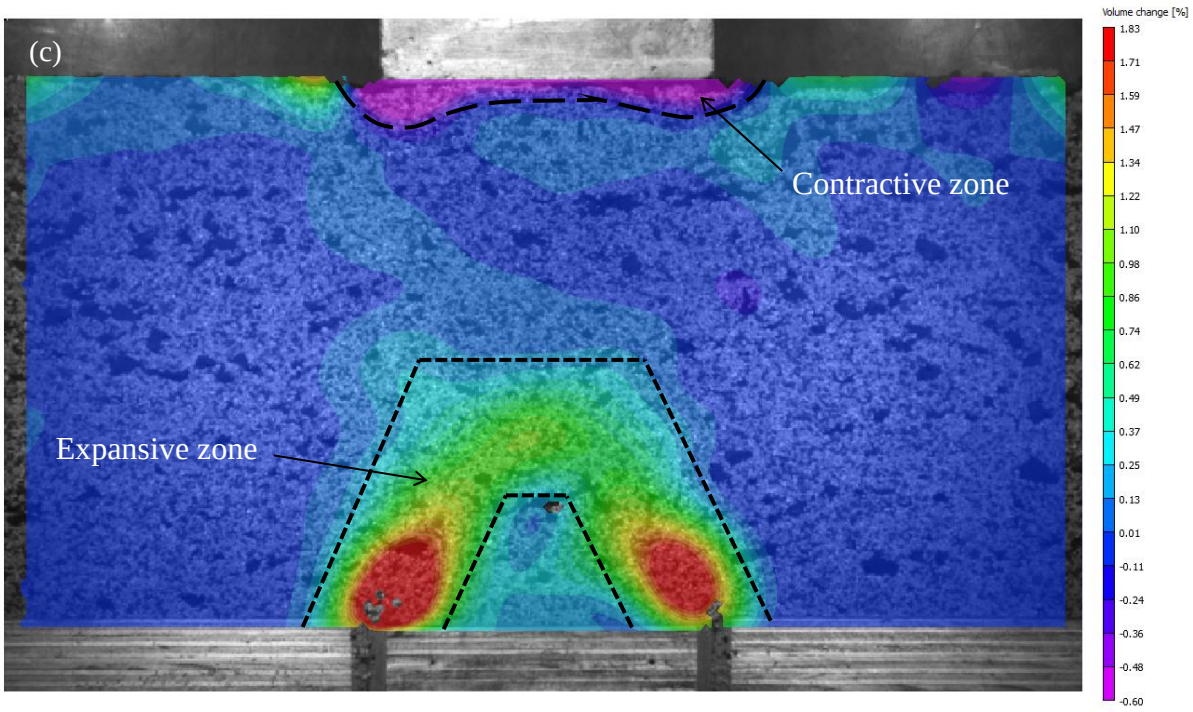

Fig. 4.19. Volume change occurred in AAWS conditions for three materials: (a) Sand, (b) 10% low rubber, and (c) 30% rubber content

4.5.2. Ground response curves

The DIC results of vertical displacements in Figs. 4.9–4.10 showed the presence of a yielding arch above the trapdoor. From a geomechanical point of view, this type of straining suggests a stress relief in the yielding segment. The stresses were recorded by the sensors installed on the base of the apparatus, as described in Section 2.2. As a validation test, the stresses were first recorded before the trapdoor was translated. Excellent agreement between the theoretical and measured values for the geostatic stresses was obtained. The stress results obtained for the Sand and Rubber–sand mixtures under the AANS and AAWS conditions were compiled to produce the so-called Ground Response (or Reaction) Curves (GRCs) in Figs. 4.20–4.25. In these figures, the vertical axis represents the normalised contact stress, which is equal to the final measured stress (σ_f) divided by the initial stress

(σ_i); and the horizontal axis represents the normalised displacement, which is equal to the trapdoor displacement divide by the trapdoor width. GRCs were first developed by Brown et al. (1983) to propose appropriate measures for underground tunnel supports. The GRCs were later adopted by Iglesia (1991) to examine the arching effect in centrifuge tests. A practical application of GRCs can be found in the research work of King et al. (2017a, 2017b), where subsoil settlement was predicted for the life of pile-reinforced embankments. A linear piece-wise idealisation of the arching GRC has been proposed recently by Han et al. (2017). Arching GRCs represent a stress–deformation relationship gauged for the model of interest, as of the stress–strain curves obtained in a triaxial compression test.

As can be seen from Figs. 4.20–4.25, the stress values evolved with the trapdoor displacement. When the trapdoor displaced by a small amount (i.e. 0.5%–4% normalised displacement), the contact stress on the trapdoor, i.e., Sensors 1–3, decreases noticeably, to the corresponding minimum stress. With further displacement of the trapdoor, the stress begins to increase gradually. When the normalised displacement reaches 15% or greater, the stress effectively stabilises. The extent of the arch, which is defined by the minimum stress, coincides with Sensor 3, i.e. the trapdoor edge. The trends shown in Figs. 4.20–4.25 exhibit a noticeable increase in stresses (up to 80%) on the stationary part of the trapdoor apparatus. The increase in stress was generally higher when the central surcharge was applied. The edge sensor on the stationary part (Sensor 4) recorded the maximum stress increase, except in the case of the 10% Rubber–sand tested with the surcharge. Therefore, in general, the edge of the stationary part is identified as the location of the maximum ‘stress concentration’ in the backfills. The increase in stress on the stationary part is related to the distance from the edge. That is, the closer to the edge, the higher the stress increase. An interesting pattern in the stress–deformation data presented in Figs. 4.20–4.25 is that the edge sensor on the stationary part showed an initial increase, followed by a decrease in stress, whereas the adjacent sensors

recorded a slight monotonic increase in stress throughout the entire range of normalised trapdoor displacement. The decrease in stress at Sensor 4 at high normalised trapdoor displacements dropped below the pre-arching stress ratio of 1, for the cases of 10% Rubber–sand with the surcharge and 30% Rubber–sand with and without surcharge. The stress recorded by Sensor 4 regained an increasing trend at normalised displacements of 18% or greater. In the areas unaffected by arching, the stress remained as a unity. The affected area due to arching on the stationary side ranged from 37.5% of TW in the Sand backfill with no surcharge to approximately 94% of TW in the 30% Rubber–sand with the surcharge. This is due to the particle size increase of the materials.

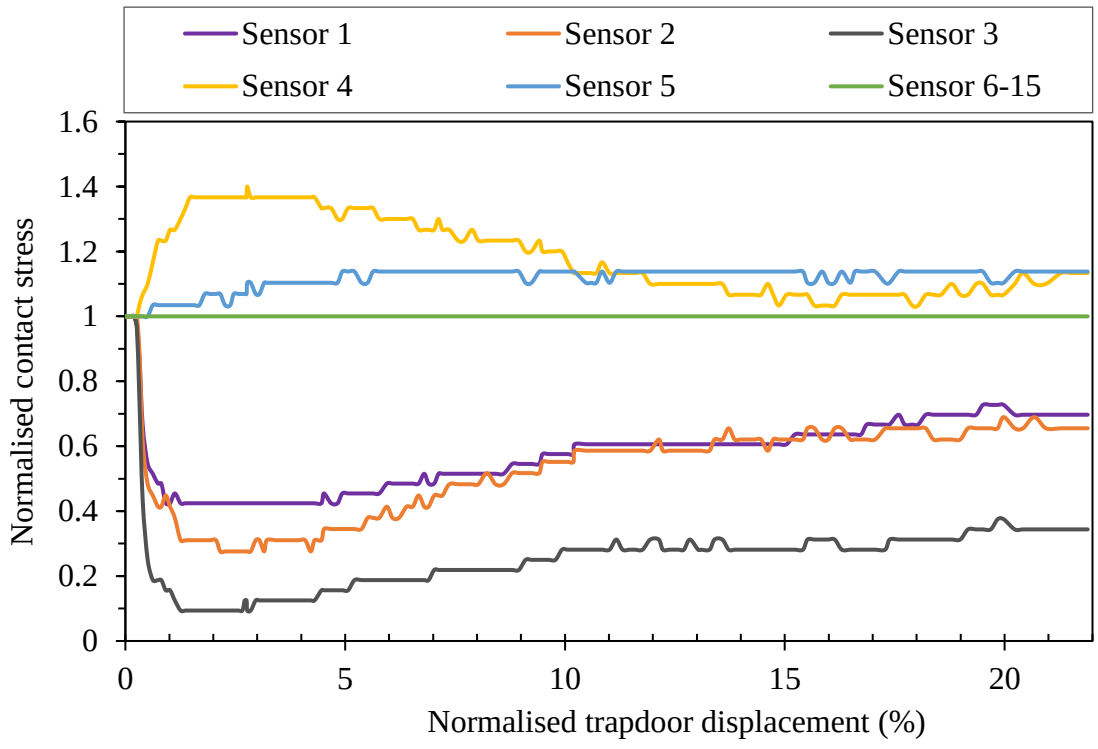

Fig. 4.20. Measured GRCs for Sand without surcharge

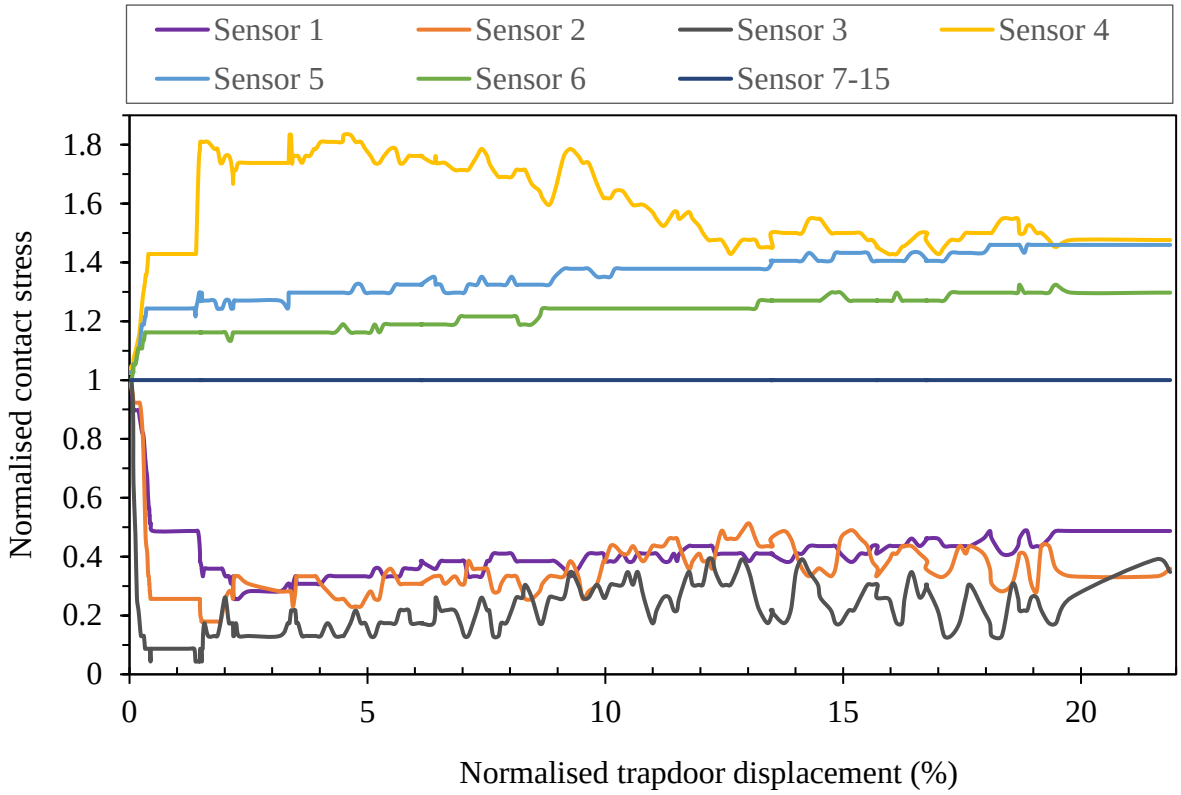

Fig. 4.21. Measured GRCs for Sand with surcharge

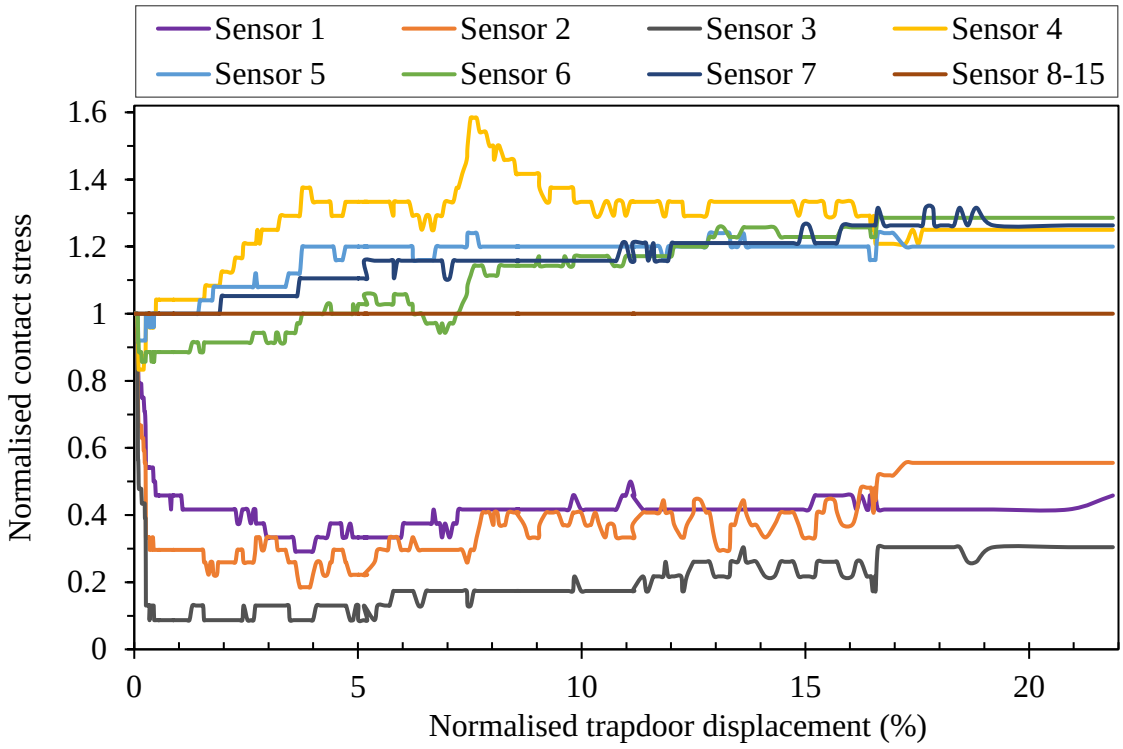

Fig. 4.22. Measured GRCs for a 10% Rubber–sand without surcharge

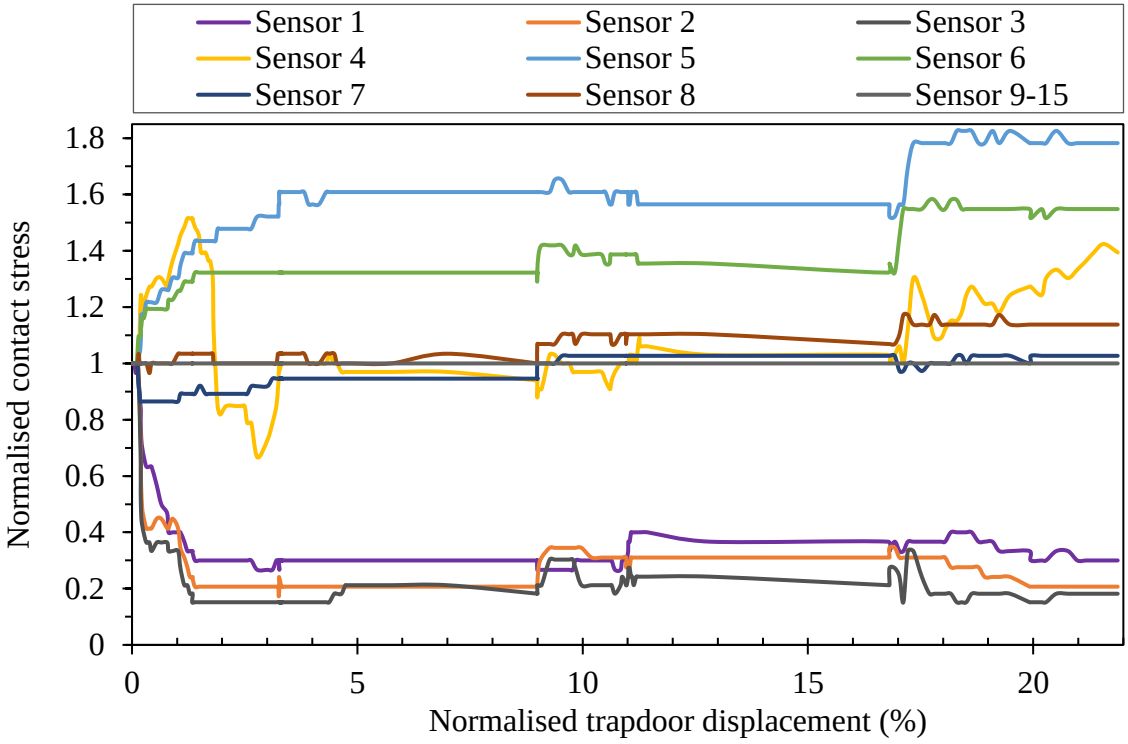

Fig. 4.23. Measured GRCs for a 10% Rubber–sand with surcharge

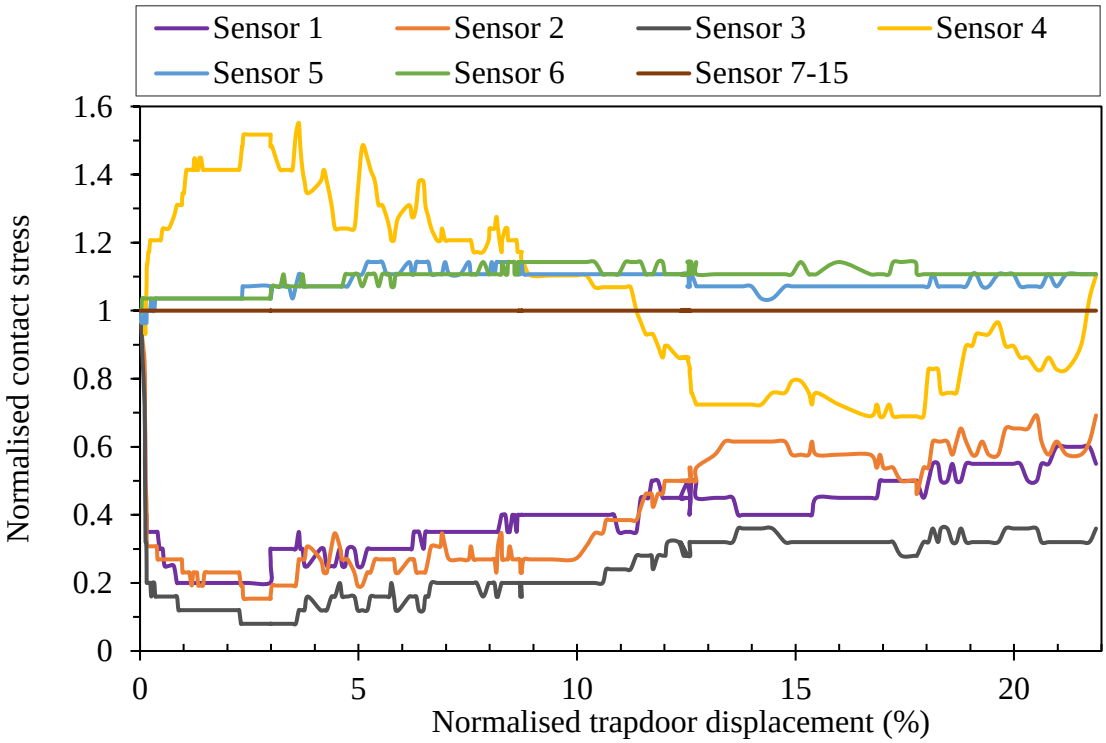

Fig. 4.24. Measured GRCs for a 30% Rubber–sand without surcharge

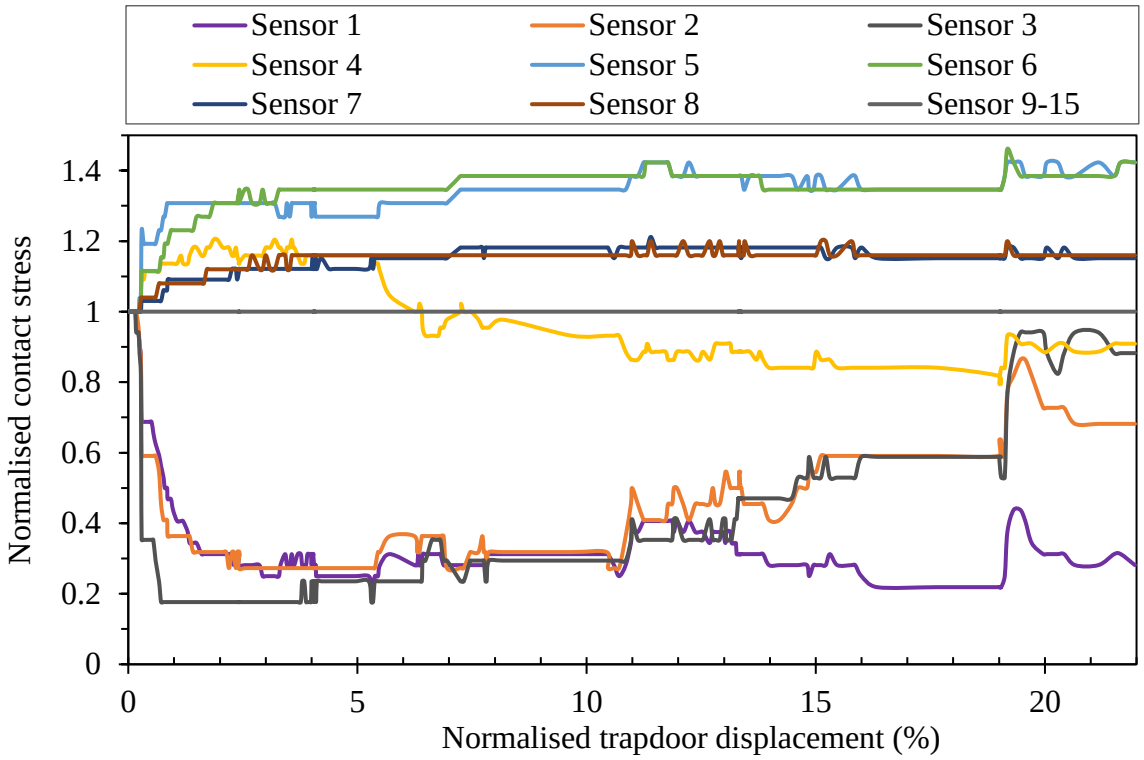

Fig. 4.25. Measured GRCs for 30% Rubber–sand with surcharge

In Figs. 4.20–4.25, it is shown that the occurrence of the maximum arching is dependent on location, such as the trapdoor centre, intermediate, and edge. Maximum arching occurred in a narrow range of 1.3% normalised displacement. The averaged normalised displacement values of maximum arching are presented in Table 4.3. The centre sensor (Sensor 1) recorded the minimum stress reduction in most cases. The intermediate sensor (Sensor 2) recorded a stress value between those by of Sensors 1 and 3, except in the case of 30% Rubber–sand. In the AANS scenario, the minimum stress across the three materials was approximately equal and was up to 92% of the stress reduction. With increasing rubber content, the stress clearly decreased. For instance, the decrease of the stress acting on the trapdoor centre was 58%, 67%, and 80% for Sand, 10% Rubber–sand, and 30% Rubber–sand, respectively. This means that the maximum arching in the rubberised backfills is accompanied by a higher stress reduction. When the central surcharge was placed on the

surface, the stresses reduced by almost an equal amount of 74%, regardless of material type. However, the aforementioned trend was reversed with the addition of rubber, at the intermediate and edge sensors of the trapdoor. At the edge sensor, for example, the lowest stress reduction was recorded in the 30% Rubber–sand, followed by the 10% Rubber–sand, with a stress reduction of 85%, and the Sand with the highest reduction of 96%. For the AAWS case, with increasing rubber content, the extent of the maximum arching along the trapdoor length became more uniform and closer to each other. This can be observed in Figs. 4.23–4.25. This may indicate that, where the stress increases in the layer under the arching effect, the stress-related arching component becomes independent of material type. From the data shown in Table 4.3, this is particularly noticeable for the rubberised backfills. The plane-strain deformation behaviour, especially the arch height and settlement discussed in the DIC results section, was found to be material-dependent.

Table 4.3. Comparison of Normalised stress for sand and rubber–sand mixtures

Testing conditions	Material	Normalised stress			Mean normalised displacement
		Centre	Intermediate	Edge	
AANS	Sand	0.42	0.28	0.09	1.56
	10% Rubber–sand	0.33	0.19	0.08	3.75
	30% Rubber–sand	0.20	0.15	0.08	1.84
AAWS	Sand	0.26	0.18	0.04	1.70
	10% Rubber–sand	0.26	0.21	0.15	1.84
	30% Rubber–sand	0.25	0.27	0.17	2.02

The GRC results obtained under a typical active arching condition is presented in Fig. 4.26, in the form of the stress evolution with respect to normalised trapdoor displacement. As can be seen, following a sharp stress decline on the trapdoor in response to the induced displacement, the normalised stress reaches a relatively short state of minimum values (maximum arching). The stresses then increase moderately with additional trapdoor displacement and, finally, a steady state is achieved. The literature suggests that maximum arching occurs within the range of up to 8.7% of the normalised trapdoor displacement. For example, Ladanyi and Hoyaux (1961) reported a high value of 8.7% for ideal plane-strain soil particles modelled as aluminium rods with a diameter of 0.32 mm and 0.48 mm. Values below 0.5% have been reported by McNulty (1965), for a sealed high-stress-level trapdoor between 500 kPa and 750 kPa. Evans (1983) observed maximum arching between 0.1–8.7% normalised trapdoor displacement, depending on soil grading and the trapdoor width. Iglesia (1991) obtained a range of 2–6% for normal gravity and centrifuge trapdoor tests. As shown in Table 4.3, the maximum arching for the three materials used in the present study was observed to be in the range of 1.5–3.75% of the averaged normalised trapdoor displacement. The stress data are consistent with the data obtained in the previous studies. Figs. 4.20–4.25 show that the maximum arching lasted generally longer in the rubberised backfills, especially when the surcharge was applied. The minimum load was maintained for up to 11% of the normalised trapdoor displacement in the 10% and 30% Rubber–sand backfills tested under AAWS conditions. For the Sand, however, the maximum arching remained for up to 4% after the minimum stress was attained.

From a review of stress measurement data in the literature (Terzaghi, 1936; McNulty, 1965, Evans, 1983; Sadrekarimi and Abbasnejad, 2010; Iglesia et at. 2013, among others) and the present study, it is suggested that the arching GRC is a function of the normalised displacement, material relative density, and soil cover ratio (= geomaterial height to trapdoor

width). In addition, the results of the present study indicate that the GRC also depends on the measurement location. In other words, based on the location of the measurements, for any arbitrary point from the trapdoor centre to edge, the GRC will vary accordingly. Unfortunately, neither an analytical solution nor an empirical relationship for the arching-induced GRC exists. The mathematical models of the active arching effect usually apply the concept of limit equilibrium to predict the minimum stress ratio or maximum arching for trapdoor centre. For example, Terzaghi (1943) proposed the following expression to predict the minimum stress ratio (σ_{min}) on a trapdoor centre:

$$\sigma_{min} = \frac{w}{2\,D\tan\varphi}\left(1 - e^{-2\frac{D}{w}K_a\tan\varphi}\right) \qquad \frac{w}{D} \leq 2 \tag{4.8}$$

where w, D, φ, and K_a represent the trapdoor width, backfill depth, the angle of internal friction, and coefficient of lateral earth pressure, respectively. Mathematical models such as Eq. (4.8) account for only a single point of the continuous and developing GRCs typified by Fig. 4.26, without considering the measurement position on the structural (trapdoor) element. In actual applications, however, the current arching state in a geomaterial–structure interaction case can be anywhere on the GRC in Fig. 4.26.

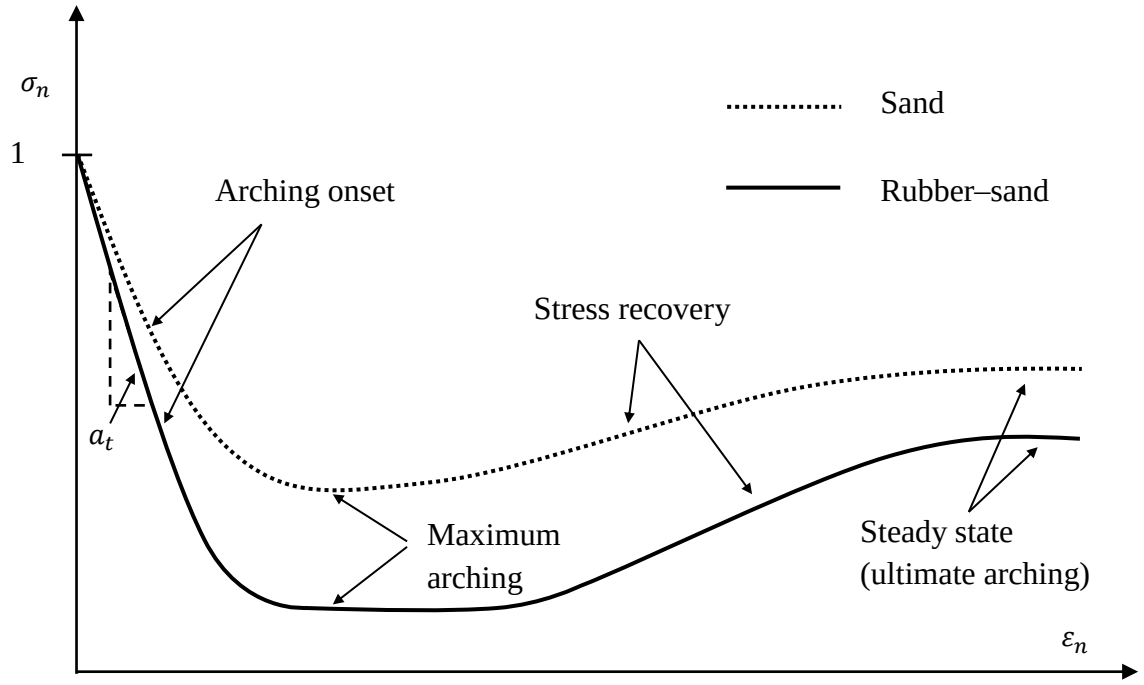

Fig. 4.26. Typical arching ground response curves for Sand and Rubber–sand (the curve for Sand is modified after Iglesia et al., 2013)

Iglesia et al. (2013) developed the concept of the *arching tangent modulus* for the initial arching segment in a GRC, as shown in Fig. 4.26. The linear relationship, that yields a value of unity for a stress ratio at zero normalised displacement, is expressed as follows:

$$\sigma_n = 1 - a_t \cdot \varepsilon_n \quad (9)$$

where σ_n and ε_n are the stress ratio and normalised trapdoor displacement respectively, and constant a_t is the arching tangent modulus. Iglesia et al. (2013) applied linear curve-fitting, together for sand and glass beads data, and obtained a single arching modulus of 125 with an R^2 value of 0.7. In this study, however, values of a_t were determined for the trapdoor centre and average trapdoor for Sand and rubberised sand for a normalised trapdoor displacement of up to 0.5% under the AANS and AAWS conditions. The results of this

analysis are presented in Table 4.4. As is evident, the arching tangent modulus is clearly material-dependent.

Table 4.4. Tangent arching modulus data from linear regression

Testing conditions	Material	Measured arching tangent modulus (a_t) on trapdoor			
		Centre	R^2	Average	R^2
AANS	Sand	70	0.6	89	0.5
	10% Rubber–sand	166	0.5	289	0.3
	30% Rubber–sand	384	0.5	367	0.5
AAWS	Sand	79	0.9	159	0.3
	10% Rubber–sand	104	0.6	159	0.4
	30% Rubber–sand	61	0.9	80	0.6

The results in Table 4.4 can be used for practical situations. Given the arching moduli of Sand and rubberised sand obtained under AANS conditions for the trapdoor centre in Table 4.4, if, for example, the trapdoor represents a geotextile element placed over two adjacent piles, where there is no load on the ground surface above the piles, for every 0.1% of settlement of the geotextile, the stresses acting on the geotextile will be reduced by 7%, 17%, and 38%, if the overlying backfill material consists of Sand, 10% Rubber–sand, and 30% Rubber–sand, respectively. It follows that, because of the high arching modulus determined from the stress measurement data and the low surface settlements observed in the deformation analysis data, a 30% Rubber–sand mixture would be the optimal backfill

geomaterial for field conditions with active arching and no applied local surcharge. For cases similar to active arching with an applied surcharge, the 10% Rubber–sand mixture exhibited low subsidence and high stress reduction. However, the selection between the subsidence and stress reduction becomes a matter of trade-off, as one may outweigh the other depending on the situation in question.

From the stress evolution due to arching (Figs. 4.20–4.25), it can be inferred that different parts of the trapdoor apparatus behaved differently. These responses are schematically shown in Fig. 4.27 for better comparison. The brittle nature of a granular soil on a yielding trapdoor structure was examined by Iglesia et al. (2013). However, a more comprehensive representation of the mechanical behaviour on the soil–structure interface in a trapdoor apparatus is presented in Fig. 4.27. As shown, brittle behaviour extends to the region immediately adjacent to the trapdoor, which, from the experimental data in the present study, is equal to approximately 20% of TW for the three materials. The granular material that is located farther away from the trapdoor and supported by the stationary part exhibits ductile behaviour, as shown in Fig. 4.27. The extent of the ductile region was generally greater in the rubberised backfills when compared to the Sand backfill and did not exceed 75% of TW. It can then be concluded that, in terms of stresses, the area disturbed by arching laterally extends approximately to a maximum length as great as the width of the yielding structure.

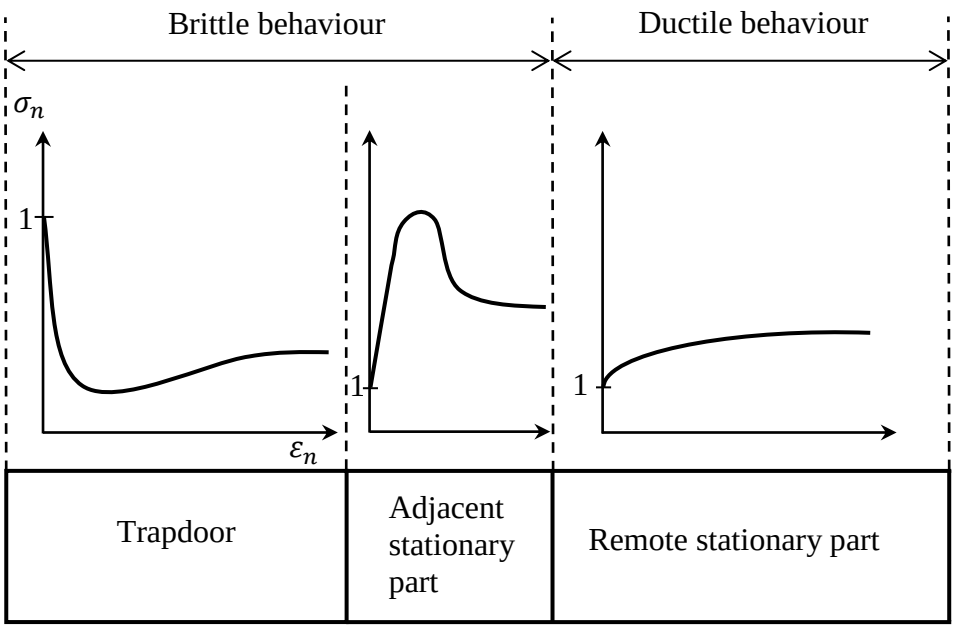

Fig. 4.27. Mechanical behaviour on the geomaterial–structure interface in a trapdoor apparatus

4.6. Conclusions

Comprehensive deformation and stress analyses have been undertaken on Sand, 10% Rubber–sand, and 30% Rubber–sand tested in a trapdoor apparatus, with or without a surcharge. The deformation of these three backfills due to arching was measured using the digital image correlation (DIC) technique and, simultaneously, the arching stress evolution was recorded by an array of stress sensors placed at the base of the apparatus. The tests and analyses have drawn the following conclusions:

- The DIC technique is a powerful and versatile tool for deformation analysis. It offers full-field measurements of deformation without sample disturbance. For the Sand and rubberised sand backfills, horizontal and vertical displacements and strains, surface subsidence, shear strains, and volume change, were obtained using this technique and interpreted.

- A curved triangular arch is formed following the downward translation of the trapdoor element. In the arch, the particles travelled together with the trapdoor; and the arch was termed ‘the arch of equal displacement’. The lateral extension of arching is slightly greater in the rubberised backfills than in the Sand backfill. The surface subsidence and final arch height decreased in the rubberised backfills. The higher the rubber content, the lower the surface subsidence and the final arch height. However, the height of the arch of equal displacement increased when 10% rubber content was added to the sand. When the rubber content was increased to 30%, the arch height was less than that formed in the Sand layer. Shear bands originating from the trapdoor and inclined inwardly were formed in all the backfills. The angle of inclination, thickness, and patterns of the shear bands were dependent on rubber content and surcharge load. Expansive and contractive volume change regions emerged in the backfills as a result of the trapdoor movement. The expansive regions coincided with the localised shear strains. Rubber content and surcharge placement significantly affected the amount and pattern of the volumetric strains. The 30% Rubber–sand mixture outperformed the other two materials in terms of yielding lower surface subsidence and higher stress reduction due to active arching.
- The stress on the trapdoor reduced for the rubberised backfills. With the surcharge loading, the stress reduction became independent of the material types. Stress concentration occurred in the stationary section. The mechanical response obtained on the material–structure interface was brittle for the trapdoor section and the stationary section adjacent to the trapdoor, and ductile for the section beyond. The arching effect depends on material type and the mechanical properties of the geomaterial.

- It is recommended that rubber be added to soil as a backfill material, as the rubber–soil mixture yields reduced surface subsidence and arch heights, higher stress reduction, and lower costs, when compared with the soil with no rubber additives. The tyre rubber has been confirmed to be environmentally safe (Edil, 2004), and hence rubber–soil mixtures can be applied to a wide range of applications.
- Ground response curves (GRCs), which represent the arching stress–deformation relationships, were obtained and analysed from the experimental data and idealised for Sand and rubberised sand on the yielding and non-yielding structural parts of the apparatus. Mathematical expressions for the GRCs may also be developed analytically and/or empirically for the study of the arching effect. The inspiration required to do so may arise from well-established constitutive models of different soil types. This is, however, beyond the scope of the present study.

Acknowledgements

The first author acknowledges the financial support provided by the University of Adelaide under the Adelaide International Scholarship (ASI) scheme 2015 and the Australian Research Council. The authors also wish to thank Mr Gary Bowman for his valuable assistance in manufacturing the apparatus and with the laboratory tests. Special thanks also go to Mr Ian Cates, Mr Thomas Stanef and Mr Simon Golding from the Instrumentation Section of the School of Civil, Environmental and Mining Engineering, and Mr Micah Simonsen from Correlated Solutions, USA, for their technical advice and assistance.

References for Chapter 4

Alshibli, K. A., Batiste, S. N., Sture, S. (2003). Strain localisation in sand: Plane strain versus triaxial compression. Journal of Geotechnical and Geoenvironmental Engineering 129 (6), 483–494.

Alshibli, K. A., Hasan, A. (2008). Spatial variation of void ratio and shear band thickness in sand using X-ray computed tomography. Géotechnique 58 (4), 249–257.

Anvari, S. M., Shooshpasha, I., Kutanaei, S. S. (2017). Effect of granulated rubber on shear strength of fine-grained sand. Journal of Rock Mechanics and Geotechnical Engineering 9, 936–944.

Argyroudis, S., Palaiochorinou, A., Mitoulis, S., Pitilakis, D. (2016). Use of rubberised backfills for improving the seismic response of integral abutment bridges. Bulletin of Earthquake Engineering 14, 3573–3590.

ASTM, 2017. Standard practice for use of scrap tyres in civil engineering applications ASTM D6270 – 17, ASTM International, West Conshohocken, PA, USA.

ASTM, 2018. Standard test method for measurement of hydraulic conductivity of materials derived from scrap tyres using a rigid wall permeameter ASTM D7760 – 18, ASTM International, West Conshohocken, PA, USA.

Standards Australia (1998). Australian Standard AS 1289.5.5.1, Soil compaction and density tests– Determination of the minimum and maximum dry density of a cohesionless material-Standard method.

Azéma, E., Linero, S., Estrada, N., Lizcano, A. (2017). Does modifying the particle size distribution of a granular material (i.e., material scalping) alters its shear strength? EPJ Web Conference 140, 6001.

Boominathan, A., Banerjee, S., Dhanya, J. S. (2015). Performance of soil-rubber tyre scrap mixture as seismic base isolators for foundations. 6th International Conference Earthquake and Geotechnical Engineering, 1–4 November 2015.

Bosscher, P. J., Edil, T. B., Kuraoka, S. (1997). Design of highway embankments using tyre chips. Journal of Geotechnical and Geoenvironmental Engineering 123 (4), 295–304.

Brown, E. T., Bray, J. W., Ladanyi, B., Hoek, E. (1983). Ground response curves for rock tunnels. Journal of Geotechnical Engineering 109 (1), 15–39.

Bruck, H. A., McNeill, S. R., Sutton, M. A., Peters, W. H. (1989). Digital image correlation using Newton-Raphson method of partial differential correction. Experimental Mechanics 29 (3), 261–267.

Chen, R. P., Wang, Y. W., Ye, X. W., Bian, X. C., Dong, X. P. (2016). Tensile force of geogrids embedded in pile-supported reinforced embankment: A full-scale experimental study. Geotextiles and Geomembranes 44, 157–169.

Costa, Y. D., Zornberg, J. G., Bueno, B. S., Costa, C. L. (2009). Failure mechanisms in sand over a deep active trapdoor. Journal of Geotechnical and Geoenvironmental Engineering 135 (11), 1741–1753.

Dewoolkar, M. M., Santichaianant, K., Ko, H.-Y. (2007). Centrifuge modelling of granular soil response over active circular trapdoors. Soils and Foundations 47 (5), 931–945.

Edil, T., Bosscher, P. (1994). Engineering properties of tyre chips and soil mixtures. Geotechnical Testing Journal 17 (4), 453–464.

Edil, T. B. (2004). A review of mechanical and chemical properties of shredded tyres and soil mixtures. Recycled Materials in Geotechnics, American Society of Civil Engineers, GSP127, Aydilek A. H., Wartman, J., eds., ASCE Baltimore, 1–21.

Edinçliler, A., Ayhan, V. (2010). Influence of tyre fiber inclusions on shear strength of sand. Geosynthetics International 14 (4), 183–192.

Evans, C.H. (1983). An examination of arching in granular soils. M.Sc. thesis, Department of Civil Engineering, MIT, Cambridge, MA.

Fagundes, D. F., Almeida, M. S. S., Thorel, L., Blanc, M. (2017). Load transfer mechanism and deformation of reinforced piled embankments. Geotextiles and Geomembranes 45, 1–10.

Ghazavi, M. (2004). Shear strength characteristics of sand-mixed with granular rubber. Geotechnical and Geological Engineering 22 (3), 401–416.

Hamidi, A., Azini, E., Masoudi, B. (2012). Impact of gradation on the shear strength-dilation behaviour of well graded sand-gravel mixtures. Scientia Iranica 19 (3), 393–402.

Han, C., Drescher, A. (1993). Shear bands in biaxial tests on dry coarse sand. Soils and Foundations 33 (1), 118–132.

Han, J., Wang, F., Al-Naddaf, M., Xu, C. (2017). Progressive development of two-dimensional soil arching with displacement. ASCE International Journal of Geomechanics 17 (12), 04017112.

Iglesia, G. R., (1991). Trapdoor experiments on the centrifuge: A study of arching in geomaterials and similitude in geotechnical models. PhD thesis, Department of Civil Engineering, Massachusetts Institute of Technology, Cambridge, MA.

Iglesia, G. R., Einstein, H. H., Whitman, R. V. (2013). Investigation of soil arching with centrifuge tests. Journal of Geotechnical and Geoenvironmental Engineering 140 (2), 04013005.

King, D. J., Bouazza, A., Gniel, J. R., Rowe, R. K., Bui, H. H. (2017a). Serviceability design for geosynthetic reinforced column supported embankments. Geotextiles and Geomembranes 45, 261–279.

King, D. J., Bouazza, A., Gniel, J. R., Rowe, R. K., Bui, H. H. (2017b). Load-transfer platform behaviour in embankments supported on semi-rigid columns: Implications of the ground reaction curve. Canadian Geotechnical Journal 54, 1158–1175.

Ladanyi, B., Hoyaux, B. (1969). A study of the trap-door problem in a granular mass. Canadian Geotechnical Journal 6 (1), 1–14.

Lee, J. H., Salgado, R., Bernal, A., Lovell, C. W. (1999). Shredded tyres and rubber-sand as lightweight backfill. Journal of Geotechnical and Geoenvironmental Engineering 125 (2), 132–141.

Lee, S. J., Lee, S. H., Koh, T. H., Shin, M. H., Lee, T. Y. (2011). Geotechnical and environmental characteristics of recycling materials for utilization as a lightweight fill material on Soft ground. Proceedings of the Twenty-first International Offshore and Polar Engineering Conference, by the International Society of Offshore and Polar Engineers (ISOPE), 590–595.

Lewis, R., Khoei, A. R. (2001). Numerical analysis of strain localisation in metal powder-forming processes. International Journal of Numerical Methods in Engineering 52 (5–6), 489–501.

Lok, T. M. H., Yu, H. J. (2006). Laboratory study on the mechanical behaviour of tyre chip-sand mixture. Pavement Mechanics and Performance, Geotechnical Special Publication No. 154, GeoShanghai, 157–164.

Marx, D. H., Jacobsz, S. W. (2018). Optimal placement of reinforcement in piggyback landfill liners. Geotextiles and Geomembranes 46, 327–337.

McNulty, J. W. (1965). An experimental study of arching in sand. PhD thesis. Department of Civil and Environmental Engineering, University of Illinois, USA.

Michalowski, R. L., Park, N. (2004). Admissible stress fields and arching in piles of sand. Géotechnique 54 (8), 529–538.

Moghaddas Tafreshi, S. N., Khalaj, O., Dawson, A. R. (2013). Pilot-scale load tests of a combined multilayered geocell and rubber-reinforced foundation. Geosynthetics International 20, 143–161.

Moghaddas Tafreshi, S. N., Khalaj, O., Dawson, A. R. (2014). Repeated loading of soil containing granulated rubber and multiple geocell layers. Geotextiles and Geomembranes 42, 25–38.

Muir Wood, D. (2002). Some observations of volumetric instabilities in soils. International Journal of Solids and Structures 39, 3429–3449.

Nadukuru, S. S., Michalowski, R. L. (2012). Arching in distribution of active load on retaining walls. Journal of Geotechnical and Geoenvironmental Engineering 138 (5), 575–584.

Ono, K., Yamada, M. (1993). Analysis of the arching action in granular mass. Géotechnique 43 (1), 105–120.

Pan, B., Qian, K., Xie, H., Asundi, A. (2009). Two-dimensional digital image correlation for in-plane displacement and strain measurement: a review. Measurement Science and Technology 20 (6), 62001.

Pan, B., Xie, H., Wang, Z., Qian, K., Wang, Z. (2008). Study on subset size selection in digital image correlation for speckle patterns. Optics Express 16 (10), 7037–7048.

Panah, A. K., Khoshay, A. H. (2015). A new seismic isolation system: Sleeved-pile with soil-rubber mixture. International Journal of Civil Engineering 13 (2), 124–132.

Peters, J., Lade, P., Bro, A. (1988). Shear band formation in triaxial and plane strain tests. Advanced triaxial testing of soil and rock, ASTM, STP 977, Donaghe, R., Chaney, R., Silver, M., eds., ASTM, 604–627.

Pham, M.-T., Briançon, L., Dias, D., Abdelouhab, A. (2018). Investigation of load transfer mechanisms in granular platforms reinforced by geosynthetics above cavities. Geotextiles and Geomembranes 46, 611–624.

Rao, G. V., Dutta, R. K. (2006). Compressibility and strength behaviour of sand-tyre chip mixtures. Geotechnical and Geological Engineering 24 (3), 711–724.

Reddy, S. B., Krishna, A. M. (2015). Recycled tyre chips mixed with sand as lightweight backfill material in retaining wall applications: An experimental investigation. International Journal of Geosynthetics and Ground Engineering 1, 31.

Rui, R., Van Tol, A. F., Xia, Y. Y., van Eekelen, S. J. M., Hu, G. (2016). Investigation of soil-arching development in dense sand by 2D model tests. Geotechnical Testing Journal 39 (3), 415–430.

Sadrekarimi, J., Abbasnejad, A. (2010). Arching effect in fine sand due to base yielding. Canadian Geotechnical Journal 47, 366–374.

Schreier, H. W., Sutton, M. A. (2002). Systematic errors in digital image correlation due to undermatched subset shape functions. Experimental Mechanics 42 (3), 303–310.

Soganci, A. S. (2015). Strength characteristics of tyre-sand mixtures. Soil Mechanics and Foundation Engineering 51 (6), 306–309.

Tanaka, T., Sakai, T. (1993). Progressive failure and scale effect of trap-door problems with granular materials. Soils and Foundations 33 (1), 11–22.

Tatlisoz, N. Benson, C. H. and Edil, T. B. (1997). Effect of fines on mechanical properties of soil-tyre chip mixtures. Testing Soil with Waste or Recycled Materials, Wasemiller, M. A., Hoddinott, K. B. (eds.), ASTM STP 1275, West Conshohocken, 93–108.

Tavakoli Mehrjardi, G., Moghaddas Tafreshi, S. N., Dawson, A. R. (2015). Numerical analysis on buried pipes protected by combination of geocell reinforcement and rubber-soil mixture. International Journal of Civil Engineering 13, 90–104.

Tavakoli Mehrjardi, G., Moghaddas Tafreshi, S. N., Dawson, A. R. (2012). Combined use of geocell reinforcement and rubber-soil mixtures to improve performance of buried pipes. Geotextiles and Geomembranes 34, 116–130.

Terzaghi, K. (1936). Stress distribution in dry and in saturated sand above a yielding trap-door. Proceedings of the International Conference on Soil Mechanics and Foundation Engineering, Vol. I, 307–311.

Terzaghi, K. (1943). Arching in ideal soils. In: Theoretical soil mechanics, chapter V. John Wiley and Sons, New York.

Tsang, H. H., Lam, J. Y. K., Yaghmaei-Sabegh, S., Lo, S. H. (2009a). Protecting underground tunnel by rubber-soil mixtures, Proceedings of the 7th International Conference on Lifeline Earthquake Engineering, ASCE-TCLEE, Oakland, California, U.S., June 28 – July 1, 2009.

Tsang, H. H., Lam, J. Y. K., Yaghmaei-Sabegh, S., Sheikh, M. N., Ziong, W., Shang, S. (2009b). Protecting low-to-medium-rise buildings by scrap tyre-soil mixtures,

Australian Earthquake Engineering Society Conference, Newcastle, Australia: AEES. 1–8.

van Eekelen, S. J. M., Bezuijen, A., Lodder, H. J., van Tol, A. F. (2012a). Model experiments on piled embankments. Part I. Geotextiles and Geomembranes 32, 69–81.

van Eekelen, S. J. M., Bezuijen, A., Lodder, H. J., van Tol, A. F., (2012b). Model experiments on piled embankments. Part I. Geotextiles and Geomembranes 32, 82–94.

Vinot, V., Singh, B. (2013). Shredded tyre-sand as fill material for embankment applications. Journal of Environmental Research and Development 7 (4A), 1622–1627.

Yoon, S., Prezzi, M., Siddiki, N. Z., Kim, B. (2006). Construction of a test embankment using a sand-tyre shred mixture as fill material. Waste Management 26 (9), 1033–1044.

Zeller, J., Wullimann, R. (1957). The shear strength of the shell materials for the Go-Schenenalp Dam, Switzerland. Proceedings of 4th International Conference on Soil Mechanics and Foundation Engineering (Vol. 2, pp. 399–404). London.

Zhang, T., Cai, G., Duan, W. (2018). Strength and microstructure characteristics of the recycled rubber tyre-sand mixtures as lightweight backfill. Environmental Science and Pollution Research 25, 3872–3883.

Zornberg, J. G., Cabral, A. R., Viratjandr, C. (2004). Behaviour of tyre shred-sand mixtures. Canadian Geotechnical Journal 41, 227–241.

Statement of Authorship

Title of Paper	Passive arching in rubberised sand backfills
Publication Status	☐ Published ☐ Accepted for Publication ☑ Submitted for Publication ☐ Unpublished and Unsubmitted w ork w ritten in manuscript style
Publication Details	

Principal Author

Name of Principal Author (Candidate)	Hamidreza Khatami		
Contribution to the Paper	Performed the literature review, conducted the experiments, gathered the data, analysed and interpreted the results, and drafted the manuscript.		
Overall percentage (%)	80%		
Certification:	This paper reports on original research I conducted during the period of my Higher Degree by Research candidature and is not subject to any obligations or contractual agreements with a third party that would constrain its inclusion in this thesis. I am the primary author of this paper.		
Signature		Date	19/09/18

Co-Author Contributions

By signing the Statement of Authorship, each author certifies that:

i. the candidate's stated contribution to the publication is accurate (as detailed above);
ii. permission is granted for the candidate in include the publication in the thesis; and
iii. the sum of all co-author contributions is equal to 100% less the candidate's stated contribution.

Name of Co-Author	An Deng		
Contribution to the Paper	Methodology and reviewing.		
Signature		Date	19/09/18

Name of Co-Author	Mark Jaksa		
Contribution to the Paper	Methodology and reviewing.		
Signature		Date	19/09/18

Please cut and paste additional co-author panels here as required.

Chapter 5: Passive arching in rubberised sand backfills

Abstract

The deformation and stress profiles of passive arching in a coarse sand and two rubberised sand backfills were investigated using a trapdoor apparatus. The trapdoor apparatus was instrumented with high-speed imaging equipment and a series of pressure sensors. The images of the deformation process in the backfills were analysed using the digital image correlation technique. The effect of a local surcharge on the deformation and stress profiles was also examined. It was observed that the rubber inclusions helped reduce the deformation of the backfills. Passive arching moduli and stress variations between the backfills examined are compared.

Keywords: Rubber–sand, arching effect, digital image correlation, deformation, trapdoor apparatus, dilation angle.

5.1. Introduction

It is estimated that approximately 48 million waste tyres are dumped annually in Australia (Tyrecycle, 2018). The large amount of waste tyres, and the increasingly stringent requirements of environmental protection legislation demand effective and sustainable management solutions. For example, the Environment Protection Authority (EPA) of South Australia no longer allows waste whole tyres to be disposed to landfill. Worldwide, the current principal waste tyre handling schemes include re-treading, energy recovery, civil engineering applications, and other miscellaneous applications, such as rubberised asphalt, agricultural fertilizers, art and crafts, furniture, and playgrounds. Civil engineering applications make a significant contribution to the sustainable use of waste tyres. In 2011, it was estimated that approximately 8% of recycled waste tyres were utilised in civil engineering applications (Rubber Manufacturers Association, 2013). Rubber-based geomaterials are one such example of a civil engineering application using recycled waste tyres and they are classified into two forms: shredded tyres as a substitute for natural aggregate, referred to as Tyre–Derived Aggregate (TDA); and recycled tyres mixed with natural sand, which are referred to as rubber–sand. Humphrey (1999) and Edil (2004) outlined the engineering characteristics of recycled tyres that can be exploited by civil and geotechnical engineers. These properties include light weight, thermal insulation, high permeability, low horizontal pressures, good damping properties, and low chemical leachate. The mechanical properties of these geomaterials for different applications, such as road construction and retaining walls, have been assessed by many researchers (e.g. Eldin and Senouchi, 1992; Humphrey and Sandford, 1993; Bosscher et al., 1997; Tweedie et al., 1998; Lee at al., 1999; Edinçliler et al., 2004; Shalaby and Khan, 2005; Yoon et al., 2006; Lee and Roh, 2007; Ahn and Cheng, 2014). Negligible impact on groundwater quality using waste

rubber has also been reported by Eldin and Senouchi (1992) and Humphrey and Blumenthal (2010).

While extensive data on the mechanical properties of rubber–sand mixtures are available in the literature, it seems that little is known about the arching behaviour of rubberised backfills. Arching influences the stress regime in a granular geomaterial, both in the vertical and horizontal directions due to induced differential displacements. Active arching occurs when the stresses decrease on the yielding part of the material assembly as a result of the mobilisation of shear resistance on the opposite direction to the induced displacement. Active arching has been examined in a number of studies (e.g. Terzaghi, 1936; Dewoolkar et al. 2007; Costa et al., 2009; Chevalier et al., 2012; Iglesia et al., 2013; van Eekelen, 2015). On the other hand, inclusion of structural elements, such as a fixed, single piles into a geomaterial, followed by movement of the surrounding geomaterial later in time, as a result of creep for example, results in a passive arching effect or increased loads on the structural element. This may in turn lead to serviceability issues or even structural failure. In addition, assessment of deformability of a geomaterial associated with a structure become more important than analysing the stresses because serviceability or failure of the structure, due to excessive settlement or deformation, may precede the failure of the geomaterial. Therefore, it is necessary to measure or predict the arching deformations and account for them in design. Other examples of passive arching include pile groups, where a pile may experience both active and passive arching on different sides (Shelke and Patra, 2008; Yuan, et al., 2014), anti-sliding or stabilisation piles inserted into soil slopes (Chen and Martin, 2002; Kahyaoğlu et al., 2012; He et al., 2015), swelling of soil around an underground structure (Aqoub et al., 2018), or even soil pressure sensors where over-registration of stress values indicate passive arching on the sensor (Talesnick, 2013).

Studies on passive arching, however, lag behind, perhaps because the active arching case is considered to be more common in practice. This current study therefore aims to address the deformation and stress response of a sand and two rubberised sand backfills subjected to passive arching. The effect of geomaterial type and local surcharge on deformation fields and stress response on the structure-geomaterial interface was studied. Shear band formation was a particular focus. The digital image correlation (DIC) technique was used to map the distribution of displacements and strains. A series of benchmark tests on the sand and rubberised sand backfills was performed using a replicate of Terzaghi's trapdoor apparatus (Terzaghi, 1936). During the arching process, the stresses were recorded using a number of stress cells and the deformations were measured using the DIC technique.

5.2. Materials and methods

Silica sand and rubber particles, both sourced from local suppliers, were used as the backfill. The rubber particles were produced from shredded recycled tyres with steel belts removed. Approximately 95% of the sand particles were in the range of 1.18–2.36 mm; and the rubber particles were between 5–13 mm in size. The other properties of Sand and Rubber–sand mixtures are provided in Table 5.1. The rubber–sand mixtures represent 10% or 30% rubber by weight calculated as follows:

$$Rubber\ content\ (\%) = \frac{mass\ of\ rubber}{mass\ of\ sand + mass\ of\ rubber} \times 100\% \quad (5.1)$$

The minimum and maximum dry density of the material samples were determined using the procedure described by the Australian Standard 1289.5.5.1 (Standards Australia, 1998a). The values of the effective angle of internal friction (φ') were determined using direct shear tests specified by AS 1289.6.2.2 (Standards Australia, 1998b). To accommodate for larger sizes, the portion of rubber particles greater than one fifth of the smallest dimension

of the shear box, which measured 60 mm × 60 mm × 38 mm, was sieved out, as proposed by Head and Epps (2010). However, the rubber percentage was maintained at the levels of 10% and 30%. The effective friction angle data from the direct shear tests, rounded to the nearest 0.5°, are also presented in Table 5.1.

Table 5.1. Physical properties of the backfill materials

Material	Density range (kg/m^3)	Backfill density	Size range of 95% of particles (mm)	Median size D_{50} (mm)	φ'
Sand	1,486–1,709	1,657	1.18–2.36	1.75	45°
10% Rubber–sand	1,367–1,574	1,515	1.18–9.5	1.81	44.5°
30% Rubber–sand	1,270–1,433	1,387	1.18–11.5	2.02	51°

As shown in Table 5.1, with the addition of rubber to Sand, the density decreased considerably, as expected. In relation to the friction angle, rubber at low percentages (e.g. 10%) had a very modest effect on the shear strength. However, increasing the rubber content to 30% resulted in a significant rise of 6° in the effective friction angle. Therefore, rubberised backfills possess the advantage of reduced weight and improved shear strength, when compared to the original base aggregate.

The DIC technique requires a random speckle pattern on the specimen surface. Therefore, prior to backfill preparation, a speckle pattern was artificially imparted to the sand particles by dying approximately 30% by weight of the particles with a matte black colour. Matte paints minimise the effect of spectral light reflection which would otherwise introduce inaccuracies in the image correlation results. A number of Sand and rubberised sand backfills were prepared in a trapdoor apparatus using the air pluviation technique. The

geomaterials were poured in equal batches from appropriate heights and modestly compacted using a hand tamper to a relative density of 76.5% ± 2.5%; hence to a medium-dense consistency. The density of the backfills tested in the trapdoor apparatus are listed in Table 5.1. Efforts were made to place the materials evenly, aiming to eliminate segregation and minimise heterogeneity in the Rubber–sand backfills.

The trapdoor apparatus was a cuboid container with dimensions of 1 m × 1 m × 0.2 m, as shown in Fig. 5.1. The front face of the trapdoor was fabricated using a transparent acrylic sheet, thus enabling imaging. The trapdoor and the static sides were constructed from rigid timber. The trapdoor element was 160 mm wide and, in order to create passive arching of the backfill, was designed, with the aid of a hydraulic jack, to translate upwards at a speed of 3.2 mm/s, to maximum displacement of 20 mm. The displacement of the trapdoor was measured by a linear variable displacement transducer (LVDT) with a sampling rate of 16 Hz installed underneath. The backfills were poured to a total depth of 250 mm, thus replicating a shallow arching condition, where the ratio of backfill depth to trapdoor width is less than 2 (Costa et al., 2009). A concrete block, 160 mm × 200 mm × 230 mm in size, was placed centrally on the backfill surface to apply a 5 kPa surcharge.

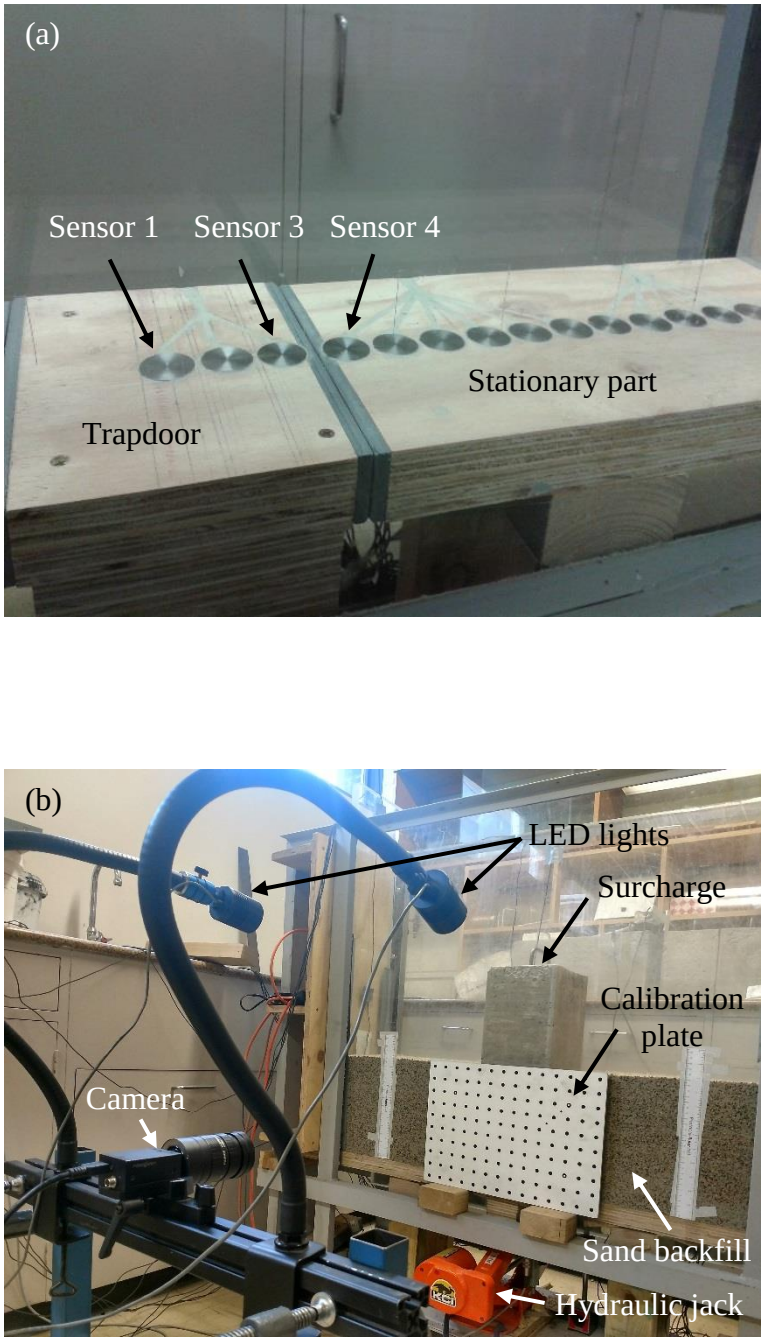

Fig. 5.1. The instrumented trapdoor apparatus: (a) stress sensor array, (b) imaging equipment

The trapdoor apparatus was instrumented with a series of pressure sensors. The sensors, 28 mm in diameter, were secured into rebates fabricated into the base board, and flush with the board surface. This arrangement minimised material deformation errors associated with the measurement process. As the trapdoor apparatus represents

axisymmetric, plane-strain conditions, the pressure sensors were placed on only one side of the apparatus. The trapdoor element had three sensors installed at centre (Sensor 1), intermediate (Sensor 2) and edge (Sensor 3) locations. The centre-to-centre distance of the sensors, or sensing interval, was 30 mm. The numbering of the sensors continued from the edge of the stationary part, from Sensor 4 to Sensor 15 which was placed 420 mm away from the edge. The sensors were calibrated using a Fluke-100g electric pressure calibrator. A data acquisition system and an associated computer program were used to record the sensor readings with a sampling rate of 16 Hz. This sampling rate was equal to that of the trapdoor LVDT and, given the displacement rate of the hydraulic jack, ensured that the pressure sensors recorded the stress data at intervals of 0.2 mm of the trapdoor displacement. The LVDT and the pressure sensor recordings were synchronised within the data acquisition system.

After preparing the backfills in the trapdoor apparatus, according to the procedure outlined earlier, recording sessions were conducted to capture images of each backfill surface as the deformation progressed. The system, which included the photographic equipment shown in Fig. 5.1(b), VicSnap software for imaging, and the VIC-2D program for image correlation analysis were supplied by Correlated Solutions, USA. A machine vision camera with conventional charge-coupled device (CCD) technology, equipped with a low distortion 75 mm Fujinon lens and aperture size range of 1/22–1/2.8, was used for imaging. An area of interest (AOI) was defined where most of the significant deformations were expected to take place. The AOI measured 500 (W) × 250 (D) mm. The image recording sessions were completed with a capture rate of 160 frames per second and a resolution of 960 × 600 pixels, using the VicSnap program. To convert the pixel scale information in the images to the more suitable physical unit of mm, scale calibration was carried out using the dot grid calibration target shown in Fig. 5.1(b). After calibration, a pixel to millimetre ratio

of 0.52 was obtained. The images were then analysed to measure deformation using the VIC-2D program, which computes displacements and strains from an image correlation algorithm. The image correlation procedure in the DIC technique involves taking a reference image of each specimen in an undeformed state at the beginning of the tests. The AOI regions in the reference images are then discretised into a grid of squared blocks, known as subsets. The speckle pattern applied in the sample preparation phase helps to identify and distinguish each subset, provided that the speckle pattern in each subset is unique. The new location of each subset in the subsequently captured images of the deforming specimen is tracked in terms of the greyscale intensity values of each of the subset pixels. The displacement of the subsets, and thus the displacements and strains that take place in the AOI, are then calculated, while the image correlation criterion is satisfied. The detailed mathematics of the DIC technique is well documented in the literature (e.g. Pan et al., 2008; Schreier et al., 2009) and is not discussed further here in the interests of brevity. In the present study, a subset size of 21 × 21 pixels (equivalent to an area of approximately 11 mm × 11 mm) was used. This size rendered the AOI into a grid of distinguishable subsets while minimising noise in the output data or an unnecessary increase in computational time. It is noteworthy that the use of a desktop computer with a high capacity, dedicated graphics card is essential for fast image processing. A high-speed CPU, on the other hand, will be of limited value compared to a professional graphics card. The computer unit used in this study was equipped with a dedicated graphics card of 16 GB memory. As a result, the image processing speed was about 25 minutes per 1,000 images.

5.3. Results and discussion

The passive arching tests were conducted with and without the applied surcharge. In addition to the rubber–sand mixtures, sand specimens were tested as a control. The test results included the distributions of displacements, strains and stresses obtained across the AOI of each specimen.

5.3.1. Horizontal displacements and horizontal strains

The horizontal displacements (u) of the Sand and rubberised sand backfills induced by the upward movement of the trapdoor, with no surcharge and with the 5 kPa central surcharge, are shown in Figs. 5.2 and 5.3 respectively. When no surcharge was applied (Fig. 5.2), the vertical translation of the trapdoor caused the particles at the surface and at shallow depths to displace horizontally from their original position towards the sides of the stationary parts. The peak values of the horizontal displacements created two semicircles immediately below the surface, as shown in Fig. 5.2. The averaged peak values from the left and right sides of the graphs were reduced from 0.65 mm in the Sand to 0.58 mm, and 0.42 mm in the 10% and 30% Rubber backfills, respectively. This difference will naturally increase as the model is up-scaled in line with actual backfilled systems. This means that the rubber inclusions help reduce horizontal swell where passive arching occurs. The rubber inclusions, however, also broadened the zones of swell. The distribution of horizontal swell changed in location, shape and depth, when the surcharge was applied, as shown in Fig. 5.3. The zones of peak swell relocated outward slightly, avoiding contact with the surcharge, but increased in size when compared with the corresponding results obtained without the surcharge. The zones of peak swell extended with the increase of rubber content. Compared with the results in Fig. 5.2, the maximum horizontal displacements increased to 0.90 mm in the Sand backfill, while

remaining unchanged in the rubberised backfills. Similar to the no surcharge case, the zones of peak swell extended when the rubber content increased.

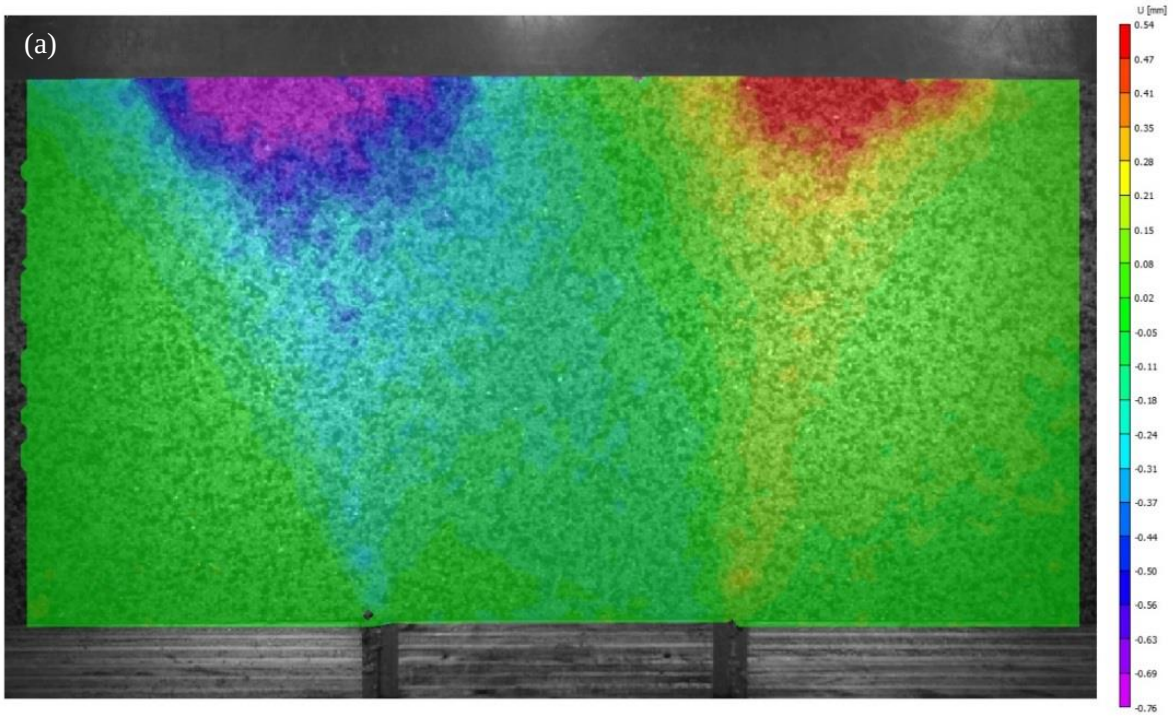

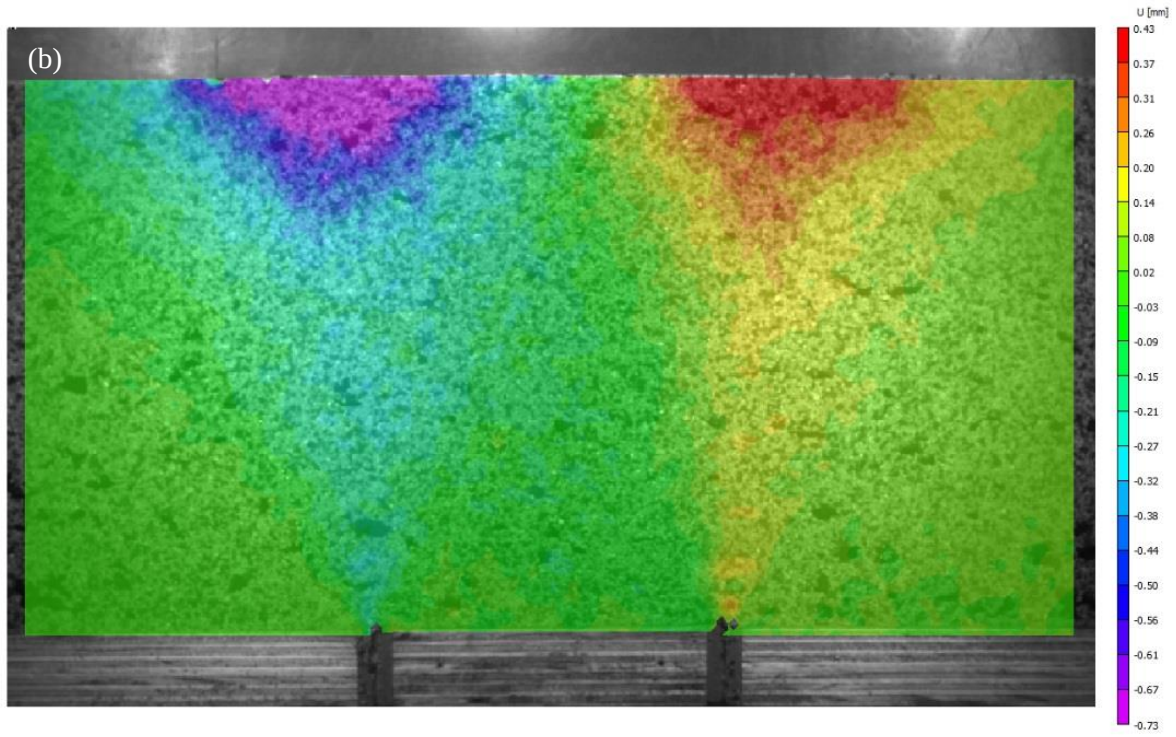

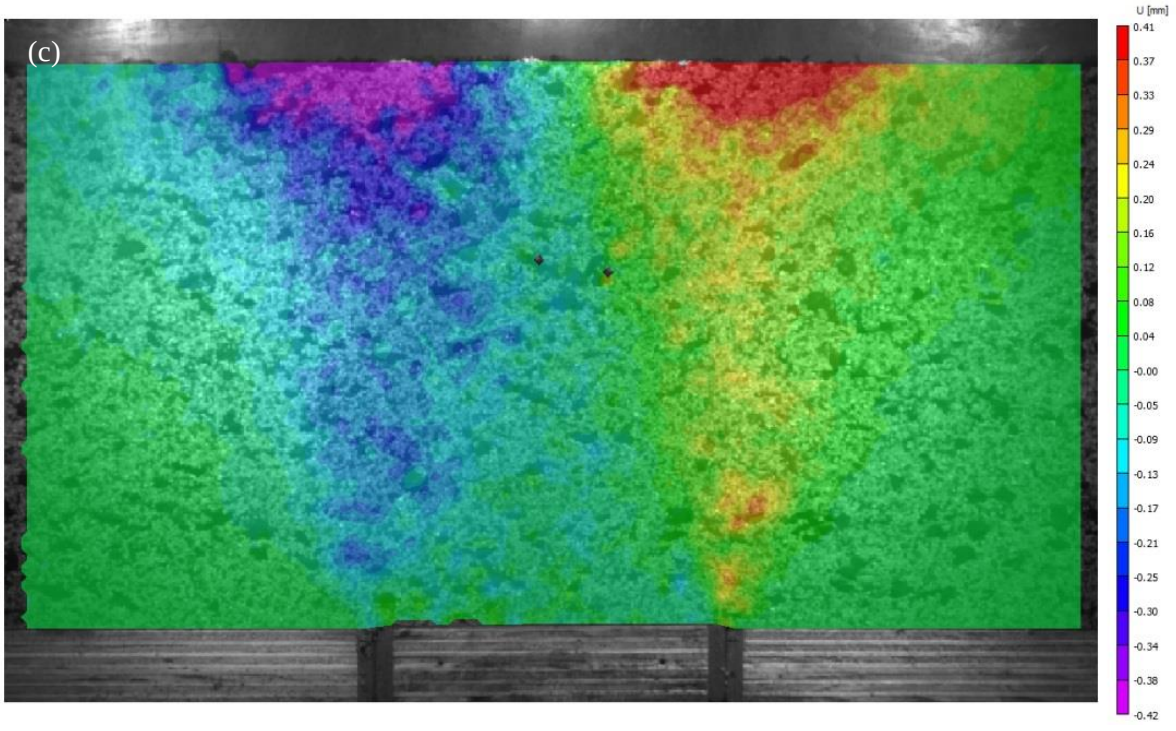

Fig. 5.2. Distribution of horizontal displacements under no-surcharge conditions for the three materials: (a) Sand, (b) 10% Rubber–sand, and (c) 30% Rubber–sand

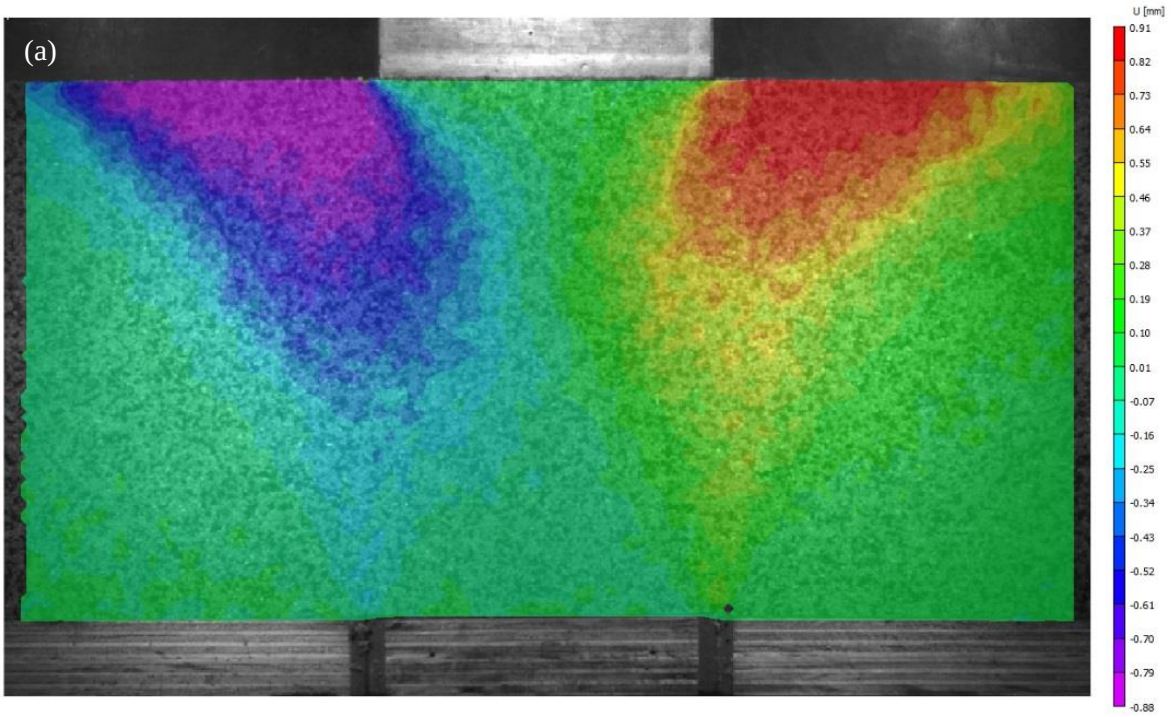
(a)
U [mm]
0.91
0.82
0.73
0.64
0.55
0.46
0.37
0.28
0.19
0.10
0.01
-0.07
-0.16
-0.25
-0.34
-0.43
-0.52
-0.61
-0.70
-0.79
-0.88

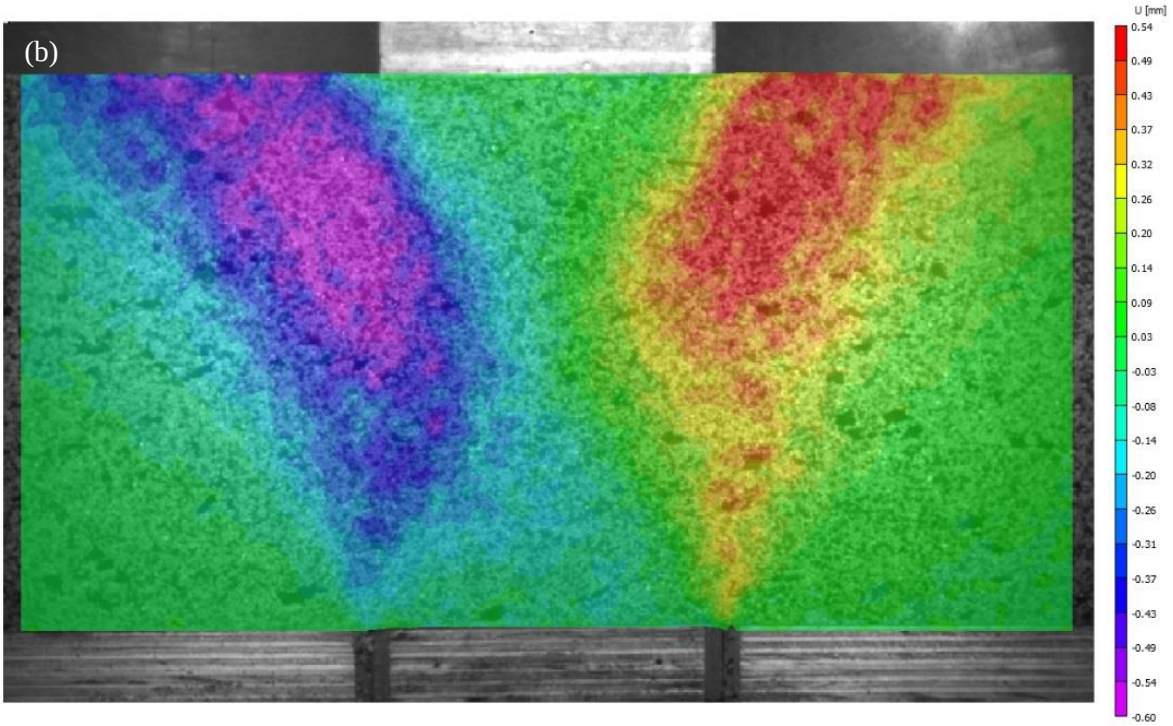
(b)
U [mm]
0.54
0.49
0.43
0.37
0.32
0.26
0.20
0.14
0.09
0.03
-0.03
-0.08
-0.14
-0.20
-0.26
-0.31
-0.37
-0.43
-0.49
-0.54
-0.60

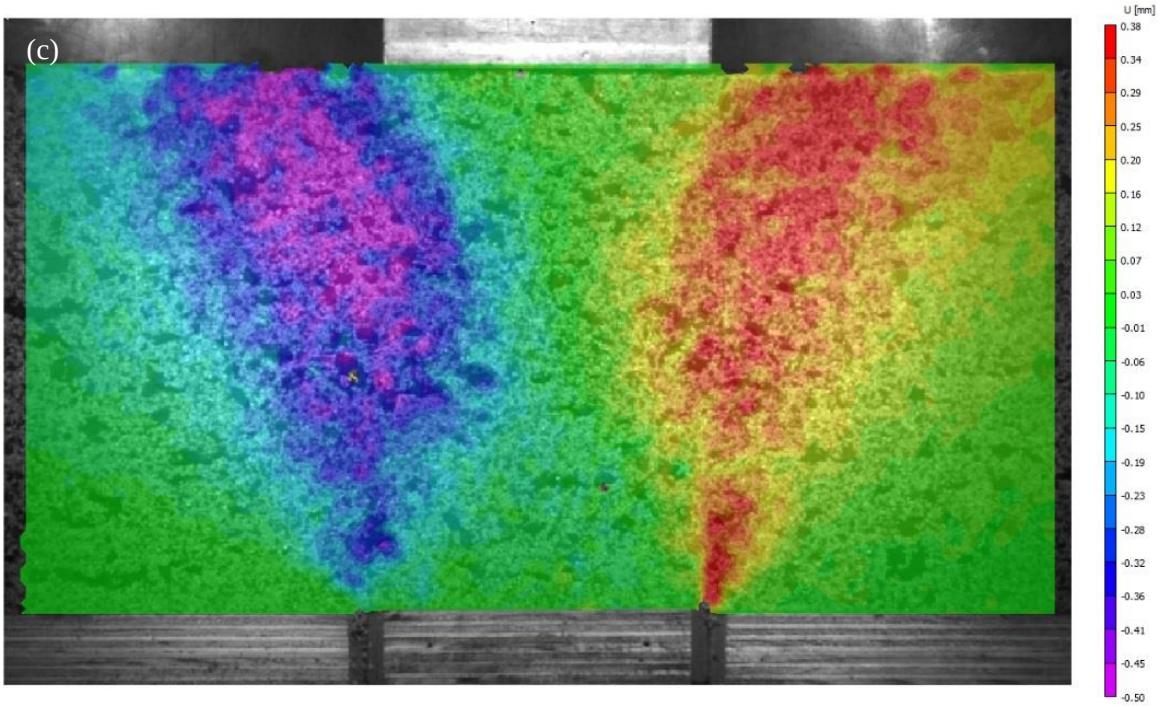

Fig. 5.3. Distribution of horizontal displacements with the application of the 5 kPa surcharge for the three materials: (a) Sand, (b) 10% Rubber–sand, and (c) 30% Rubber–sand

The distributions of horizontal strains (ε_{xx}) in the backfills subjected to no surcharge and with the application of the 5 kPa surcharge are presented in Figs. 5.4 and 5.5 respectively. As can be observed, under all testing conditions, tensile strains governed the central areas. The tensile areas were sandwiched by areas of compressive strains, which include the peripheral wedge areas enveloping the tensile regions. The wedge areas initiated from the edges of the stationary parts and expanded progressively and outwardly towards the surface. Immediately above the trapdoor is a zone of null horizontal strains, forming a trapezoidal shape. The height of the trapezoid decreased as the rubber content increased, or the surcharge was applied. In each backfill, the extent of the horizontal strains was greater under the surcharge condition than with no application of surcharge, where the materials remained the same. Figs. 5.4 and 5.5 also indicate that the AOIs increased with rubber

content and the application of the surcharge. The AOI became greatest in the case of the 30% Rubber–sand under surcharge loading [Fig. 5.5(c)], where almost the entire AOI exhibits strain.

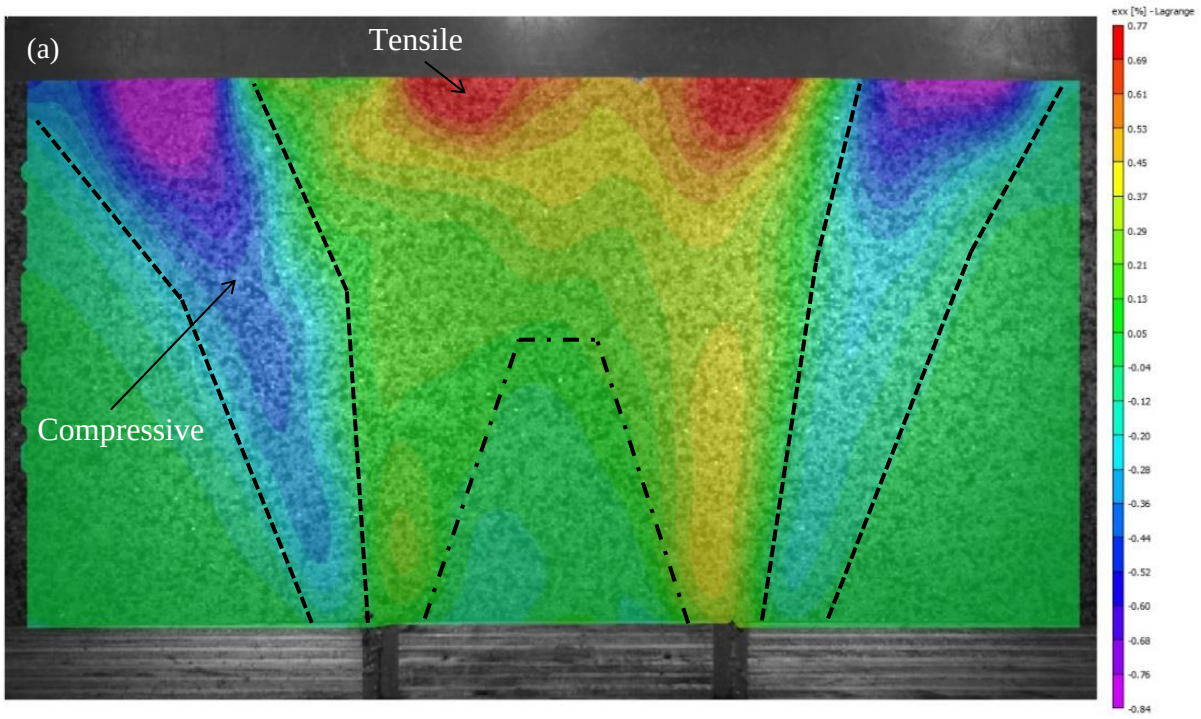

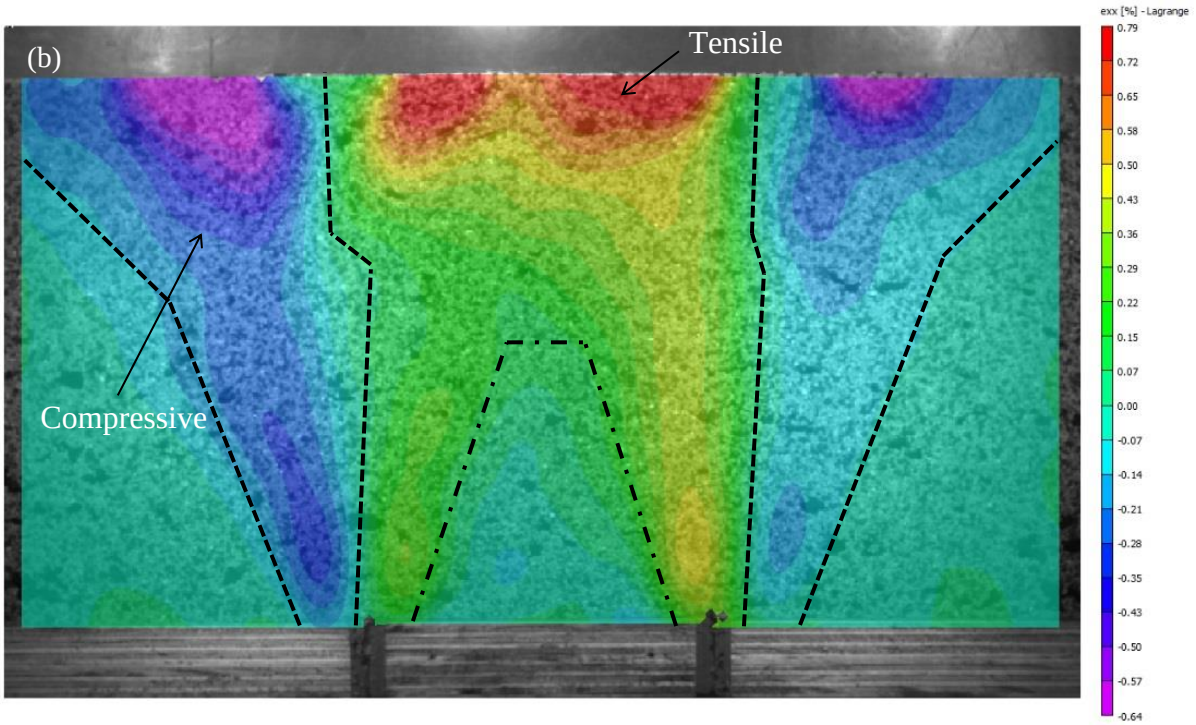

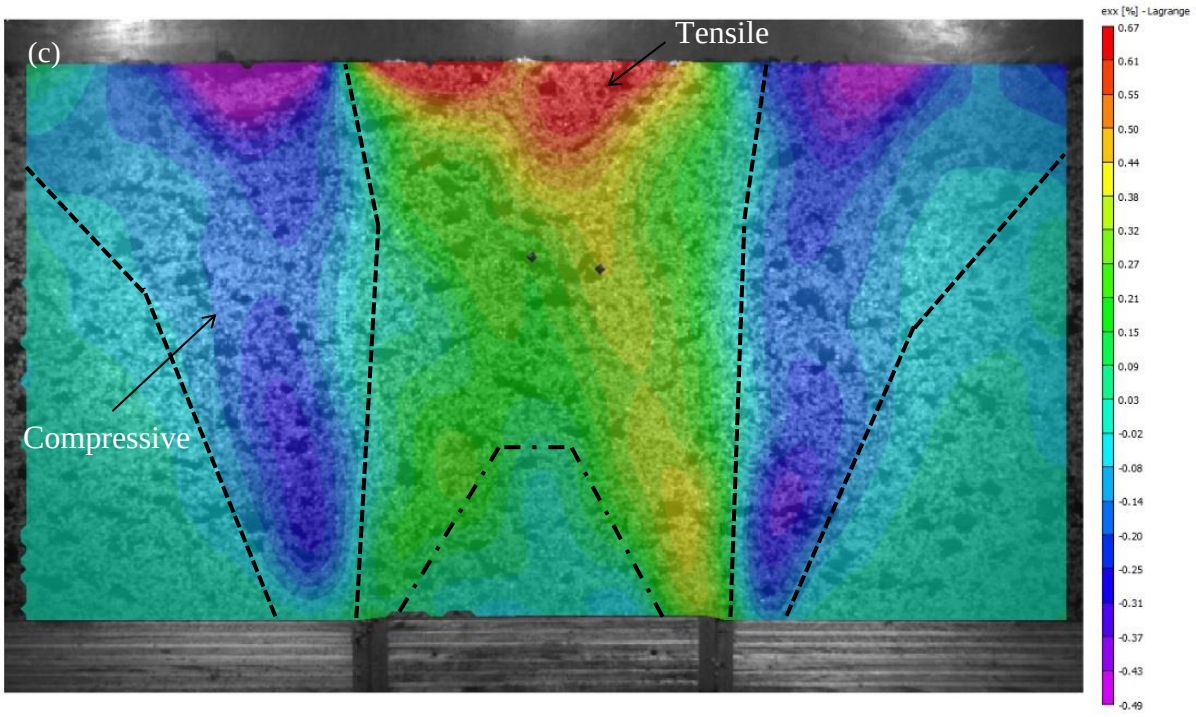

Fig. 5.4. Horizontal strain distributions under no surcharge conditions for the three materials:

(a) Sand, (b) 10% Rubber–sand, and (c) 30% Rubber–sand

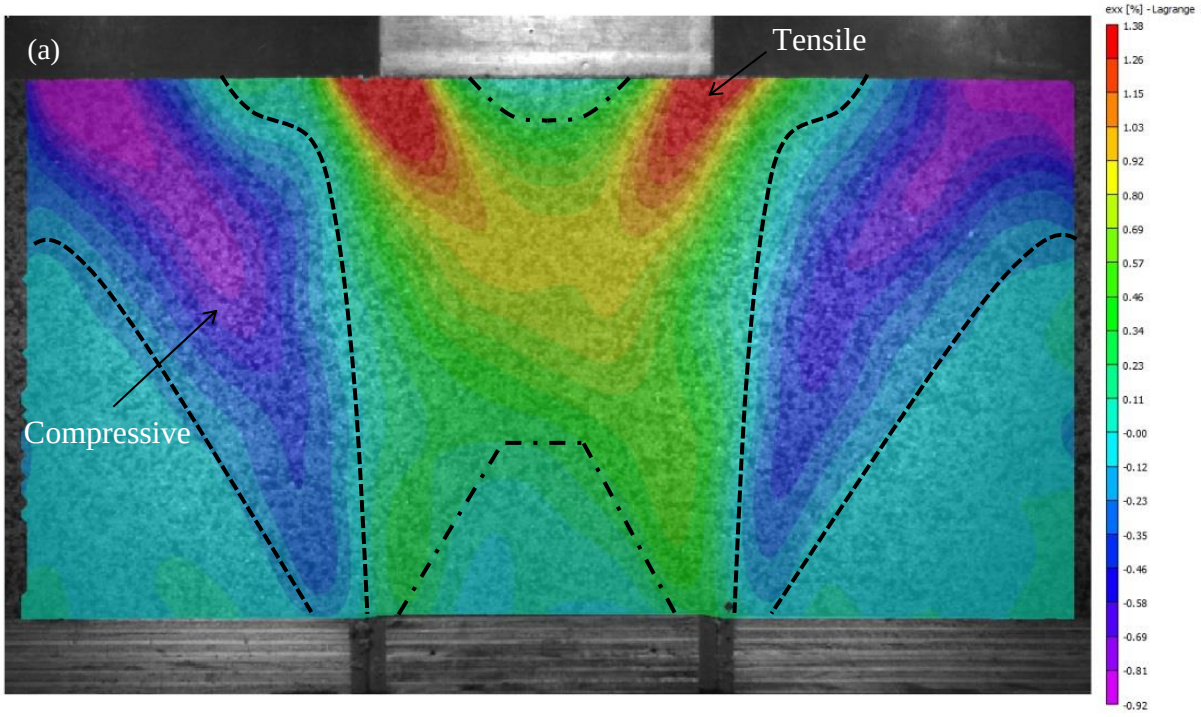

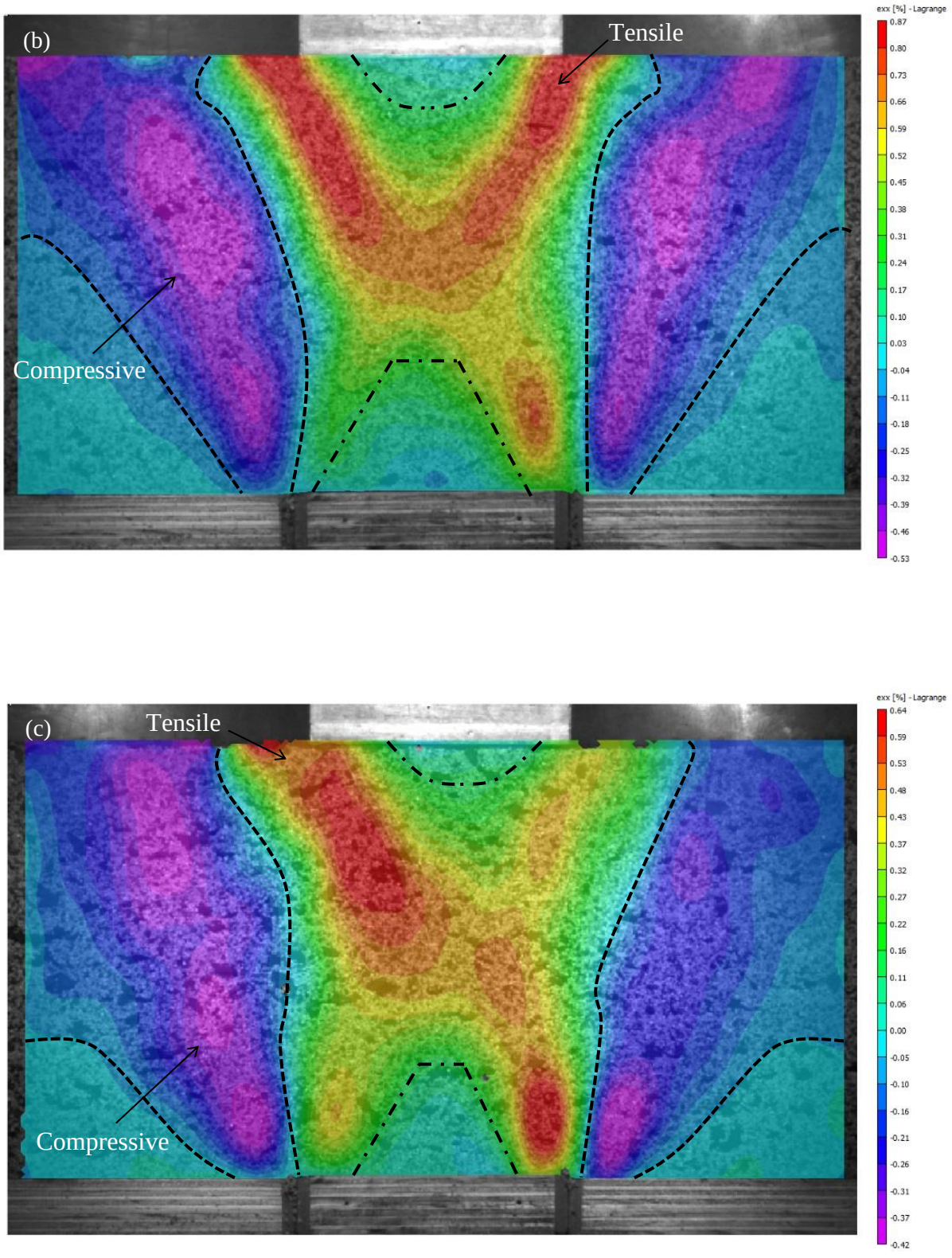

Fig. 5.5. Horizontal strain distributions with the application of surcharge for the three materials: (a) Sand, (b) 10% Rubber–sand, and (c) 30% Rubber–sand

The maximum tensile and compressive horizontal strains decreased with increased rubber content, whereas the other characteristics remained unchanged. For example, under the no surcharge condition, the maximum compressive horizontal strains reduced from a maximum of 0.84% in the Sand backfill to 0.64% for the 10% Rubber–sand backfill and 0.49% for the 30% Rubber–sand backfill. For the Sand backfill, the use of the surcharge increased from 0.84% to 0.92%, for the peak compressive horizontal strain, and from 0.77% to 1.38% for the peak horizontal tensile strain. However, the opposite occurred to the rubberised backfills. The use of the surcharge reduced the horizontal strains on average by 0.13% for the 10% Rubber–sand backfill and by 0.05% for 30% Rubber–sand backfill. The measurements presented in Figs. 5.2–5.5 show that the backfill deformation extends laterally to greater areas with the rubber inclusions and the use of surcharge. However, the peak tensile and compressive horizontal displacements and strains were reduced by the rubber inclusions.

5.3.2. Vertical displacements and vertical strains

The distribution of vertical displacements (v) mapped for Sand and Rubberised–sand under no surcharge and the application of surcharge are presented in Figs. 5.6 and 5.7 respectively. When the trapdoor rose, the layers were divided into three zones depending on the level of displacement. The first zone (Zone 1), identified in red in Figs. 5.6 and 5.7, comprised an assembly of particles that shifted upwards together with the trapdoor. As the displacement remains the same as that of the trapdoor, this zone is termed the ‘arch of equal displacement.’ The second zone (Zone 2), highlighted in purple, comprised of two rigid bodies, above the stationary parts of the apparatus, where the vertical displacements were negligible. Finally,

the third zone (Zone 3), intermediate between the two sets of rigid bodies having negligible and the greatest displacements, was created by the relative displacements of these rigid bodies with respect to each other. This is a zone of transition, implying that the displacements ranged from effectively zero to a value close to the displacement of the trapdoor. Application of the central surcharge notably affected the distribution of vertical displacements. In the rubberised backfills, in particular, an inverted arch-shaped region appeared beneath the surcharge block. The values of vertical displacements in this region were in the range of 0.6–0.7 mm, in the low rubber content backfill, and reduced to 0.2–0.3 mm in the high rubber content backfill.

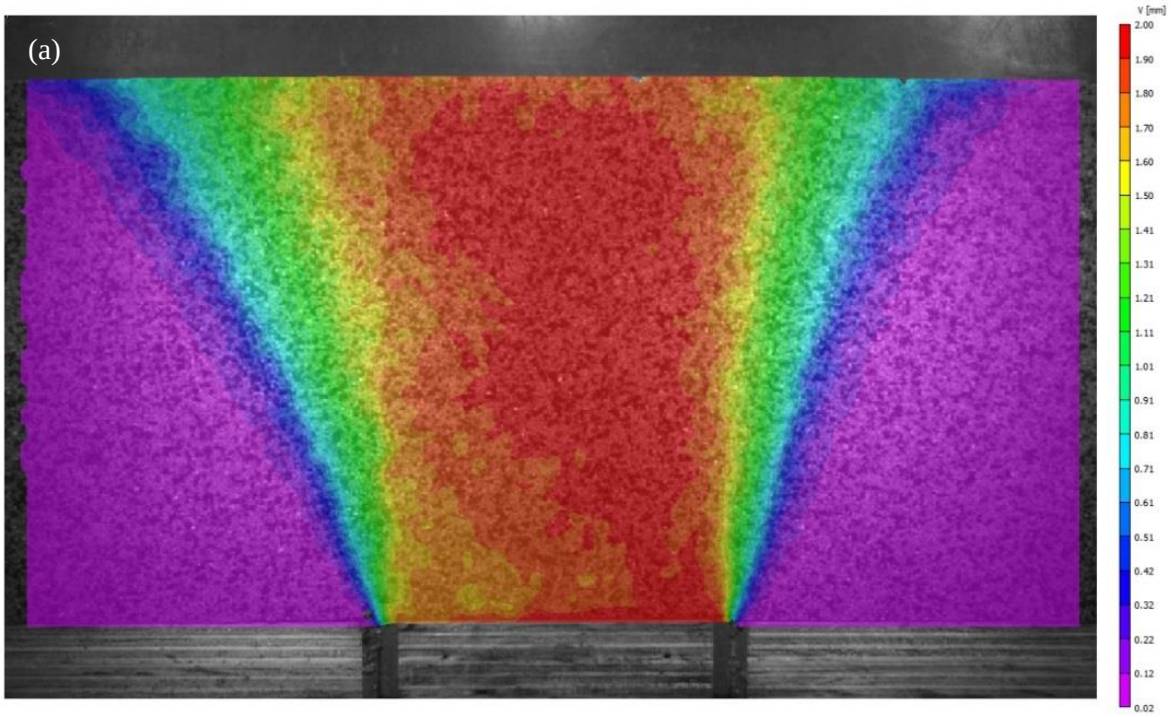

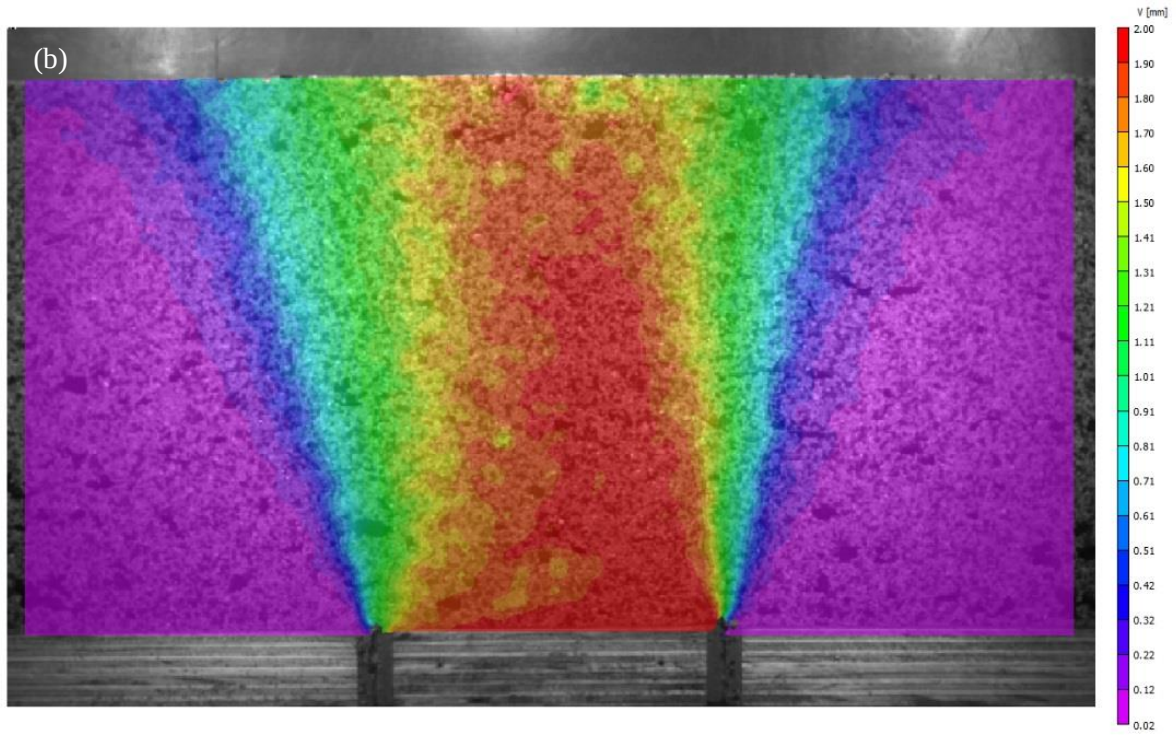

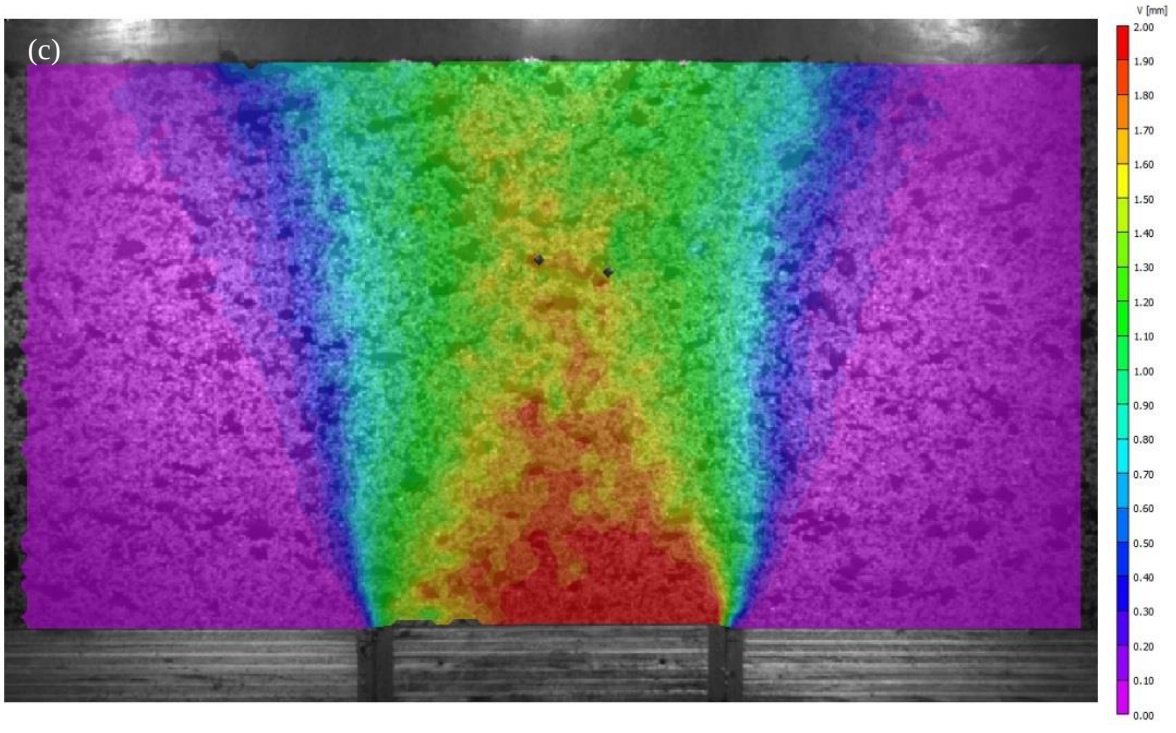

Fig. 5.6. Distributions of vertical displacements under no surcharge conditions for the three materials: (a) Sand, (b) 10% Rubber–sand, and (c) 30% Rubber–sand

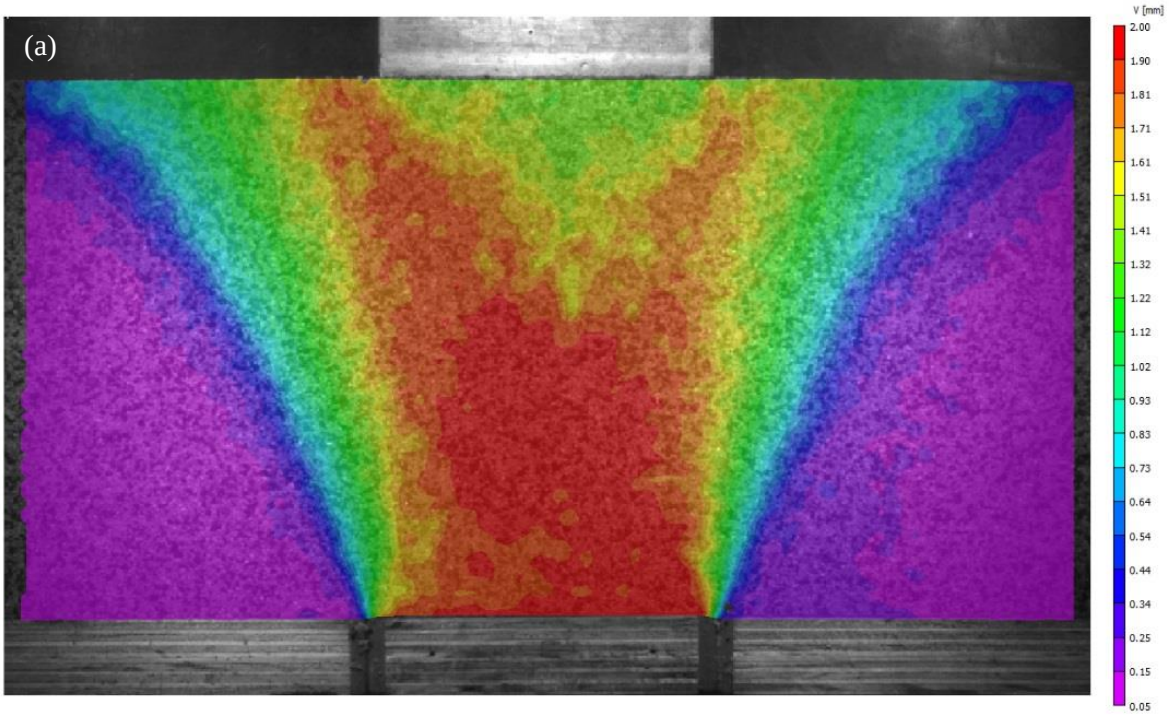
(a)
V [mm]
2.00
1.90
1.81
1.71
1.61
1.51
1.41
1.32
1.22
1.12
1.02
0.93
0.83
0.73
0.64
0.54
0.44
0.34
0.25
0.15
0.05

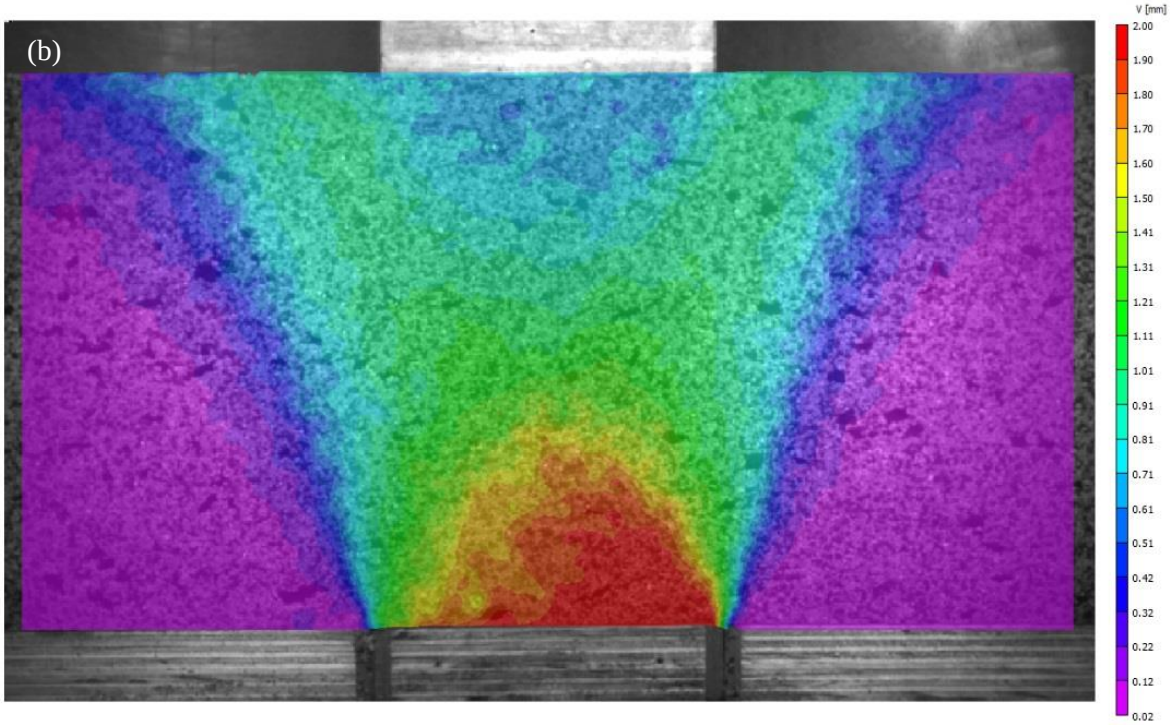
(b)
V [mm]
2.00
1.90
1.80
1.70
1.60
1.50
1.41
1.31
1.21
1.11
1.01
0.91
0.81
0.71
0.61
0.51
0.42
0.32
0.22
0.12
0.02

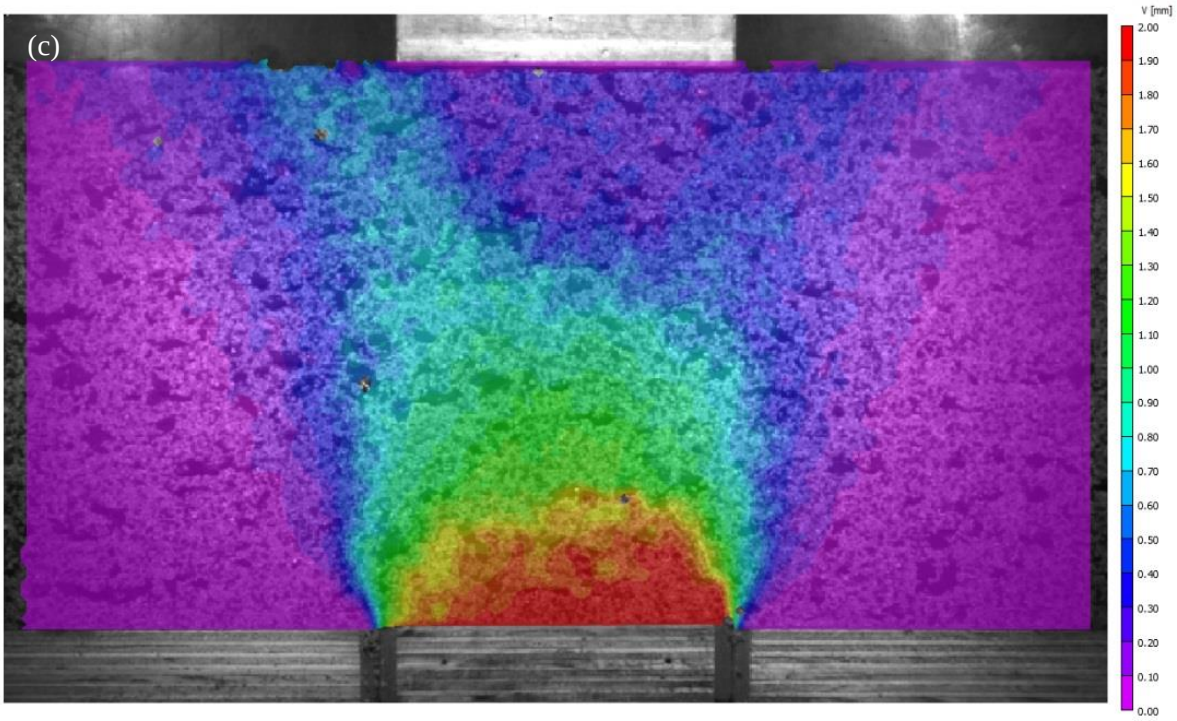

Fig. 5.7. Distributions of vertical displacements with the application of surcharge for the three materials: (a) Sand, (b) 10% Rubber–sand, and (c) 30% Rubber–sand

Zones 1 and 3 can be combined and idealised into an inverted isosceles trapezoid forming the total arch area. To examine the effects of rubber inclusions on the evolution of the arches, the area of the arches was measured, and the results are provided in Table 5.2 in the form of the area of the arch, and the normalised height of the arches of equal displacement with respect to the trapdoor width. It is evident that the area of the trapezoids decreased with increased rubber inclusion, and the coverage decreased roughly by 5%, depending on the rubber content and in the situation where the surcharge condition remained the same. With the application of the surcharge, the area of the arch increased by 5.5% for Sand, 5.7% for 10% Rubber–sand, and 6.3% for 30% Rubber–sand. On the other hand, the application of the surcharge reduced the side slopes of the arch, thus deforming the arches outward.

Table 5.2. Area of arch and crest height of the arch of equal displacement in different backfills

Test conditions	Material	Total arch area (mm^2)	Percentage of AOI covered	Normalised arch height (%)
No surcharge	Sand	74,625	59.7	153
	10% Rubber	69,375	55.5	125
	30% Rubber	62,688	50.2	32
With surcharge	Sand	78,722	63.0	92
	10% Rubber	73,325	58.7	39
	30% Rubber	66,663	53.3	24

Rubber inclusions also lowered the crest of the arches of equal displacement. As shown in Table 5.2, the crest diminished by 28% of the trapdoor width for 10% Rubber–sand, and 121% for 30% Rubber–sand, for the no surcharge case. A similar trend was observed in the case of surcharge loading. The effect of surcharge on the variation of the crest was more pronounced in the Sand and 10% Rubber–sand than in the 30% Rubber–sand. Specifically, the surcharge reduced the arch crest by 61% of the trapdoor width in the Sand and 86% in 10% Rubber–sand, but only by 8% in the 30% Rubber–sand. Figs. 5.6 and 5.7 and Table 5.2 suggest that adding rubber to the sand helped reduce the area of arching. A similar reduction occurred when the surcharge was applied.

The distributions of vertical strains (ε_{yy}) in the Sand and Rubberised–sand, when subjected to passive arching with no surcharge and under surcharge loading, are presented

in Figs. 5.8 and 5.9 respectively. In each of the backfills, the tensile strains originated from the trapdoor edges and formed two outwardly oriented bands which extended up to the surface. The tensile bands gradually increased as they evolved up to the surface and became noticeably thicker at the surface when the surcharge was applied. The greatest vertical tensile strains occurred in the Sand. The strains were 1.2% with no surcharge and 0.6% under the application of the surcharge. This suggests that rubber inclusions reduce the peak vertical strain arising from arching. Specifically, adding 10% rubber reduced the strain by approximately 50%, whether the surcharge was applied or not. Adding 30% rubber further reduced the strains by approximately 22% in the no surcharge case, and 30% with surcharge.

Vertical compressive strains were also mapped along the cross-sections of the backfills, as shown in Figs. 5.8 and 5.9. In all cases, the compressive regions were bounded by the bands of tensile strain. The maximum compressive strains fell into a narrow range of 0.7–0.8% for all no-surcharge cases. When the surcharge was applied, the peak values of compressive strains increased by up to 0.4%, but nevertheless fell into a narrow range of 1–1.1%. It is noteworthy that a band of compressive strain formed beneath the surcharge block [Fig. 5.9(c)]. Closer examination of this band highlighted the presence of concentrated rubber particles which resulted in a small degree of heterogeneity. Furthermore, the backfill layers near the surface are usually, moderately less compacted when compared to the deeper layers, due to the reduced overburden weight. Therefore, this band beneath the surcharge block experienced significantly higher compressive vertical strains in comparison to the rest of the backfill. The distributions in Figs. 5.8(c) and 5.9(c) emphasise the importance of homogeneity and appropriate compaction of rubberised backfills.

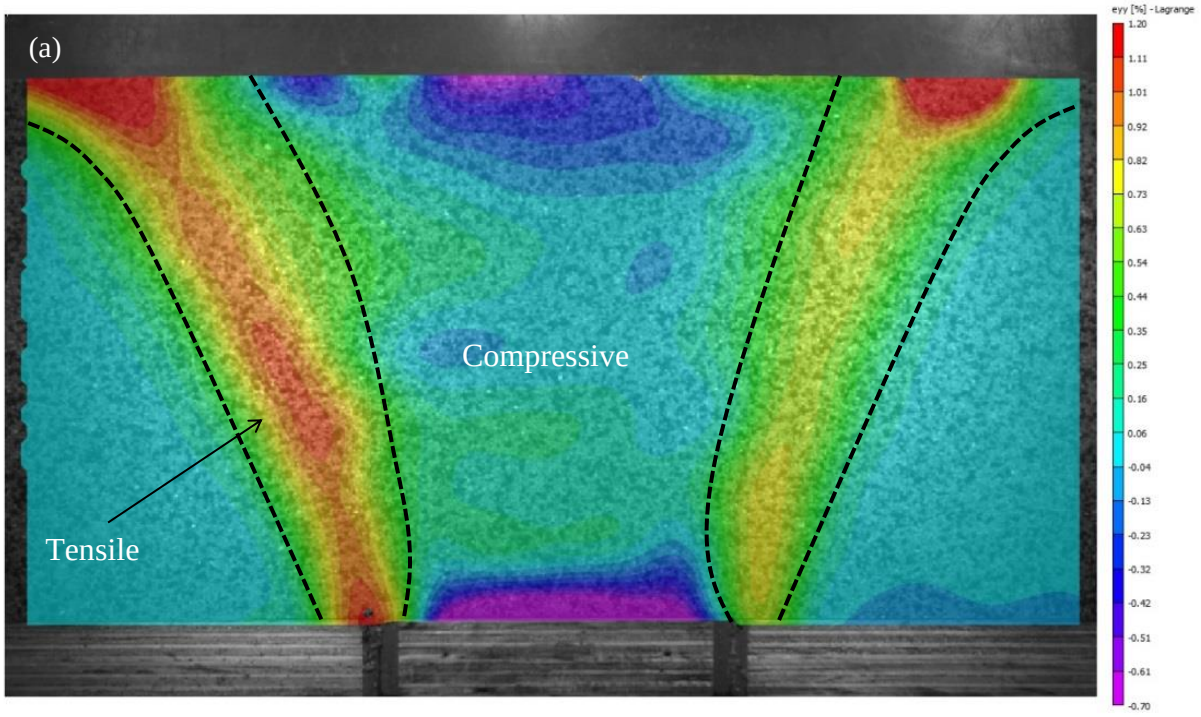
(a)
Compressive
Tensile
eyy [%] - Lagrange
1.20
1.11
1.01
0.92
0.82
0.73
0.63
0.54
0.44
0.35
0.25
0.16
0.06
-0.04
-0.13
-0.23
-0.32
-0.42
-0.51
-0.61
-0.70

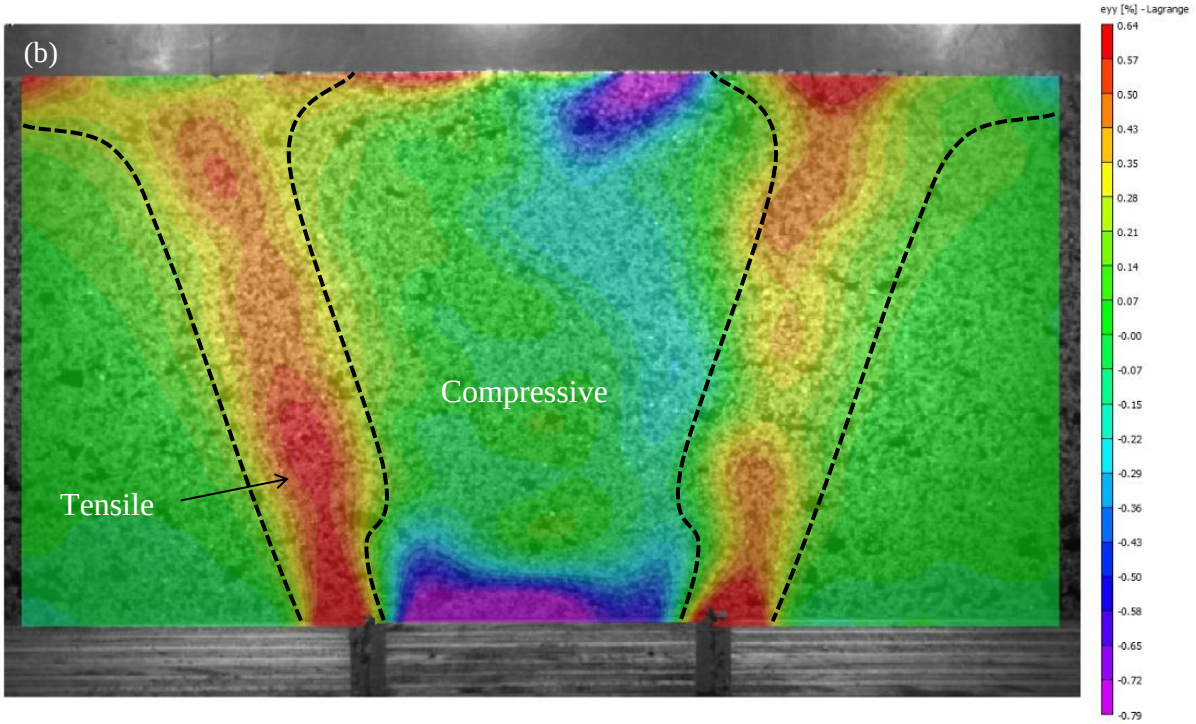
(b)
Compressive
Tensile
eyy [%] - Lagrange
0.64
0.57
0.50
0.43
0.35
0.28
0.21
0.14
0.07
-0.00
-0.07
-0.15
-0.22
-0.29
-0.36
-0.43
-0.50
-0.58
-0.65
-0.72
-0.79

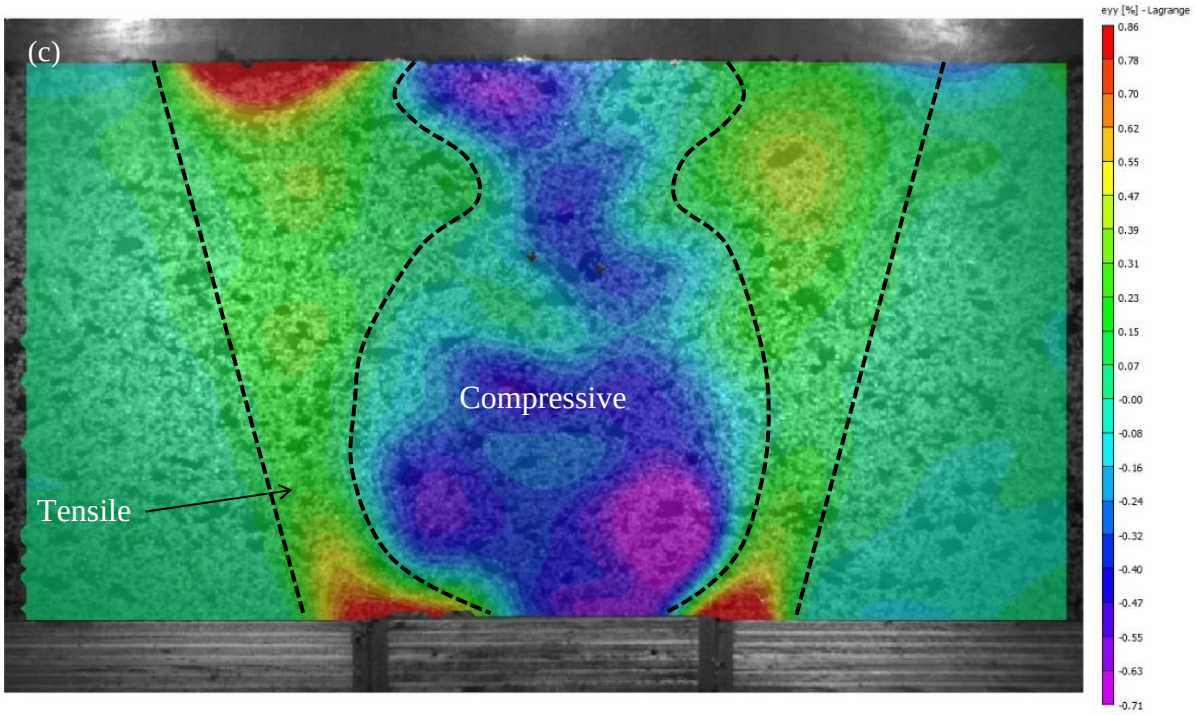

Fig. 5.8. Vertical strain distributions under no surcharge for the three materials: (a) Sand, (b) 10% Rubber–sand, and (c) 30% Rubber–sand

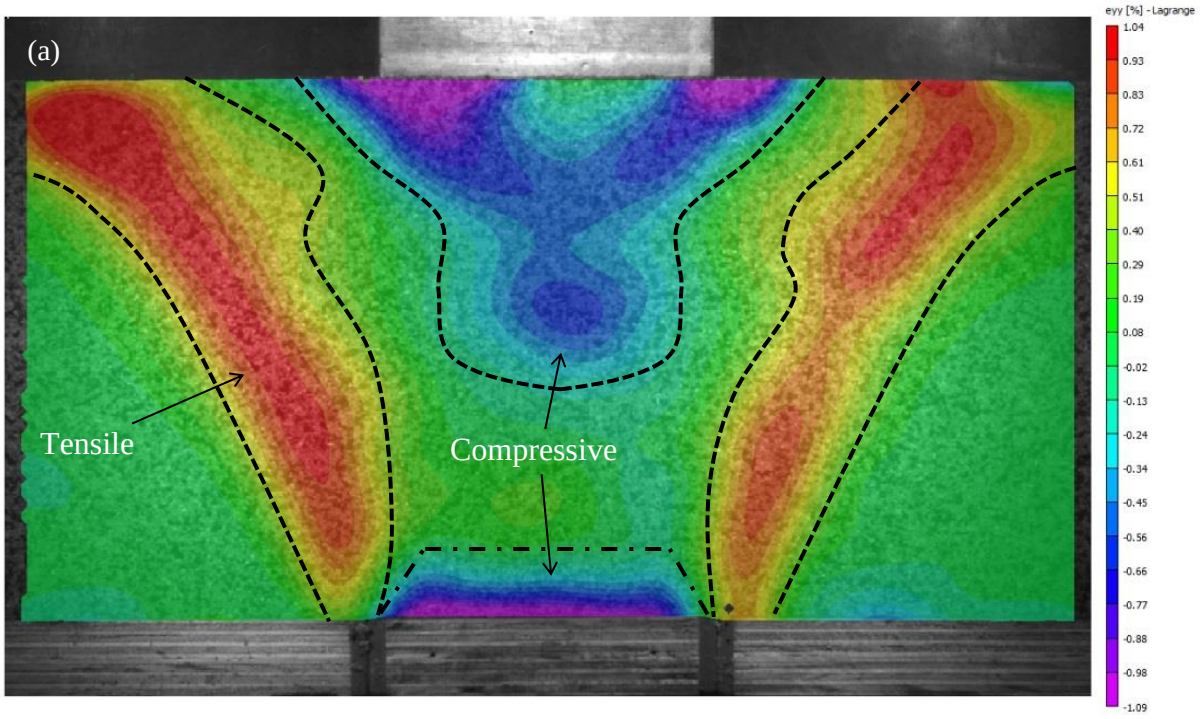

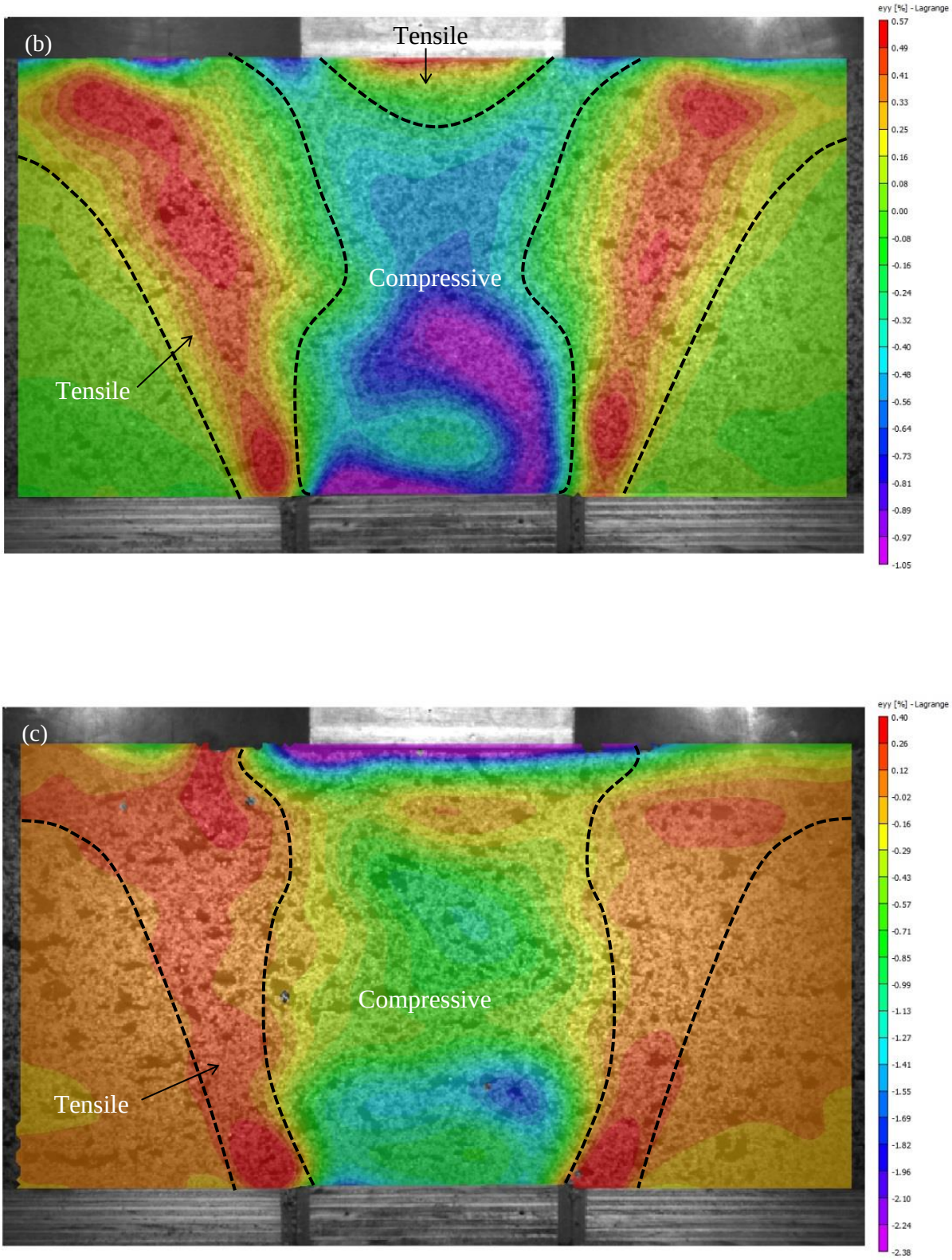

Fig. 5.9. Vertical strain distributions with the application of surcharge for the three materials: (a) Sand, (b) 10% Rubber–sand, and (c) 30% Rubber–sand

5.3.3. Shear strains and shear bands

The distribution of shear strains (ε_{xy}) developed in the Sand and rubberised backfills under passive arching with no surcharge and with the application of the 5 kPa surcharge are presented in Figs. 5.10 and 5.11 respectively. The intensity of shear straining was generally reduced when rubber was mixed with sand. In the no surcharge cases, the average value of the maximum shear strains decreased from 1.65% in the Sand to 1.53% in the low rubber-content backfill, and to 1.37% in the high rubber-content backfill. The application of surcharge decreased the corresponding maximum values. In this case, with the addition of rubber to the Sand, the average maximum shear strains reduced to from 1.4% to 1.2% in both rubberised backfills. Shear strains therefore decreased when the Sand backfill was rubberised. Both 10% and 30% rubber content backfills showed similar shear deformability under surcharge loading.

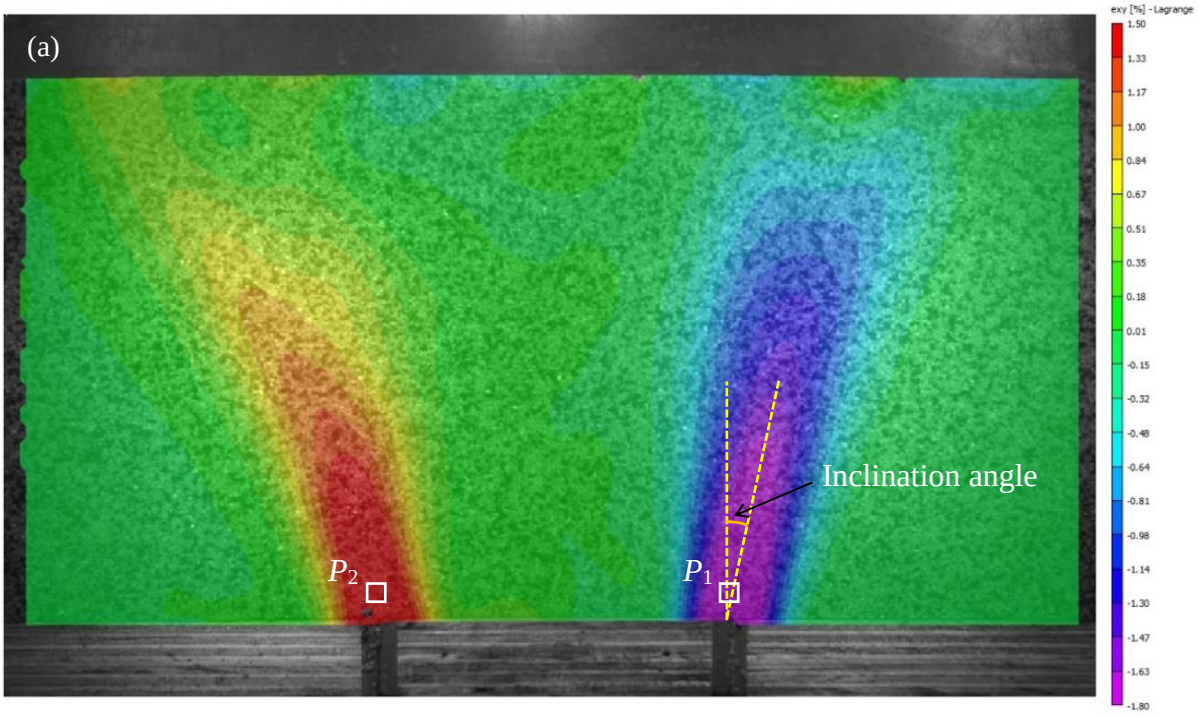

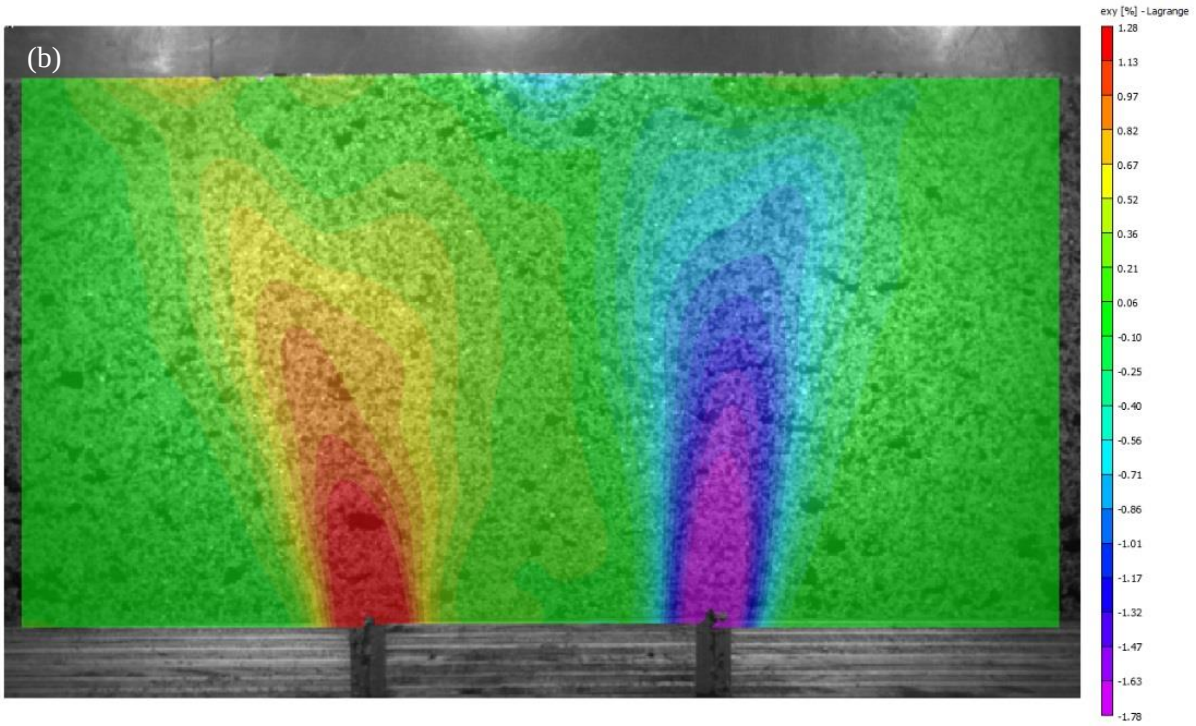

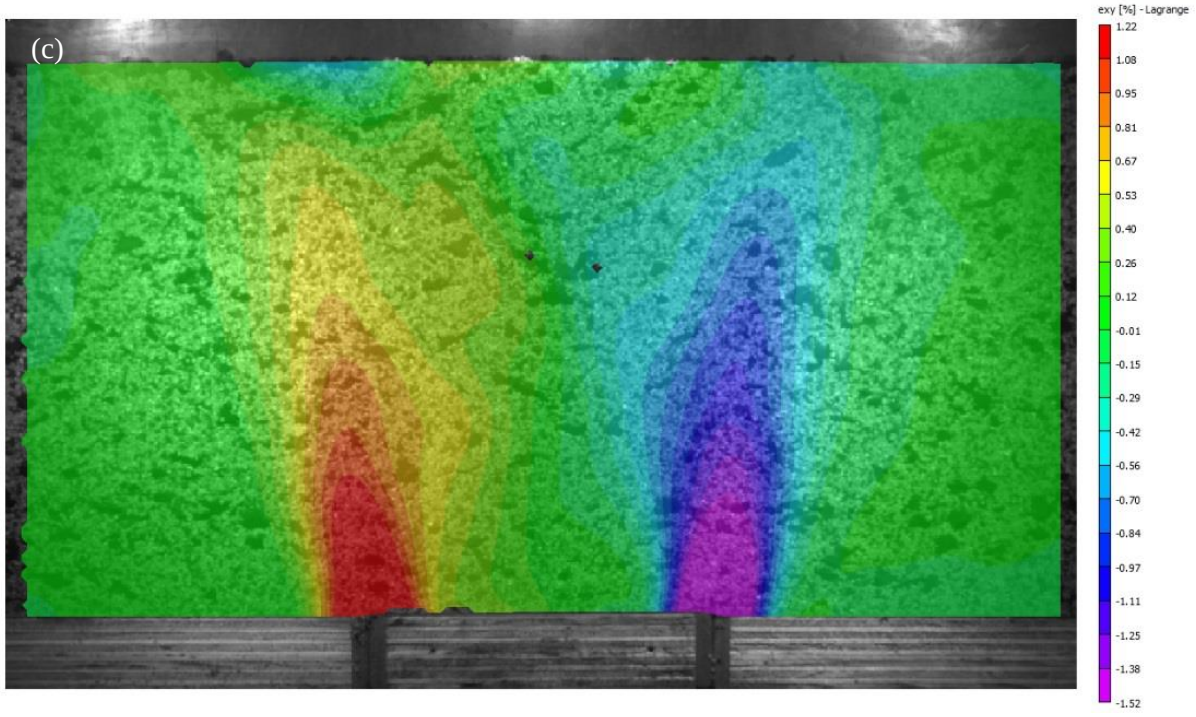

Fig. 5.10. Shear strain distribution under no surcharge condition for three materials: (a) Sand, (b) 10% Rubber–sand, and (c) 30% Rubber–sand

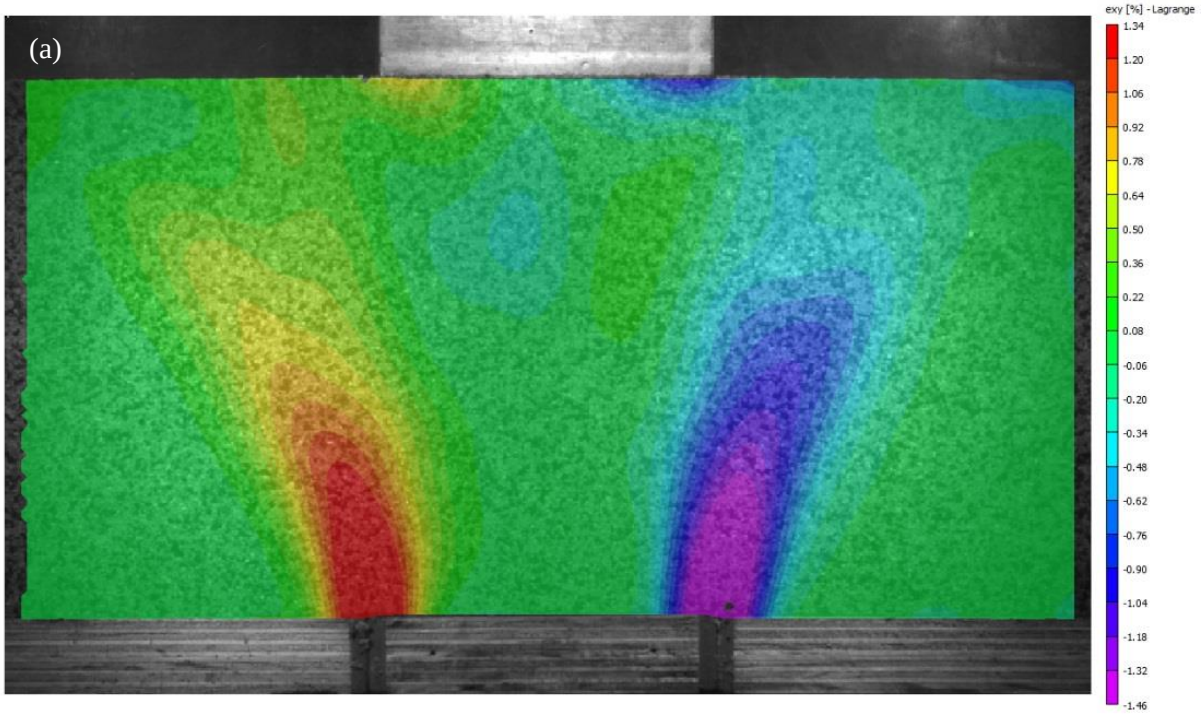
(a)
exy [%] - Lagrange
1.34
1.20
1.06
0.92
0.78
0.64
0.50
0.36
0.22
0.08
-0.06
-0.20
-0.34
-0.48
-0.62
-0.76
-0.90
-1.04
-1.18
-1.32
-1.46

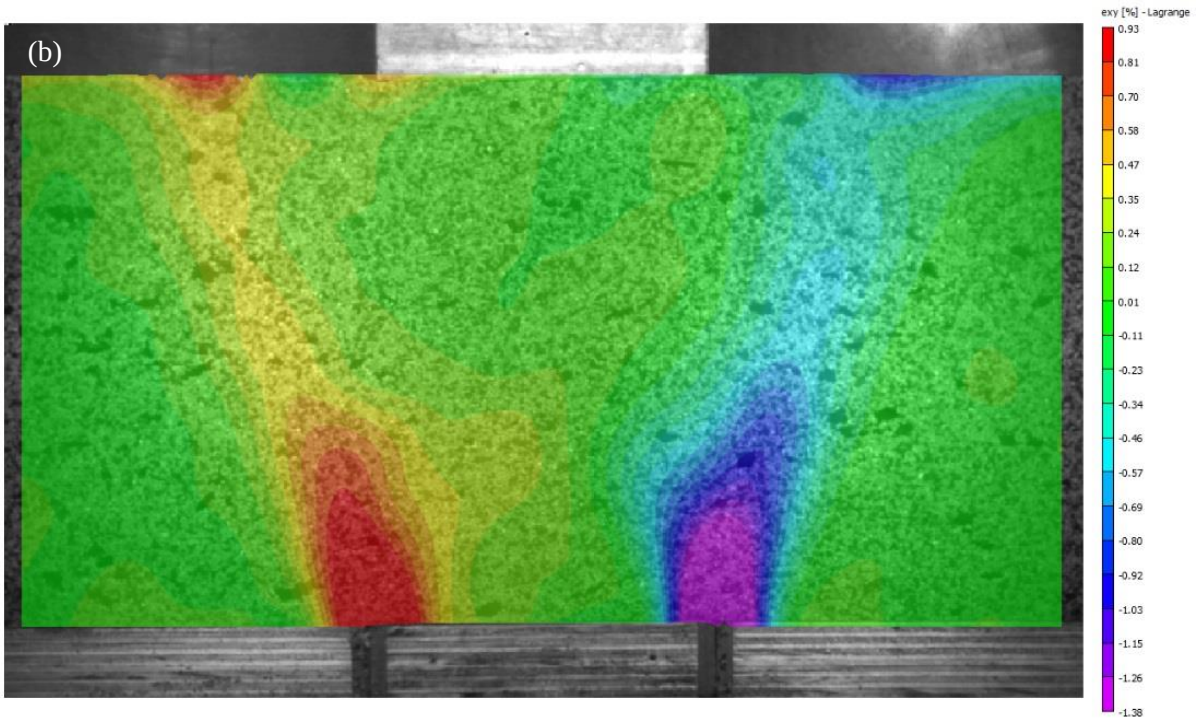
(b)
exy [%] - Lagrange
0.93
0.81
0.70
0.58
0.47
0.35
0.24
0.12
0.01
-0.11
-0.23
-0.34
-0.46
-0.57
-0.69
-0.80
-0.92
-1.03
-1.15
-1.26
-1.38

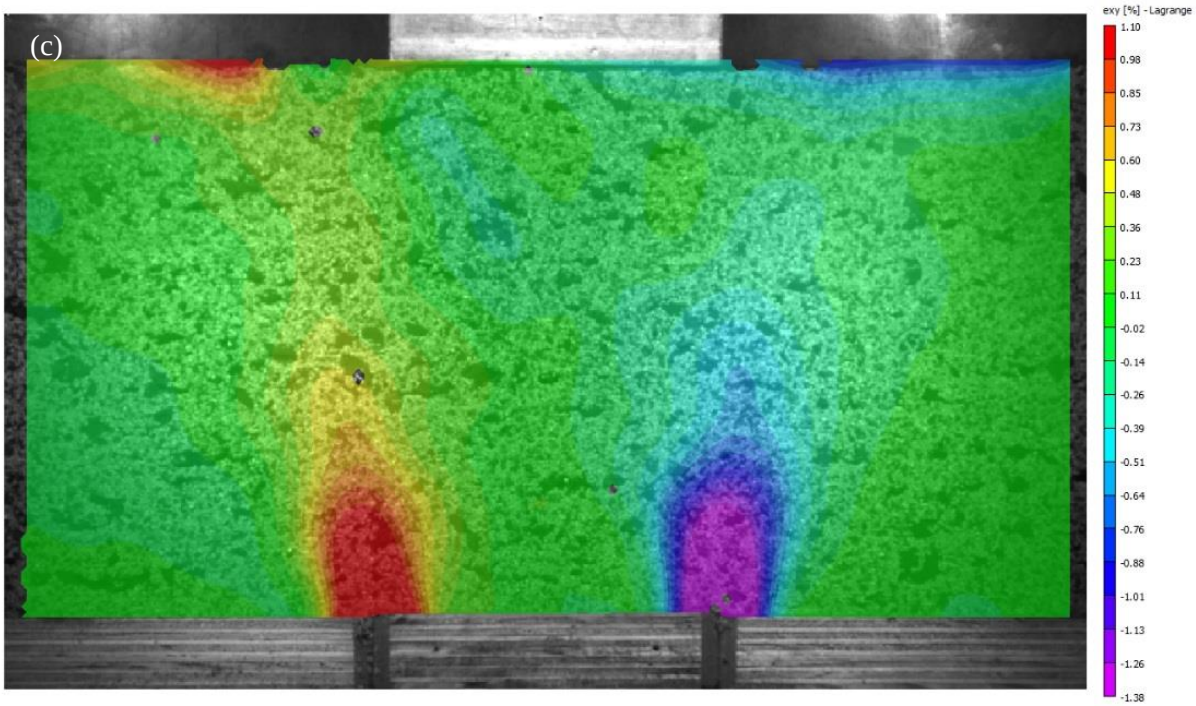

Fig. 5.11. Shear strain distribution under surcharge loading condition for three materials: (a) Sand, (b) 10% Rubber–sand, and (c) 30% Rubber–sand

As shown in Figs. 5.10 and 5.11, in all cases, the shear bands initiated from the trapdoor edges and symmetrically continued in an outward orientation toward the backfill surface. Strain localisation or shear band formation represents the typical deformation behaviour of granular materials under plane-strain conditions (Peters et al., 1988; Alshibli et al., 2003). The shear bands are usually characterised by their angle of inclination and width normalised with respect to particle median size, D_{50}. Table 5.3 provides the width and inclination angles of the shear bands that evolved in the Sand and rubberised backfills. The angles were measured from the vertical direction and averaged for the two bands. For each band, the width was measured over two profiles in the lower and upper parts of the band, perpendicular to the band axis, where the shear strain values were greater than 50% of the peak shear strain value. As shown in Table 5.3, regardless of the application of the surcharge,

the shear band width increased minimally with the addition of 10% rubber to the Sand, and then reduced with the further increase in the rubber content to 30%. In the no surcharge case [Fig. 5.10(a)], the inclination angle of the shear bands decreased with rubber content. The 30% rubber backfill exhibited the lowest inclination angle and the same trend was also observed in the backfills under surcharge loading. The reduction in the inclination angle indicates a shrinkage in the area of the arch. The variation of arching area agrees with the results obtained from the vertical displacement, as presented in Table 5.2 above.

Table 5.3. Shear band characteristics under passive arching

Testing conditions	Material	Inclination angle	Dilation angle	Normalised shear band thickness
No surcharge	Sand	12.5°	13°	25.3
	10% Rubber	6.5°	8°	25.9
	30% Rubber	6°	6°	24.2
With surcharge	Sand	13°	8.5°	26.3
	10% Rubber	9.5°	3°	26.7
	30% Rubber	7.5°	5°	22.3

The inclination angle of shear bands in a rising trapdoor is believed to be equal to the angle of dilation of the granular material contained in the apparatus (M.D. Bolton, personal communication, 2018). The angle of dilation is regarded as the characteristic measure of a dilatant material subjected to shearing. On the other hand, negative values of dilation angle

will occur in very loose sand with a relative density smaller than 23% (obtained empirically) or dense sand sheared at extremely high normal or confining pressures, where particle crushing becomes thermodynamically less energy-intensive compared to particle rolling (Bolton 1979, 1986). In these cases, a negative dilation angle indicates contraction during shearing. The amount of plastic volumetric strain developed during plastic shearing is determined by the angle of dilation which is assumed to remain unchanged during plastic yielding. At the idealised critical state, it is naturally inferred that the dilation angle finds a value of zero, hence denoting shearing at constant volume. For natural sand, a dilation angle exceeding 20° is extremely rare (Bolton, 1986). Unlike the friction angle, whose definition remains the same for different modes of shearing (e.g. direct shear test, biaxial or triaxial compression or extension, plane-stain shearing), the expression for the dilation angle depends on the mode of deformation and, therefore, for every case a separate dilation angle is determined mathematically only from plastic strains (Vermeer and de Borst, 1984). By neglecting small elastic strains, for plane-strain conditions, the following expression for the dilation angle (ψ) was proposed by Bolton (1986):

$$\psi = \arcsin\left(-\frac{d\varepsilon_1 + d\varepsilon_2}{d\varepsilon_1 - d\varepsilon_2}\right) \tag{5.2}$$

where $d\varepsilon_1$ and $d\varepsilon_2$ denote the major and minor principal strain rates. In plasticity theory, the strain rate, denoted here by the letter d preceding the strain ε, are introduced artificially to emphasise an incremental, constitutive response and does not imply a dynamic or rate-related effect (Borja, 2013). The first negative sign is omitted if the tensile strains are considered positive, as is the case in this study. Fig. 5.12 shows the angle of dilation on a typical Mohr circle of strain, where shear strains are plotted against the normal strains.

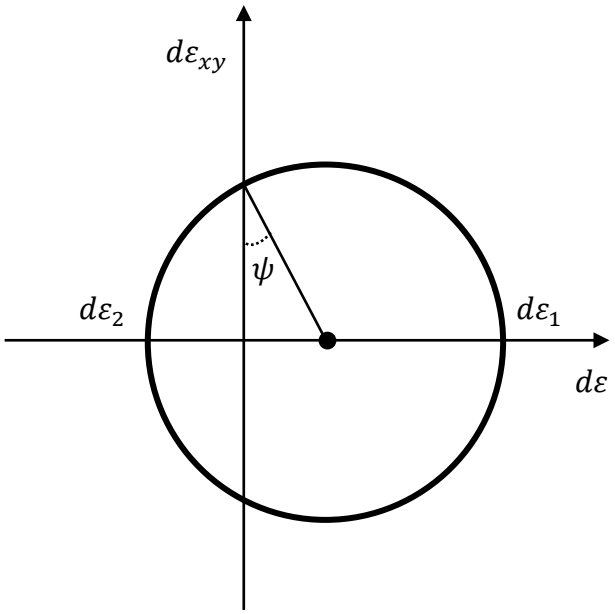

Fig. 5.12. Mohr circle of strain and the dilation angle for plane-strain conditions

Using the representation in Fig. 5.12, one can derive the following alternative expression for the angle of dilation under plane-strain conditions in terms of normal and shear strains:

$$\psi = \arcsin\left(\frac{C}{R}\right) \tag{5.3a}$$

$$C = \frac{d\varepsilon_{xx}+d\varepsilon_{yy}}{2} \tag{5.3b}$$

$$R = \sqrt{\left(\frac{d\varepsilon_{xx}-d\varepsilon_{yy}}{2}\right)^2 + d\varepsilon_{xy}^2} \tag{5.3c}$$

where C and R are the x-axis component of the centre point and radius of the Mohr circle of strain, respectively. The average of the horizontal, vertical, and shear strains of two small square elements P_1 and P_2, which are situated inside the shear bands, above the edges of the trapdoor, and have the size of one subset, were extracted from the strain distributions in Figs. 5.10 and 5.11 for all the backfills. The corresponding Mohr circles of strain were constructed to obtain the angle of dilation for each shear band. Figs. 5.13 and 5.14 show the Mohr circle

of strain for the right-hand-side shear bands in the Sand and rubberised backfills. Mohr circles of strain at element P_1, in Fig. 5.10(a), suggest that the rubber inclusion reduced the deformability of this element. This is reflected in reduced tensile major principal strains. The application of the surcharge resulted in shifting the strains toward one more compressive in nature at this element rather than a tensile one, as shown in Fig. 5.14. The values of the angle of dilation were then averaged (and rounded to the nearest 0.5°) for each case and are presented in Table 5.3.

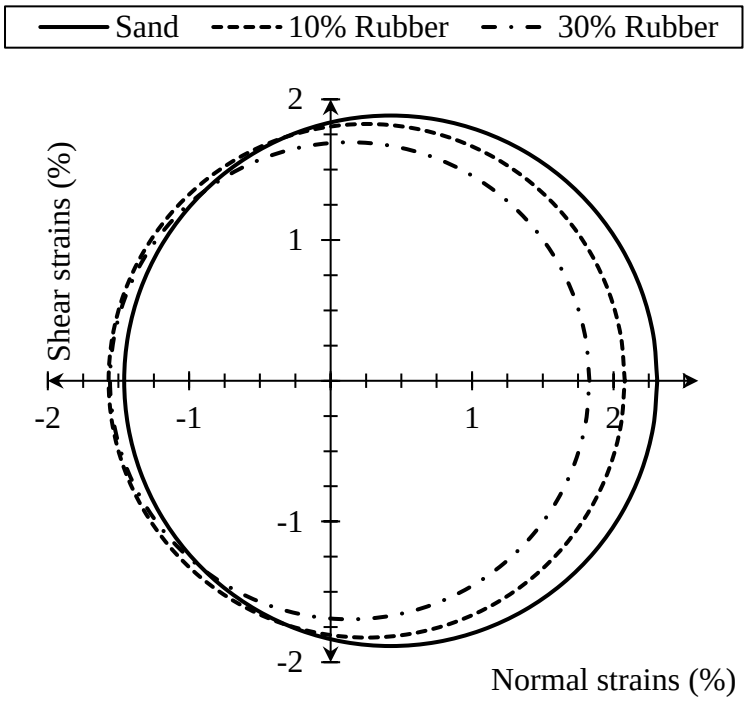

Fig. 5.13. Mohr circle of strain for element P_1 in the Sand and Rubber–sand backfills with no surcharge loading

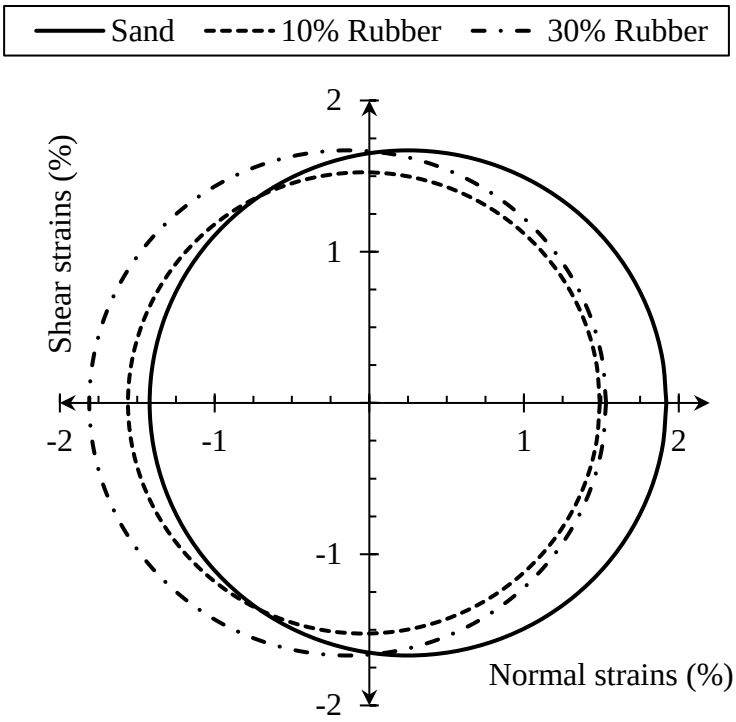

Fig. 5.14. Mohr circle of strains for element P_1 in the Sand and Rubber–sand backfills under the application of surcharge

As shown in Table 5.3, for the no surcharge cases, excellent agreement is obtained between the angle of dilation of the geomaterials and the angle of inclination of the shear bands. Moderate differences exist between the two sets of values when the surcharge was placed. This reflects the fact that the angle of inclination is dependent on boundary conditions. The local surcharge directed the shear bands to a 'less outward' inclination, where the shear bands became restricted to a rather vertical orientation. Placement of the surcharge block also prevented the growth of the shear bands in the backfills. That is, the shear bands did not evolve upwards, in the surcharge case, to as high an extent as in the no surcharge case. A comparison of the values of the inclination angles of the shear bands with the friction angle (Table 5.1) and dilation angle (Table 5.2) suggests that the latter is the more appropriate measure to determine the orientation of the yield surface in the trapdoor

apparatus. Use of the friction angle as the inclination angle, on the other hand, more likely leads to erroneous predictions (for example, in the finite element modelling by Wang et al., 2017). In addition to the evidence of direct deformation measurements in this study on the unsuitability of the use of the friction angle, a mathematical sensitivity analysis on the stresses by Singh et al. (2010) showed that soil arching is almost independent of the backfill friction angle.

5.3.4. Stresses

The results of the DIC analysis in the three backfills tested in this study indicated that differential strains were developed in response to the trapdoor displacement. Differential strains in turn result in a redistribution of stresses. The stresses were first recorded on the structure interface for the undeformed Sand and Rubber–sand samples. Verifications were performed on the accuracy of sensors by running trials on at-rest backfills. Excellent agreement was obtained between the theoretical results (based on vertical stress calculations) and the results measured by the sensors. It was observed that, on average, the sensors overestimated the theoretical geostatic stresses by 0.5 kPa for the Sand and by 0.16 kPa for the rubberised backfills. The improved accuracy associated with the rubberised backfills likely arose from the superior adaptation of the rigid sensor surfaces to soft materials, such as the rubber.

The stress results of all cases examined in this study are presented in Figs. 5.15–5.20. The stress data captured by the sensors, σ_f, were normalised to the at-rest stress, σ_i, and plotted with respect to trapdoor displacement normalised to the trapdoor width. As can be observed, upon completion of passive arching, the contact stress increased on the trapdoor surface and decreased on the stationary section.

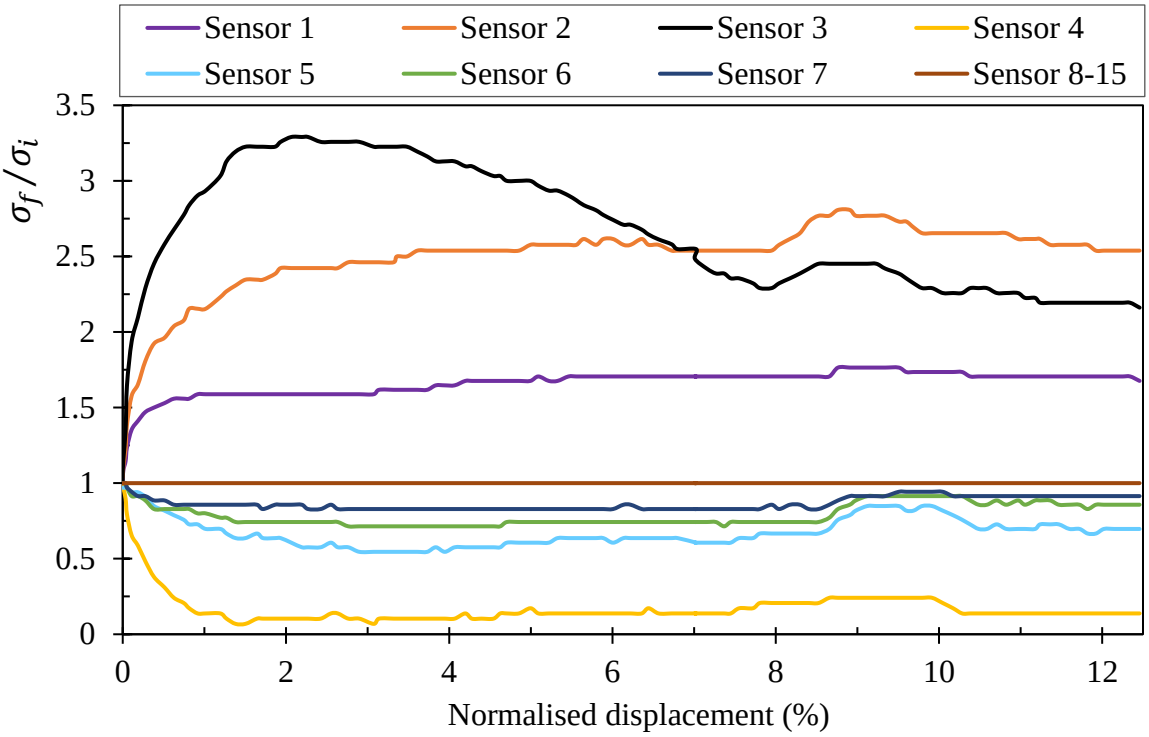

Fig. 5.15. Measured stress ratios with normalised trapdoor displacement in Sand with no surcharge under passive arching conditions

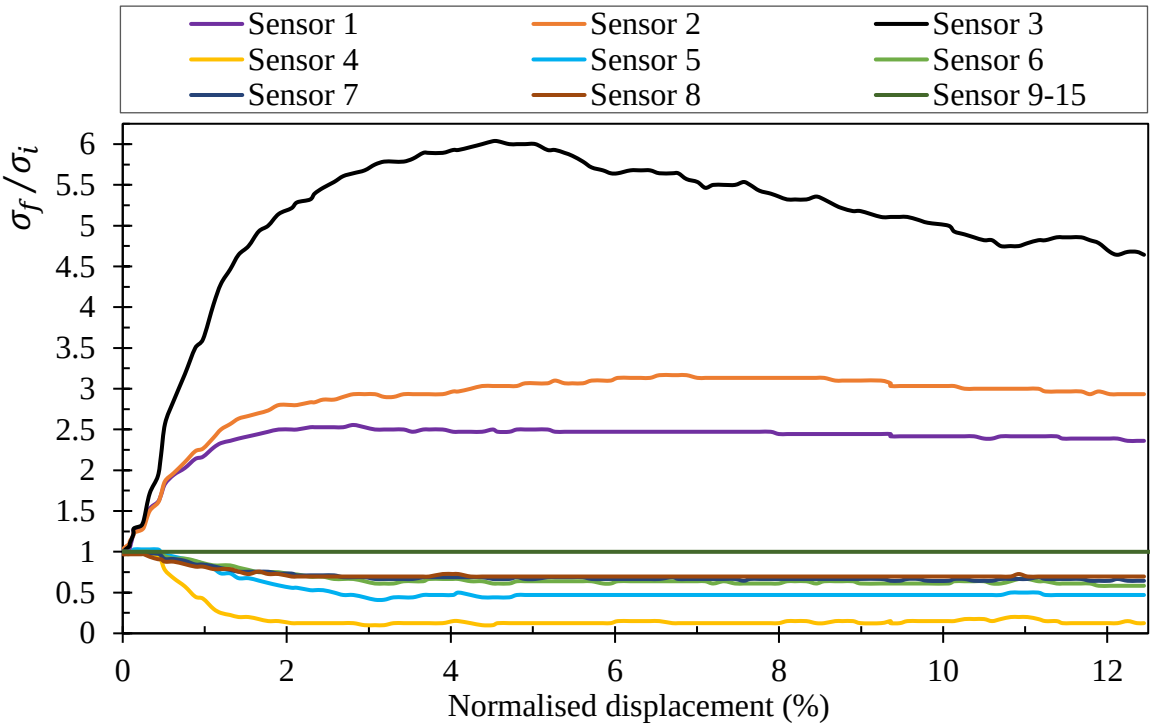

Fig. 5.16. Measured stress ratios with normalised trapdoor displacement in Sand with a 5 kPa surcharge under passive arching conditions

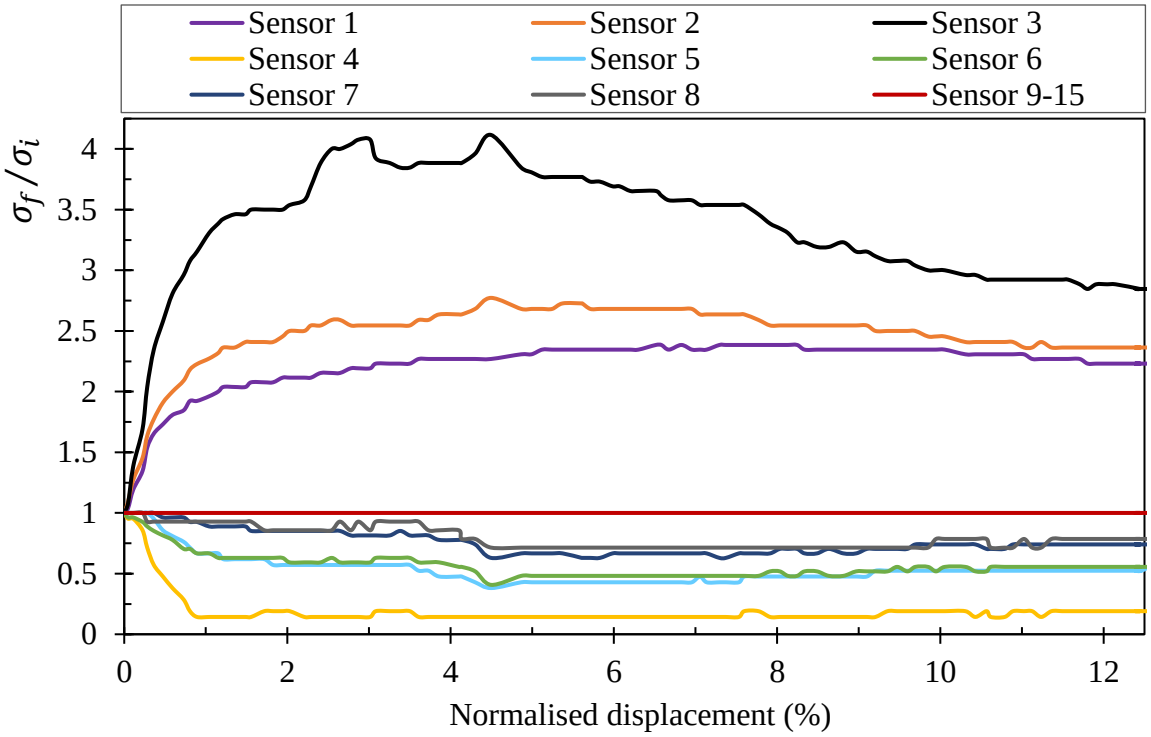

Fig. 5.17. Measured stress ratios with normalised trapdoor displacement in 10% Rubber–sand with no surcharge under passive arching conditions

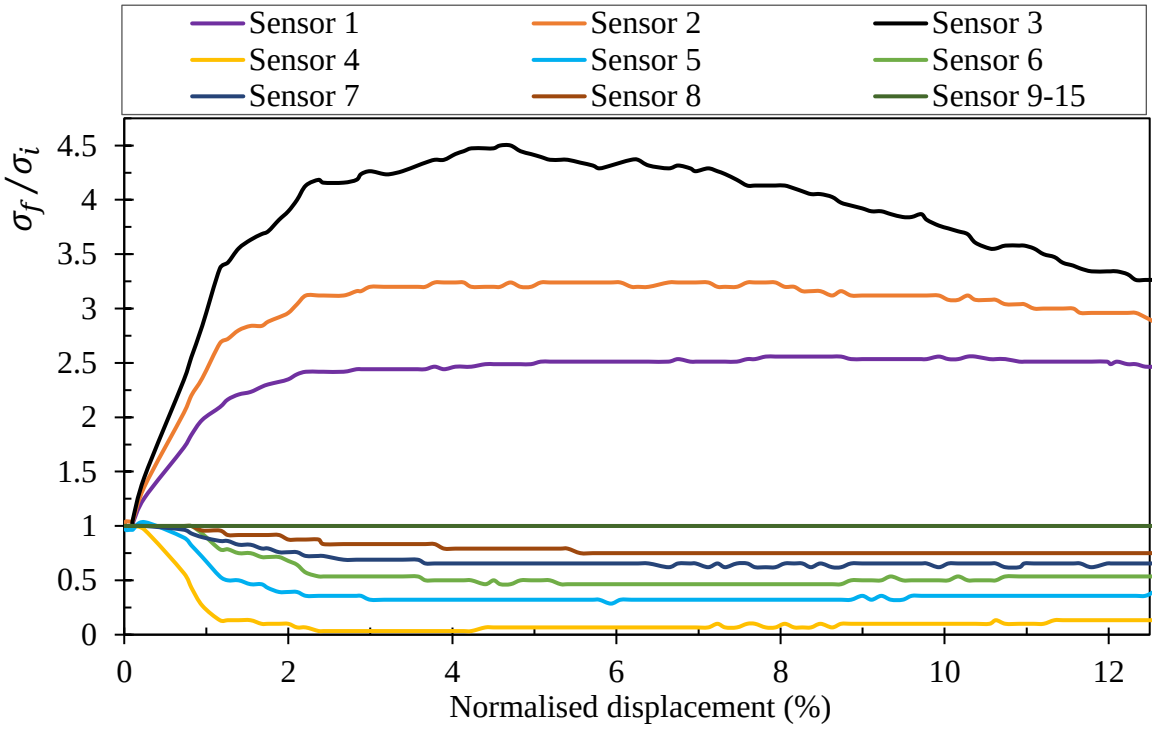

Fig. 5.18. Measured stress ratios with normalised trapdoor displacement in 10% Rubber–sand with a 5 kPa surcharge under passive arching conditions

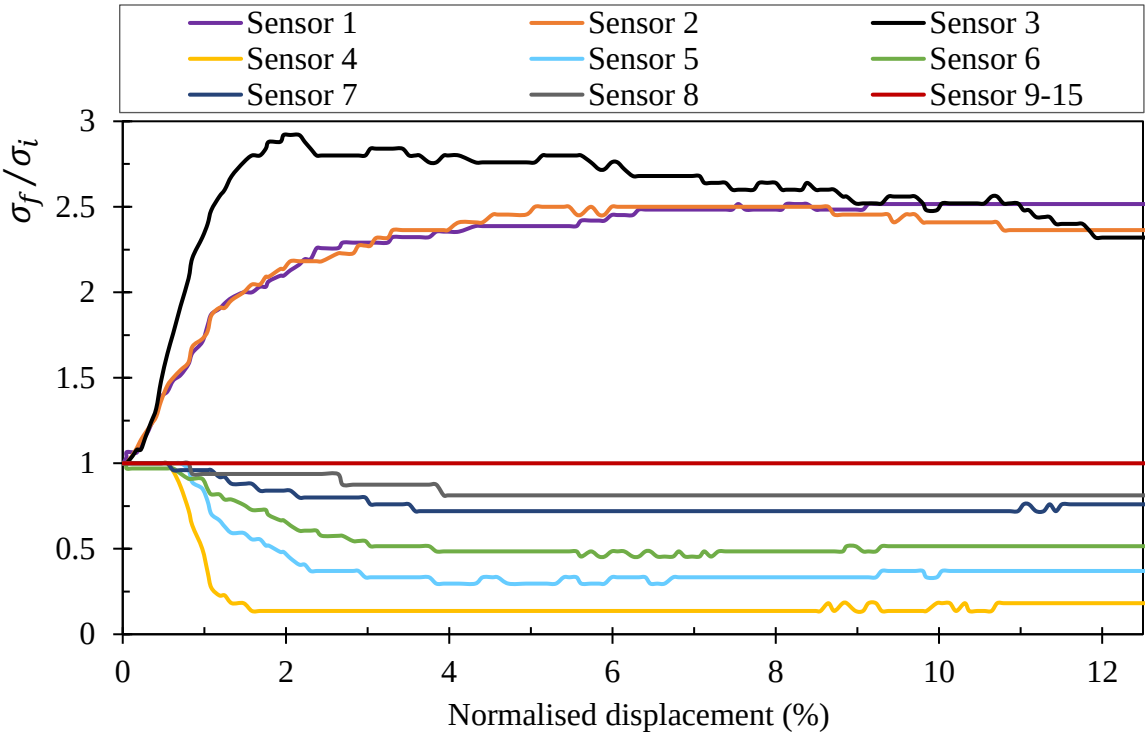

Fig. 5.19. Measured stress ratios with normalised trapdoor displacement in 30% Rubber–sand with no surcharge under passive arching conditions

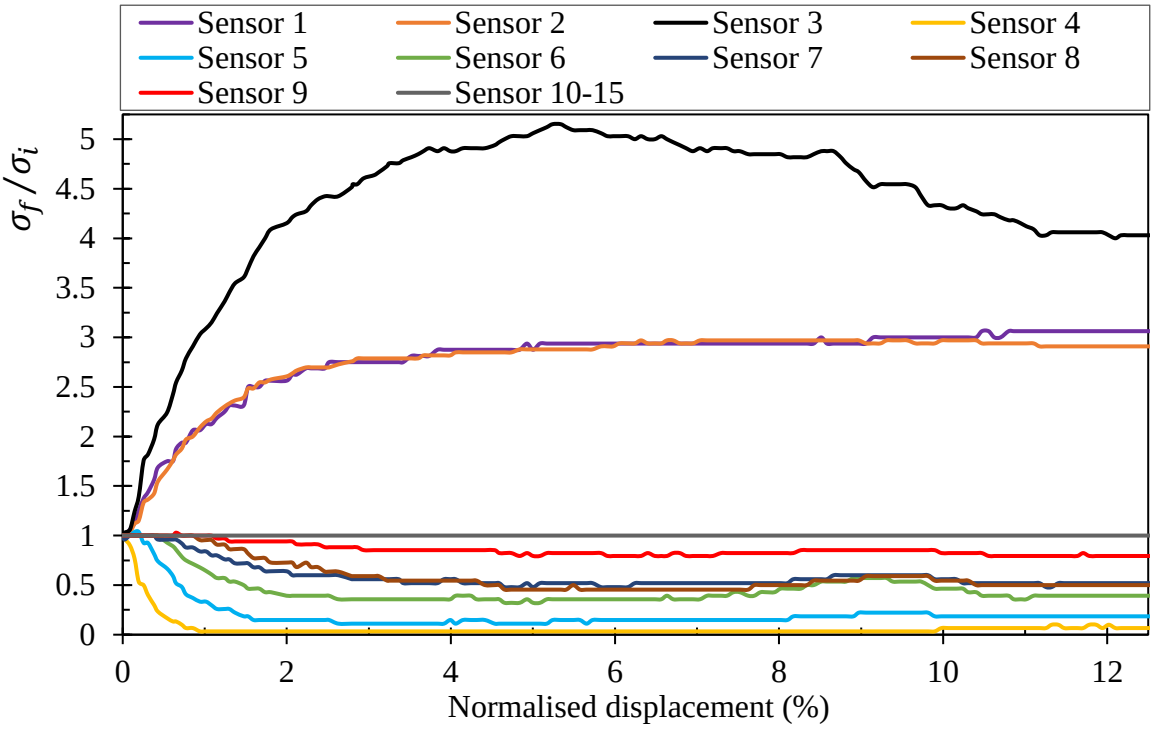

Fig. 5.20. Measured stress ratios with normalised trapdoor displacement in 30% Rubber–sand with a 5 kPa surcharge under passive arching conditions

On the trapdoor surface, the stress increase was highest at the trapdoor edge (i.e. Sensor 3), for all cases. At this location, without a surcharge loading, the stresses increased by a factor of 3–4. The factor further increased to 4.5–6 when the surcharge was applied. The stresses for locations distant from the edge (i.e. Sensors 1 and 2) increased by a factor of 1.5–3. The Sand and rubberised backfills exhibited a brittle behaviour along the length that the trapdoor edge sensor represented, i.e. approximately 20% of trapdoor width (TW). However, as the trends, recorded by the trapdoor centre (Sensor 1) and intermediate (Sensor 2) sensors in Figs. 5.15–5.20 indicate, the mechanical behaviour of the geomaterials at the interface exhibited a ductile behaviour along the remaining 30% of the trapdoor half-width (recalling that only half of TW was instrumented for stress measurement due to axisymmetry). Therefore, the same geomaterial showed different mechanical behaviours along the length supported by the same structure; that is, brittle behaviour on the outer regions close to the edge of the structure, and ductile behaviour along the internal regions. The least stress change occurred at the trapdoor centre (Sensor 1), in particular, in the cases of Sand and 10% Rubber–sand. Interestingly, very similar stress results were obtained from Sensors 1 and 2 in the 30% Rubber–sand backfill. This similarity in stress values was related to reduced spatial variability and the surcharge loading.

The contact stress distribution depended on at least two factors: the backfill particle size and the surcharge load transferred to the backfill. As the percentage of large rubber particles in the backfills increased, the measurements at the trapdoor centre and intermediate stress sensors gradually became more closely aligned. In other words, the variability in the stress regime decreased. This pattern can be expressed quantitatively if the structure length is normalised with respect to the D_{95} values presented in Table 5.1 above. The ratios of trapdoor width to the particle size which 95% of the backfill particles are smaller than, are approximately 68, 17, and 14 for the Sand, 10% Rubber–sand, and 30% Rubber–sand

backfills, respectively. Comparing the stress ratio values recorded by the different sensors in Figs. 5.15–5.20 with these structure length-to-D_{95} ratios, one concludes that lower spatial variability is observed in the backfill with the smaller structure length to particle size ratio. Applying the surcharge also created a similar effect in reducing variability, as reflected in Figs. 5.15–5.20. The influence of decreased stress variability due to surcharge loading was extended to the stationary part of the apparatus, as shown by the very close or, on some instances, overlapping sensor readings in this region (e.g. Sensors 7 and 8 in Fig. 5.20).

On the stationary section of the base of the apparatus, the stress at the interface decreased. The reduction in stress continued until the trapdoor attained to a normalised displacement of 2–3% in all cases, and then the stress remained relatively unchanged with trapdoor displacement, thus exhibiting a ductile response. For all cases, the greatest decrease (of up to 96%) occurred at Sensor 4, which was adjacent to the edge of the stationary section. The influence on stress extended to Sensor 9, in the 30% Rubber–sand with the applied surcharge, and to Sensor 8 in the other cases. This suggests that the passive arching created a zone of influence of 94–113% of the trapdoor width, for the cases examined in this study.

To compare the arching behaviour of Sand and rubberised sand, the concept of tangent arching modulus, first developed by Iglesia et al. (2013) for the active arching mode, is generalised here to the passive arching case at small displacements. A linear relationship between the normalised stress (σ_n) and normalised displacement (ε_n) under passive arching, with an intercept value of unity at zero displacement, can be established from the following expression:

$$\sigma_n = 1 + p_t \cdot \varepsilon_n \tag{5.4}$$

where p_t denotes the tangent passive arching modulus at small normalised displacements up to 0.5%. The results of ordinary least squares regression, using Eq. (5.4) for the three backfill

materials, are summarised in Table 5.4. The results are obtained in terms of the stress measured by Sensor 1, and the average stress of Sensors 1–3. As shown in Table 5.4, the linear relationship fits very well the normalised stress σ_n and normalised displacement ε_n, with a coefficient of determination R^2 of 0.7–1, for all cases examined. Linearity became more pronounced when the stress level in the backfills was increased by the surcharge loading. The Sand showed the highest passive arching modulus among all the backfills tested in this study. Under no surcharge conditions, the arching modulus decreased with increasing rubber content. For example, at the centre of the trapdoor, the modulus decreased by 19% for the 10% Rubber–sand and 66% for the 30% Rubber–sand. These percentages are approximately twice that of the rubber content. When the surcharge was applied, the passive arching moduli reduced in the Sand and 10% Rubber–sand. However, the surcharge loading increased the arching modulus in the 30% Rubber–sand. In the case of 30% Rubber–sand, the moduli increased approximately to the corresponding levels in the Sand. The data in Table 5.4 indicate that, when a structural element is displaced into sand and rubberised sand backfills (or the backfills move in relation to the structure), as long as the displacements are small, the stress increase at the centre of the jacked structure will be greater in the sand when compared with the rubberised sand backfills.

Table 5.4. Passive arching moduli in Sand and Rubber–sand mixtures at small normalised displacements

Testing conditions	Material	Measured arching tangent modulus (p_t) on trapdoor			
		Centre	R^2	Average	R^2
No surcharge	Sand	206	0.7	370	0.5
	10% Rubber	167	1	239	0.8
	30% Rubber	69	0.9	71	0.9
With surcharge	Sand	151	1	167	0.9
	10% Rubber	96	1	138	0.9
	30% Rubber	146	1	172	0.7

5.4. Conclusions

The deformation and stress profiles in Sand, 10% Rubber–sand and 30% Rubber–sand backfills subjected to passive arching in a trapdoor apparatus were presented. The profiles were captured using the DIC technique and a set of stress sensors installed in the apparatus. The following concluding remarks are drawn from the results of the experiments conducted:

- The DIC technique is an effective tool enabling the mapping of deformations in an assembly of granular materials. The technique identified the presence of an arch of equal displacement. In addition, critical zones of straining and local spots of heterogeneity were observed in the distributions of displacements and strains for a given backfill.

- Rubber inclusions of up to 30% reduced backfill deformation. The 30% Rubber–sand exhibited the lowest shear strains compared to the other two geomaterials, irrespective of the surcharge conditions. The distribution area of vertical displacements was inversely proportional to the rubber content. The addition of rubber to sand marginally influenced the lateral extent of horizontal displacements and strains. Overall, recycled rubber materials can be used to reduce the deformability of the backfills.
- The evolution of shear bands can be predicted by the use of the dilation angle of the materials. The friction angle, on the other hand, is deemed to be unsuitable for the prediction of the shear band evolution. The width and inclination angle of the shear bands were found to be dependent on material type and surcharge conditions.
- Significant increase in stresses on the jacked trapdoor and decrease in the stationary section occurred with the onset of the passive arching. Within the range of small normalised structure displacements (< 0.5%), rubber inclusions helped reduce the arching modulus, thus suggesting a diminished increase in the stresses at the trapdoor. The stress values varied with the measurement location, for all cases. However, in the cases of the rubberised backfills, the difference in stress values between two neighbouring sensors decreased due to the presence of the rubber particles.

Acknowledgements

The first author would like to thank Emeritus Professor Malcom D. Bolton, The University of Cambridge, for his insights on the DIC results presented in the paper. The financial support provided by the University of Adelaide under the Adelaide International Scholarship (ASI) scheme and the Australian Research Council is also acknowledged. The authors wish

to thank Mr Gary Bowman for his invaluable assistance in manufacturing the trapdoor apparatus and with the laboratory tests. Special thanks also go to Mr Ian Cates, Mr Thomas Stanef and Mr Simon Golding from the Instrumentation Group of the School of Civil, Environmental and Mining Engineering, and Mr Micah Simonsen from Correlated Solutions, USA, for their valuable technical advice and assistance.

References for Chapter 5

Ahn, I. S., Cheng, L. (2014). Tyre derived aggregate for retaining wall backfill under earthquake loading. Construction and Building Materials 57: 105–116.

Alshibli, K. A., Batiste, S. N., Sture, S. (2003). Strain localisation in sand: Plane strain versus triaxial compression. Journal of Geotechnical and Geoenvironmental Engineering 129(6): 483–494.

Aqoub, K., Mohamed, M., Sheehan, T. (2018). Analysis of sequential active and passive arching in granular soils, International Journal of Geotechnical Engineering DOI: 10.1080/19386362.2018.1473195.

Bolton, M. D. (1979). A guide to soil mechanics. Macmillan, London.

Bolton, M. D. (1986). The strength and dilatancy of sands. Geotechnique 36(1): 65–78.

Bolton, M.D. (2018). Personal communication.

Borja, R. (2013). Plasticity: Modelling and computation (Chapter 1). Berlin: Springer.

Bosscher, P. J., Edil, T. B., Kuraoka, S. (1997). Design of highway embankments using tyre chips. Journal of Geotechnical and Geoenvironmental Engineering 123(4): 295–304.

Chen, C.-Y., Martin, G. R. (2002). Soil–structure interaction for landslide stabilizing piles. Computers and Geotechnics 29(5): 363–386.

Chevalier, B., Combe, G., Villard, P. (2012). Experimental and discrete element modelling studies of the trapdoor problem: Influence of the macro-mechanical frictional parameters. Acta Geotechnia 7(1): 15–39.

Costa, Y. D., Zornberg, J. G., Bueno, B. S., Costa, C. L. (2009). Failure mechanisms in sand over a deep active trapdoor. Journal of Geotechnical and Geoenvironmental Engineering 135(11): 1741–1753.

Dewoolkar, M. M., Santichaianant, K., Ko, H. Y. (2007). Centrifuge modelling of granular soil response over active circular trapdoors. Soils and Foundations 47(5): 931–945.

Edil, T., Bosscher, P. (1994). Engineering properties of tyre chips and soil mixtures. Geotechnical Testing Journal 17 (4): 453–464.

Edil, T.B. (2004). A review of mechanical and chemical properties of shredded tyres and soil mixtures. Recycled Materials in Geotechnics, American Society of Civil Engineers, GSP127, Aydilek, A. H., Wartman, J., (eds.), ASCE Baltimore, pp.1–21.

Edinçliler, A., Baykal G., Dengili, K. (2004). Determination of static and dynamic behaviour of recycled materials for highways. Resources, Conservation and Recycling 42: 23–237.

Eldin, N. N., Senouti, A. B. (1992). Use of scrap tyre in road construction. Journal of Construction Engineering and Management 118: 561–576.

He, Y., Hazarika, H., Yasufuku, N., Han, Z. (2015). Evaluating the effect of slope angle on the distribution of the soil–pile pressure acting on stabilizing piles in sandy slopes. Computers and Geotechnics 69: 153–165.

Head, K., Epps, R. J. (2010). Manual of soil laboratory testing: Permeability, shear strength and compressibility tests (Volume 2, Chapter 12), 3rd edition, Whittles Publishing.

Humphrey, D. N., Sandford, T. C. (1993). Tyre chips as lightweight subgrade fill and retaining wall backfill. Proceedings of the Symposium on Recovery and Effective reuse of Discarded Materials and By-Products for Construction of Highway Facilities, Federal Highway Administration, Washington, D.C.

Humphrey, D. N. (1999). Civil engineering applications of chipped tyres. Research Report, North Platte, Nebraska.

Humphrey, D. N., Blumenthal, M. (2010). The use of tyre-derived aggregate in road construction applications. Green Streets and Highways 2010: An interactive Conference on the State of the Art and How to Achieve Sustainable Outcomes. Weinstein, N., ed., Reston, VA, USA: American Society of Civil Engineers, 2010.

Iglesia, G. R., Einstein, H. H., Whitman, R. V. (2013). Investigation of soil arching with centrifuge tests. J. Geotechnical and Geoenvironmental Engineering 140(2): 04013005.

Kahyaoğlu, M. R., Onal, O., Imançlı, G., Ozden G., Kayalar, A. Ş. (2012). Soil arching and load transfer mechanism for slope stabilized with piles, Journal of Civil Engineering and Management 18(5): 701–708.

Lee, H. J., Roh, H. S. (2007). The use of recycled tyre chips to minimize dynamic earth pressure during compaction of backfill. Construction and Building Materials 21: 1016–1026.

Lee, J. H., Salgado, R., Bernal, A., Lovell, C. W. (1999). Shredded tyres and rubber-sand as lightweight backfill. Journal of Geotechnical and Geoenvironmental Engineering 125 (2): 132–141.

Pan, B., Xie, H., Wang, Z., Qian, K., Wang, Z. (2008). Study on subset size selection in digital image correlation for speckle patterns. Optic Express 16(10): 7037–7048.

Peters, J., Lade, P., Bro, A. (1988). Shear band formation in triaxial and plane strain tests. Advanced triaxial testing of soil and rock, ASTM, STP 977, Donaghe, R., Chaney, R., Silver, M., (eds.), ASTM, 604–627.

Rubber Manufacturers Association (RMA), (2013). U.S. Scrap tyre market summary in 2011.

Schreier, H., Orteu, J., Sutton, M. (2009). Image correlation for shape, motion and deformation measurements. Springer US, Boston, MA.

Shalaby, A., Khan, R. A. (2005). Design of unsurfaced roads constructed with large-size shredded rubber tyres: a case study. Resources, Conservation and Recycling 44: 318–332.

Shelke, A., Patra, N. R. (2008). Effect of arching on uplift capacity of pile groups in sand. International Journal of Geomechanics 8(6): 347–354.

Singh, S., Sivakugan, N., Shukla, S. (2010). Can soil arching be insensitive to φ? International Journal of Geomechanics 10(3): 124–128.

Standards Australia (1998a). Australian Standard AS 1289.5.5.1 Soil compaction and density tests – Determination of the minimum and maximum dry density of a cohesionless material – Standard method.

Standards Australia (1998b). Australian Standard AS 1289.6.2.2 Methods of testing soils for engineering purposes – Soil strength and consolidation tests – Determination of shear strength of a soil – Direct shear test using a shear box.

Talesnick, M. (2013). Measuring soil pressure within a soil mass. Canadian Geotechnical Journal 50(7): 716-722

Terzaghi, K. (1936). Stress distribution in dry and in saturated sand above a yielding trap-door. Proceedings of the International Conference on Soil Mechanics and Foundation Engineering, Vol. I, pp. 307–311.

Tweedie, J.J., Humphrey, D.N., Sandford, T.C. (1998). Full scale field trials of tyre shreds as lightweight retaining wall backfill, at-test condition. Preprint, Transportation Research Board, Washington, D.C.

Tyrecycle (2018). http://www.tyrecycle.com.au. Accessed 20/09/18.

van Eekelen, S. J. M. (2015). Basal reinforced piled embankments: Experiments, field studies and the development and validation of a new analytical design model. PhD thesis, Department of Geoscience and Engineering, Delft University of Technology.

Vermeer, P. A., de Borst, R. (1998). Non-associated plasticity for soils, concrete and rock. HERON 29(3): 1984.29.

Wang, L., Leshchinsky, Evans, T. M., Xie, Y. (2017). Active and passive arching stresses in c'-φ' soils: A sensitivity study using computational limit analysis. Computers and Geotechnics 84: 47–57.

Yoon, S., Prezzi, M., Siddiki, N. Z., Kim, B. (2006). Construction of a test embankment using a sand-tyre shred mixture as fill material. Waste Management 26(9): 1033–1044.

Yuan, B., Chen, R., Teng, J., Peng, T., Feng, Z. (2014). Effect of passive pile on 3D ground deformation and on active pile response. The Scientific World Journal 2014: 904186.

Chapter 6: Conclusions

In the current research thesis, the arching effect in sand and rubber–sand mixtures with different rubber contents, namely 10% and 30% rubber, was examined using the Digital Image Correlation (DIC) technique and a series of stress measurement tests. A trapdoor apparatus was manufactured and instrumented with 15 pressure sensors. The effect of a local surcharge on the arching behaviour of the geomaterials employed in this study was also investigated. As mentioned in Chapter 1, the aims of this research were

1. To examine the applicability of the Digital Image Correlation (DIC) technique for displacement and strain analyses in granular soil, to identify the most relevant factors for successful implementation of the technique, and to assess the full-field deformation characteristics of granular soil subjected to arching;
2. To identify the key differences in the arching deformation of sand and rubber–sand backfills, particularly the strain localisation;
3. To analyse and compare the stress redistribution behaviour of sand and rubber–sand backfills at geomaterial–structure interface; and
4. To investigate the effect of a local surcharge on the stress and deformation response of sand and rubberised sand backfill subjected to arching.

The research was commenced by investigating the active arching effect in a coarse sand. Aim 1 was met by the experimental procedure and results of this study described and presented in Chapter 2. The imaging equipment and requirements necessary for a successful DIC analysis for granular material were discussed. High imaging speed, low distortion lens, appropriate subset size and step size, preparation of a speckle pattern and soil colouration, and upper limit of traditional DIC were recognised as the major factors in the implementation of the DIC technique for geotechnical research. A simple statistical method for determining the accuracy of any DIC system was examined. This method involves capturing a number

of images of the specimen prior to testing and obtaining the plots of the most relevant displacement or strain variable from image correlation. The closer the values of the deformation variable to zero the higher the accuracy of the DIC system used. Chapter 1 also showed that shape of the arch at normalised displacements up to ≈1.9% is triangular or curved triangular. The shape and the occurrence locations of the zones of low and high vertical strains within the sand backfill was identified and an idealised map of the vertical strains were presented. In addition, by measuring the stresses on the trapdoor, it was shown that the past mathematical models used to predict the stress reduction on an active trapdoor lack precision due to oversimplification. The DIC results of the study in Chapter 1 provides a stepping stone for better mathematical modelling of the arching effect in future.

Aim 1 was also pursued in Chapter 2 where the correct alignment of camera with respect to the specimen and minimum imaging speed are discussed. A baseline imaging speed of 80 frames per second for granular soil was proposed in this chapter. Strain localisation in active and passive arching modes in a coarse sand was particularly studied in details and shear bands were modelled. The shear bands were formed at locations where the gradient of the vertical displacements is maximum. It was observed that the passive arches encompass greater areas than the active arches do. Also, the normalised shear band thickness is greater in the passive arching mode. It was shown that the inclination angle of the shear bands correlates with the dilation angle, instead of the friction angle of the sand. Critical regions of substantial expansion or contraction developed in the sand layers were identified using the DIC technique. The shape and extension of the major volume change areas were found to be dependent on the arching mode, surcharge loading, and trapdoor displacement.

Aims 2–4 were attained in Chapter 3 that examined the active arching case in a sand and two rubber–sand mixtures. It was observed that the rubber inclusion improved the shear strength and reduced the material density. The DIC results showed that the rubber inclusions

also reduced surface subsidence and total arch height. The normalised shear band thickness was slightly increased at low rubber content and reduced in the high-rubber-content backfill to a level smaller than the original sand. Dilative regions were coincided with the shearing regions while the contractive regions appeared on the surface where subsidence occurred. The distribution of horizontal displacements and strains were found to be similar in pattern in the three backfills. However, the distributions of vertical strains were quite different and depended on material type and surcharge loading conditions. The presence of a curved triangular arch of geomaterial with the same amount of vertical displacement as the trapdoor element was realised in all the geomaterials tested. This region was referred to as 'the arch of equal displacement'. Stresses were measured continuously on the trapdoor and the adjacent stationary side. It was observed that, in the rubber–sand mixtures, the minimum stress ratio is maintained for a greater range of the trapdoor displacement compared to the sand backfill. Tangent arching modulus values were found to be pivoted on the geomaterial type. It was observed that rubber inclusion results in higher stress reduction due to active arching. Both ductile and brittle behaviour along the lengths of the trapdoor and the adjacent stationary side was observed. Overall, the deformation and stress behaviours in the active arching were found to be a function of material type or rubber percentage, and surcharge loading. However, the stress behaviour at structure–geomaterial interface was found to be also distance dependent.

For the passive arching case, Aims 2–4 were attained in Chapter 5. It was observed that the addition of rubber to sand considerably decreased deformability and the area affected by passive arching. The deformation behaviour due to passive arching was found to be a function of material type and surcharge conditions. It was shown by direct measurements that the dilation angles of the sand and rubber–sand specimens represent the inclination angle of the shear bands developed by a rising trapdoor. An alternative mathematical expression

for determining the dilation angle from a Mohr's circle of strains was proposed. A linear model for the calculation of tangent passive arching modulus was developed. The passive arching modulus values were obtained by regression for the sand and rubber–sand specimens. It was observed that, at small normalised displacements, the rubberised sand specimens show lower increase in the stresses due to passive arching. In addition, the rubberised sand specimens show a more uniform stress regime.

The overall contributions of this research thesis are summarised as follows:

- Evaluation and customisation of the DIC technique, and provision of the guidelines for the successful use of this technique for granular geomaterial;
- Determining the idealised vertical strains and shear band patterns in sand subjected to arching;
- Investigating the arching effect in rubberised sand backfills, and realising the geomaterial type, measurement location, rubber content, surcharge loading, and the mode of arching as the most relevant variables in the study of the arching behaviour;
- Considerably improved understanding of the arching effect in granular geomaterial by analysing and interpreting the deformation behaviour of different geomaterial from determining horizontal and vertical displacements and strains;
- Obtaining idealised ground response curves and arching moduli for sand and rubber–sand for active and passive arching cases from a series of stress measurement tests;
- Identification of the existence of 'the arch of equal displacement' in granular geomaterial subjected to arching, also determining the arch shapes in passive and arching cases;

- Experimentally proving that inclination angle of shear bands equals the angle of dilation of the backfill material; and
- Showing experimentally that the addition of rubber to granular soil results in reduced deformability and surface settlement, and higher stress reduction in the active arching case and lower stress increase in the passive arching case at small displacements.

6.1. Recommendations for future work

The values of the inclination angle of shear bands were slightly different in the passive and active arching effect as shown in Tables 3.1, 4.2, and 5.3. The reason for this observation can be the effect of the direction of deformation. In the active arching case, major displacements occur in the same direction as the gravitational force. On the other hand, in the passive arching scenario, the direction of displacement is against the gravity. As mentioned earlier, the value of the dilation angle, which determines the inclination angle, changes with boundary conditions and other physical conditions of deformation. Another possible explanation is a slight difference in the apparatus wall friction coefficient in downward (active arching) and upward (passive arching) directions. The following potential areas for further investigation are proposed on the basis of the findings of this research:

- The trapdoor experiments were conducted for shallow conditions where the ratio of geomaterial cover to the structure (trapdoor) length was less than 2. It is recommended to study the arching effect in deep conditions and compare the results.
- A local surcharge loading scheme was adopted in the current study. However, surcharge loading conditions such as the load amount, width of the surcharge block, number of surcharge blocks, and position of surcharge loading can be changed for future investigations.

- Mathematical modelling of the arching effect can be carried out using the deformation and stress behaviours observed in this study. In fact, this information will act as the stepping stone for more reliable and precise mathematical modelling. For example, the shape of arch can be considered by adopting the dilation angle of the geomaterial and a limit equilibrium analysis of the forces/stresses will lead to new mathematical expressions.
- Numerical modelling of the arching effect can be conducted using the finite element method or the discrete element method. As the DIC results are obtained from direct measurements, they will act as the criterion to judge the accuracy of the numerical methods. Appropriate constitutive relations for arching can be identified by comparing the outputs of the finite element modelling and the DIC results. The distribution of stresses in different geomaterial backfills can also be predicted using the finite element modelling. However, as granular materials show a non-associated behaviour, the modelled stress and measured deformation maps are expected to differ to some extent.
- The upper limit of the traditional DIC for the analysis of deformations in the trapdoor apparatus used in this study was 4.5 mm (a shear strain about 6%). It is recommended to use the co-called incremental DIC for larger displacements. It is intuitively expected that distribution regimes of the displacements and strains will be quite similar for a broad range of trapdoor displacement. However, the magnitude of strains will naturally increase with trapdoor displacement. The use of the incremental DIC will be challenging as the accuracy of the currently available algorithms is limited. Development of a more accurate image correlation algorithm, however, will be beyond the expertise of a geotechnical engineer.

- It is recommended to investigate the effects of scale and wall friction of the apparatus on stress and deformation. The influence of wall friction can be examined by installing walls of known, quantifiable, and different friction coefficients.